Subsurface Mapping of Deserts and Polar Regions Using Radar Data on Earth and Mars

Siting Xiong

A thesis submitted for the degree of

Doctor of Philosophy

Mullard Space Science Laboratory

Department of Space and Climate Physics

University College London

12 January 2019

I, Siting Xiong, confirm that the work presented in this thesis is my own. Where information has been derived from other sources, I confirm that this has been indicated in the thesis.

Abstract

There are abundant resources buried underground that are difficult to be investigated remotely. This thesis is concerned with the development and utility of various novel processing methods for different radar instruments in the field of subsurface mapping on Earth and Mars. Firstly, advanced Synthetic Aperture Radar (SAR) imaging and Interferometric SAR (InSAR) techniques are applied to assess their potential for revealing subsurface features in the eastern Sahara Desert. The radar penetration depth at L-band (1.25 GHz) is estimated to be 1-2 m over paleochannels in the Sahara Desert, given an initial assumption that radar penetration occurs in the sand accumulation areas. The L-band frequency of previous and existing spaceborne SAR mission is shown to limit the penetration depth to a few metres below the surface. However, over the terrestrial ice-sheets, a radar instrument, the Multi-Coherent Radar Depth Sounder (MCoRDS) from the NASA Operation Ice Bridge (OIB) mission, can penetrate the ice sheet down to 3 km, revealing extensive englacial layers. An automated layer tracing method based on the Continuous Wavelet Transform (CWT) and Hough Transform (HT) is proposed to detect and digitise these englacial layers in Greenland. The results show that this proposed method can restore at least 72% of the isochrones when compared with previous results. Given the research interests of the department and inspired by the similarity of the layering phenomenon between the Earth and Martian polar regions, the layer tracing method is adjusted and applied to SHAllow RADar (SHARAD) radargrams from the Mars Reconnaissance Orbiter. This method is demonstrated on the SHARAD data in Promethei Lingula as this

is the only region with coherent subsurface echo returns near the south pole, resulting in the extraction of six distinct subsurface interfaces, which record past depositional and erosional history and may be associated with past climate change on Mars.

Impact Statement

This thesis contributes to the development of a novel method for detecting englacial layers as well as three applications of radar subsurface mapping, to terrestrial deserts, ice sheets and the Martian south pole.

Radar penetration depth at L-band over dry sand areas in the eastern Sahara is estimated to be 1-2 metres by using the InSAR technique for the first time. The estimated penetration depth suggests that it is not feasible to map subsurface bedrock topography from L-band ALOS/PALSAR, ALOS-2/PALSAR-2 but is likely to be able to be constructed for low-frequency radar systems, such as the forthcoming P-band BIOMASS, in applications in deserts as well as englacial layers in ice sheets.

Subsurface mapping down to thousands of metres below the solid land surfaces on the Earth and Mars depends on the low frequency of radar sounding technique. However, existing analysis of radar sounding data is currently performed with high time and consequent high labour costs when using manual delineation and visual inspection with currently available semi-automated tools. Automated tools to perform such tasks are in high demand in both commercial and academic fields. This thesis proposes two new automated methods for radar sounding data obtained over ice sheets and the Martian south pole.

Corresponding high-level GIS tools are developed for these automated methods, which are believed to be useful prototypes and which can be further developed in related applications given the fact that the source codes are released to the public as open source. These automated methods can largely improve the efficiency of interpreting the subsurface images leaving more time for scientific users to concentrate on a scientific analysis of these detected subsurface features.

The first tool developed is an automated layer-tracing tool for MCoRDS data. This avoids manual interventions in the seed point selection, and significantly improves the density of traced layers. The efficiency and efficacy of the layer-tracing procedure is improved compared to published results in the literature. This automated method could potentially play a significant role in future studies about reconstruction of isochrones, englacial ice flows and subglacial lakes.

The second tool is modified from the aforementioned one and applied to SHARAD data near the south pole of Mars. Subsurface interfaces have previously been described and delineated manually in SHARAD radargrams over the Martian south pole in other published work. However, for the first time 3-D subsurface interfaces are automatically reconstructed by applying a processing system to the SHARAD dataset of Promethei Lingula near the Martian south pole. The results indicate a promising application over other sites on Mars like Elysium Planitia. This automated workflow avoids manual delineation on SHARAD radargrams, which used to take up a large amount of time. The reconstructed subsurface interfaces are generally in accordance with previously published

results which were delineated manually. Furthermore, another deeper irregular radar reflection interface is reported in this thesis, which may be another erosional episode during the formation of the SPLD. This finding should inspire future research associating this interface with past climate variation on Mars.

Acknowledgements

As my PhD years approach an end, I am very grateful that I have been accompanied all the way with several individuals, without whom this thesis would not have been possible. First and foremost, I offer my deepest gratitude to my supervisor, Prof. Jan-Peter Muller, whose encouragement, guidance and support from the beginning of my PhD study to the final writing year, have helped me on the track to become an independent researcher. My sincere gratitude goes to my secondary supervisors, Prof. Sanjeev Gupta and Dr. Dave Walton for suggesting interesting topics and useful tools related to my research and being so helpful and supportive all the time.

I also would like to express my sincere gratitude to members of the imaging group in Mullard Space Science Laboratory (MSSL) for offering multi-disciplinary knowledge in group meetings and daily discussions. Special thanks go to Ms. Rosalind Medland, Ms. Libby Daghorn, Ms. Suzanne Winter, Ms. Samantha Babister, Ms. Julia Wehrle, Ms. Phillippa Elwell and Dr. Daisuke Kawata for continuous support and help in various ways, including arranging panel meetings, booking flights for conferences, help in finding accommodations and so on. I am also grateful to computing group members in MSSL for their help in sorting out all kinds of problems related to devices.

As an overseas student, I am grateful that I have been able to immerse myself for four years in such a harmonious atmosphere in MSSL and meet so

many individuals of great personality, who are kind, friendly and helpful all the time.

Table of Contents

List of Figures

List of Tables

Abbreviations

AAS	Alcatel Alenia Spazio
AIS	Antarctica Ice Sheet
ALOS	Advanced Land Observation Satellite
APP	Automatic Phase Picker
APS	Atmospheric Phase Screen
ARESP	the Automatic Radio Echo Sounding Processing
ASF	Alaska Satellite Facility
ASI	Italian Space Agency
AVNIR	Advanced Visible and Near-Infrared Radiometer type
AUR1	Regional Angular Unconformity 1
BFL	Bench Forming Layer
BM3D	Block-Matching and 3D
BU	Basal Unit
CDF	Cumulative Distribution Function
CEP	Central Elysium Planitia
CReSIS	Centre for Remote Sensing of Ice Sheets
CS	Coefficient Summation
CTX	Context Camera

CWT	Continuous Wavelet Transform
DAF	Dorsa Argentea Formation
DBSCAN	Density-Based Spatial Clustering of Application with Noise
DEM	Digital Elevation Model
DInSAR	Differential SAR interferometry
DLR	German Space Agency
DORIS	the Delft Object-oriented Radar Interferometric Software
DOY	Day Of Year
ECMWF	European Centre for Medium-Range Weather Forecasts
EFZ	Echo Free Zone
EGM96	the Earth Gravitational Model 1996
EM	ElectroMagnetic
Envisat	Environmental Satellite
EO	Earth Observations
ERA	European Reanalysis
ERS	European Remote Sensing
ESA	European Space Agency
FBD	Fine Beam Dual-polarisation
FBS	Fine Beam Single-polarisation

FNF	Forest and Non-Forest
FR	Faraday Rotation
GMT	Generic Mapping Tools
GOTCHA	Gruen-Otto-Chau
GPR	Ground Penetrating Radar
GrIS	Greenland Ice Sheet
HiRISE	High Resolution Imaging Science Experiment
HRSC	High Resolution Stereo Camera
HT	Hough Transform
ICESat	the Ice, Cloud and Land Elevation Satellite
IEM	Integral Equation Model
IL	Inferred Layer
InSAR	Interferometric SAR/ SAR Interferometry
IRH	Internal Reflection Horizons
JAXA	Japan Aerospace Exploration Agency
JERS	Japanese Earth Resources Satellite
JPL	Jet Propulsion Laboratory
KISR	Kuwait Institute for Scientific Research
LCED	the L-band and C-band Elevation Difference

LiDAR	Light Detection And Ranging
LOS	Line Of Sight
LWT	Lifting Wavelet Transform
MARSIS	Mars Advanced Radar for Subsurface and Ionospheric Sounding
MCoRDS	Multi-channel Coherent Radar Depth Sounder
MEGDR	Mission Experiment Gridded Data Record
MEX	Mars Express
MEXH	Mexican hat
MGS	Mars Global Surveyor
MOC	Mars Orbital Camera
MODIS	MODerate-resolution Imaging Spectro-radiometer
MOLA	Mars Orbiter Laser Altimetry
MORL	Morlet
MRO	Mars Reconnaissance Orbiter
NASA	National Aeronautics and Space Administration
NEEM	North Greenland Eemian Ice Drilling
NGA	National Aeronautics and Space Administration
NPLD	North Polar Layered Deposit

NRIC	North Residual CO_2 Ice Cap
NSAS	Nubian Sandstone Aquifer System
NSIDC	the National Snow and Ice Data Center
OIB	Operation IceBridge
PALSAR	Phased Array type L-band Synthetic Aparture Radar
PL	Promethei Lingula
PLD	Polar Layered Deposit
PLL	Promethei Lingula Layer
PO	Planetary Observations
POL	Polarisation
PRF	Pulse Repetition Frequency
PRISM	Panchromatic Remote-sensing Instrument for Stereo Mapping
PWV	Precipitable Water Vapour
RDS	Radar Depth Sounder
RIC	Residual Ice Cap
RRRAG	Radiostratigraphy and Age Structure of the Greenland Ice Sheet
RT	Radon Transform
SAMPA	Semi-Automated Multilayer Picking Algorithm

SAR	Synthetic Aperture Radar
SHARAD	SHAllow RADar
SHOC	SHARAD Operation Centre
SIR	Shuttle Imaging Radar
SNAPHU	Statistical-cost, Network-flow Algorithm for Phase Unwrapping
SNR	Signal to Noise Ratio
SPLD	South Polar Layered Deposit
SRIC	South Residual CO_2 Ice Cap
SRTM	Shuttle Radar Topography Mission
SVD	Singular Vector Decomposition
SVM	Support Vector Machine
TEC	Total Electron Content
THEMIS	Thermal Emission Imaging System
TIN	Triangulated Irregular Network
TUDelft	Technical University of Delft
TWT	Two-Way Travel
USGS	United States Geological Survey
VICAR	Video Image Communication And Retrieval
WGS84	World Geodetic System 1984

WUSTL-PDS	Planetary Data System at Washington University in St. Louis, USA

List of Symbols

c	speed of light
ε	permittivity of medium
μ	permeability of medium
ε_0	permittivity of free space
μ_0	permeability of free space
v	velocity of the EM wave
ε_r	relative permittivity
ε_r'	the real part of the relative permittivity
ε_r''	the imagery part of the relative permittivity
$tan\delta$	the loss tangent
n	the refractive index
E_i	the incident EM radiation
E_r	energy of reflected EM radiation
E_t	energy of transmitted EM radiation
λ	wavelength
θ	incidence angle
h	the average vertical height of micro-relief

d	the thickness of the subsurface medium/ penetration depth
t	time delay
M	master acquisition of an InSAR pair
S	slave acquisition of an InSAR pair
I_m	intensity of the master acquisition
I_s	intensity of the slave acquisition
ϕ_m	phase of the master acquisition
ϕ_s	phase of the slave acquisition
$\Delta\phi$	phase difference of the master and slave acquisitions
R_m	slant range of the master acquisition
R_s	slant range of the slave acquisition
ΔR	slant range difference
H	height of the ground target
$B_\perp$	the perpendicular baseline
d_{disp}	land displacement
ϕ_{orb}	phase component caused by orbit error
ϕ_{ion}	phase component caused by ionospheric effect
ϕ_{tro}	phase component caused by tropospheric effect
ϕ_{dis}	phase component caused by surface displacement

ϕ_{ele_dif}	phase component caused by penetration at different wavelengths
ϕ_{noi}	phase component caused by noises
p	topographic variation
σ_h	elevation dispersion (standard deviation)
σ_ϕ	phase dispersion (standard deviation)
NL	number of looks
r	coherence
ΔTEC	difference in Total Electron Content
Ω	Faraday rotation angle
e	the elementary charge
m_e	the electron mass
θ_t	the angle between the SAR signal propagation direction and the B-field
f	carrier frequency of the radar
$\boldsymbol{B}$	magnetic field
ΔTEC	difference in Total Electron Content
N	number of samples
σ_{SD}	standard deviation of samples
σ_{SM}	standard deviation of mean

A	area of one surface type
R	spatial correlation distance
$x(t)$	a series of the two-way travel time radar signals
$\psi(t)$	the wavelet
C	the wavelet coefficient
a	scale of the wavelet
b	translation of the wavelet
i	row number of one pixel in image
j	column number of one pixel in image
θ_l	angle of a line calculated from horizontal axis
ρ_l	distance from the image centre to a line feature
$HT(\rho_l, \theta_l)$	image intensity in Hough Transform domain
$G(f, \alpha)$	log-Gabor filtering at frequency, f, and orientation, α
T	the threshold used in log-Gabor filtering
f_0	the central frequency of log-Gabor filtering kernels
α_0	the central orientation of log-Gabor filtering kernels
σ_f	the bandwidth parameter for log-Gabor filtering
σ_α	the width parameter of the orientation filters
σ_g	standard deviation of the amplitude response of radargram

(μ_r, σ_r)	Parameters describing the Rayleigh distribution
j_c	column number of one pixel in a cluttergram
t_c	time delay (row number) of one pixel in a cluttergram
(x, y)	the projected geographical position of a reflector
$\xi(j_c, t_c)$	intensity of pixels in the cluttergram

Chapter 1

Introduction

1.1 Background and Motivation

Remote sensing is a well-established technique for detecting, measuring and monitoring surface targets by using electromagnetic waves without direct contact. It has been widely applied to monitor environment changes occurring on the Earth (i.e. Earth Observations, EO), such as biomass changes (Cloude & Papathanassiou, 1998), monitoring of sea ice and sea wind (Zwally et al., 2002), 3-D city mapping (Sirmacek et al., 2012). Remote sensing tools have also been used to map surface features on other planets (i.e. Planetary Observations), such as surface terrain measurements (Kim & Muller, 2009), atmospheric conditions and dust monitoring on Mars (Hamilton, McSween & Hapke, 2005). One subject of remote sensing in geology is to study what is going on below planetary surfaces using surface geomorphology observed by remote sensing instruments, such as multispectral imagers, hyperspectral imagers and imaging radars (Siegal & Gillespie, 1980). Interpreting surface geomorphology to obtain knowledge about subsurface regions depends on an interpreters' knowledge and understanding about local geology. Passive remote sensors like hyperspectral imagers record reflectance of targets in sunlight, while active remote sensing instruments such as radars which transmit electromagnetic waves to targets and

receive backscattered waves. Technically, direct observations of subsurface regions can be realised by pointing a radar antenna to the ground and given the right frequency range, the radar waves can penetrate below the ground surface. The corresponding penetration depth ranges from several centimetres up to several kilometres, depending on the wave frequency and the intervening environment which the waves are propagating through. Radar returns from dielectric boundaries below the surface provide knowledge about subsurface features. This is of great value to the science community as it can provide direct observations of subsurface features such as underground aquifers or geologic stratigraphy, which shed light on the evolution of the land, forests or ice cover.

In Earth Observation, radar systems operating at frequencies across the Very High Frequency (VHF, ranging from a wavelength of 1-10 m, and a corresponding frequency range of 300 -30 MHz) to microwave (ranging from 0.1 cm - 100 cm, 300 GHz - 300 MHz) bands are usually used in subsurface remote sensing. Synthetic Aperture Radar (SAR) systems use radars which operate at the microwave spectrum and the current lowest frequency used in orbits is L-band (1.25 GHz). This frequency will be extended lower to P-band (435 MHz) in the future European Space Agency (ESA) BIOMASS mission (expected to be launched in 2021) (ESA, 2015). It is harder to use lower frequency radar systems in orbit because the ionosphere causes a large delay to low frequency radar waves or even reflects them when it comes to frequencies ranging from 3 MHz to 30 MHz. Radar sounders are another type of radar used for subsurface mapping, and they are designed to be employed on an aircraft to measure ice

thickness since the 1960s (Evans, 1961; Waite & Schmidt, 1962). Depending on the specific requirements of different applications, radar sounders differ in radar configuration and imaging geometry. In different application domains, they are termed different names, such as radar depth sounders, radio echo sounders and ice-penetrating radars. In this thesis, the generic term “radar sounder” is used to refer to instruments that penetrate through the surface and detect subsurface targets for consistency. Observations from radar sounders are limited to a local scale with far smaller areas sampled as they are usually configured on aircraft or vehicles on the Earth. In Planetary Observations, radar sounders are routinely used to study subsurface stratigraphy and dielectric properties. Thanks to the thin atmosphere on Mars and the lack of a significant ionosphere, orbital radars have been used to collect data for decades, and these data are visually inspected and manually digitised, where they are inspected. Compared to surface mapping, subsurface mapping has limitations of data coverage on the Earth and of the lack of analysis tools for application to both Earth and Mars. Considering that significant resources, such as water and minerals are buried underground, as well as new information on planetary geological history contained beneath the surface, subsurface mapping using multi-source remote sensing instruments is being increasingly recognised as having great potential by the remote sensing community.

Spaceborne SAR is a well-developed technique that is used to acquire 2-D imagery of the Earth surface (Zebker & Goldstein, 1986; Rufino, Moccia & Esposito, 1998; Ferretti, Prati & Rocca, 1999; Ferretti et al., 2007; Gruber et al.,

2012). Different SAR systems, such as the X-band TerraSAR, C-band ERS/Envisat, Radarsat-1/2, and Sentinel-1, L-band JERS and ALOS-1/2, have all been used to produce Digital Elevation Models (DEMs) as well as for estimating canopy-top height (Cloude & Papathanassiou, 1998; Papathanassiou & Cloude, 2001; Walker et al., 2007; Walker, Kellndorfer & Pierce, 2007). When using SAR data, it should be noted that radar waves at different wavelengths have different penetration depths over the same land surface cover, and this penetration depth increases with decreasing wave frequency (i.e. increasing wavelength). Utilising this penetration depth difference, different frequencies are suitable for different land surfaces, such as forest, ice and sand. For instance, L-band SAR imagery from the SIR-A mission first revealed buried paleochannels (a paleochannel is a remnant of an inactive river or stream channel that has been filled or buried by younger sediment) down to 5 m in the Sahara desert (McCauley et al., 1982), while Rignot, Echelmeyer & Krabill (2001) have reported that the X-band, C-band and L-band SAR images show increasing penetration depths in glaciers. Although InSAR has been developed into a standard technique for DEM production, the derived elevations are often assumed to be surface elevations, the same as the elevations derived from laser altimetry and stereo-photogrammetry. It is therefore worthwhile studying to what extent the elevation derived by using InSAR is affected by the penetration of radar waves.

On the Earth, glaciers and deserts are two typical land types where subsurface mapping at regional scales relies mainly on radar sounders, such as the Multi-channel Coherent Radar Depth Sounder (MCoRDS) of the National

Aeronautics and Space Administration (NASA) Operation IceBridge (OIB, 195 MHz - 14 GHz) mission (Shi et al., 2010; Studinger, Koenig & Martin, 2010) as well as another NASA airborne project over the Kuwait desert (Buis, 2011). The latter one is a collaboration between the Kuwait Institute for Scientific Research (KISR) and NASA. It purportedly carried out a mapping survey of subsurface water resources by using the same radar sounding technology that has been used in Mars exploration which is at a much lower frequency than systems like MCoRDS. In the field of Mars exploration, two radar sounders, the Mars Advanced Radar for Subsurface and Ionospheric Sounding (MARSIS) (Jordan et al., 2009) and the SHAllow RADar (SHARAD) (Seu et al., 2004), were placed in orbit around Mars in 2005 and 2006 respectively to investigate the existence of subsurface geological structures, which may be associated with ice and water. Data from MARSIS and SHARAD have been successfully used to map basal topography and to estimate the volume of the Martian Polar Layered Deposits (PLDs). Since subsurface water is suspected to exist on other planets, such as the Moon (Porcello et al., 1974) and Europa (Bruzzone et al., 2011; Bruzzone et al., 2013), similar radar sounders for subsurface mapping are currently being developed for the NASA Europa Clipper and ESA JUICE missions.

Some radar sounding systems also use a synthetic aperture technique in the along-track direction, but they are different from SAR systems in several ways. They use a lower frequency and a different imaging geometry. Radar sounders can penetrate to a lower depth and can thus reveal the vertical structure of deeper buried subsurface features. Different from SAR, the radar sounder is a nadir

looking radar instrument, which means that the format of the radar sounding data are 1-D profiles rather than 2-D maps in the horizontal plane. One frame of radar sounding data from one orbit with a consistent radar configuration is usually called a radargram. The current extraction and tracing of subsurface features in radargrams primarily relies on human digitisation. In order to be able to perform information extraction in a much more efficient and speedy manner, It is necessary to develop automated methods for subsurface feature extraction. It is also important to develop methods to combine radar sounding data from adjacent and intersected orbits/transects to map the 3-D geometry of subsurface features associated with subsurface stratigraphy. In addition, these subsurface features or stratigraphy can be studied and fused with external surface data, such as surface DEMs from lidar which on Mars means Mars Orbiter Laser Altimeter (MOLA) as well as with stereo from the High Resolution Stereo Camera (HRSC), the Context Camera (CTX) and the High Resolution Imaging Science Experiment (HiRISE).

1.2 Aims and Objectives

The original aim was to apply InSAR for the exploration of paleochannels driven by the L-band observations of Paillou et al. (2009) which itself was based on the initial work performed on SIR-A data in the 1980s. In particular, the detection of bedrock where the overlying sand was dry enough and the bedrock close enough to the surface. Observations by NASA which were reported in an online press release using a much lower frequency (40 MHz) radar over Kuwait that an aircraft had mapped subsurface aquifers at depths ranging from 20 to 65

m (Buis, 2011). Subsequently, after the research had proceeded for almost a year, a report from the British Geological Survey showed that aquifers in the Sahara desert were at depths of about 25-100 m below the surface (MacDonald et al., 2011). This is well beyond the range of L-band SAR and probably beyond the range of the NASA low-frequency radar. In addition, it was impossible to carry out field work using a GPR for verification in the eastern Sahara Desert due to the political instability in the region.

Regardless of the failure of detecting subsurface aquifers, the InSAR technique was successfully applied to the eastern Sahara Deserts to acquire several interferograms. Starting from these L-band SAR interferograms, elevation information was retrieved in an investigation into the possibility of using SAR imagery to estimate the penetration depth of L-band radar waves in paleochannels of the Kufra region was performed.

After this study was concluded looking at deserts, it is clear that until the ESA BIOMASS mission is launched that there is little chance that the mapping of bedrock subsurface topography from EO SARs is feasible. It was therefore decided to shift the focus to the exploration of radar sounder data over large ice sheets as the radar sounder data over Kuwait was not available. It is worth noting that radar sounders have played an important role in revealing subsurface layers in terrestrial ice sheets. Although a large amount of radar sounding data has been accumulated, its analysis involves a significant amount of manual work to digitise visible boundaries of englacial layers. Therefore, one objective of this thesis was to design an automated method to extract subsurface layers from radar sounding

data. Having developed a novel technique for englacial layer detection, it was decided to apply this to the subsurface of Mars where new datasets had recently become available and where the potential for major new discoveries was higher. Therefore, the third and final objective was to apply this layer detection to multi-track radar sounding data and then to reconstruct a 3-D structure of subsurface features (such as layers or interfaces).

Based on the aims of this thesis, the following research questions are addressed here:

- demonstrate to what degree L-band SAR penetration beneath surfaces of dry sand cover, can be employed to map the associated penetration depth. This is based on previous work which showed substantial differences in radar backscatter amplitude at particular polarisations over deserts as well as follow-up fieldwork which showed these features referred to buried paleochannels that were not observed in visible satellite imagery,
- Radar sounding technique have been demonstrated to have utility in subsurface mapping over terrestrial ice sheets and the Martian PLDs. Following on from this, what is similarity of these two applications and datasets? Is it possible to develop one common automated method to process radargrams for these two applications? What is their effectiveness and efficiency compared to manually delineated results?
- If an automated method can be developed to extract subsurface layers from radargrams, is it possible to reconstruct a 3-D “block diagram” of subsurface regions/layers using radar sounding data from multiple orbits?

And can such a reconstruction be applied to MCoRDS and SHARAD datasets?

By addressing the above-mentioned questions, the following results should be able to be achieved.

- SAR imagery acquired by C-band SRTM and L-band PALSAR will be compared to Landsat imagery to investigate the different appearances of features that are invisible in Landsat imagery and which appear to originate from subsurface reflections. Building on this, InSAR techniques will be applied to an L-band ALOS/PALSAR dataset. Taking the C-band SRTM DEM as a reference surface, the elevation difference is mapped between them to provide a way to estimate the penetration depth at L-band radar waves of paleochannels underneath the sand cover of the Kufra region.
- Methods for extracting and tracing layers in ice bodies from radargrams are reviewed. After showing the results and limitations of existing methods, an automated method is developed to extract layers from radargrams. Then, this proposed method is tested by applying it to MCoRDS data of Greenland and subsequently SHARAD data of the Martian PLDs.
- Finally, the proposed automated layer extraction method is adapted and applied to radargrams of Martian PLDs combining these subsurface DEMs in order to reconstruct a 3-D “block diagram”.

1.3 Thesis Structure

The structure of this thesis is listed as below.

In Chapter 2, a literature review of the current state of knowledge in the context of the aims and objectives of the thesis is presented and summarised.

In Chapter 3, a study on penetration depth estimation in deserts using L-band ALOS/PALSAR datasets is presented. The main part of this chapter has been published as “The Application of ALOS/PALSAR InSAR to Measure Subsurface Penetration Depths in Deserts” in Volume 9, Issue 6 of Remote sensing, 2017.

In Chapter 4, an automated method for tracing subsurface englacial layers from radargrams in Greenland is designed and described in detail. The main part of this chapter has been published as “A New Method for Automatically Tracing Englacial Layers from MCoRDS data in NW Greenland” in Volume 10, Issue 1, page 43 of Remote sensing, 2017.

In Chapter 5, the aforementioned automated method is modified and applied to Martian SHARAD data and used to reconstruct 3D subsurface interfaces of the Promethei. The main part of this chapter has been published as “Automated Reconstruction of Subsurface Interfaces in Promethei Lingula near the Martian South Pole by using SHARAD Data” of Planetary and Space Science, 2018.

Finally, the results are concluded along with a future look at the state of the art in terms of SAR and radar sounding techniques for subsurface mapping in Chapter 6.

Chapter 2

Literature Review

This chapter aims at providing background information and fundamental concepts used in the following chapters to readers. Firstly, the propagation of radar waves in subsurface media is introduced, especially where the waves encounter subsurface layers. Secondly, three radar instruments, namely a spaceborne SAR, GPR, and radar sounders, are introduced. Finally, the state of the art of their applications in subsurface mapping over deserts, polar ice sheets and the Martian PLDs are reviewed and summarised.

2.1 Electromagnetic (EM) radiation

Electromagnetic (EM) radiation consists of photons or waves of oscillating electric and magnetic fields. In the radar remote sensing field, EM radiation is treated in the form of waves. When the EM wave propagate in the probed medium, its velocity depends on the permittivity ε, and permeability μ, of the probed medium as shown in Equation (2.1). Permittivity determines how the substance modifies an electric field while permeability describes the modification of the magnetic flux in the region by the substance.

$$v = \frac{1}{\sqrt{\varepsilon\mu}} \tag{2.1}$$

The propagation velocity of the EM radiation in a free space is $c = 2.99\times10^{8}\ ms^{-1}$. This velocity is related to the permittivity ε_0, and permeability μ_0, of free space as shown in Equation (2.2).

$$c = \frac{1}{\sqrt{\varepsilon_0 \mu_0}} \tag{2.2}$$

Different materials behave differently with the varying wavelengths of the incident EM radiation, which lays the basis for radar remote sensing. Most transparent materials are nonmagnetic, so they have magnetic permeabilities that are very close to the free space value. Therefore, the velocity of the incident radar wave in a transparent medium can be calculated using the permittivities of free space and the medium, which are often substituted by a dimensionless relative permittivity ε_r (dielectric constant) in Equation (2.3).

$$v = \frac{c}{\sqrt{\varepsilon/\varepsilon_0}} = \frac{c}{\sqrt{\varepsilon_r}} \tag{2.3}$$

The dielectric constant can be expressed as a complex number as shown in Equation (2.4). The real part of the complex permittivity, ε_r' , directly influences the propagation velocity of the EM radiation. The imaginary part, ε_r'', is related to the dielectric loss of the EM radiation caused by the conductivity of the probed medium. The loss tangent is defined as the ratio of the imaginary part to the real part of the permittivity as shown in Equation (2.5). It shows the amount of the EM radiation which is transformed into heat. Impurities of conducting materials can change the dielectric behaviour of the medium. In addition, scattering losses from the EM radiation results from volume scattering in the medium if it is

inhomogeneous. The refracted energy of the EM radiation is attenuated exponentially. The attenuation caused by both dielectric loss and scattering loss limits the penetration depth.

$$\varepsilon_r = \frac{\varepsilon}{\varepsilon_0} = \varepsilon_r' - j\varepsilon_r'' \tag{2.4}$$

$$tan\delta = \frac{\varepsilon_r''}{\varepsilon_r'} \tag{2.5}$$

At the boundary of two layered media with different permittivities, a part of the EM energy is reflected and another part is refracted, which is shown in Figure 2.1. This boundary is called the dielectric boundary. The amount of reflected energy, E_r, and transmitted energy, E_t, are determined by Equations (2.6) and (2.7), respectively, where $n = \sqrt{\varepsilon_r}$ is the refractive index of the medium and E_i is the energy of the incident EM radiation. The higher the difference between the refraction indices of the two media is, the more energy is reflected.

$$E_r = \left(\frac{n_2 - n_1}{n_2 + n_1}\right) E_i \tag{2.6}$$

$$E_t = \left(\frac{2n_1}{2n_2 + n_1}\right) E_i \tag{2.7}$$

Overall, the EM radiation is either reflected or transmitted in the subsurface medium at a dielectric boundary. The reflection at the surface can be specular from a smooth surface, diffuse from a rough surface or a combination of both, as shown in Figure 2.2. If the local slope angle is high, the backscattering energy from specular reflection can be high, as shown in Figure 2.2(d). The roughness of the surface is a relative concept, which relates how the EM radiation is

scattered at wavelength, λ, with incidence angle, θ. Their relationship can be defined by the Rayleigh criterion, which considers a surface to be smooth if the average vertical height of micro-relief meets the following criterion, which is shown in Equation (2.8) (McCauley et al., 1982; Berlin et al., 1986).

$$h < \frac{\lambda}{8cos\theta} \tag{2.8}$$

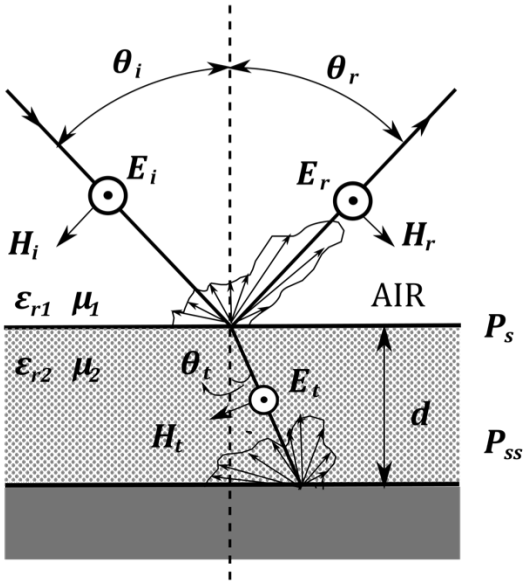

Figure 2.1: A sketch showing reflection and transmission of a horizontally polarised wave, adapted from (McCauley et al., 1982).

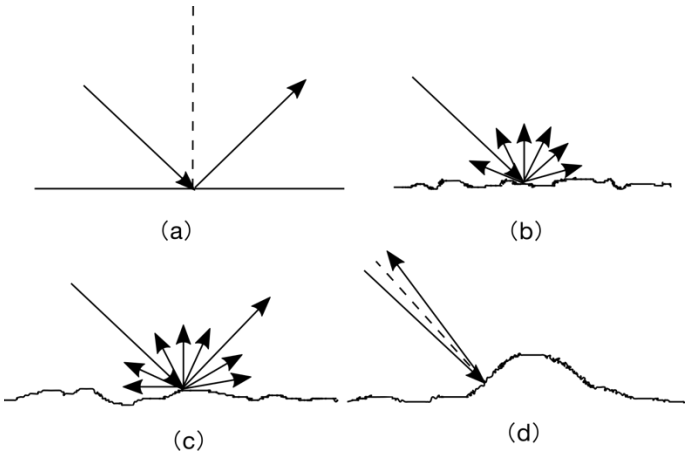

Figure 2.2: (a) Specular reflection; (b) diffuse scattering; (c) a combination of specular and diffuse reflections; (d) corner reflection.

In the nadir looking geometry, the velocity of the EM radiation in a medium can also be calculated by using the time delay t, and the depth of a subsurface reflection d, as Equation (2.9). Basically, if we know the time delay and the depth of the subsurface reflection, the relative dielectric constant, ε_r, of the subsurface medium can be derived from Equations (2.3) and (2.9) (Nouvel et al., 2006; Watters et al., 2007).

$$v = \frac{2d}{t} \tag{2.9}$$

In conclusion, the penetration depth of radar waves from free space to a medium depends on several factors including (1) properties of the incident waves, such as wavelength and polarisation, (2) incident geometry, like incident and azimuth angles, and (3) the characteristics of the probed medium, such as surface roughness, dielectric properties and volume scattering coefficient in inhomogeneous media (McCauley et al., 1982).

2.2 Radar systems for Subsurface Mapping

Radar systems generally consist of a transmitter (Tx), a receiver (Rx), and a corresponding pair of antennas. The transmitter generates a pulse of radar waves which are propagated to the ground surface where they are reflected or refracted. The receiver detects the reflected signal and the direct air wave. The direct air wave is transmitted from the transmitter to the receiver directly and has no contact with the ground. In some radar systems, the Tx and Rx share the same antenna, thus, there is no direct air wave. In the following subsections, three types of radar systems which have been used for subsurface mapping will be introduced. They are spaceborne SAR, GPR and radar sounders.

2.2.1 Spaceborne SAR

SAR is used for acquiring the 2-D microwave backscatter imagery of the land surface. The resolution of radar imaging is limited by the physical aperture length. Synthetic Aperture refers to the method of simulating the effect of a large aperture by using the spacecraft motion. Any SAR system can be configured on a spacecraft or aerial platform and usually utilises the side-looking imaging geometry, as shown in Figure 2.3. It transmits pulsed radar waves and receives backscattered signals. The transmitter and receiver usually share the same antenna. The earliest civilian success of a spaceborne SAR mission was the Seasat L-band mission in 1978. After its success, more and more countries have sought to develop spaceborne SAR systems, such as the L-band systems for JERS-1 and ALOS-1/2 developed and launched by Japan; ERS-1/2, Envisat and

Sentinel-1A launched by ESA; RADARSAT-1/2 by Canada; TerraSAR-X by Germany and COSMO-SkyMed by Italy. Among these SAR missions, the Japanese ALOS-1/2 are two successive spaceborne SAR missions, in which L-band SAR systems were used. L-band has many advantages over other wavelengths (X-band and C-band) in terms of subsurface mapping over sandy and icy areas since a deeper penetration depth can be achieved with a lower frequency (Rignot, Echelmeyer & Krabill, 2001). Imagery from JERS-1 and ALOS-1 have been used for mapping subsurface features in a sandy area in the eastern Sahara (Paillou & Rosenqvist, 2003; Paillou et al., 2009; Paillou et al., 2010). Other previous studies of subsurface mapping using spaceborne SAR data are reviewed in Section 2.3.

In January 2006, the Japan Aerospace Exploration Agency (JAXA) launched an Earth Observation satellite, the Advanced Land Observing Satellite (ALOS), which carried two optical instruments (Panchromatic Remote-sensing Instrument for Stereo Mapping, PRISM and Advanced Visible and Near-Infrared Radiometer type 2, AVNIR-2), and an L-band SAR, the Phase Array L-band SAR (PALSAR). ALOS was declared operational on October 23, 2006, after commissioning, calibration and validation during the first nine months of the mission (Rosenqvist et al., 2007). From PALSAR's 132 possible mode options, Fine Beam Single-polarisation (FBS), Fine Beam Dual-polarisation (FBD), full POLarisation (POL) and ScanSAR were chosen as the default modes (Rosenqvist et al., 2007). Parameters of these SAR configuration are listed in Table 2.1.

Table 2.1: ALOS/PALSAR operational imaging modes (FB is acronym of Fine Beam and pol. denotes polarisation), parameters are extracted from (Rosenqvist et al., 2007).

Mode	FB Single pol.	FB Dual pol.	Full pol.	ScanSAR
Centre frequency	1270 MHz (L-band, wavelength, 23.6 cm)			
Band width	28 MHz	14 MHz	14 MHz	14/28 MHz
Polarisation	HH/VV	HH+HV/ VV + VH	HH+HV+VV+VH	HH
Incidence angle	8° - 60°	8° - 60°	8° - 30°	18° - 43°
Azimuth resolution	10 m	20 m	30 m	100 m
Range resolution	7 – 44 m	14 – 88 m	24 – 89 m	100 m
Swath width	40 - 70 km	40 - 70 km	20 - 65 km	250-350 km
Pass direction	Ascending	Ascending	Ascending	Descending

Different polarisation modes represent different combinations of transmitted and received radar waves. For example, HH denotes horizontal wave is sent and received by the radar, and HV means radar sends out horizontal wave but receives vertical wave. Paillou et al. (2010) demonstrated that by combining HH and HV, bedrock features could be observed across the Sahara Desert and that paleochannel (which he called paleo-river) features are visible at both polarisations with the FBD observations that were typically used for measuring forest height, which is similar to measuring penetration depths of radar waves in sandy areas. In addition, the FBD mode is the default mode of PALSAR, therefore the FBD mode data is suggested to be used primarily. The penetration depth is affected by different polarisation modes, which is further discussed in Section 2.3.1. FBS observations are scheduled during the (Northern Hemisphere) winter

ranging from December to March, and FBD observations are scheduled during summer months ranging from June to October. The imaging geometry of several ALOS/PALSAR operative modes is illustrated in Figure 2.3.

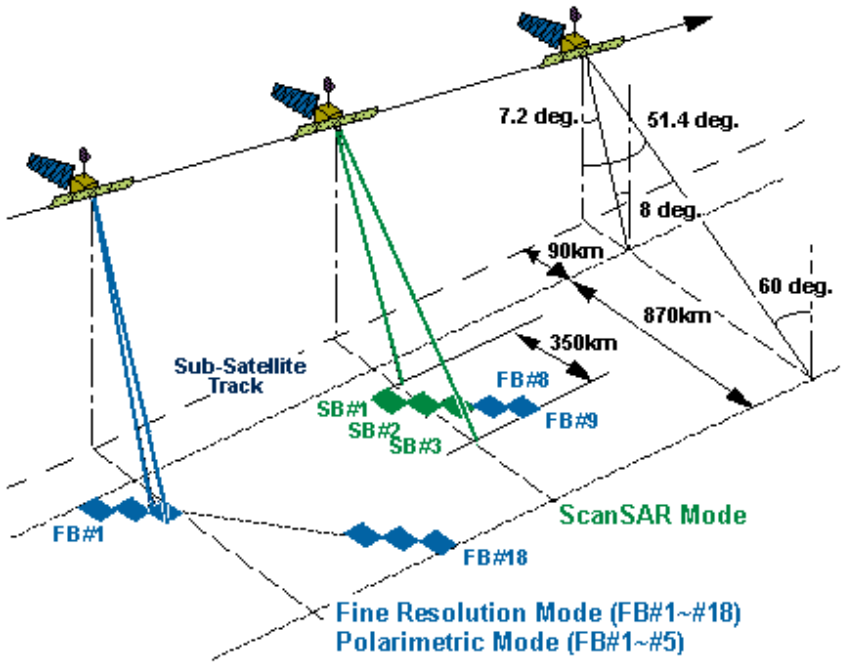

Figure 2.3: Imaging geometry of the operative modes of ALOS/PALSAR. (Image source from http://www.eorc.jaxa.jp/ALOS/en/about/palsar.htm).

2.2.2 Radar sounders

Radar sounding is an established geophysical technique for studying subsurface areas primarily in deserts and glaciers on the Earth. It has been applied to subsurface studies on planets, such as the Moon and Mars. Moreover, it will be used on Jupiter's icy moon, Ganymede, where the existence of a large ice body is strongly suspected in the subsurface areas (Bruzzone et al., 2011). Two radar sounders will be introduced in this section. One is the MCoRDS that

has been used for subsurface mapping of Greenland Ice Sheet (GrIS) and Antarctica Ice Sheet (AIS), and the other is the SHARAD onboard Mars Reconnaissance Orbiter (MRO). The radar sounders are usually nadir-looking as shown in Figure 2.4, which is different from spaceborne SAR systems. The data acquired by radar sounders are termed radargrams, in which the x-axis is the geographical location and the y-axis denotes the two-way travel time or depth (often assuming a single dielectric constant of free space).

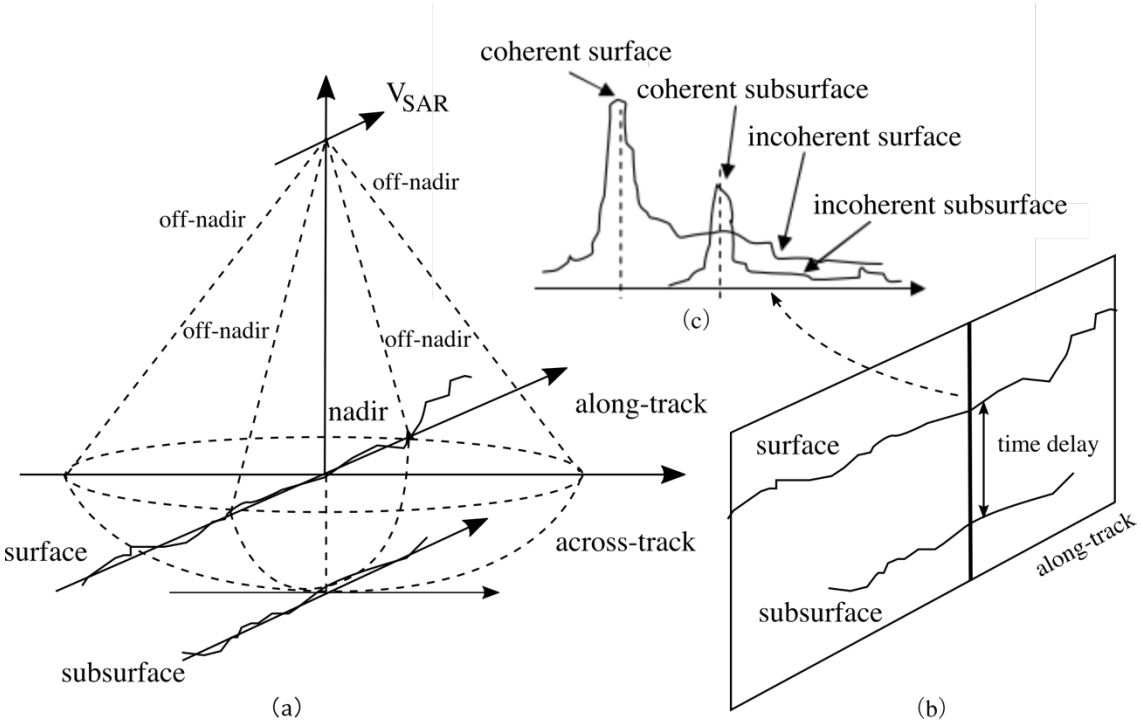

Figure 2.4: (a) The imaging geometry and (b) formation of radargrams from radar sounders; (c) surface and subsurface reflections from a series of signals. Images are adapted from Iorio et al. (2007)'s paper.

As we can see in Figure 2.4, radargrams usually suffer from off-nadir clutter effect. Some off-nadir echoes from high elevation areas may travel the same or shorter distances than the nadir echoes travel, which results in false subsurface

echoes. In other words, subsurface reflections in radargrams may be confused between real subsurface features and artefacts arising from off-nadir surface reflections. The clutter reflections depend on the topography of the area and appear frequently in heavily cratered areas. The clutter reflections affect the interpretation of SHARAD data and can be severe when the radar beam has a larger horizontal coverage with a dramatic topographic variation. There are many studies about removing or mitigating the clutter effect by modelling the coherent or incoherent surface reflections with surface DTMs, such as MOLA DTM (Campbell, Ghent & Shepard, 2003; Ilyushin, 2004; Russo et al., 2008; Spagnuolo et al., 2011; Ferro et al., 2013; Wu et al., 2015; Choudhary, Holt & Kempf, 2016). Most of these studies demonstrated the simulation of clutter reflections from surface DTMs; however, few of them discussed the removal of clutter reflections from radargrams.

MCoRDS in the OIB mission

The MCoRDS was developed by the Center for Remote Sensing of Ice Sheets (CReSIS) in the University of Kansas, and is one of the five radar instruments used in the Operation IceBridge mission which aims to bridge the temporal gap between the Ice, Cloud and Land Elevation Satellite (ICESat) which ceased in 2009 and ICESat-2 planned to be launched in 2018. The MCoRDS is a nadir-looking, five-channel, monostatic radar system (Shi et al., 2010). It operates at low frequency and is designed to penetrate up to several kilometres into the polar ice sheets. Before 2010, the radar system operated at a centre frequency of 150 MHz, and a bandwidth of 17 MHz with a peak transmit power of

200 W. From 2010 onwards, the centre frequency was changed to 195 MHz with a bandwidth of 30 MHz and with increasing peak transmit power up to 1200 W. Detailed parameters about the radar instrument are listed in Table 2.2.

SHARAD on board MRO

SHARAD is used for mapping the subsurface area of the Martian crust. It works at one frequency centred at 20 MHz with a bandwidth of 10 MHz, which leads to a range resolution of about 15 m in free space. The spatial resolution in the cross-track direction is 3-6 km and 0.3-1 km in the along-track direction after synthetic aperture processing along this direction. The characteristics of the SHARAD are listed and compared with the MCoRDS in Table 2.2. The SHARAD radargrams are available from the Geosciences Node of the Planetary Data System at Washington University in St. Louis, USA (WUSTL-PDS) in two types of datasets. One type is processed and provided by the SHARAD Operation Centre (SHOC) of Alcatel Alenia Spazio (AAS) in Rome, Italy. The other type is provided by SHARAD team in JPL, USA. The two datasets are processed using different parameters in range and doppler focusing. Table 2.2 lists the nominal resolutions of the SHARAD. Products from Italian and US teams may differ from each other in some of the listed processing parameters in Table 2.3.

Table 2.2: Characteristics of the MCoRDS and the SHARAD subsurface radar profilers.

Instrument Names	**MCoRDS**	**SHARAD**
Launch year	2009	2005
Mission	NASA's Operation IceBridge	NASA's Mars Reconnaissance Orbiter
Technique	SAR	SAR
Frequency	195 MHz	20 MHz
Bandwidth	30 MHz	10 MHz
Antenna	$\lambda/2$ bow-tie dipole	10 m tip-to-tip dipole
Transmitted power	1200 W	10 W
Pulse repetition frequency (PRF)	9000 Hz	700 or 350 Hz
Platform altitude	~ 500 m	255-320 km
Vertical resolution	~ 2.8 m (V2)	15 m (vacuum)
Along-track resolution	~ 13.6 m (V2)	0.3-1 km
Across-track resolution	641~5416 m (DC-8) 323~651 m (P-3)	3-6 km
Penetration depth	> 3 km	< ~ 1 km

Table 2.3: Comparison between US and Italian SHARAD radargram processing parameters (Campbell, 2014).

Parameters	**US Product**	**Italian Product**
Chirp Envelope	Uniform with frequency	Ground Calibration
Ionospheric Compensation	Empirically derived function	Phase gradient autofocus
Aperture Length	8.77 seconds	1-2 seconds
Along-track Posting	128 ppd = 460 m	300 m
Delay Resolution	0.0375 μs	0.0659 μs
Number of Looks	7	1

The frequencies used by the radar sounders depend on the requirements of different applications. The MCoRDS and the SHARAD feature a common synthetic aperture processing in the along-track direction, which improves the along-track resolution. Radargrams are the common data format acquired by these two radar sounders. Radargrams record radar reflections which denote the subsurface dielectric boundaries. The radargrams directly record the internal structures and stratigraphy of the probed bodies, such as terrestrial glaciers and Martian PLDs. The extraction and tracing of the internal layers have largely depended on the manual delineation of the radargrams. Some studies attempted to develop automated or semi-automated methods for this task, such as the development of Semi-Automated Multilayer Picking Algorithm (SAMPA) for picking layers in near-surface areas by using the Radon Transform (Onana et al., 2015), and methods for automatically identifying subsurface signals from SHARAD radargrams (Freeman, Bovik & Holt, 2010; Ferro & Bruzzone, 2012; Ferro & Bruzzone, 2013). When the direct extraction of subsurface layers is not necessary, quantifying the continuity of the layers (Karlsson et al., 2012; Bingham et al., 2015) or calculating the slope of the layers (Shi et al., 2010; Panton & Karlsson, 2015) is sufficient.

The detection of subsurface features not only depends on the configuration of radar systems and the method to extract these features, but it also critically depends on the dielectric properties of the sensed sites, which is usually defined by the petrology and mineralogy of the intervening materials (Heggy et al., 2001). Ice is a medium having low attenuation to radar waves, thus, the MCoRDS can

reveal the internal structure of the whole ice mass of GrIS which is thicker than 3 km. However, most of the Martian surface presents a volcanic context and is covered by an iron oxide-rich dust layer, which is more probably constituted of altered basalts (Christensen et al., 2000), hematite, maghemite and other ferromagnetic minerals (Hargraves et al., 1977). These minerals have a higher attenuation to the radar signal compared to ice; thus, the SHARAD probes only to a depth of several hundred metres (up to 1 km) into the Martian crust. Although the MARSIS is capable to penetrate several kilometres, it has too coarse resolution to reveal shallow buried layers. The shallow buried thin lava flows in the Tharsis region, which vary between 30 and 70 m thick as measured from MOLA data, can be observed by the SHARAD (Simon et al., 2014). It should be noted that if there is a thick (few hundred metres) volcanic layer of fractured basalt and lava flows underneath the dust layer, the radar signal can be significantly attenuated, thus leading to an absence of subsurface reflections in radargrams (Heggy et al., 2001).

There is a lack of volcanic related geomorphology over the Martian polar regions. The Residual Ice Cap (RIC) is composed of CO_2 ice in the SPLD and H_2O ice in the NPLD. Both the CO_2 ice and H_2O ice contribute to low electric and magnetic losses, which means a low attenuation to the transmitted radar signal. Besides, SHARAD has a more comprehensive coverage of Martian polar regions due to the polar orbit when compared to the equatorial and mid-latitude areas. Therefore, there are intensive studies of subsurface features by using SHARAD data in the Martian polar regions (Flamini et al., 2007; Grima, Kofman & Mouginot,

2008; Grima et al., 2009; Mouginot et al., 2009; Selvans et al., 2009; Brothers, Holt & Christian, 2010). Radar stratigraphy has been observed in both the PLDs by using SHARAD data (Byrne & Murray, 2002; Fishbaugh & Hvidberg, 2006; Milkovich & Plaut, 2008; Phillips et al., 2008; Milkovich et al., 2009; Smith, Holt & Christian, 2009; Karlsson & Holt, 2011). Both the PLDs are thought to be composed of atmospherically deposited dust and water ice (Cutts, 1973). MARSIS penetrates to the base of both PLDs and provides a strong constraint on the bulk composition, showing that the northern (Picardi et al., 2005) and southern (Plaut et al., 2007) deposits are almost pure water ice with upper limits on the volume fraction of dust of 2% and 10%, respectively (Byrne, 2009). SHARAD penetrates to the base of NPLD (Phillips et al., 2008) but not SPLD (Seu et al., 2007), possibly due to a wavelength-dependent effect. A detailed description of the structures, stratigraphy and compositions of the Martian PLDs will be introduced in Section 2.5.

2.3 SAR Subsurface Mapping in Terrestrial Deserts

The discovery of subsurface valleys in the eastern Sahara in the 1980s by the Shuttle Imaging Radar-A (McCauley et al., 1982) started a new era in subsurface mapping by using spaceborne SAR systems. Since then, the studies focusing on mapping subsurface features and detecting subsurface penetration depths in deserts can be categorised into three stages.

The first stage is from the 1980s to the early 2000s, when the images acquired in the SIR-A/B missions (McCauley et al., 1982; McCauley et al., 1986; Schaber et al., 1986) were intensively studied for their potential usefulness to

map the subsurface areas of the terrestrial deserts (El-Baz, 1998). Berlin et al. (1986) found that L-band radar waves penetrated a depth larger than 1 m by comparing SIR-B images to field observations in Saudi Arabia. Farr et al. (1986) estimated skin depths between 0.5 and 1.7 m by studying the backscattering of L-band radar waves with buried receivers in the Nevada desert. Dabbagh, Al-Hinai & Asif Khan (1997) used SIR-C/X-SAR data in north-eastern Sudan and demonstrated that the penetration depth of L-band radar waves is of the order of several metres. Later, Schaber, McCauley & Breed (1997) used the multi-frequency and polarimetric data from the SIR-C mission and concluded that the cross-polarised HV component at L-band has the best capabilities among HV, HH, VH and VV to display subsurface geologic features like relic fluvial channels in the eastern Sahara. In this stage, radar penetration depths were either measured by field excavations or calculated by laboratory permittivity measurements of soil samples collected from fieldwork. To avoid the devastating excavation, GPR investigations (e.g. 500 MHz that is similar to P-band and 900 MHz) were adopted to validate the subsurface features and to investigate the subsurface structures (Paillou, Grandjean et al., 2003; Grandjean et al., 2006).

Over the following decades, based on the success of the SIR missions, many spaceborne SAR systems were developed and launched. In this stage, the surface morphologies of SAR images were intensively studied and compared to optical images like Landsat images, to identify subsurface features in deserts. The backscattering coefficient or backscatter cross section describes the amount of radar energy reflected from land surface. It corresponds to the grey tone in a

radar image, which is hence used for qualitatively mapping the subsurface features (Guo et al., 2000; Paillou, Rosenqvist et al., 2003; Robinson et al., 2006; Robinson et al., 2007; Paillou et al. 2010), detecting crater-like features (Paillou, Rosenqvist et al., 2003; Paillou et al., 2006), revealing shallow groundwater (Sternberg & Paillou, 2015), investigating paleodrainage flow direction (Robinson et al., 2000) and hydrological connections (Grenier et al., 2009; Skonieczny et al., 2015). These studies, some of which used multi-wavelength and multi-polarisation radar images (Robinson et al., 2000; Robinson et al., 2007), mostly focused on identifying features by analysing the image tone.

During the last two decades, spaceborne SAR systems have been improved and extended to lower frequency and full polarimetric capability. Subsurface mapping in terrestrial deserts usually entails SAR topographic and polarimetric data (Lasne et al., 2004; Ghoneim & El-Baz, 2007; Lasne et al., 2009; Paillou et al., 2014). InSAR is a developed technique for obtaining surface elevation by using two or more than two SAR images (Graham, 1974; Zebker & Goldstein, 1986). However, Dall (2007) pointed out that the geometry of the conventional InSAR method is to ignore any consideration of whether or not radar penetration occurs when the low-frequency radar data is used. Therefore, Elsherbini & Sarabandi (2010) proposed a two-frequency radar system and a new InSAR model to address this problem. Recently, Gaber et al. (2015) used ALOS/AVNIR-2, ASTER, AVNIR-2/PALSAR, ASTER/PALSAR, quad polarized ALOS/PALSAR and quad polarized Radarsat-2 to classify the surface sediments in El-Gallaba Plain, Egypt. The ALOS/PALSAR data revealed a set of linear features that were

hidden under windblown sand and were not visible in the field of other datasets. Their GPR survey confirmed these hidden lineament features. Liu et al. (2015) used the co-polarised phase difference to retrieve the depth of the subsurface brine layer in Lop Nur in Xinjiang, China. Chen et al. (2016) compared multi-wavelength orbital radar data and found a cultural heritage in the western regions of the Silk Road Corridor. In the following sections, SAR polarisation and interferometry will be introduced, especially in terms of penetration depth estimation.

2.3.1 SAR polarisations

Schaber, McCauley & Breed (1997) analysed X-, C- and L-bands polarimetric data from SIR-C/X-SAR to identify the subsurface features and concluded that lower frequency bands and cross-polarisations should be the prior choice in general for geologic mapping in the Bir Safsaf, Egypt. The co-polarised signal contains surface and non-surface scattering components, while the cross-polarised signal contains only the non-surface scattering components, such as subsurface and volume scattering (Grandjean et al., 2001). Grandjean et al. (2001) found different land cover features showing different sensitivities to HH, HV, VH and VV polarisations, which leads to the different values of HV/HH ratio, HH-VV correlation and HH-VV phase difference. Therefore, they proposed these polarisation signatures to detect buried paleosoils of Pyla Dune in France. According to their study, areas with volume and subsurface scattering (non-surface scattering) should appear in both HH and HV images, and present a higher HV/HH ratio and a lower HH-VV correlation. Based on Grandjean et al.

(2001)'s work, Lasne et al. (2004) confirmed that the phase signature (ϕ_{HH-VV}) where ϕ is the phase in radius, is a function of the dielectric constant which increases with the moisture content of the paleosoil. Multi-polarisation and multi-frequency are also helpful in monitoring the change of hypersaline deposits (Lasne et al., 2009).

To estimate dielectric properties of subsurface materials, field measurements need to be carried out to map the land cover types and their dielectric properties. Then, a quantitative relationship between these properties and radar backscatter coefficient can be constructed. GPR, which is non-contact without damaging to the land surface, is a replacement to field excavation (Grandjean et al., 2001; Paillou, Grandjean et al., 2003; Lasne et al., 2004; Grandjean et al., 2006; Paillou et al., 2006). The reflection coefficients from GPR can be used for calculating the propagation velocity, and estimating the signal attenuation and the dielectric permittivity (Reppert, Morgan & Toksöz, 2000).

2.3.2 SAR interferometry and penetration depth estimation

DEMs play an important role in studying subsurface features. DEMs used to be produced using survey profiles and/or photogrammetric contours which were interpolated to a grid of values as a 2-D format in a traditional manner. With the development of remote sensing technology, DEMs can be acquired with a large coverage and at a low cost by using several types of remote sensing methods, such as optical photogrammetry, InSAR and Light Detection And Ranging (LiDAR). DEMs provide not only the variation of topography but also

slope and aspect information for further studying these hydrological and geological features, such as reservoir estimation of paleolakes (Grenier et al., 2009).

DEMs derived by using optical photogrammetry usually represent the land surface height since incident optical waves are usually reflected from a bare surface with negligible penetration depth. However, InSAR-derived topographic expression, such as GTOPO30 (Global 30 arc-second, now updated to GDEM2010) DEM (Robinson et al., 2000) and SRTM DEM (Robinson et al., 2006; Ghoneim & El-Baz, 2007; Robinson et al., 2007; Grenier, Paillou & Maugis, 2009), is sometimes affected by the penetration process of the incident radar waves. DEMs not only provide surface geomorphologic information to analyse the subsurface features over sandy areas, but also the elevation information for further analysis, such as the flow direction of the paleorivers. Since InSAR has become an accepted remote sensing tool for deriving DEMs, it is considered worthwhile to investigate whether the InSAR DEMs produced by using different microwave frequencies detect the same elevation or not.

Over the past three decades, SAR interferometry has played an important role in measuring land topography and surface displacement (Massonnet & Feigl, 1998). DEMs covering large areas are relatively easily produced by deploying the SAR system on either an airborne or spaceborne platform. Measurement of ground height is achieved by comparing the phase of the received radar waves from two satellite viewpoints, the geometry of which is illustrated in Figure 2.5. The SAR raw signal data can be processed into Single Look Complex data, which

contain amplitude and phase components. After coregistration of two images acquired at positions of S_m and S_s, these two images can be represented by the following Equation (2.10).

$$M = |I_m| \exp(j\phi_m), S = |I_s| \exp(j\phi_s) \tag{2.10}$$

where M and S are two images acquired at the two positions; I_m and I_s denote intensities; ϕ_m and ϕ_s are the phases of master and slave acquisitions. The phase difference between these two SAR signals can be used to measure the target height, which can be seen in Figure 2.5.

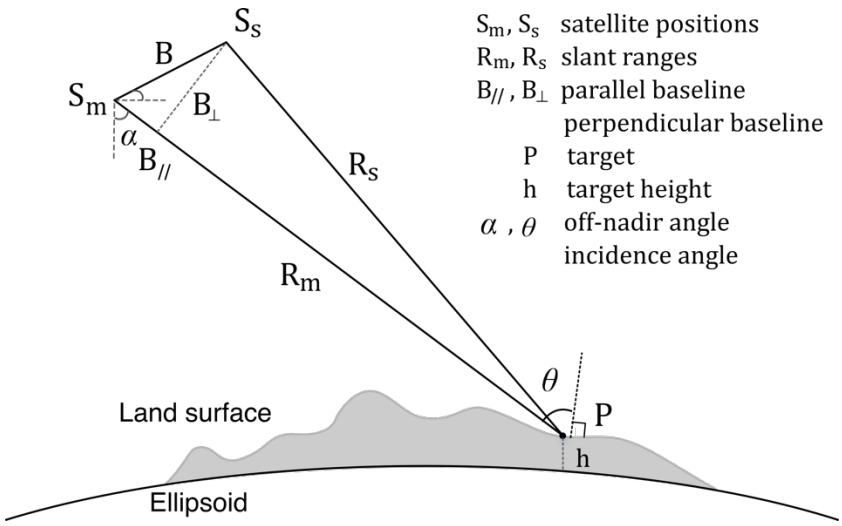

Figure 2.5: The SAR Interferometry viewing geometry.

The total phase difference, $\Delta\phi$, can be calculated by Equation (2.11). It is the subtraction of phase between master and slave acquisitions. According to the InSAR viewing geometry shown in Figure 2.5, this phase difference can also be related to ranges from two satellite positions to the ground target, which are R_m and R_s, respectively. Finally, it is described by the differing range distances, ΔR,

and wavelength, λ. This phase difference is composed of several components caused by different factors, such as land topography, surface displacement, differing atmospheric delays and signal noise. The topographic phase accounts for most of the total phase difference, thus the height can be inverted from the total phase difference through Equation (2.12), where $B_{\perp}$ is the perpendicular baseline and θ is the incident angle.

$$\Delta\phi = \phi_m - \phi_s = -\frac{4\pi(R_m - R_s)}{\lambda} = -\frac{4\pi}{\lambda}\Delta R \tag{2.11}$$

$$H = -\frac{\lambda R_m sin\theta}{4\pi B_{\perp}}\,\Delta\phi \tag{2.12}$$

The main component of topographic phase can be simulated by using an independent DEM. In this case, the rest phase components can be calculated by subtracting the simulated topographic phase from the total phase difference. In this application of estimating the surface displacement by using this Differential InSAR (DInSAR) technique, this residual phase component is mostly regarded as a phase component caused by land displacement in the radar line of sight direction. Conversion between phase and land displacement only relates to the wavelength as shown in Equation (2.13). Measuring surface displacement using DInSAR techniques can achieve high accuracy of up to a few millimetres.

$$d_{disp} = -\frac{\lambda}{4\pi}\,\Delta\phi \tag{2.13}$$

The independent DEM which is commonly used for DInSAR is the Shuttle Radar Topography Mission (SRTM) DEM.

Table 2.4 lists different characteristics between SRTM and ALOS/PALSAR. The SRTM was launched in February 2000 and ran for 11 days. It was an international joint project between the National Geospatial Intelligence Agency (NGA) and NASA, including the participation of the Italian Space Agency (ASI) and German Space Agency (DLR). InSAR was used to generate a high-resolution DEM covering all areas between 60°N and 56°S of Earth. SRTM had a C-band and X-band SAR system onboard, which were used to generate C- and X-band DEMs respectively. The former was processed and released by NASA, the latter by DLR (Marschalk et al., 2004). The original version 1 & 2 SRTM C-band DEMs were first released with a global 3 arc-second (~90 m) resolution (1 arc-second for the continental USA), but the recent release version in 2014 is at 1 arc-second resolution (~30 m) globally, which is the same resolution as the SRTM X-band DEM. The X-band DEM, however is not continuous, as ScanSAR was not employed. Apart from the global DEM, the corresponding C-band combined images (sub-swath images of HH and VV are combined) (LP DAAC, 2014) are also released via Land Processes Distributed Active Archive Center (LP DAAC). The data can be accessed from https://lpdaac.usgs.gov/nasa_shuttle_radar_topography_mission_srtm_combined_image_data_set_and_swath_image_data_release.

In theory, the radar signal at a lower frequency achieves a deeper penetration depth. The SRTM-C band DEM has a penetration depth of 1.7-3.4 m on glaciers over the Pamir-Karakoram-Himalaya (Gardelle et al., 2013), which was estimated to be 1.5-2.5 m (Kääb et al., 2012). The surface elevation

measured from airborne SAR data varies at different wavelengths. On cold polar firn at the Greenland summit, the penetration depth is 9 m and 14 m at C- and L-bands, respectively and 1 m and 3 m at C- and L-bands on the exposed ice surface of Jakobshavn Isbrae, west Greenland (Rignot, Echelmeyer & Krabill, 2001).

Table 2.4: Systematic parameters of ALOS/PALSAR FBD (Fine Beam Dual polarisation) mode and SRTM/SIR-C SAR ScanSAR mode (ESA, 2017).

Platform/Instrument Mode	**ALOS/PALSAR (Rosenqvist et al. 2007)**	**SRTM/SIR-C SAR ScanSAR**
Centre Frequency	1.27 GHz	5.3 GHz
PRF	1500–2500 Hz	1344–1550 Hz
Range Sampling Frequency	32 MHz (FBS) 16 MHz (FBD)	Transmit pulse width 34 μs
Chirp Bandwidth	28 MHz (FBS) 14 MHz (FBD)	10 MHz
Polarisation	HH + HV or VV + VH	HH and VV
Off-nadir angle	9.9°–50.8°	15°–55°
Swath Width	70 km (FBS, FBD @34.3°)	225 km
Ground Resolution	10 m × 5 m (FBS @34.3°) 20 m × 5 m (FBD @34.3°)	30 m × 30 m
Transmission Peak Power	2 kW	1.2 kW

Two of the main limitations of InSAR techniques are spatial and temporal decorrelation. Radar returns are coherent with each other when the two viewpoints are not too far away. When the baseline between the two viewpoints exceed a critical point, then received waves are not correlated anymore and the phase difference cannot be recovered. Temporal decorrelation is usually caused

by surface changes between the two observation times. It often occurs in vegetated areas, because the low correlation prevents the recovery of the phase measurement. Coherence between acquisitions are used to evaluate the extent of decorrelation.

2.4 Tracing englacial Layers from radar sounding data

2.4.1 Englacial layers and folds

Currently, we are in an interglacial period which started 11 kya within the Quaternary period (Gradstein et al., 2012). Ice core studies revealed the glacial-interglacial cycles of the last 800 ky (Wolff et al., 2010). Age dating with ice cores utilises gases, such as carbon dioxide, methane and nitrous oxide preserved in sealed bubbles in the ice core (Raynaud et al. 1993). The examination of englacial structures can reveal valuable information about the dynamics of the ice sheet (Keisling et al., 2014; Florentine et al., 2018) and reveal the relationship between depth and ice age (MacGregor et al., 2015a). Englacial layers and the folding of the layers in terrestrial ice bodies reflect the cumulative strain of ice as it is developing for centuries or millennia.

The englacial layers sometimes referred to as Internal Reflection Horizons (IRHs) can be caused by several factors. One factor is the density variation in the transition from snow to ice that usually occupies the upper several hundred metres of the ice sheet. The top layers in the ice sheets are within the region of snow and firn, which is between dry snow and pure ice. Precipitated dry snow has a low density of 50-70 kg m^{-3} whereas the density of pure glacier ice without

bubbles is 917 kg m^{-3} (Cuffey & Paterson, 2010, pp.11–27). Firn becomes ice (with a density of 830 kg m^{-3}) at a depth of 64 m at Byrd and 95 m at Vostok, which are both in the dry snow zone in Antarctica (Cuffey & Paterson, 2010, p.16). Higher pressure leads to a higher ice density which decreases with increasing temperature. Ice near the basal area is within a few degrees of melting point, which decreases the ice density. Therefore, ice should attain its greatest in situ densities (about 923 kg m^{-3}) at mid-range depths in the ice sheets, where low temperatures (-40 to -20°C) and moderately high pressures ($\sim 7\times10^5$ Pa) co-exist (Cuffey & Paterson, 2010, pp.11–27).

Fujita et al. (1999) used a two-frequency radar (60 MHz and 179 MHz) to probe the ice sheet in Eastern Antarctica. They found that in the top several hundred metres, the permittivity variations are dominated by changing density. In the deeper part of the ice sheet, the variation of radar reflections is correlated to large volcanic eruptions, which increase the level of acidity in precipitation over polar regions for one or more years after each eruption. The deeper englacial layers which are related to the permittivity variations can also be caused by changes of crystal fabric orientations of the ice, which is the grain-scale (millimetres to decimetres) structural properties of ice as polycrystalline. This grain scale is between the micro-structural scale which relates to molecules in crystal lattices and grain boundaries, and the macro-structural scale of features like crevasses and foliation. The fabric orientation represents the direction along which ice is harder to be deformed by a shear stress. Except for the englacial

layers caused by the crystal fabric orientations, the others are thought to be isochrones which have the same depositional age (Fujita et al., 1999).

Folding of englacial layers has been observed through radar sounding data at several sites in Greenland and Antarctica. A study of the North Greenland Eemian Ice Drilling (NEEM) ice core revealed that englacial layers are observed in the upper ~2.2 km of the NEEM ice core while the englacial layers are subjected to folding below ~2.2 km (NEEM community members, 2013). The MCoRDS data over this ice core show that the deeper englacial layers are less distinct and less continuous. Undulations and even overturned folds and shearing of basal material are observed in the lower part of the ice sheet. The transition between clear and less distinct layers often appears at the interface between ice from the glacial and Eemian interglacial periods (130-115 kya BP) (NEEM community members, 2013). The viscosities of the glacial and interglacial ice differ by a factor of 50-100, allowing the former to deform very easily while the latter remains more rigid. Apart from the differing viscosities, other mechanisms such as basal ice melting (Bingham et al., 2015) and basal sliding (Wolovick & Creyts, 2016) can play a role in forming this transition between clear and less distinct layers. In parallel, undulations of englacial layers are also observed in Antarctica below ~2.1 km according to ice core data (Drews et al., 2009). Echo Free Zone (EFZ) describes the area from this depth to ice bottom since it features an absence of continuous internal layering. The onset of the EFZ is characterised by a sudden drop of the radar amplitude in the radargrams. The power loss can be explained by dipping or roughness of layers in the EFZ (Drews et al., 2009).

2.4.2 Automated layer-tracing from the radar sounding data

The radio sounding technique has been used in glaciology since the 1960s to map the bed topography and layering of the ice sheets in Greenland and Antarctica (Drewry & Meldrum, 1978). Analysis of the englacial layers has shed lights on many aspects of ice dynamics, such as past accumulation rates (Leysinger Vieli, Siegert & Payne, 2004; Medley et al., 2015), ice flow changes (Rippin et al., 2006; Bingham et al., 2015), bed variations and their relationship to surface conditions (Drews et al., 2009; Wolovick & Creyts, 2016).

Radar sounding data are very useful in studies of bedrock elevations, in which only the bottom layers imaged by radar sounders are used. Apart from this, many englacial layers which are thought to be isochrones, are also observed in radar sounding data. However, analysis of the englacial layers by using a large volume of radar sounding data is limited by the lower efficiency associated with manual tracing. The englacial layers usually exhibit less EM contrast than surface and bed layers; therefore, tracing englacial layers can be a laborious and time-consuming manual task. For instance, tracing 20 layers in a 20 000 km radar sounding survey required a skilled operator 10 years to complete (Sime, Hindmarsh & Corr, 2011). The increasing volume of radar sounding data has motivated the development of automated or semi-automated methods to trace these internal reflections. Most of the layer-tracing methods involve manual selection of seed points and are based on the estimation of slope angles which are used for propagating the seed points (Panton, 2014). The propagation is called peak-following. Sime, Hindmarsh & Corr (2011) proposed a method for

deriving layer slope using a binary thresholding system but it struggles with noisy and discontinuous data. Paton proposed two automated methods for tracing the internal reflections, one of which produced an initial estimation of layer positions and the other, known as the SNAKE, traced a layer from the initial estimation (Panton, 2014). However, this method produced many false positive results for low-amplitude reflectors (Holschuh et al., 2017). MacGregor et al. presented two phase-based methods to infer the layer slope and to estimate the ice ages of traced englacial layers by using ice drilling core data (Macgregor et al., 2015a); however, this method required complex radar data. In the most commonly applied peak-following method, one critical problem is that the layer-tracing is liable to steer into neighbouring layers in regions where the visible stratigraphy degrades (Panton, 2014). Instead of peak-following, Onana et al. and Holschuh et al. proposed to use the Radon Transform (RT) to trace layers with an assumption that a layer segment over a short distance is a straight line. Their methods were tested with Ku-band radar and MCoRDS data respectively (Onana et al., 2015; Holschuh et al., 2017). Another tracing scheme was tested with three frames of MCoRDS data near NEEM ice core where ice folding was observed (Xiong & Muller, 2016). This tracing scheme combined the RT and Fahnestock et al.'s method which was based on cross-correlation and peak-following (Fahnestock et al., 2001). The layers traced by using this tracing scheme were discontinuous because (1) there was no way to discriminate small peaks which might be caused by instrumental or environment noises, and (2) the radar signal attenuation caused inaccurate estimation of slope angle. In addition, correlation calculation of too many peak-pairs limited the efficiency.

2.5 Radar sounding of the Martian SPLD

2.5.1 Structures of the Martian SPLD

The Mariner 9 photography revealed a thin annual carbon dioxide frost deposit and the exposed deposit beneath the CO_2 frost was inferred to be composed of water ice (Murray et al., 1972). Observations from the Mariner 9 and Viking missions established the distribution of three basic polar units, seasonal CO_2 frost caps, residual summer caps of frost, and layered deposits (Thomas et al., 2000). The Martian south polar cap was identified containing perennial water ice in extended areas, and a small admixture to CO_2 in the bright regions and to dust, without CO_2 at the edges through spectrometer analysis using OMEGA observations (Bibring et al., 2004). The characteristics of the SPLD and its comparison with the NPLD are listed in Table 2.5, which are concluded from a review paper by Byrne (2009). The structure of the PLDs is shown in Figure 2.6 (Byrne, 2009).

Table 2.5: Characteristics of the Martian SPLD and NPLD, which is concluded from Byrne's review paper published in 2009 (Byrne, 2009).

Characteristics	**SPLD**	**NPLD**
CO_2 frost	< 10 m thick	sublimate in summer deposit in winter
Smoothness	n/a	Smooth at hectometre scales
	"swiss cheese"	"cottage cheese"
Surface morphologies	fingerprint terrain	sand dunes
	spider patterns	polar dunes
Composition	Primarily composed of water ice	
Deposit year	Last 10^5-10^6 EY	Last ~ 4 $\times 10^6$ EY
Volumes (km^3)	~1.60 million	~1.14 million
Impurity fraction	< 10 %	5 %
Thickness (km)	~3.7	~3
Area(km^2)	1.16×10^{12}	1.12×10^{12}
Extent	Extend to 71° S	Extend to 80° N
Basal elevation	5 km	1-1.5 km
Basal surface age	> 10^7 EY	Less than 10^5 EY old

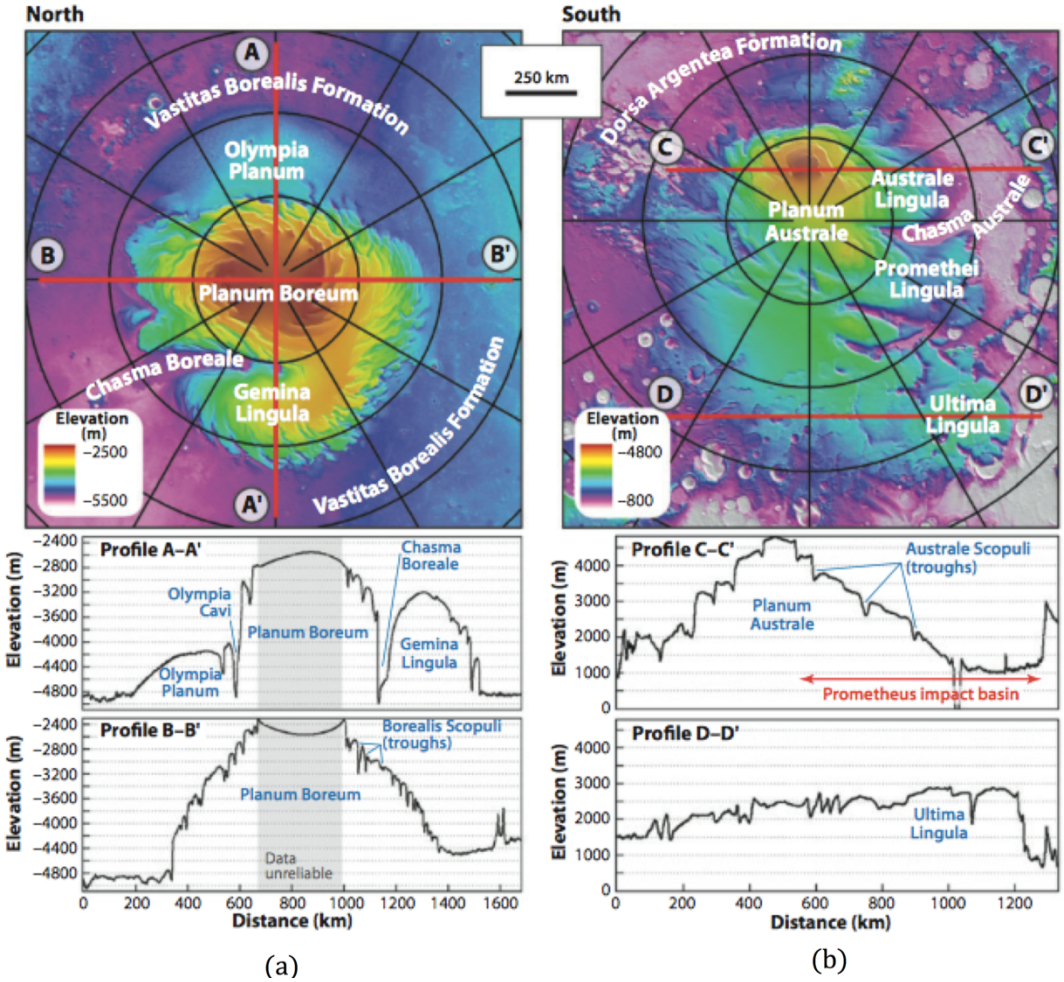

Figure 2.6: The structure of the PLDs and examples of topographic profile (Byrne, 2009).

The major component of the Martian atmosphere, CO_2, condenses in the polar regions during the winter seasons and precipitates as CO_2 frost (Kieffer, 1979; Kelly et al., 2007). In the Martian south pole, the solid CO_2 ice cap is the top layer deposit and has a thickness of a few metres. The seasonal CO_2 ice cap retreats in the summer. Surface morphologies, such as flat-floored quasi-circular pits (Swiss cheese features), linear ridges (fingerprint terrain) and spider patterns, can be observed in high-resolution imagery (Thomas et al., 2000; Lefort, Russell & Thomas, 2010).

The Martian SPLD known as Planum Australe is a dome-like feature. The SPLD sits on the top of the heavily cratered southern highlands, which is 3.5-4 km higher than the northern Borealis basin. The SPLD is about 3.7 km in the thickest regions. The SPLD is considered to be mainly composed of water ice with a mixture of dust in varying percentage producing the distinct layers (Cutts, 1973). This is proved by the observed albedo of 0.5 from Viking thermal infrared observations (Kieffer, 1990) and is later constrained by using MARSIS observations (Picardi et al., 2005). CO_2 ice is also suspected to be sequestered in the SPLD, but its volume has no big consequence to the overall SPLD (Phillips et al., 2011). The volumes of NPLD and SPLD (respectively 1.6×10^6 km^3 and 1.14×10^6 km^3) together are of the same order as that of the Greenland ice sheet (2.6×10^6 km^3), with a similar average thickness of about 1-1.5 km (Plaut et al., 2007; Smith et al., 2001). Both the PLDs are incised with troughs and scarps, which expose interior layers (Byrne, 2009). In the NPLD, the spiral troughs and scarps are more intensively formed than in the SPLD, and they have constructional migration (Smith, Holt & Christian, 2009; Smith & Holt, 2010). Radar observations show few reflectors near the troughs in the SPLD (Smith & Holt, 2010).

2.5.2 Radar Stratigraphy of the SPLD

The mass balance of the Martian PLDs are driven by deposition and erosion (Byrne, 2009). The mass balance is positive when the polar ice deposits are increasing. These deposits composed of dust and ice are usually thought to be isochronous layers which have accumulated under climate cycles having periods

of several tens of thousands of years (Kieffer, 1990). Although the relationship between the internal layering and the climate variations is not very well understood yet, it is believed that the rhythmic nature of the deposits is related to variations in Mars orbit parameters, especially its spin axis obliquity (Toon et al., 1980). Studying the stratigraphy of the Martian PLDs facilitates our understanding of this relationship and the past climate change on Mars.

Compared to the NPLD (Putzig et al., 2007; Phillips et al., 2008; Putzig et al., 2009; Brothers, Holt & Christian, 2010; Holt et al., 2010; Putzig et al., 2010), radar stratigraphy of the SPLD is less well studied. The stratigraphy of the Martian PLDs can be characterised in detail by using topographic, thermal, radar, hyperspectral, and high-resolution imaging data. Radar sounding data record the subsurface dielectric boundaries while high-resolution imaging data usually reveal the layer exposures on the troughs and scarps. Several instruments can be used to acquire high-resolution imagery and DEMs, which are listed in Table 2.6. The presence of layers in the high-resolution imagery is understood to be related to the contrasting albedo between layering materials (Milkovich & Plaut, 2008; Milkovich et al., 2009). The albedo variations between the layers are thought to be caused by varying mixtures of ice and dust (Milkovich & Plaut, 2008). Exposed layers shown in the Mars Orbital Camera (MOC, 4-11 m/pixel) images demonstrate that the scale of the layering is a few metres which is the same as the resolution of the MOC images (Malin & Edgett, 2001). HiRISE data have fully resolved the thinnest layers of NPLD layer exposure to be tens of metres thick (Herkenhoff et al., 2007).

Table 2.6 Instruments used for acquiring surface imagery and DEMs (ppd: pixel per degree) (Kim & Muller, 2008).

Properties	**MOLA**	**HRSC**	**CTX**	**HiRISE**
Start month/year	03/1999	12/2003	03/2006	03/2006
Mission	MGS	MEX	MRO	
Orbit altitude (km)	378	270-1000	370-400	
Image Resolution	n/a	12.5 m/pixel	6 m/pixel	0.25 m/pixel
DEM resolution	256 ppd	25 m/pixel	12-18 m/pixel	0.5-4 m/pixel

Previous researchers have studied the major stratigraphic sequences that define distinct units of the SPLD by using optical images and radargrams (Kolb & Tanaka, 2001; Byrne & Ivanov, 2004; Kolb & Tanaka, 2006; Seu et al., 2007; Milkovich & Plaut, 2008; Milkovich et al., 2009; Guallini et al., 2017). Byrne & Ivanov (2004) and Milkovich & Plaut (2008) investigated the 3-D stratigraphic structure of the SPLD by analysing the exposed layers on the scarps using the Thermal Emission Imaging System (visible THEMIS, 18-36 m/pixel), MOC images and MOLA DTM. Byrne & Ivanov (2004) identified a Bench Forming Layer (BFL) which is well approximated as a parabolic dome near the centre of the SPLD indicating a topographic dome buried underneath. They concluded that layer formation is regionally uniform and lacks internal defects, such as faulting, within the SPLD. Apart from the BFL, Milkovich & Plaut (2008) identified another two layer sequences below the BFL, which are the Promethei Lingula Layer (PLL) and the Inferred Layer (IL), shown in Figure 2.7. The absence of several identified layer sequences over most areas in the SPLD as well as the presence of several

unconformities, notably in the Promethei Lingula (PL) region, indicate that the deposition and erosion processes have not been uniform around the SPLD.

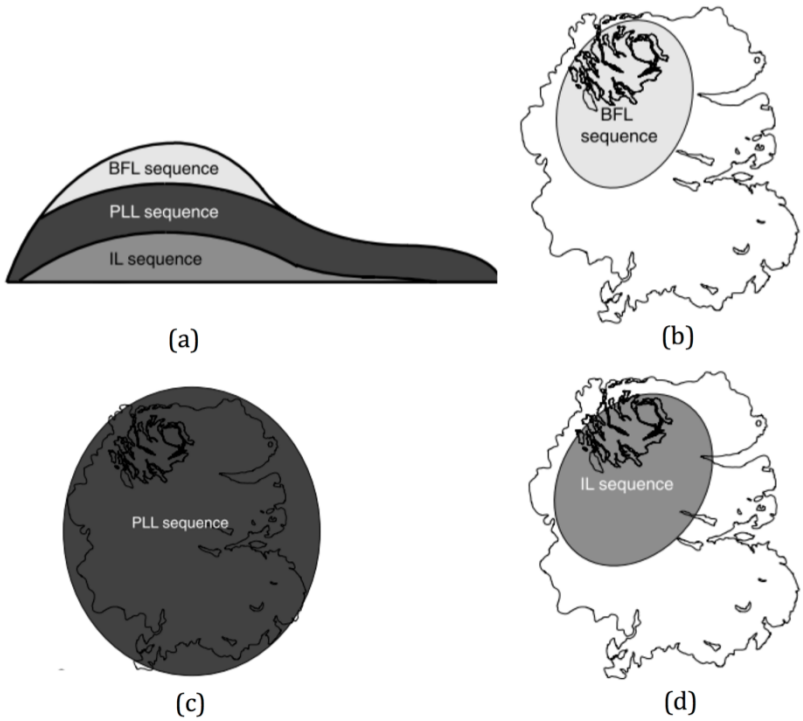

Figure 2.7: (a) Sketch of the internal structure of the SPLD; coverage of (b) the BFL, (c) the PLL sequences; and (d) coverage of the IL sequence. Images are sourced from Milkovich & Plaut's study (2008).

These previous studies attracted a great deal of interest in the PL region since the irregular depositional history may relate to past Martian climate change. The PL is a lower-relief plateau at the margin of the SPLD, as shown in Figure 2.8. Together with Ultimi Lobe (UL), it is dissected and separated by three canyons, namely Chasma Australe (CA), Promethei Chasma (PC) and Ultimum Chasma (UC) (Byrne & Ivanov 2004). The Promethei and Ultimum Chasma have rugged floors exposing Hesperian and Noachian materials. A similarly oriented

but shallower canyon, Australe Sulci, features dense, parallel sets of curvilinear grooves, canyon-transecting sinuous ridges and circular and elongated mounds (Kolb & Tanaka 2006).

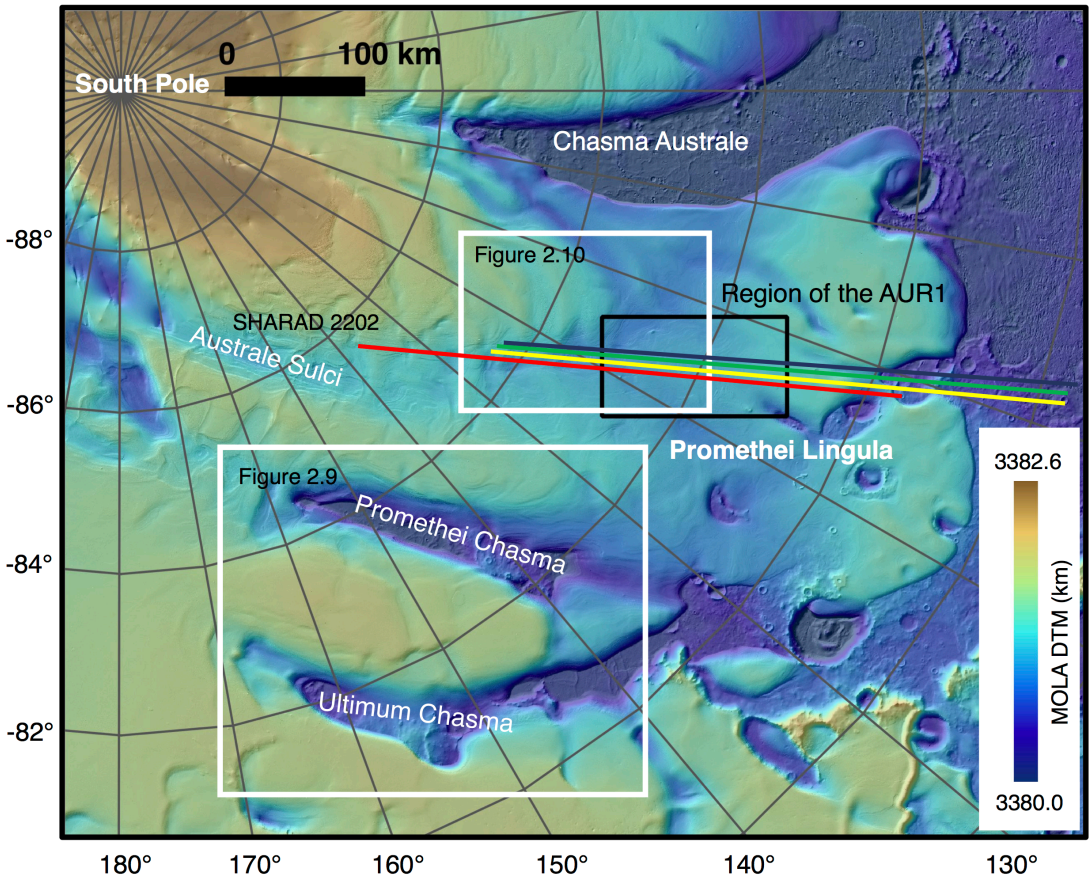

Figure 2.8: (a) The geographical location of the Promethei Lingula (PL) in the SPLD, SHARAD acquisitions shown in red for orbit 2202, yellow for orbit 2413, green for 2624 and blue for 2835. Geological units of regions in white rectangles are analysed in Figure 2.9 and Figure 2.10. The background image is the MOLA DTM (MEGDR at 512 pixels/degree or ≈115 m/pixel, the elevation is referenced to the centre of mass of Mars).

Kolb & Tanaka (2001) analysed the geological history of the Martian Polar regions based on MOLA and MOC observations. The morphology, composition and thickness of the SPLD led to their postulation that it is composed of porous unconsolidated layers which are more likely to be formed by wind scouring and ablation (Kolb & Tanaka, 2001; Tanaka et al., 2008; Warner & Farmer, 2008) rather than glacial-type processes (Clifford, 1987; Anguita et al., 2000). However, no widespread unconformities, discontinuities and pinch-outs were identified in their study. In 2006, they concentrated on characterising the geologic units of the PL region, especially in regions shown in white rectangles in Figure 2.8 (Kolb & Tanaka, 2006). The SPLD in the PL region was divided into Planum Australe 1 and 2 units (Aa_1 and Aa_2, respectively). The later has a thickness of < 300 m and the former can be further divided into lower and upper members, which are denoted as Aa_{1a} and Aa_{1b} and have a thickness of 300-1000 m and a few to several hundred metres respectively as illustrated in Figure 2.9 and Figure 2.10.

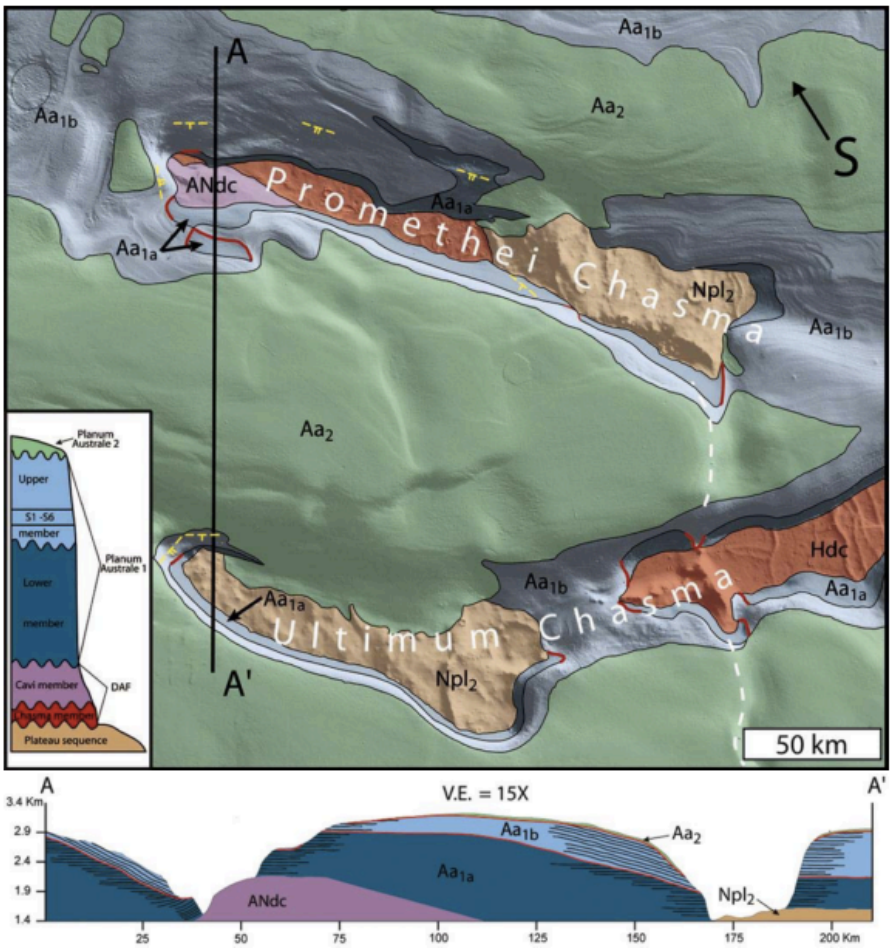

Figure 2.9: The geological units of the region shown as the white lower rectangle in Figure 2.8. This image is sourced from the study by Kolb & Tanaka (2006) (A = Amazonian, H = Hesperian, and N = Noachian).

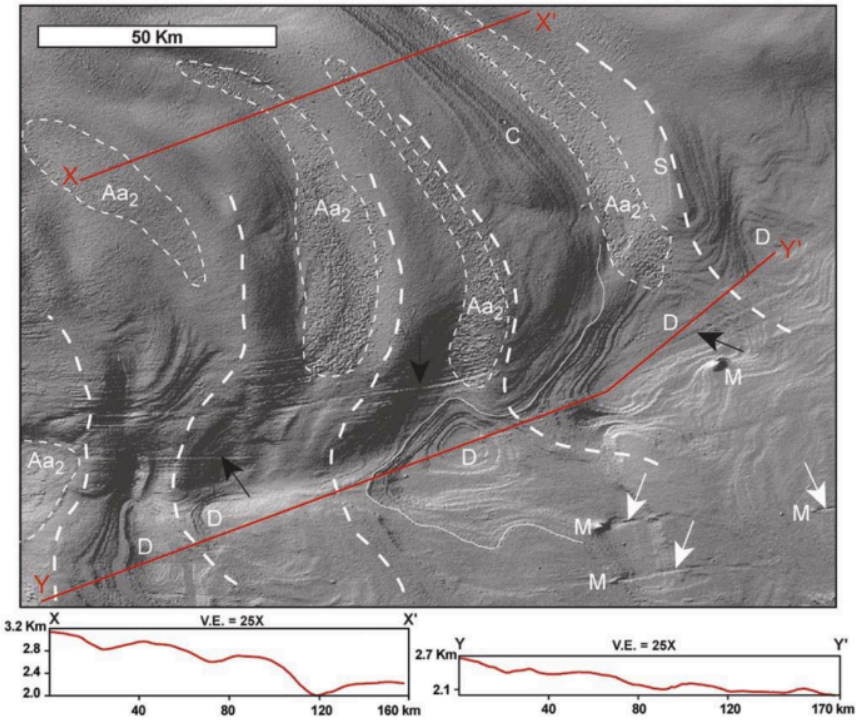

Figure 2.10: The geological units and topographic profiles of the region shown as the upper white rectangle in Figure 2.8. The image is sourced from Kolb & Tanaka (2006)'s study (D = depressions, S = streamlined ridges, M = mounds, and white arrows = sulci grooves).

Seu et al. (2007) first used SHARAD radargrams to analyse the layer sequences in the PL region. Four sets of reflectors are delineated as shown in Figure 2.11, in which lines 1 and 2 together illustrate a wedge-shape layer sequence. It is restricted to ~108°-123°E, and narrows and ultimately extrudes out toward the SPLD margin. Correlation between four radargrams from orbits 2202, 2624, 3890 and 4312 (Figure 2.12) demonstrates that the wedge-shape layer sequence extends several kilometres laterally. This wedge is ~200 m thick and ~100 km long at its thickest and longest location and gets thinner towards the west. Seu et al. (2007) inferred that this wedge feature is an indication of

surface erosion caused by katabatic winds being channelled through the canyon at the mouth of Australe Sulci.

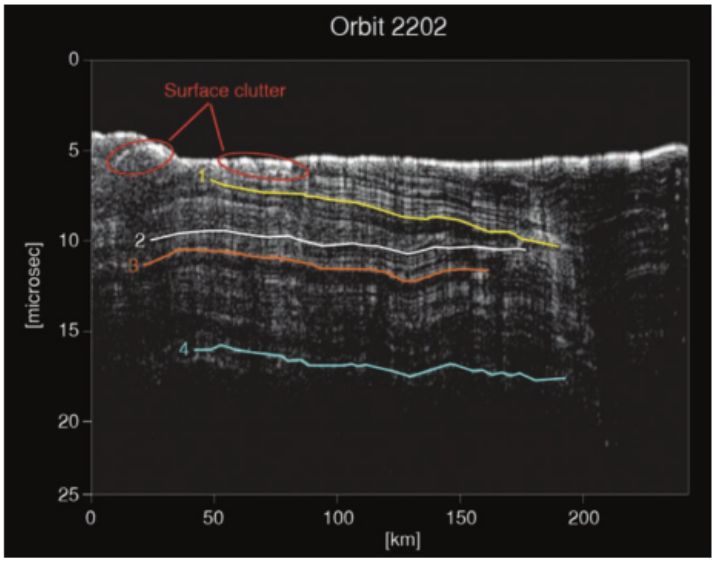

Figure 2.11: The SHARAD radargram from orbit 2202 showing a subsurface wedge. This image is referred in Seu et al. (2007).

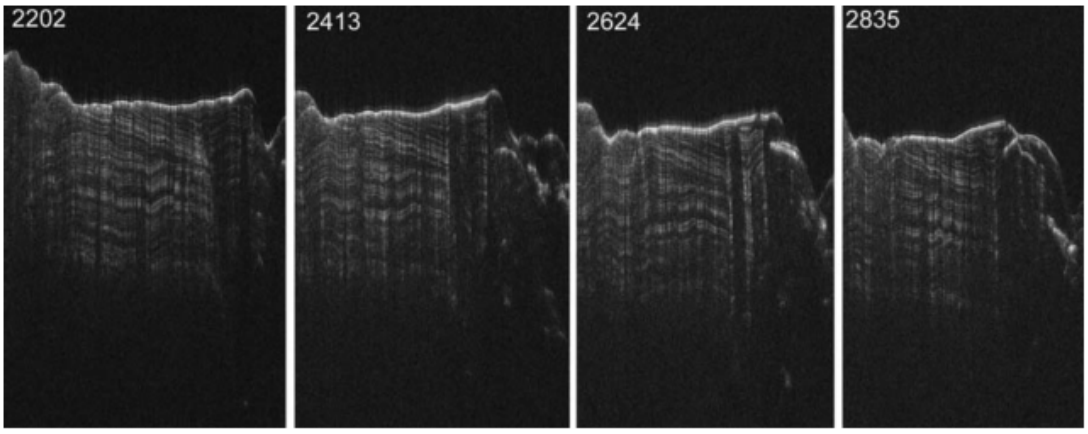

Figure 2.12: Radargrams from the neighbouring orbits of orbit 2202 showing the same wedge feature. This image is referred in Seu et al. (2007).

Milkovich et al. (2009) compared the MARSIS and SHARAD datasets acquired in the PL region. MARSIS detects up to three reflections, which correlate to the boundaries of packets of reflections in the SHARAD data summed to tens of reflections. SHARAD reflections in some areas were compared directly with layers in the THEMIS and MOC images, which showed that an individual reflection corresponds to 3-7 layers in images at a resolution of 6 m/pixel. It was concluded that most of the layers extend throughout the region.

Based on the previous conclusion that a discontinuous depositional record indicated by the buried unconformity is preserved in the PL region, Guallini et al. (2017) analyse the stratigraphy of the SPLD using ~100 CTX images and ~600 SHARAD radargrams. They reconstructed the topography of the angular unconformity (or the regional discontinuity) by manually screening the SHARAD dataset, the results of which are shown in Figure 2.13. From the CTX images, the lower sequence is characterised mainly by a “ridge and trough” morphology and the upper sequence shows mainly a “stair-stepped” morphology. This transition corresponds to the interface between units of Aa_{1a} and Aa_{1b}, which were proposed by Kolb & Tanaka (2006), and to discontinuities of topographic contour as a slight slope break in some areas (Guallini et al., 2017). According to the derived geological units, Guallini et al. postulated that the oscillations in Martian axial obliquity could have controlled local climate conditions in the past, leading to the current geological records in the PL region.

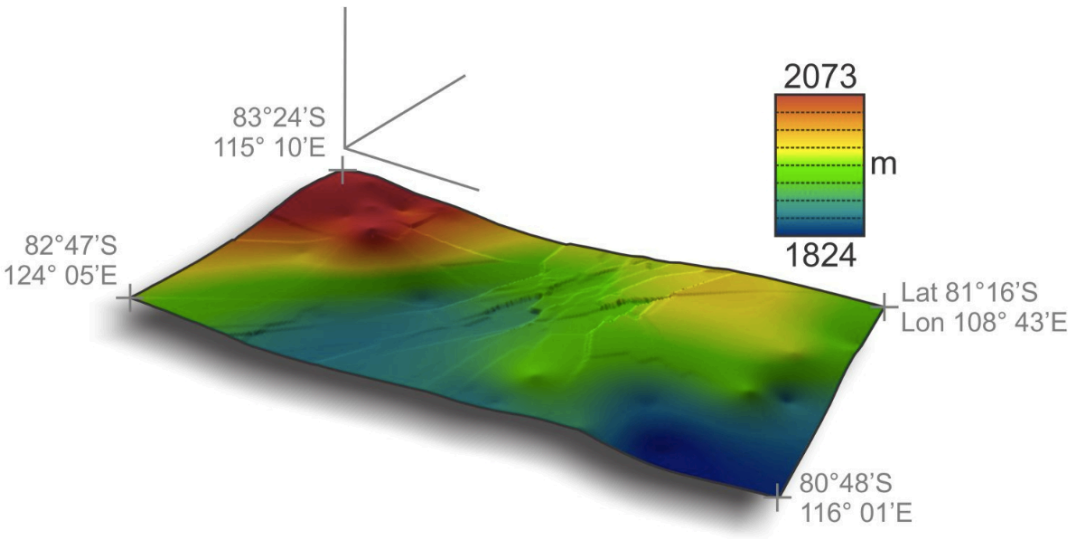

Figure 2.13: The topography of the buried angular unconformity in the region shown by the black rectangle in Figure 2.8, which is reconstructed by Guallini et al. (2017). The topography is colourised by the depth from surface to the unconformity reflections.

2.5.3 Radar stratigraphy of the Elysium Planitia

Apart from the PLDs, the SHARAD has been used for subsurface mapping in mid-latitude areas (Holt et al., 2008; Plaut, Safaeinili, Holt et al., 2009) and other sites of interest, such as Arcadia Planitia (Plaut, Safaeinili, Campbell et al., 2009; Bramson, Byrne & Putzig, 2014; Bramson et al., 2015), Amazonis Planitia (Campbell et al., 2008), Utopia Planitia (Stuurman et al., 2016) and Elysium Planitia (Orosei et al., 2007; Boisson et al., 2009; Alberti et al., 2012). In this section, only the interest in studying the Elysium Planitia by using the SHARAD data is briefly introduced, since the origin of terrains in this region has been hotly debated for a long time and no clear consensus has been reached.

The Central Elysium Planitia is located between 144°E and 180°E, and between 5°S and 10°N, which includes main Cerberus basin, Athabasca Valles, Athabasca Basin and part of Marte Valles. The Cerberus Fossae, a series of kilometre-wide fractures, extends for over 1000 km to the southeast of the Elysium rise. Athabasca Valles is a fluvial channel carved by catastrophic floods that erupted from the Cerberus Fossae and terminated in a large, flat-floored basin (Burr, 2002; Burr et al., 2002), which is termed Athabasca Basin. The floor of this basin is covered by distinctive platy and polygonal terrain. The platy deposits in this basin are proposed to represent either flood lavas or a debris-covered, paleolake or frozen sea according to conclusions by Balme et al. (2010).

The flood lava origin was concluded based on visual similarities between terrestrial lava flow surfaces and the platy terrains on the channel and basin floors (McEwen et al., 1998; Hartmann & Berman, 2000; Keszthelyi, McEwen & Thordarson, 2000; Plescia, 2003). Jaeger et al. (2007) studied the small pitted mounds and cones in Athabasca Valles and argued that the cones are volcanic rootless cones and that the platy terrain must also therefore be lava. Orosei et al. (2007) investigated both MARSIS and SHARAD datasets in this region and found that MARSIS cannot clearly detect any subsurface interface, which perhaps is due to the relatively fine subsurface layering hypothesised for this area, while SHARAD data contains subsurface reflections over most of the area, with varying depths and strengths. According to the results from SHARAD data, low-loss surface material was found in small patches over the putative frozen sea, while high losses were seen throughout most of the area. Alberti et al. (2012) studied

different approaches for addressing signal inversion of subsurface sounding radar data (Picardi et al., 2007; Zhang et al., 2008) and attempted to constrain the material by inverting the dielectric constant from the SHARAD data. They identified three distinct geological formations, namely a part of Zephyria Planum, the Cerberus plains and the bedrock beneath the plains. The retrieved electromagnetic parameters suggest a mixture of volcanic rocks with either ice or air, not supporting the conclusion of a frozen sea in this region.

On the other hand, Balme et al. (2010) suggested that the typical "platy/polyconvex" surfaces that are bounded by a clear morphological contact contrast strongly in terms of both morphology and number of impact craters (i.e., surface age), with the surrounding volcanic plains associated with the Olympus Mons volcano to the north. The "platy-ridged" terrain is composed of a jumble of fractured plates and sinuous ridges that are similar in form to terrestrial pack-ice (Brakenridge, 1993; Rice Jr et al., 2002; Murray et al., 2005), providing evidence for the fluvial origin of this region. Murray et al. (2005) suggested that the surface of the platy terrain has lowered by several tens of metres since formation, inferring that fluid drained from beneath the platy surface or was lost by sublimation. They proposed this as an evidence for a frozen sea which was also demonstrated by the unconformity between the rim height and crater diameter. Besides, the constructional landforms, such as the pitted mounds, polygonally patterned ground and sorted patterned ground were unlikely to occur for very young lava flows near the Martian equator unless they were later inundated with fluvially deposited materials (Balme et al., 2010). Substantial evidence for fluvial

erosion, including relict cataracts, down-cut erosional channels, streamlined islands in the channels, fluvial distributaries, hanging valleys, eroded topographic obstacles, can also be observed in this region, supporting the argument that fluvial episodes existed in the past. Regional slope across the basin is extremely low (about 10 m over a 500-km distance), which is strongly against volcanic deposition given the lower gravity on Mars and the non-Newtonian rheology of lavas (Balme et al., 2010).

All in all, geomorphologic, topographic and stratigraphic observations can all be explained by a fluvial origin of the Athabasca Basin, while the volcanic origin cannot explain the observations comprehensively. With the accumulation of SHARAD data and more subsurface layers being revealed in a wider region (Morgan et al., 2013), it is possible now to investigate the buried subsurface features over the Elysium Planitia and even over a wider region.

2.5.4 Automated extraction of subsurface layers

Studying the stratigraphy of the PLDs deepens our understanding of their formation and relevant past climate changes. Subsurface layers in the upper ~1000 m of PLDs have been revealed by SHARAD with a vertical resolution of about 15 m assuming a dielectric constant of free space. SHARAD has been orbiting Mars and collecting a huge amount of data for more than ten years, especially with a more comprehensive data coverage of the polar regions. However, the analysis of subsurface layers by using the radargrams is carried out mainly by manual investigation at present. The huge data collection task calls

for the development of automated or semi-automated techniques for analysing the SHARAD data and extracting relevant information in an effective and fast way. First, extracting subsurface reflections from the SHARAD radargrams is usually a preliminary step before studying the subsurface stratigraphy.

The development of techniques for the automated layering extraction from radargrams has not been addressed sufficiently in the literature, particularly using automated methods developed for analysing GPR data which can be taken as a starting point (Gamba & Lossani, 2000; Sokolov, 2012; Liu, Song & Lu, 2017; Ghozzi et al., 2017; Zhu et al., 2017). Limited studies on the automated detection of subsurface linear features in Martian radar sounding data have been reported in the literature. Freeman, Bovik & Holt (2010) used a combination of filters followed by a thresholding operation to extract subsurface layers from the SHARAD radargrams, but they did not address the task of labelling layers which are formed in different ages. Ferro & Bruzzone (2012) analysed the statistical properties of SHARAD data and proposed an automated detection of subsurface linear features from radar sounding data acquired in Martian icy regions which contain extended layers (Ferro & Bruzzone, 2013). In their work, a BM3D filter (Dabov & Foi, 2007) followed by a Steger filter (Steger, 1998) is used to extract the linear features from radargrams. Since the ice layers in the radargrams share similarity with fingerprints, log-Gabor filters (Kovesi, 1999), which are widely used for fingerprints enhancement (Lee & Wang, 1999; Munir & Javed, 2004), have the possibility to work well with the SHARAD radargrams as well, although no work has been reported on its application in this field in the literature.

The 3-D reconstruction of the stratigraphic structures and inversion of the dielectric constant by using the SHARAD data are two applications after the detection of subsurface reflections. Several studies attempted to develop methods for the 3-D reconstruction of the subsurface features and subsurface planes (Kleuskens & Oosthoek, 2009; Morgan et al., 2013). Foss et al. (2017) accomplished the 3-D volumes for both polar regions of Mars. The 3-D volume imaging is built up with 2-D interpolated images of every time delay position. The 3-D volumes of SHARAD of Martian polar regions are available at https://sharad.psi.edu/3D/. They demonstrated that the clutter effect can be mitigated by a combination of multi-orbit data. However, the following detection of subsurface features and planes still depends on human visualisation and interpretation.

Estimation of the dielectric constant can be achieved by either a surface model or a two-layer model (Zhang et al., 2008; Campbell & Putzig, 2011; Campbell et al., 2013; Putzig et al., 2014). In the surface model, only the surface reflections are analysed and the estimated dielectric constant is affected by the top part of the probed medium, which has a thickness of several metres or even less. In the two-layer model, usually, the ratio between surface reflection and subsurface reflection is calculated and is related to the dielectric constant of the subsurface medium which is bounded between the surface and subsurface reflections and is assumed to be homogeneous. Grima et al. (2012) produced a Martian radar reflectivity map using SHARAD data and compared it to the correlation length, absolute slope and root mean square height derived from

MOLA DTM. Comparatively, MARSIS data was also analysed by using the surface radar reflectivity, which was related to the inventory of subsurface H_2O (Mouginot et al., 2010). Using a two-layer model of CO_2 and H_2O, Mouginot et al. (2009) also constrained the CO_2 dielectric constant of the South Residual Ice Cap (SRIC) to be about 2.2 and estimated the CO_2 and H_2O mixing ratio over the Martian south pole.

2.6 Summary

This Chapter summarised previous studies about subsurface mapping in deserts, terrestrial ice sheets and the Martian SPLD by using radar instruments, which include spaceborne SAR and radar sounders. On Earth, using spaceborne or airborne radar systems to investigate subsurface resources or features attracts more and more interest due to their high efficacy for research at regional scales. The success of radar sounding in detecting features within ice bodies also facilitates the adaptation of the radar sounders to be applied to studies of the Martian polar regions. Based on the previous studies, several points can be concluded, as follows.

1. L-band SAR systems can be used to investigate buried features in the eastern Sahara and InSAR shows potential to be used for estimating the penetration depth of L-band SAR systems.
2. Existing automated methods for extracting linear features from radar sounding data acquired over ice sheets can be improved since the application of peak detection methods (e.g. wavelet transform), which have been applied to the GPR data, have not yet been fully investigated

with the radar sounding data. Peak detection methods used for GPR data, such as the wavelet transform, have high potential to be applied in detecting subsurface features in radar sounding data acquired by the SHARAD orbiting Mars.

3. Although many studies have been carried out to study the stratigraphy of the PLDs, the extraction of effective subsurface reflections from SHARAD radargrams takes considerable efforts and time. The extraction of subsurface features can be automated and improved by introducing digital image processing methods, such as Wavelet Transform and log-Gabor filtering. The 3-D block reconstruction of the Martian PLDs can be realised automatically and the buried features are likely to be highly enhanced in the 3-D data format.

Chapter 3

Subsurface Mapping and Penetration Depth Estimation in the eastern Sahara

SAR imagery is superior to optical imagery for subsurface mapping due to the fact that radar waves can penetrate through a sufficiently dry sandy layer while optical waves are always reflected and only display surface morphology (Elachi & Granger, 1982; McCauley et al., 1982). In some hyper-arid regions where the top cover layer consists of fine-grained, homogeneous, and sufficiently dry materials, radar penetration of several to tens of metres is likely to occur. Experiments showed that dry desert sand has a penetration depth of 5 m or more (Elachi & Granger, 1982). Based on the sand samples collected from the Selima Sand Sheet at the border of Egypt and Sudan, the penetration depths of radar waves are calculated as the depth when the radar wave is attenuated to 1/e = 37% of its original, which is about 0.1–0.3 m for X-band (λ = 3 cm), about 0.2–0.5 m for C-band (λ = 5.7 cm), and about 1.5–2 m for L-band (λ = 23.5 cm) (Schaber, McCauley & Breed, 1997). Moreover, the penetration depth at L-band is postulated to be deeper than 2 m because the paleochannels in the Selima Sand Sheet are visible in L-band images from SIR-A where the thickness of the sand cover layer is more than 2 m (McCauley et al., 1982; Robinson et al., 2006).

Since this revelation of SAR penetration under the Selima Sand Sheet, SAR penetration has attracted more and more attention in the eastern Saharan region. In the eastern Sahara, Robinson et al. (2006) reported a paleodrainage system located in the Kufra region, southeast of Libya, by analysing Radarsat-1 C-band (5.6 GHz/5.5 cm) images. This paleodrainage system passes through this region from south to east until Sarir Dalmah in Libya and is not displayed in the United States Geological Survey (USGS) HYDRO1k database which is derived directly from the surface topography, suggesting that it may be of subsurface origin (Robinson et al., 2006). Following this, a more complete JERS-1 L-band radar coverage of the eastern Sahara was used to create the first regional-scale radar mosaic covering Egypt, northern Sudan, eastern Libya, and northern Chad (Paillou & Rosenqvist, 2003). Subsequently, ALOS/PALSAR L-band data allowed, for the first time, an accurate mapping of a continuous 900 km-long paleodrainage system, which is termed the Kufra River (Paillou et al., 2009).

The sand cover overlies the Nubian Sandstone Series, which are composed of sands, sandstones, clays, and shales (Lüning et al., 1999). The Nubian Sandstone Aquifer System (NSAS) is the largest known fossilised water aquifer system on Earth. It is located underground in the eastern Sahara and spans just over 2×10^6 km^2, including north-western Sudan, north-eastern Chad, south-eastern Libya, and most of Egypt (Robinson et al., 2007). It contains an estimated 1.5×10^5 km^3 of groundwater and has a thickness ranging from 140 to 230 metres (Dahab, Ebraheem & El-Sayed, 2001). More than 360 borehole records near the centre of the Nubian Sandstone basin in Egypt show that the groundwater depth

ranges from 500 to 1200 m and reveals three groups of aquifers at depths of about 200 m, 400 m and 650 m from the surface (Shata, 1982).

Exploration of paleorivers here was driven by the L-band observations of Paillou et al. (2009, 2010). The Kufra River sitting on the NSAS in the eastern Sahara was chosen as the study site as it covers one tributary of a paleoriver. Four ALOS/PALSAR datasets were processed using the InSAR technique. However, after this work, it appeared unfeasible to map subsurface aquifers which are buried hundreds of metres underground using InSAR. This is because only a few metres elevation difference to the surface can be measured using L-band SAR data. As a by-product, a method is proposed to derive a single estimate of the penetration depth using ALOS/PALSAR InSAR results by differentiating between sandy and non-sandy areas using SAR backscattering differences and InSAR results. The coverage and acquisitions of data is presented in Section 3.1. The analysis and application of the data is separated into two parts, one of which is to compare SAR imagery with other images in terms of their ability to reveal sand buried features, such as the paleochannels in the Kufra region of the eastern Sahara. The second part is to investigate the capability of the InSAR technique to estimate penetration depth. To this end, differing elevations detected by the L-band ALOS/PALSAR and C-band SRTM are obtained by using differential SAR interferometry. Finally, the different elevations are analysed to estimate the penetration depth of L-band SAR with respect to C-band SRTM. In addition, ICESat elevations are used to confirm the estimated penetration depth.

3.1 Study Site and Data

The study site (centre latitude and longitude are 23.265°N, 23.603°E), which is indicated by the red rotated rectangle in Figure 3.1(a), covers one of the eastern tributaries of the Kufra River that is delineated as blue lines in Figure 3.1(a). This tributary arises in northern Uweinat close to the Sudanese border and is named the Uweinat tributary (Robinson et al., 2006). Figure 3.1(b) shows the ALOS/PALSAR HH amplitude image (70 × 110 km), along with three close-up images from Google Earth to show three bright spots in the ALOS/PALSAR HH amplitude image. Figure 3.1(c1, c2) display two areas which appear to be plants covered by sand. These features have green spots which look like plants when zoomed in Google Earth. Figure 3.1(c3) shows an area which seems to be outcrop rocks. These features show bare surface manifestation in the Landsat image while have high reflectance in the ALOS/PALSAR amplitude image. These characteristics are consistent with those of rocks or consolidated sand/soil. The white diamond in Figure 3.1(c) denotes the location of a reference point used in the following InSAR processing.

Over the study site, seven types of data are collected, which include: (1) ALOS/PALSAR; (2) Landsat; (3) SRTM C-band amplitude image, which is combined by sub-swaths 1 & 4 of HH and sub-swaths 2 & 3 of VV polarised images; (4) SRTM C-band DEM; (5) the MODerate-resolution Imaging Spectro-radiometer (MODIS) Precipitable Water Vapour product, PWV (MYD05 collection 06); (6) the ERA (European Reanalysis)-Interim data from the European Centre for Medium-Range Weather Forecasts (ECMWF) and (7) ICESat/GLA14. The

MODIS PWV and ERA-Interim data are used for analysing the phase component in InSAR results, while the ICESat/GLA14 elevation is used as a surface elevation reference, and is thus only used in the final stage to confirm the estimated penetration depth at L-band.

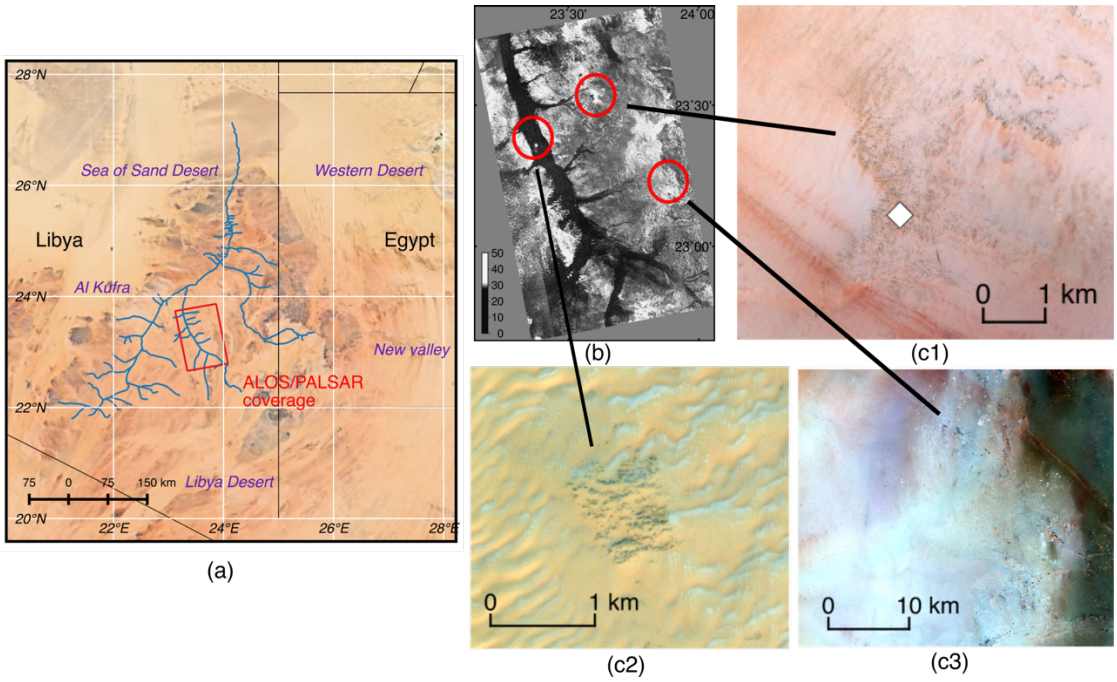

Figure 3.1: The geographical location and coverage of the study site and three close-up pictures from Google Earth showing the surface features. The background image in (a) is from Google Earth and is georeferenced in QGIS.

Four acquisitions of ALOS/PALSAR data are collected and their key features are listed in Table 3.1. The ALOS/PALSAR acquisitions are from ascending orbits of 13 August 2007, 13 February 2008, 30 September 2008, and 31 December 2008, respectively. Two of them are acquired in the Fine Beam Dual (FBD) polarisation of HH and HV, while two of them are obtained in the Fine Beam Single (FBS) polarisation of HH. The HV observations from two FBD

acquisitions suffer from striping artefacts. In addition, to make the most of all four acquisitions, HH polarisation is used to form interferograms. The incident angle is 34.3° for all acquisitions. According to the acquisition time of the PALSAR data, the available MODIS and ERA-Interim data that are acquired closest to the acquisition time of PALSAR data are collected. The dates and times of these data are listed in Table 3.2.

Table 3.1: Information on the four ALOS/PALSAR acquisitions.

Acquisition Dates	Orbit No.	Path	Frame	Polarisation	Product Type
13 August 2007	8268	627	450	HH/HV	Level 1.0 raw data
13 February 2008	10952			HH	
30 September 2008	14307			HH/HV	
31 December 2008	15649			HH	

Table 3.2: Acquisition dates and times of ALOS/PALSAR, MODIS PWV, and ERA-Interim data (DOY denotes day of year).

No.	Date	DOY	ALOS/ PALSAR	MODIS PWV	ERA-Interim
			UTC Time		
1	13 August 2007	225	21:00:24	11:35	18:00
2	13 February 2008	044	20:58:56	12:25	
3	30 September 2008	274	20:58:25	11:50	
4	31 December 2008	366	21:00:00	12:20	

ICESat was an earth observation mission primarily designed for measuring ice sheet mass balance from 2003 to 2009 when the satellite failed. ICESat/GLA14 elevation data is acquired by LiDAR altimetry and has a vertical

accuracy up to 0.04 m (Zwally et al., 2002; Carabajal & Harding, 2006). The land altimetry of ICESat was carried out over footprints of 70 m diameter which are spaced every 150 m. The ICESat altimetry data is referred to the TOPEX/Poseidon ellipsoid, and thence transformed to elevations that are referred to the WGS84 ellipsoid.

3.2 Surface Morphology of SAR Images

In this section, the surface appearances of different images are first inspected and compared. Figure 3.2 shows different types of images regarding their surface morphology over the Uweinet Tributary in Kufra. Figure 3.2(a) and Figure 3.2(d) are Landsat images in 2000 and 2007 which are extracted from Google Earth. Figure 3.2(b) is a SRTM C-band amplitude image. Figure 3.2(c) shows a colourised and hill-shaded SRTM C-band DEM, which is generated using the open source GMT (Generic Mapping Tools) with the publicly available SRTM C-band DEM (https://earthexplorer.usgs.gov/). Figure 3.2(e) shows the ALOS/PALSAR HH amplitude image.

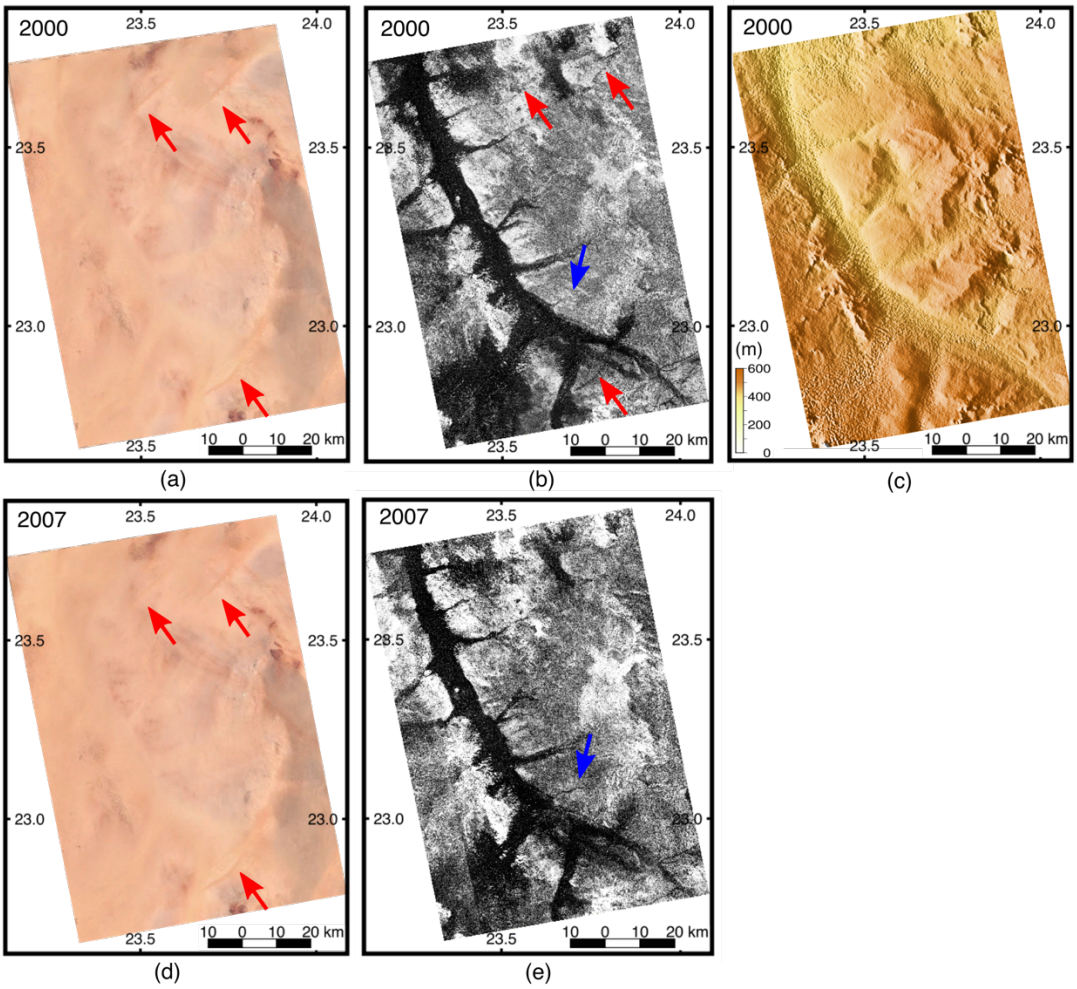

Figure 3.2: Comparison of different morphologies of (a, d) Landsat images (resolution is 30 m), (b, c) SRTM C-band amplitude image and DEM (grid-spacing is 30 m) and (e) ALOS/PALSAR HH amplitude image (range resolution is ~37 m and azimuth resolution is ~56 m). Years are labelled in the upper left corner of each sub-image. The red and blue arrows show interesting features which are explained later in the text.

Firstly, the Landsat images show no obvious subsurface channel morphology in this area and almost no change between 2000 and 2007. On the other hand, the SAR images, including PALSAR amplitude, SRTM amplitude and DEM, all display channels. In the two amplitude images, the channel areas show

dark tones and appear like fluvial branches. The clear edge of the channels separate the channel areas from other parts of the image. The channel areas maintain a much darker tone than the surrounding areas, indicating a different wave radiation mechanism between the channel and other areas. Dark tones within the channel areas indicate low backscatter, which can be explained by two scenarios considering the side-looking property of PALSAR. One scenario suggests a smooth surface of the radar wavelength, which causes specular reflection of the incident radar waves. Alternatively, the incident radar wave penetrates the sand layer and is greatly attenuated due to dielectric losses or volume scattering losses in this sandy cover material. The latter scenario implies that SAR penetration may occur within the channels. The brighter areas around the channels may result from surface scattering. The rougher the surface, the more energy can be reflected towards the direction of the receiver. Therefore, the medium tone can be explained by a rough surface if no penetration occurs. The medium tone may result from another scenario in which the radar wave transmits into the subsurface and is reflected by a shallow buried dielectric boundary, while a part of the wave energy is attenuated during the transition between the surface and dielectric boundary. Above all, the channel areas are the most probable areas that radar wave penetration may occur, although radar waves may be attenuated during the wave propagation and no definitive conclusion can be reached without independent measurements whether or not the L-band radar waves penetrate down to the sand-bedrock interface without visiting the region.

Red arrows in the Landsat images (Figure 3.2a and Figure 3.2d) point out three noteworthy areas, the upper and lower of which are enlarged in Figure 3.3(a) and (b), respectively. These areas are observed as sand dune like features in the Landsat images and are recognisable in the SRTM C-band amplitude image (Figure 3.2b) as well. However, these areas cannot be identified in the PALSAR image (Figure 3.2e). One possible explanation for this is that the surface may be smooth at L-band (~23.6 cm), but rough at C-band (~5.6 cm). An alternative is that the sand dunes are transparent at PALSAR wavelengths and that the appearance of the PALSAR image is mainly due to low backscatter caused by attenuation during wave propagation below the visible land surface. The SRTM C-band DEM shows the main channel and its branches, which are incised into the mountains. However, it is hard to delineate the morphology of short branches or where branches flow into the open areas by examining the SRTM C-band DEM.

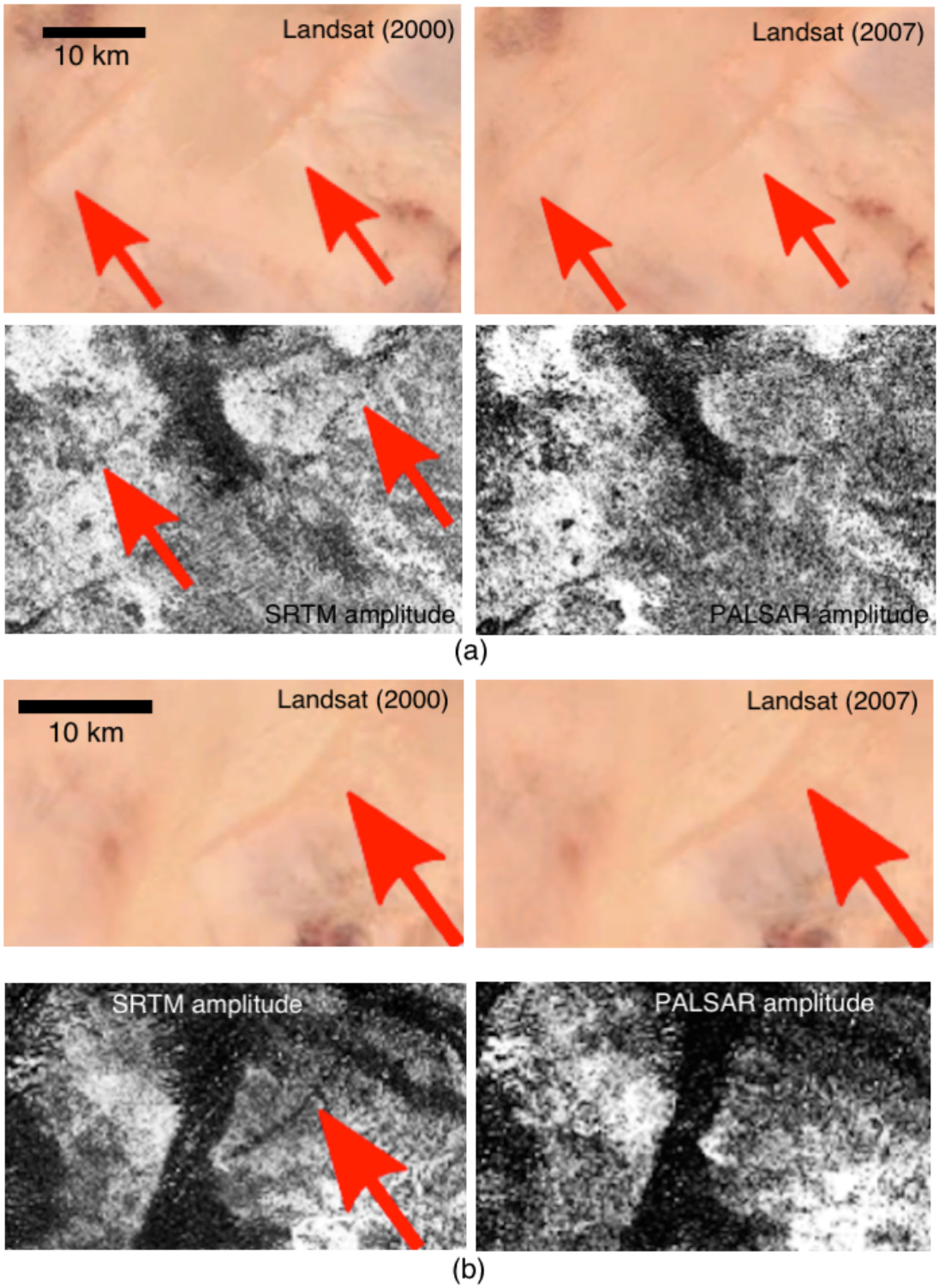

Figure 3.3: Close-up of the comparison of the sand dune areas between Landsat colour composite, SRTM amplitude and ALOS/PALSAR backscatter amplitude images. Red arrows point to features which are inferred to be sand dunes.

Both the SRTM C-band amplitude image (Figure 3.2b) and the PALSAR image (Figure 3.2e) not only clearly display the main channel, but also show some branches. There is a very high contrast along the edges of the channels. The areas highlighted by the blue arrows in Figure 3.2(b, e) are enlarged in Figure 3.4. The PALSAR image shows a subtle branch, while in the SRTM amplitude image, the corresponding channel is shorter and fainter. These differing observations imply that the PALSAR's L-band radar waves may penetrate deeper than SRTM's C-band radar wave.

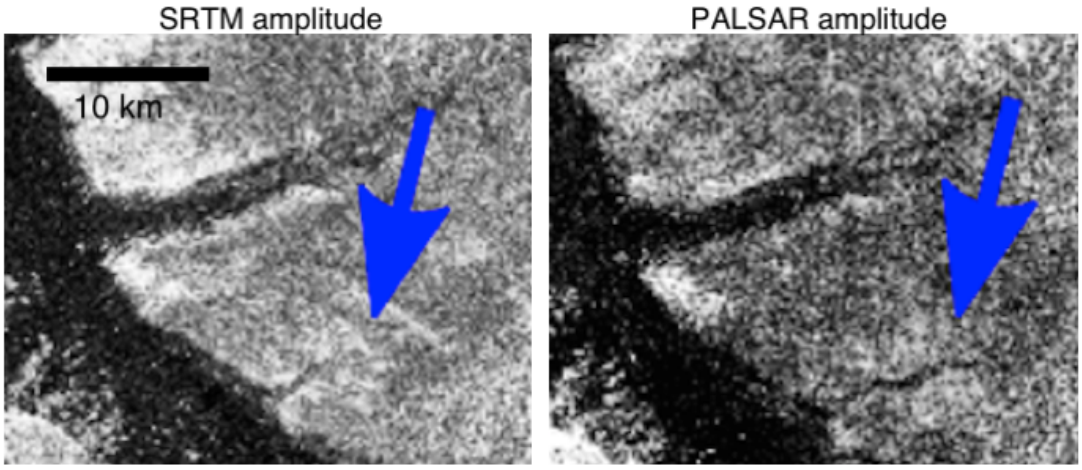

Figure 3.4: Comparison of the small branch of the main channel in the SRTM amplitude compared with a corresponding ALOS/PALSAR amplitude image. Blue arrows indicate one subtle branch which appears to be extending longer in the PALSAR amplitude image.

In summary, the channel areas are the most likely places where fine grained dry sand deposits allowing radar penetration within the channel regions. The SRTM DEM shows that the appearance of this channel may be associated with topographic variation. In addition, it appears that the L-band radar wave

penetrates deeper than the C-band within the channel areas. Therefore, it can be inferred that if the elevation difference could be measured by using L-band and C-band InSAR results, this elevation difference would be most pronounced within the channel areas.

3.3 Methods and Results

In the previous section, it was shown that SAR penetration most likely occurs within the channel areas, which is implied by the very low backscatter amplitude, and it appears that the penetration depth at L-band is suspected to be deeper than that at C-band. In this section, a method based on InSAR processing for estimating the penetration depth at L-band is presented.

In the InSAR processing as mentioned in Section 2.3.2, the remaining phase after removing the orbital and topographic phase, which is termed the differential phase, includes ϕ_{tro}, ϕ_{ion}, ϕ_{dis}, and ϕ_{noi}. However, if an L-band SAR image pair is utilised to form an interferogram and an external C-band SRTM DEM is employed to simulate the topographic phase, an additional phase component, ϕ_{ele_dif}, which results from the difference between L- and C-band, should be included. The overall differential phase components are expressed in Equation (3.1), while the additional phase component, ϕ_{ele_dif}, can be related to topographic variation p as Equation (3.2), where $\lambda, B_{\perp}, R, \theta$ are the wavelength, perpendicular baseline, slant range, and incident angle, respectively. The phase component caused by surface displacement is as the same as Equation (2.13), and can be rewritten into Equation (3.3) in this chapter.

$$\Delta\phi = \phi_{orb} + \phi_{ion} + \phi_{tro} + \phi_{dis} + \phi_{ele\_dif} + \phi_{noi} \tag{3.1}$$

$$\phi_{ele\_dif} = -\frac{4\pi}{\lambda}\frac{B_{\perp}}{Rsin\theta}p \tag{3.2}$$

$$\phi_{dis} = -\frac{4\pi}{\lambda}d_{disp} \tag{3.3}$$

The DInSAR (Differential InSAR) processing flow and analysis of different phase components are shown in Figure 3.5. Using DInSAR in this application has two objectives. On the one hand, after removing the topographic and orbital phase, the remaining phase is likely to be caused by surface displacement and/or topographic phase residual, which may result from the different penetration depths detected by L- and C-band SAR. On the other hand, analysis and conversion of the elevation differential phase, ϕ_{ele_dif}, is direct and more accurate than including the topographic phase because unwrapping is more accurate when removing topographic phase.

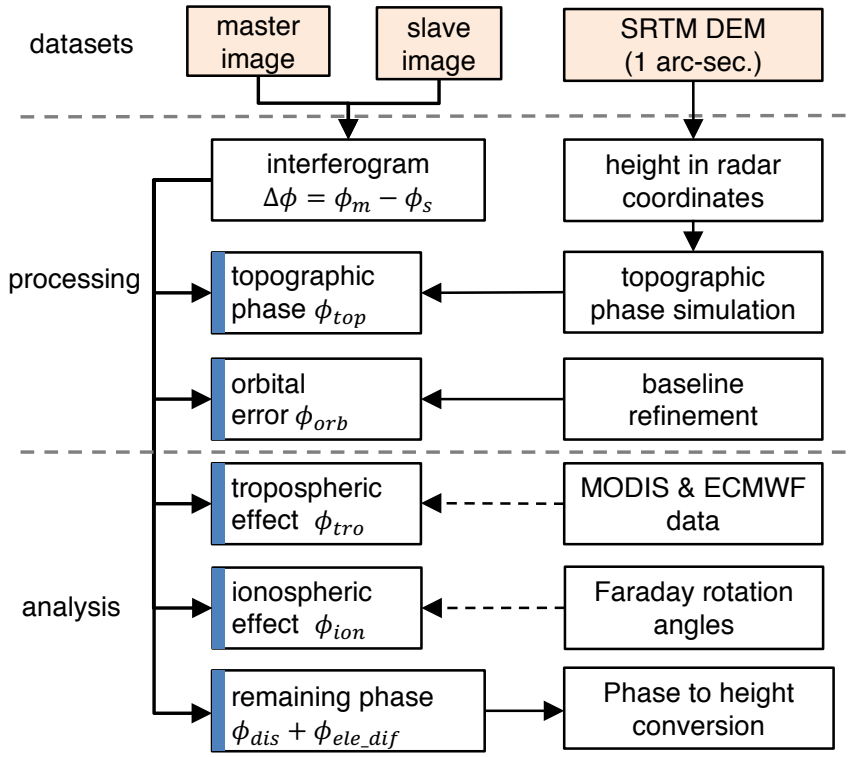

Figure 3.5: Flowchart of InSAR processing and analyses of phase.

3.3.1 Formation of Initial Interferogram

InSAR utilises the phase differences of the waves, so it requires signals from two different acquisitions to be coherent. Multi-look processing is a traditional method to reduce phase noise in SAR processing, while it reduces the resolution of interferograms. The phase noise can be estimated from an interferometric SAR pair using coherence. The coherence is the cross-correlation coefficient of the SAR image pair, which is estimated over a small window (a few pixels in range and azimuth). The theoretical elevation dispersion (standard deviation), σ_h, can be calculated from the perpendicular baseline and coherence as Equation (3.4) (Ferretti et al., 2007).

$$\sigma_h = -\frac{\lambda R sin\theta}{4\pi B_\perp} \cdot \sigma_\phi = -\frac{\lambda R sin\theta}{4\pi B_\perp} \cdot \frac{1}{\sqrt{2NL}} \cdot \frac{\sqrt{1-r^2}}{r}, \quad (3.4)$$

where λ is the wavelength, R is the range, θ is the incidence angle, $B_\perp$ is the perpendicular baseline, and NL, r are the number of looks and coherence which ranges between 0 and 1, respectively. Figure 3.6(a) shows the relationship between coherence and elevation dispersion as a function of different perpendicular baselines when NL = 8, while Figure 3.6(b) presents the relationship between coherence and elevation dispersion for different numbers of looks when the perpendicular baseline is set to 2000 m. Parameters used in the calculation are from the ALOS/PALSAR system: $\lambda = 0.236$ m, $R = 843{,}343$ m and $\theta = 34.3°$. NL = 8 is set to improve the coherence and maintain the spatial resolution (range direction is ~37 m and azimuth direction is ~56 m). We can see from Figure 3.6(b) that the coherence above 0.218 leads to an elevation dispersion within 5 m when the perpendicular baseline is 2000 m and NL = 8.

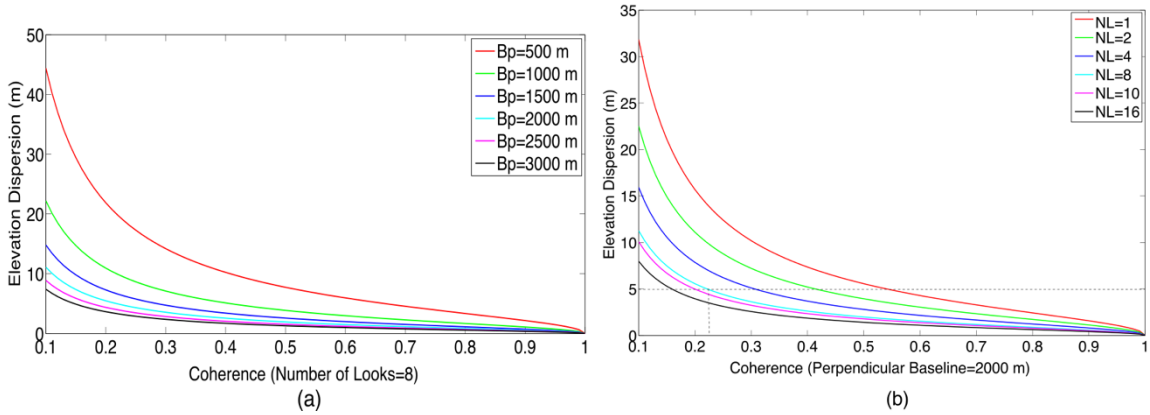

Figure 3.6: Relationship between coherence and elevation dispersion in (a) different perpendicular baselines and (b) different numbers of looks.

The temporal and spatial baselines of the four ALOS/PALSAR images were calculated and are shown in Figure 3.7. Six radar image pairs can, in theory, be formed by using the four radar acquisitions. However, two of the pairs (13 February 2008–30 September 2008 and 13 February 2008–31 December 2008) have large perpendicular baselines beyond 2000 m, which cause difficulties for co-registration. Thus, only four radar image pairs are processed. InSAR processing was applied to the four ALOS/PALSAR InSAR image pairs of 13 August 2007–13 February 2008, 13 August 2007–30 September 2008, 13 August 2007–31 December 2008, and 30 September 2008–31 December 2008. These four pairs are processed using the InSAR processing availabe in The Repeat Orbit Interferometry PACkage, ROI_PAC (WInSAR, 2017), developed by NASA's Jet Propulsion Laboratory (JPL).

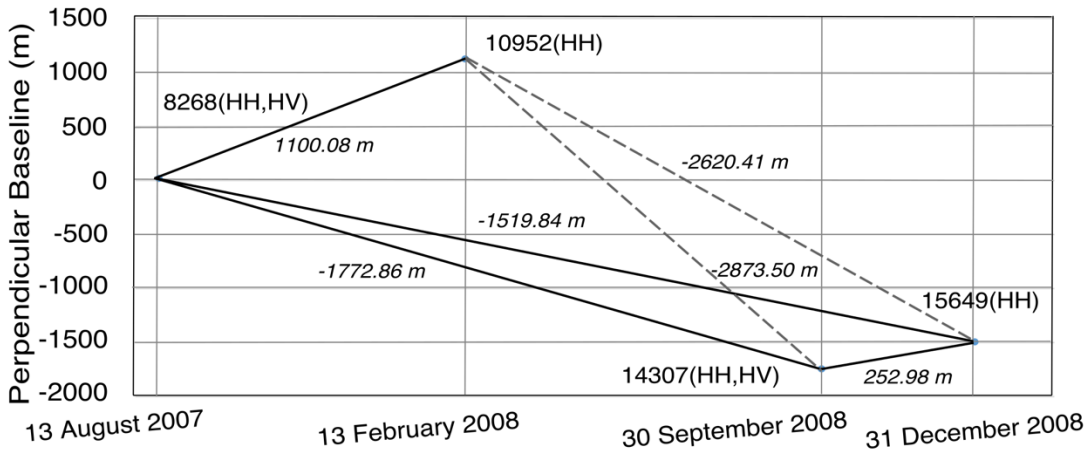

Figure 3.7: Perpendicular baselines of different InSAR pairs between four ALOS/PALSAR acquisitions. The numbers in the figure are the orbit numbers (8268, 10,952, 14,307, and 15,649). Baselines which are larger than 2000 m are indicated by dashed lines.

3.3.2 Removal of Topographic and Orbital Phase

The external DEM used to simulate topographic phase is SRTM C-band DEM (Version 3, resolution of 1-arc second ~30 m), whose elevations are referenced to the Earth Gravitational Model 1996 (EGM96) geoid, while the World Geodetic System 1984 (WGS84) ellipsoid is used in InSAR processing. The SRTM C-band DEM datum is converted from EGM96 to WGS84 by using an EGM96 15' geoid height mode. Differential interferograms shown in Figure 3.8(a1–a4) are formed by subtracting the simulated topographic phase from the initial interferograms. These interferograms include all the phase components in Equation (3.1), and phase ramps are observed to be along both the range and azimuth directions. These phase ramps may be caused by imprecise baselines which are estimated from inaccurate orbit information of the satellite positions or can be caused by both orbital inaccuracies and the different atmospheric delay between two acquisitions. In other words, orbital phases and atmospheric phase may be mingled together, and therefore behave as a phase ramp along both the azimuth and range directions (Xiong et al., 2014).

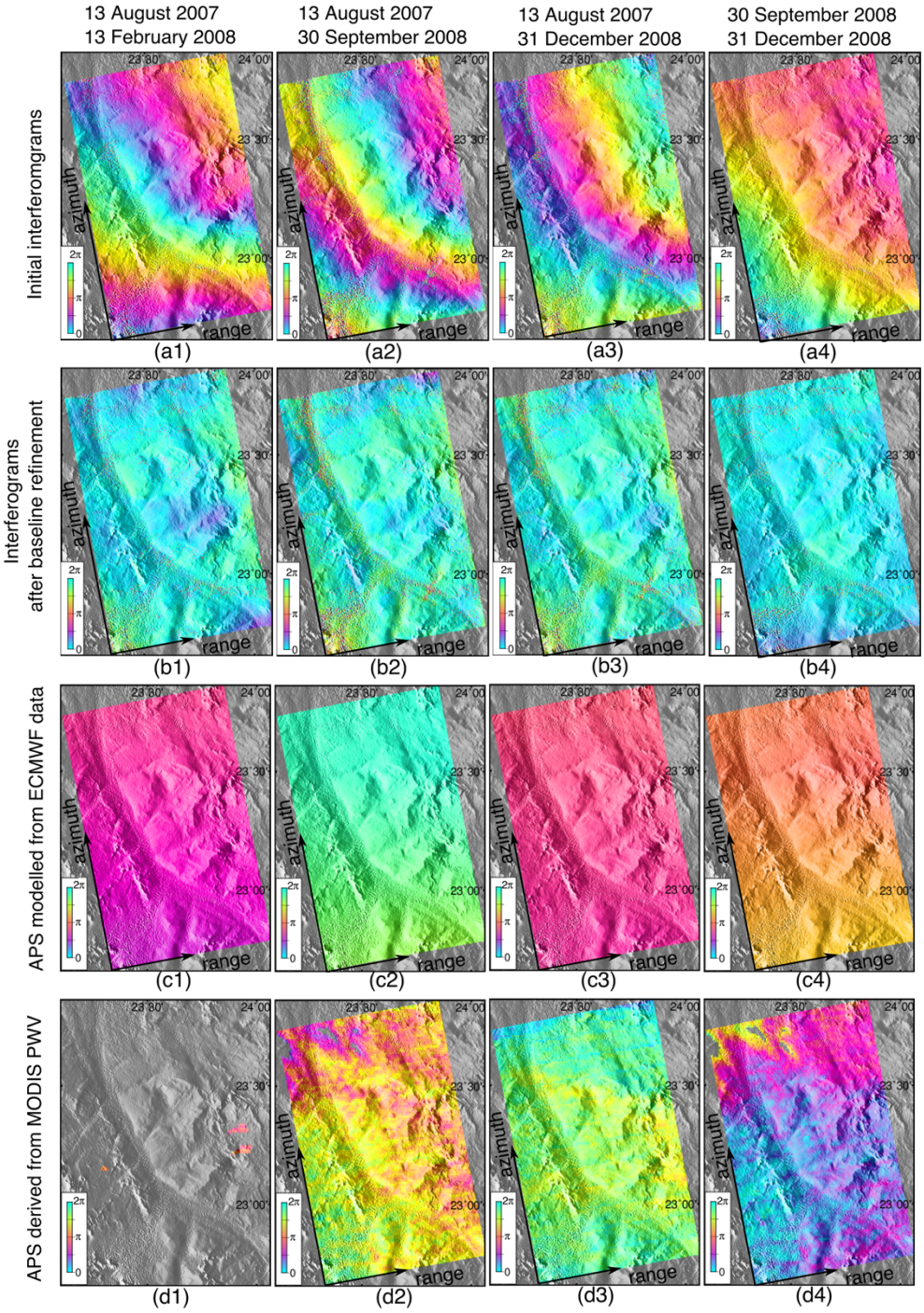

Figure 3.8: (a1–a4) Initial interferograms; (b1–b4) Interferograms after baseline refinement; (c1–c4) APS modelled from ERA-Interim data; (d1–d4) APS derived from MODIS near-infrared PWV.

The orbital phase ϕ_{orb}, which is another contributor to the $\Delta\phi$, is caused by the orbital trajectories. It can be removed given the knowledge of the satellite trajectories. For some missions, this knowledge is not sufficiently to the scale of the wavelength, leading to errors in the baseline estimation and leaving regular fringes in the interferogram. These periodic fringes can be used in turn to refine the relative separation between the two trajectories, which is termed baseline refinement. In ROI_PAC, the baseline refinement is realised by a quadratic model fitted between the total phase and surface elevation from an external topographic data source (Ferretti et al., 2007). Baseline refinement is applied to the interferograms when periodic fringes are observed after removing topographic orbital phase. The remaining phase is unwrapped by using the phase unwrapping algorithm, which in this case is the Statistical-cost, Network-flow Algorithm for Phase Unwrapping (SNAPHU) (Chen & Zebker, 2002). Figure 3.8(b1–b4) shows the interferograms after baseline refinement. The phase ramps appear to have been successfully removed. Phase distributions in Figure 3.8(b2, b3) resemble each other, while Figure 3.8(b1) has more spatial variation and Figure 3.8(d4) is more uniform in space.

3.3.3 Analysis of Remaining Phase Components

Radar waves of very low frequency propagate through the ionosphere undergoing Faraday Rotation (FR), i.e., rotation of the polarisation vector. This is mainly caused by the anisotropy of Total Electron Content (TEC) in the ionosphere, the values of which are currently very low in the 11-year solar cycle (Wegmuller et al., 2006). In addition, most PALSAR acquisitions occur at a local

time of 23:00, when TEC content is also typically low (Chen & Zebker, 2012). The Faraday rotation angles associated with the ionospheric effects are attached in the PALSAR catalogue metadata which can be downloaded from the Alaska Satellite Facility (ASF). For SAR acquisitions of 13 February 2008 and 31 December 2008, the estimated Faraday rotation angles are 1.3° and 1.4°, respectively. According to Equation (3.5) and (3.6), the phase difference caused by inhomogeneity of the ionosphere, $\Delta\phi_{tro}$, can be estimated using the Faraday rotation angles, Ω_m and Ω_s. In this case, the phase difference is much less than one radian. In addition, the interferograms in Figure 3.8(b1–b4) do not show noticeable artefacts along the azimuth direction. Therefore, the ionospheric effects are thought to have no significant impact on the interferograms and can thus be neglected in this case.

$$\Delta\phi_{tro} = \frac{8.45\times10^{-7}}{f}\Delta TEC = \frac{8.45\times10^{-7}}{k\boldsymbol{B}cos\theta_t}(\Omega_m - \Omega_s) \tag{3.5}$$

$$k = \frac{|e|^3}{8\pi^2 c\varepsilon_0 m_e^2} \tag{3.6}$$

$$\Delta\phi_{tro} = k_t\frac{(\Omega_m - \Omega_s)}{cos\theta_t} \tag{3.7}$$

where ΔTEC is the difference in TEC, and k is a constant with e being the elementary charge, c is the speed of light, ε_0 is the permittivity of free space, m_e is the electron mass, and θ_t is the angle between the SAR signal propagation direction and the B-field and f is the carrier frequency of the radar. In Equation

(3.7), the k_t is calculated to be 0.687-1.787 when using a $\boldsymbol{B}$ value of 0.25-0.65 gauss.

The radar wave is delayed when it propagates through the troposphere and ionosphere, resulting in ϕ_{tro} and ϕ_{ion} respectively. The sum of these two components is called the atmospheric effects. Phase delay through the troposphere is primarily caused by PWV. In hyper-arid regions, such as the Sahara Desert, the temporal and spatial variation of the PWV within a SAR frame is likely to be less significant than over other areas because of the low humidity in this region. To confirm this, MODIS PWV and ERA-Interim data are used to compute the phase delay differences between two acquisitions, termed Atmospheric Phase Screen (APS). The methods used to generate an APS from the MODIS Precipitable Water product and ERA-Interim data are discussed in studies of Li et al. (2009) and Jolivet et al. (2011), respectively.

The results of these two methods are shown in Figure 3.8(c1–c4) and (d1–d4), respectively. The acquisition of 13 August 2007 is affected by cloudy weather which can be observed in the MODIS cloud mask, so Figure 3.8(d1) shows almost no result from the MODIS PWV. We can see from Figure 3.8(c1–c4) that the APS modelled from the ERA-Interim temperature and pressure data are uniform in the range direction, but follow a linear trend along the azimuth direction. This may be the azimuth component to the phase ramp in Figure 3.8(a1–a4), and if it is, it may have been removed with orbital phase during the baseline refinement. The spatial variations of these four APSs are much less than 1 radian, which correspond to an elevation variation of 4.46 m when the perpendicular

baseline is 2000 m. However, compared to the APS modelled by ERA-Interim data, the APS derived from the MODIS near-infrared PWV (Terra L2 product from collection 006) have more spatial variation, which are within 1 radian (Figure 3.8d1–d4). The striping artefact in Figure 3.8(d1–d4) is caused by well-known uncorrected radiometric calibration differences. Errors in the derived water vapour of MODIS near-infrared retrieval are estimated to be 5–10%, and errors can be up to 14% under hazy conditions (Li, Muller & Cross, 2003). Considering that new systematic errors may be imported if these APSs are not accurate, the APS is not subtracted from interferograms. The interferometric phase in Figure 3.8(b1) is suspected to be suffering from the worst atmospheric effects among these four pairs. The spatial similarity between Figure 3.8(b2, b3) provides indirect evidence that these two pairs do not appear to suffer from serious atmospheric effects.

Another phase component ϕ_{dis} is caused by surface displacement during the time period between the SAR image pair. Surface displacement might be due to crustal movement, groundwater withdrawal, or sand movements in this study site. However, no nearby fault and no earthquake was reported from 13 August 2007 to 31 December 2008 over this area with the geologic map and earthquake event records that are available at http://portal.onegeology.org/OnegeologyGlobal/ and https://earthquake.usgs.gov/earthquakes/search/, respectively). Over a wider region which includes this study area, the land deformation that is caused by groundwater withdrawal is on the level of a few millimetres per year (Hamling &

Aoudia, 2011). This will cause an elevation error on the order of 0.5 m when it is wrongly interpreted as ϕ_{ele_dif}. Sand movements are composed of a mixture of deposition and erosion. However, if the L-band ALOS/PALSAR could observe sand movements such as sand dune motion, this area would probably appear as an area of low coherence because sand dune motion between acquisitions is likely to result in temporal decorrelation for any InSAR processing.

3.3.4 Estimation of penetration depth

After the analysis in Section 3.3.3, the remaining phase is mainly caused by the differences between L- and C-band SAR, thus the L-band and C-band Elevation Difference (LCED, L-band minus C-band) can be calculated by using Equation (3.4). The differential phase (remaining phase) is converted to height by using the Delft Object-oriented Radar Interferometric Software (DORIS) developed by the Technical University of Delft (TUDelft) (Kampes & Usai, 1999). The four LCED maps are shown in Figure 3.9(a1–a4), along with the InSAR coherence maps (Figure 3.9b1–b4). During the conversion, a reference point of high coherence is selected as the zero-phase reference. It is located at 23.52°N, 23.604°E and denoted by the white diamond in Figure 3.9(a1–a4). The first InSAR pair of 13 August 2007–13 February 2008 appears to be suffering from severe atmospheric effects because it involves the acquisition on 13 February 2008 when it was cloudy, according to MODIS observation on this day. Regarding 30 September 2008–31 December 2008, the perpendicular baseline is too short to derive the topographic variation of the interferometric phase. For instance, a topographic variation of 5 m only contributes to a phase change of 0.14 radians

within the InSAR frame according to Equation (3.2). Therefore, two of the InSAR pairs, 13 August 2007–13 February 2008 and 30 September 2008–31 December 2008, are discarded. The elevation difference caused by the L- and C-band SAR system is a spatial and temporal low-frequency signal in the LCED maps. Two LCED maps in Figure 3.9(a2, a3) are averaged into a final LCED map to reduce the impact from high-frequency components.

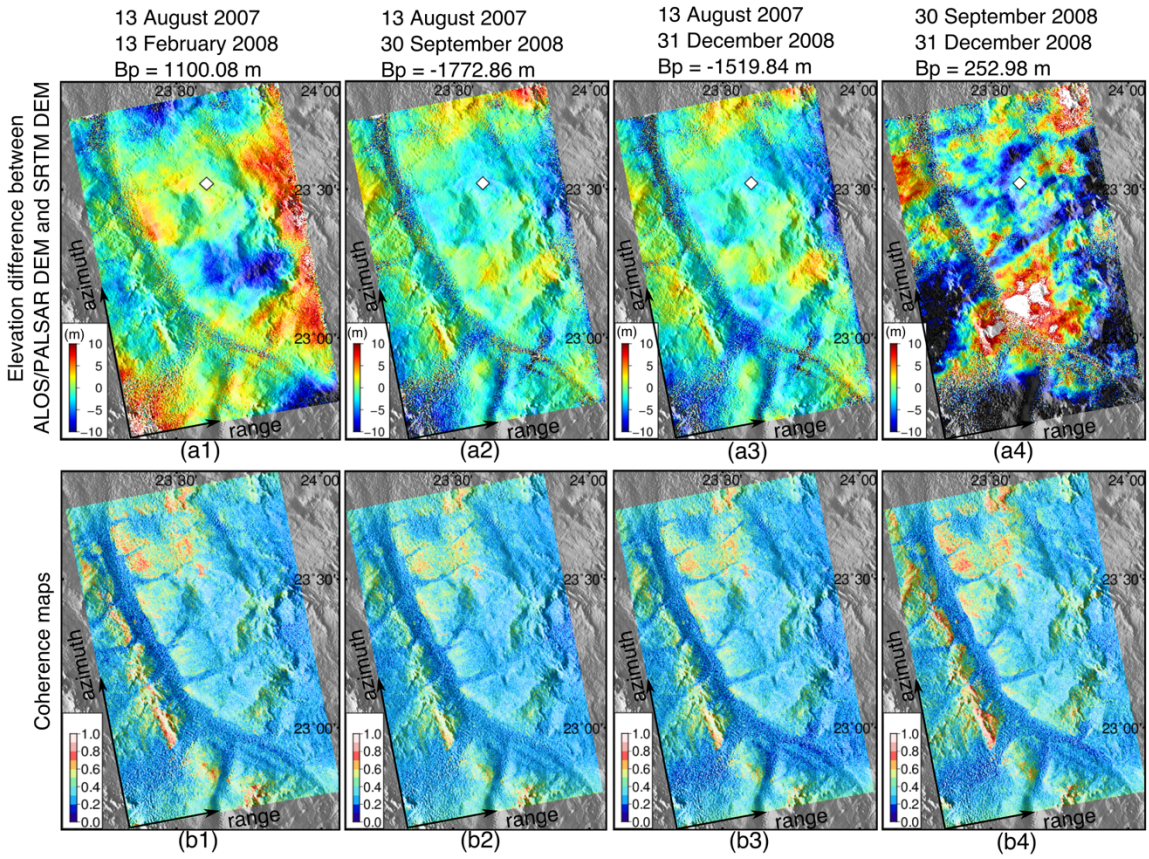

Figure 3.9: (a1–a4) Elevation difference maps converted from interferograms shown in Figure 3.8(b1–b4; (b1–b4) Coherence maps of the four InSAR pairs.

Theoretically, LCED on rock outcrops should be zero and be a negative value in the area where there is fine-grained sand cover. Therefore, the resulting LCED map would indicate the L-band C-band penetration difference if the LCED

has a negative shift in the channel areas compared to that of the non-channel areas. To confirm this idea, the study area is classified into three types, i.e., hilly, channel, and plain areas, by applying a supervised classification method, the Support Vector Machine (SVM) (Huang, Davis & Townshend, 2002), to an ALOS/PALSAR amplitude image, SRTM C-band DEM, and InSAR coherence, which are shown in Figure 3.6(a-c). These data are chosen for classification because the channel area is most pronounced in these images. The amplitude decreases when the elevation difference increases according to a study of elevation difference between SRTM DEM and ICESat elevations over a wider region in Kufra (Wang et al., 2015). Training samples fed to the SVM are chosen manually and divided in a proportion of 50% to 50% for training and testing the SVM classification. The overall accuracy of the classification is 97.28%. The study site is classified into three groups and the classification result is shown in Figure 3.10(d).

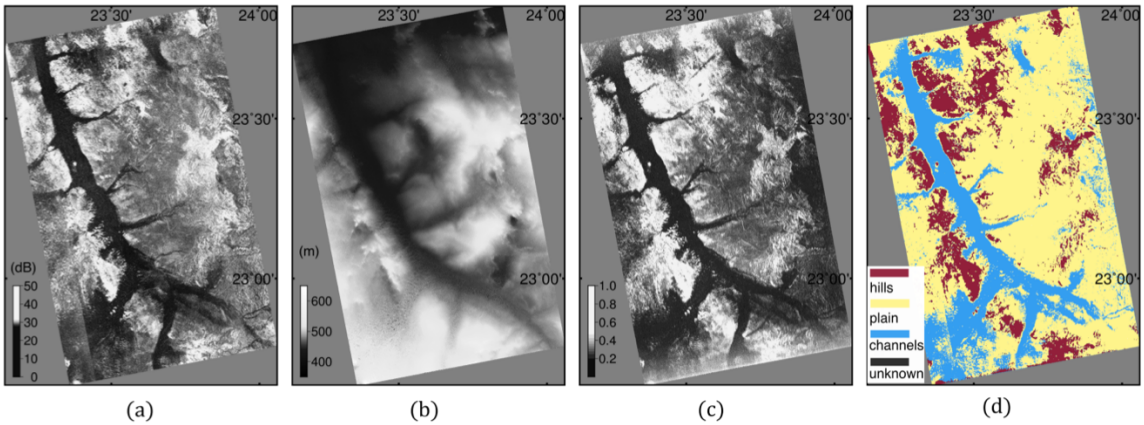

Figure 3.10: Land surface classification of the study site by using (a) the ALOS/PALSAR amplitude image; (b) SRTM C-band DEM; (c) the averaged coherence map from Figure 3.9(b1–b4); (d) SVM supervised classification.

Within each of the three land types, the histograms of LCED are analysed. In these histograms, the mean value of the histogram will be regarded as the penetration depth, which represents all the measurements in the surface type. The standard error of mean, $\sigma_{SM} = \sigma_{SD}/\sqrt{N}$, can be used to estimate the accuracy of this mean value. The σ_{SD} is the standard deviation of the histogram and N is the number of samples, which are the effective measurements within the surface type area in this case. Due to spatial correlation, the number of independent measurements is not the actual numbers of pixels within each surface type. This number of independent measurements can be estimated by dividing the area A of each surface type into areas with a radius of correlation range, R, which is $N = A/R^2$. A variogram can be used to evaluate the spatial correlation of measurements (Kääb et al., 2015; Li & Lin, 2017). The correlation range, R, is generated by analysing the variogram of measurements within each surface type.

Figure 3.11(a–c) show the histograms of the LCED within each group along with normal distributions fitted to the histograms. From these histograms and normal distributions, we can observe increasing negative elevation differences in the plain and channel areas compared to those in the hilly area. Although some locations in the hilly areas show positive elevation differences, the mean value is still negative, as we can see in Figure 3.11(a). The elevation difference in the hilly area is −0.983 ± 2.284 m, whilst in the plain area and channel area, it is −1.348 ± 2.463 m and −2.744 ± 3.244 m, respectively. The standard deviation is relatively large, which may be the result of the inclusion of many measurements of low

coherence. However, these low coherence measurements cannot totally be ruled out because the penetration process is more likely to occur where the coherence is low. Thus, only measurements of coherence lower than 0.218 are excluded. The larger skewness of the hilly area and channel areas indicate that more measurements tend to show negative shift values of LCED.

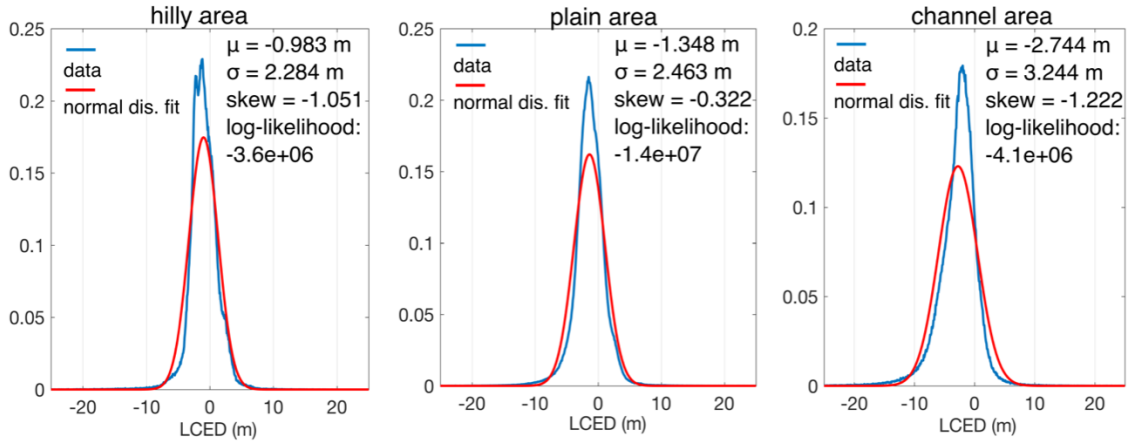

Figure 3.11: Analyses of elevation difference maps averaged from Figure 3.9(a2, a3): (a–c) are the results of fitting the elevation difference with normal distributions for the three types of land surface. Although the coherence is low over the channel and some plain areas, the PALSAR DEM detects lower elevations of 1–3 m compared with the SRTM DEM.

To evaluate the mean value obtained by the histogram, independent sample numbers need to be considered. The correlation range of the LCED map is calculated to be about 2.2 km in this study area. The calculation and statistical information is listed in Table 3.3. According to the calculation in Table 3.3, the standard errors of the mean are all within 0.1 m, which indicates that the derived shift is reliable.

Table 3.3: Statistics of the classification results and effective measurements. (Each pixel denotes an area of ~$56\ \mathrm{m} \times 37\ \mathrm{m} = 2\ 072\ \mathrm{m}^2$).

Statistical Measures	**Hilly Area**	**Plain Area**	**Channel Area**
Numbers of Pixels	1,610,483	6,113,905	1,566,449
Area (A, km^2)	3336.9	12,668.0	3175.2
Range from variogram (R, km)		2.2	
Independent sample numbers ($N = A/R^2$)	1517	5758	1443
Mean (m)	−0.983	−1.348	−2.744
Standard deviation (68.3%) (σ_{SD}, m)	2.284	2.463	3.244
Standard error of mean (68.3%) (σ_{SM} , m) $\sigma_{SM} = \sigma_{SD/\sqrt{N}}$	0.059	0.032	0.085

3.4 Validation of the penetration depth

The LCED indicates the differing penetration depths between the L-band PALSAR and C-band SRTM over different land surface types. Since the SRTM C-band DEM may also detect elevations lower than the surface, it is necessary to validate the SRTM C-band DEM to surface elevations. In the literature, the SRTM C-band DEM shows an average penetration depth of 1.7 m when compared with SRTM X-band DEM and around 7–9 m when compared with ICESat data over glaciers in the Pamir–Karakoram–Himalaya (Gardelle et al., 2013). The SRTM X-band DEM shows a systematic bias from SRTM C-band DEM, which is pronounced in Africa and South America (Hoffmann & Walter, 2006). ICESat elevations are considered to represent the surface elevations over glaciers and peatland areas (Ballhorn, Jubanski & Siegert, 2011; Gardelle et al.,

2013). Therefore, the land altimetry product (GLA14) from ICESat is used as a reference.

ICESat has three transects in this study area, which are labelled as ICESat-T1, ICESat-T2, and ICESat-T3 in Figure 3.12(a, b). The base map of Figure 3.12(a) is the same classification result shown in Figure 3.11(d). The base map of Figure 3.12(b) shows the elevation difference, which is averaged from Figure 3.9(b2, b3). Along these transects, the LCED and elevation difference between SRTM C-band DEM and ICESat elevations are compared. Figure 3.12(c1–c3) shows the comparisons. From Figure 3.12(c1–c3), we can see that in the hilly area, both the SRTM and PALSAR DEM agree closely with the ICESat elevations. However, when it comes to the plain and channel areas, both the SRTM DEM and the PALSAR DEM show lower elevations than the ICESat elevations, and the PALSAR elevations deviate even more than the SRTM DEM from the ICESat elevation. The red rectangle highlights the area where a negative shift of PALSAR DEM from SRTM DEM and ICESat elevations can be observed. Over the channel area, the PALSAR DEM is noisy due to low coherence; however, it clearly shows that there are lower elevations than either the SRTM DEM or ICESat elevations.

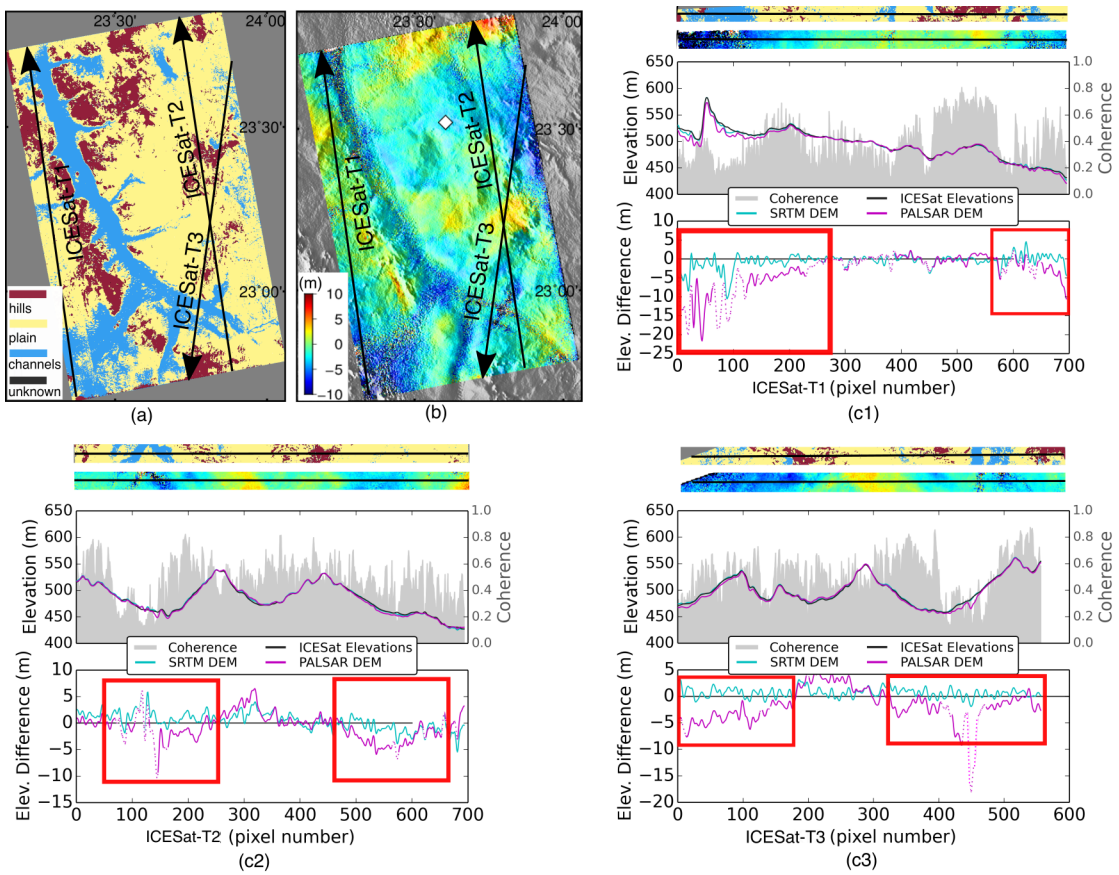

Figure 3.12: (a) The classification result, which is the same as Figure 3.10(d); (b) Elevation difference map averaged from Figure 3.9(a2, a3); (c1–c3) Comparisons between ALOS/PALSAR InSAR derived DEM, SRTM DEM, and ICESat elevations along three ICESat transects (ICESat-T1/T2/T3) across the study site. The dashed line segments in the lower panels of subfigures (c1–c3) are where the coherence is lower than 0.218.

3.5 Analysis of Badain Jaran Desert

Apart from the eastern Sahara, the Badain Jaran desert in Inner Mongolia in China is also analysed by comparing the geomorphologies from a Landsat image and radar images at L- and C-band. Comparison between a Landsat-8/OLI RGB composite image (band 7,4,2), PALSAR image, SRTM C-band DEM and amplitude image in the Badain Jaran Desert is shown in Figure 3.13. This Figure

shows an area between the Badain Jaran Desert and the Tengger Desert. These images reveal a fault (dashed line in Figure 3.13), which is the result of geological activity that caused the dislocation of the sand strips (Guo et al., 2000). The rectangle A in this figure shows river-like features, which are obvious in the ALOS/PALSAR image, and in the SRTM C-band DEM, which is partly due to the higher contrast between the dark tone sand strips and brighter tone from the surrounding areas. The rectangles B and C show two areas of sand dunes. In the SRTM C-band amplitude and DEM show clearer sand dunes than those of ALOS/PALSAR amplitude image, which implies greater penetration depth when using ALOS/PALSAR.

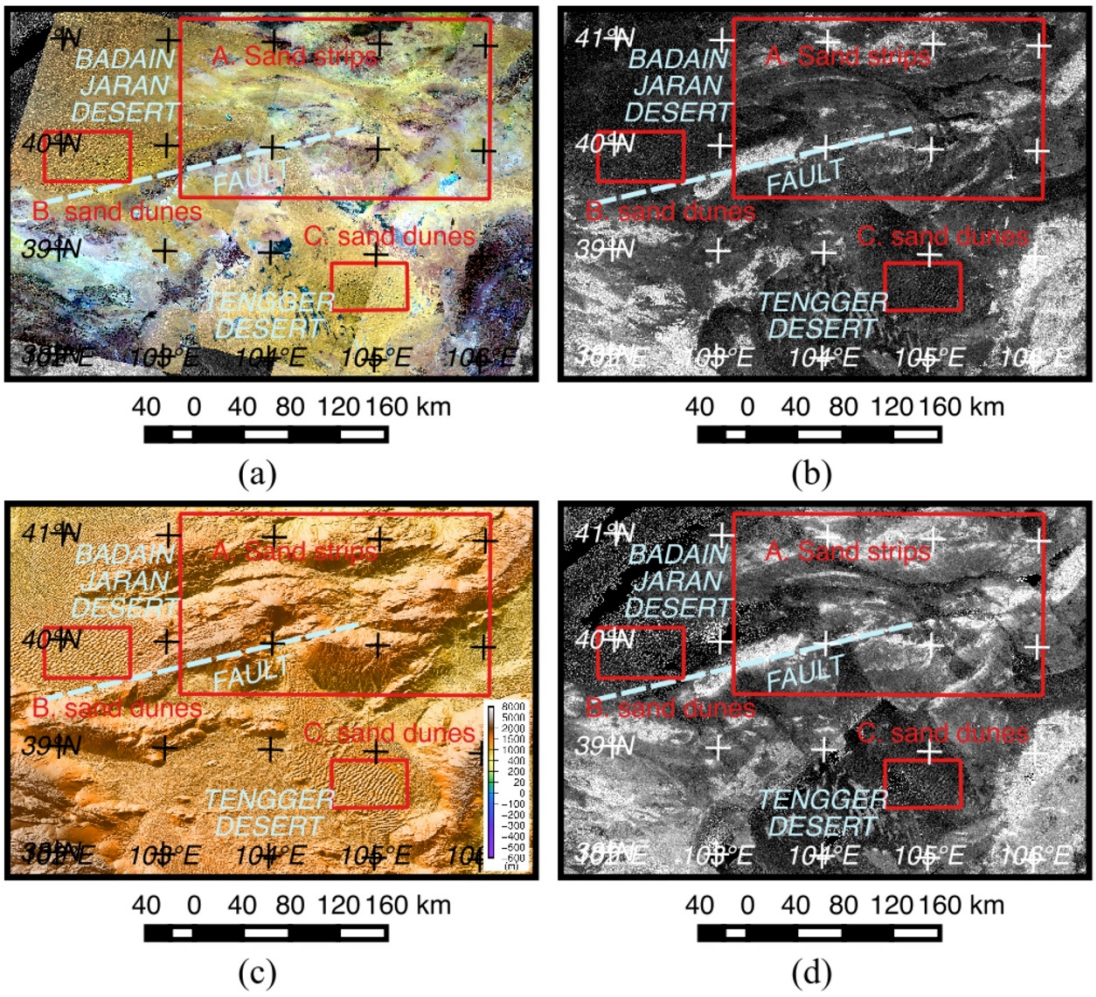

Figure 3.13: (a) Landsat-8 image (2015); (b) ALOS/PALSAR image (mosaiced from forest/non-forest maps derived from data between 2007-2010); (c) The SRTM C-band DEM (2000); (d) The SRTM C-band amplitude image (2000).

Three areas A, B and C in Figure 3.13 are chosen and enlarged in Figure 3.14, which highlights an area containing quasi-linear features (that appear like sand strips) and two areas of sand dunes. These quasi-linear features and sand dunes are visible in all the PALSAR image, the SRTM amplitude image and Landsat image. The SRTM C-band DEM vaguely shows the quasi-linear features indicated by arrows 1 and 2. However, the elevation variation does not clearly

indicate the geomorphology of the river network, which may be the result of interruption by the fault, hence, the DEM is insufficient to observe quasi-linear features given no prior knowledge. The SRTM amplitude image has higher contrast to show the quasi-linear features indicated by arrows 3 and 4 than the PALSAR image, which is the same situation as that in the Kufra drainage area. The dark tone features in SRTM amplitude image indicate where a penetration process may occur, while their lower contrast with surrounding bedrocks in the PALSAR image compared with the SRTM amplitude image implies deeper penetration depth by L-band SAR images.

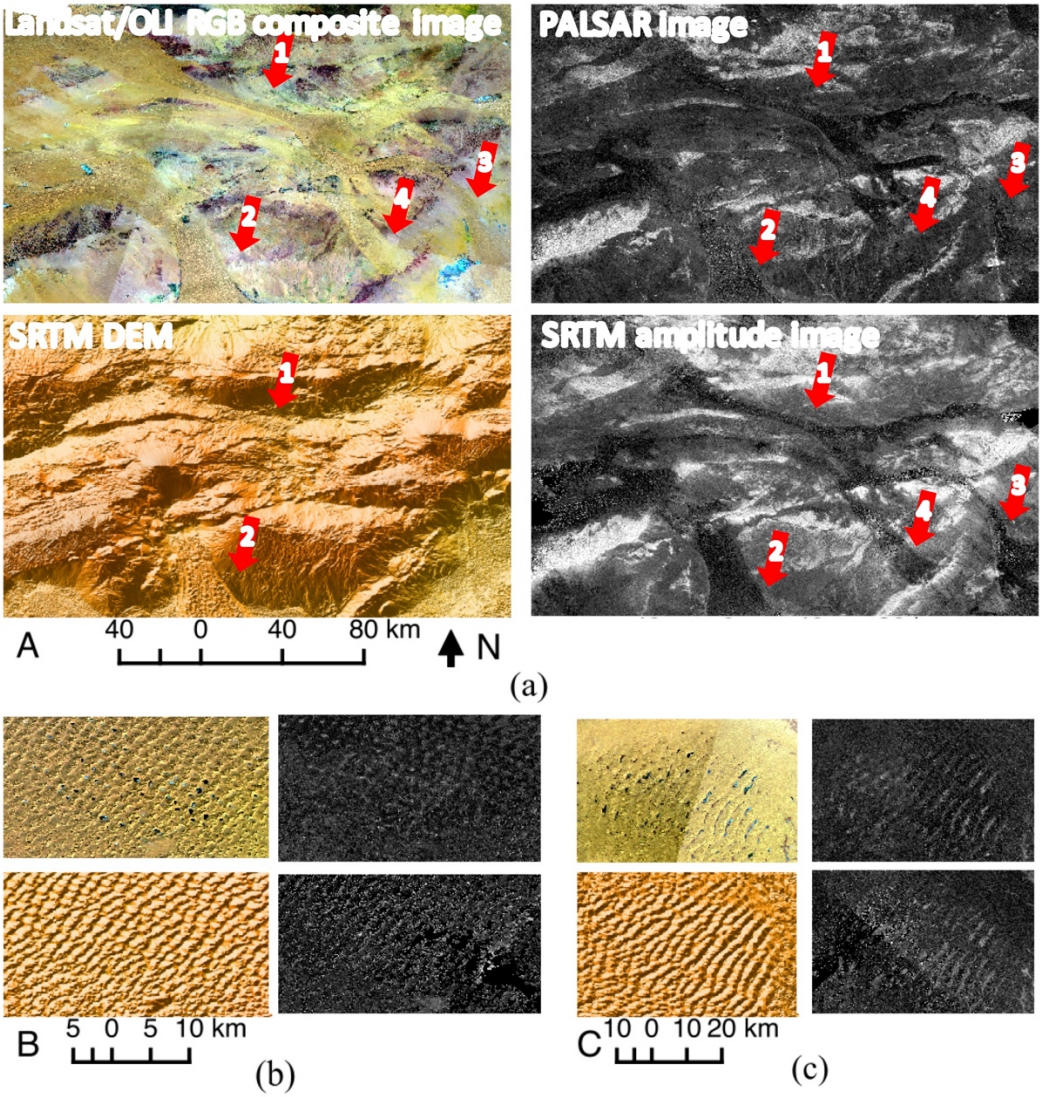

Figure 3.14: (a) Area A in Figure 3.13, showing quasi-linear features; (b) Area B and (c) Area C in Figure 3.13, showing sand dunes and Landsat image showing inter-dune lakes. (The arrows highlight the river-like features. The seamline in Landsat image of C is caused by mosaicking images from adjacent orbits).

Sand dunes are obvious in all four kinds of images in Figure 3.14(b-c), while inter-dune lakes are prominent only in the Landsat image. The existence of inter-dune lakes indicates high moisture content of the sand layers. Therefore, this area is not suitable for applying InSAR processing because of decorrelation of

the interferometric phase caused by near-surface water and possibly the movement of sand dunes (Chen & Liu, 2011). In addition, the low backscattering (dark tone in SAR image), such as that in the sand dune and inter-dune areas, is implying decorrelation of the InSAR processing. The method used in the Sahara Desert can be tried in this area if no in-situ measurements or other techniques (such as GPR and radar sounders) can be applied over this area in the future.

3.6 Discussion

This chapter presents the method based on DInSAR for estimating penetration depth. The accuracy of the elevation difference measured by the DInSAR technique depends on internal errors, such as unwrapping errors and baseline errors, and external influences, such as atmospheric effects and surface displacement.

The ambiguity in the number of waves between the transmitter and the ground results in unknown numbers of phase differences between two SAR acquisitions. This phase difference is cycled between 0 and 2π, which means that multiples of 2π are discarded. Phase unwrapping is used to re-engineer the actual phase by calculating the numbers of multiples of 2π, can be converted to a true range value. Given a single height reference point, these unwrapped ranges can be directly converted into elevation. Phase unwrapping usually takes advantage of the phase differences between neighbouring pixels; however, errors can occur when propagating this unwrapping across a whole image, especially when encountering pixels of low coherence. The unwrapping error causes a phase ambiguity which leads to a height ambiguity. According to

Equation (3.4), the height ambiguity for ALOS/PALSAR is 28 m. Most of the pixels in this dataset have been correctly unwrapped and this is supported by the fact that here are only a few outliers of LCED larger than 28 m, while most pixels have the LCED within 28 m as shown in the histograms. In any case, the estimation of depth is not carried out by analysing the histograms, but rather each individual pixel, which should reduce the impact of unwrapping error to the final estimates. The baseline error leading to an error in the height measurement can be expressed as $\Delta h = \Delta B_{\perp} \cdot h / B_{\perp}$. The height variation in this study site is about 400–600 m, thus, $\Delta B_{\perp}$ of 10 m can cause a height error of 1 m for the ALOS/PALSAR dataset when the perpendicular baseline is 2000 m, while the baseline error should be much less than this after baseline refinement.

According to Section 3.3.3, the APS simulated by using the ERA-Interim data features primarily as signals of low spatial frequency, which can be removed during the baseline refinement. Even though a residual of the atmospheric phase may be preserved in the final unwrapped phase, its impact on the LCED is suppressed by selecting long perpendicular baselines, according to Equation (3.4). Surface displacement caused by sand dune motion is not considered in this study as any significant motion of surface material usually causes severe decorrelation. Surface displacement caused by an earthquake is unlikely to be the main issue due to no earthquake record as a primary source of surface displacement in this region. In addition, areas appearing to be rippled sand dunes are observed in the SRTM C-band image which are not observed in the ALOS/PALSAR image. This indicates that sand movements are very likely to be

transparent to an L-band SAR system. Groundwater withdrawal is highly unlikely to cause such a large elevation shift between the channel and non-channel areas. Currently, there are a limited number of acquisitions of L-band ALOS/PALSAR data. Given more SAR datasets, the phase components from sources like atmosphere and surface displacement could potentially be analysed in more detail given the right observation conditions.

From the above analysis of the error sources, the remaining phase is believed to be mainly caused by the differences between the PALSAR and SRTM systems, which may result from different incident angles or different penetration depths at L- and C-bands. If the PALSAR and SRTM penetrate to the same depth, then this penetration depth needs to be 18.48 m to meet an LCED of 2 m considering their incident angles of 34° and 60° respectively and a dry sand refractive index of 1.67 (Mätzler, 1998). This underground propagation difference is unlikely in this region compared to excavated sandy layer depths of several metres from a field expedition in the eastern Sahara during the SIR-A mission (McCauley et al., 1982). Considering the different acquisition time of PALSAR and SRTM data, an alternative explanation of this difference can be due to the sand erosion from 2000 to 2008. However, this implies the necessity for further studies on the locations and changes in the sand deposits and erosions, which is beyond the scope of this study. It may be discussed in the future if sand movement data were to become available for this study site.

Therefore, the offset of the LCED between the channel and non-channel areas is currently regarded to be mainly caused by different penetration depths,

as reported over several other locations in the eastern Sahara (McCauley et al., 1982; Schaber, McCauley & Breed, 1997). Moreover, the increasing negative elevation differences from hilly areas to plain areas, and to channel areas support this argument. The negative shift LCED of about 1.76 m from the hilly to channel areas should be due to a greater penetration depth if no penetration is present in the hilly area. However, the comparison between SRTM DEM and ICESat/GLA14 elevations demonstrates that the SRTM DEM also detected a subsurface elevation rather than a surface one. Therefore, the actual penetration depth of the L-band PALSAR DEM should be larger than the previous estimates of 1–2 m.

3.7 Summary

This chapter presented a comparison of ALOS/PALSAR L-band SAR images, Landsat images and SRTM C-band amplitude images regarding different surface morphologies and the inferred differences in the SAR penetration depth. The L-band ALOS/PALSAR amplitude image shows the most detailed channels and branches, which imply a deeper penetration by the L-band radar wave compared with the C-band. An L-band and C-band elevation difference map was produced using the InSAR technique and used to estimate the penetration depth in the Kufra region. The results show that over one tributary of the paleochannel in the Kufra region, the ALOS/PALSAR detects surfaces at least 1–2 m lower than the corresponding C-band SRTM.

Although the original aim of this thesis was to map bedrock topography and investigate whether buried aquifers could be detected in deserts by using observations from the L-band ALOS/PALSAR, it turned out that detecting such

buried aquifers in hyperarid regions using spaceborne SAR at L-band is not feasible. This was unknown at the start of the research but was revealed sometime later in a report which was discovered from the British Geological Survey (MacDonald et al., 2011), concluding that the aquifers in the Eastern Sahara are around 25-100 m depth below the ground level. In order to keep the original goal of mapping the subsurface, the focus of this thesis was therefore changed to radar sounding techniques, which utilise lower frequencies and penetrate several kilometres into ice caps on the Earth and Mars. Unfortunately, no such radar sounding data is publicly available over desert areas. It was therefore decided to switch the centre of attention to polar ice regions where plentifully data exist. In the following two chapters, two applications of detecting subsurface interfaces using radar sounding data are demonstrated.

Chapter 4

Automated Layer-tracing from Radar Sounding Data in Greenland

4.1 Scientific Context

Apart from hyperarid regions, radar penetration plays an important role in subsurface mapping in icy regions as well. Spacecraft radar sounding is unlikely to be considered as a suitable platform for low frequency radar systems due to the large attenuation associated with fluctuations in the ionosphere. On the other hand, airborne and ground-based radar sounding techniques have been developed since the 1960s to map the topography under glaciers. A penetration depth of more than 3 km over the Greenland and Antarctica Ice Sheets can be achieved by radar sounders operating at frequencies of several hundred megahertz. One of the interesting subsurface features that can be observed in the RES data is the layering phenomenon within large ice bodies, e.g. Greenland Ice Sheet (GrIS) and Antarctica Ice Sheet (AIS).

One important application of radar sounding data is to measure ice thickness and basal topography. In this case, only the basal layer is utilised (Bamber et al., 2013). In addition, the distribution of englacial and basal layers containing records about the formation of the ice sheets, and providing

information about ice flow and ice dynamics, that are happening nowadays. As stated in Section 2.4.1, englacial layers in the upper hundreds of metres are caused by variations in ice density, which are associated with yearly snow accumulation. Therefore, the boundaries of these layers can be used to reconstruct ice sheet accumulation rates (Leysinger Vieli, Siegert & Payne, 2004; Cassanelli & Head, 2015). In the middle depths, englacial layers are often associated with past volcanic eruptions, so tephra layers can be used to reconstruct surface topography before these volcanic eruptions (Brandt, Björnsson & Gjessing, 2005; Kekonen et al., 2005). In the lower part of the ice sheets, the englacial layers generally result from changes of crystal orientation fabrics (Siegert & Kwok, 2000).

In addition, changes in vertical stratigraphy and planar continuity of englacial layers can be used to study regional ice flow structure and ice dynamic changes (Rippin et al., 2006; Karlsson et al., 2012; Bingham et al., 2015; Holschuh et al., 2017). Layer disturbances are also useful information, as they may be caused by internal ice flows (Drews et al, 2009), or by moulins or crevasses that deliver surface meltwater to the base of the ice sheets (Catania & Neumann, 2010). The meltwater may refreeze and produce basal ice units (Bell et al., 2014). Subglacial lakes are also identified by plane basal layers (Bingham & Siegert, 2009; Palmer et al., 2013). Another application of studying englacial layers is to select ice drilling sites that are usually expected to contain continuous layers instead of disrupted layers (Frezzotti et al., 2004).

Detection and extraction of these layers are usually preliminary work before relating them to the accumulation of snow, the internal ice dynamics and past climate changes. Building on the previous research, this chapter presents the usage of peak detection methods for detecting the Internal Reflection Horizons (IRHs) and a layer-tracing procedure to trace continuous layers from radar sounding data. The proposed methods are tested with MCoRDS data from the pre-IceBridge and OIB missions (Shi et al. 2010; Studinger, Koenig & Martin 2010; Leuschen & Allen, 2011). The test data and its geographical coverage are introduced in Section 4.2. A detailed description of the proposed layer-tracing method is presented in Section 4.3. Following in Section 4.4, the results are presented and compared to isochrones extracted in an independent study by Macgregor et al. (2015a). Finally, a summary of the benefits and disadvantages of the proposed method is discussed in Section 4.5.

4.2 Study Site and Data

4.2.1 NEEM ice drilling core site

The study site is south of the North Greenland Eemian Ice Drilling (NEEM) site in northwestern Greenland. The NEEM drilling project aims to extract a Greenland ice core with a complete record of the Eemian interglacial (130 to 115 kya) when the climate was warmer than present. The NEEM ice core was drilled down to 2 540 m during 2008-2012. This region is an area of great interest within the OIB mission as it is located on an ice divide, which is a boundary separating opposing flow directions of ice. In this region, folding layers close to the bed are

observed in the radar sounding and ice core data (NEEM community members, 2013; Panton & Karlsson, 2015). The proposed layer-tracing method is tested with twelve transects of MCoRDS data, whose flight tracks and geographic information are shown in Figure 4.1 and listed in Table 4.1, respectively.

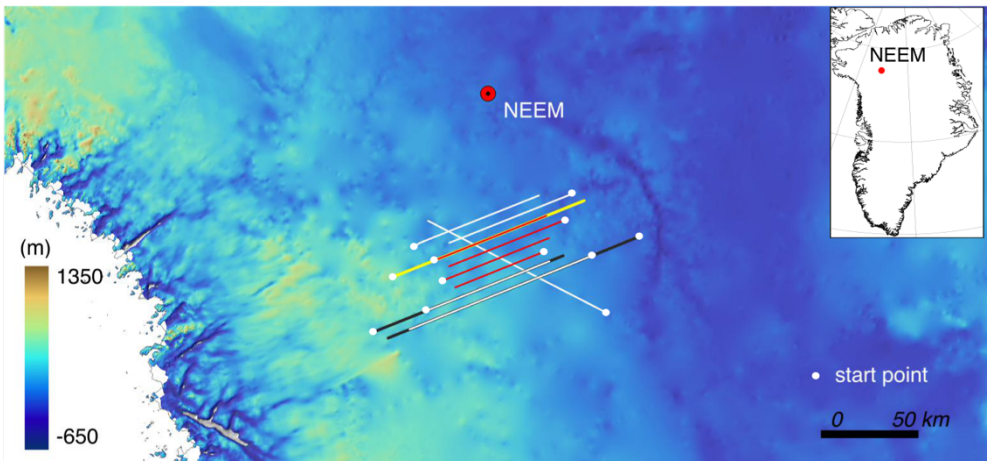

Figure 4.1: The study site and the flight tracks of MCoRDS data which are selected for testing the layer tracing method. The background image is the bed topography (Morlighem et al., 2015). The yellow transects were acquired in 2011, red 2012, black 2013, white 2014.

Table 4.1: MCoRDS data which are investigated.

Line No.	Date of Segment	Frames	Distance (km)	Start lat/lon	End lat/lon
1	20110329_02	019-021	150.15	76.169° N 52.197° W	76.774° N 46.964° W
2	20120508_04	005-007	90.36	76.296° N 51.208° W	76.661° N 48.054° W
3	20120508_07	005-007	90.36	76.633° N 47.567° W	76.273° N 50.727° W
4	20120507_03	011-012	82.93	76.181° N 50.810° W	76.514° N 47.939° W
5	20120507_07	011-012	68.90	76.414° N 48.125° W	76.137° N 50.498° W
6	20130419_01	012-014	75.74	75.784° N 52.561° W	76.400° N 47.514° W
7	20130419_01	057-060	100.22	76.536° N 45.387° W	76.163° N 48.916° W
8	20140515_02	011-012	98.15	76.387° N 51.734° W	76.794° N 48.303° W
9	20140515_02	060-061	98.24	76.819° N 47.304° W	76.430° N 50.790° W
10	20140521_01	012-013	98.33	75.960° N 51.245° W	76.358° N 47.896° W
11	20140521_02	022-024	76.42	76.415° N 46.602° W	75.826° N 51.632° W
12	20140514_01	058-060	147.47	76.030° N 46.261° W	76.562° N 51.467° W

4.2.2 MCoRDS L1B dataset and Ancillary dataset

The MCoRDS L1B data are released in two versions (Leuschen & Allen, 2011; Leuschen et al., 2014), the first of which has a temporal coverage from 16

October 2009 to 06 November 2012, and the second from 12 October 2012 to the present. Data acquired on each day are divided into segments. A segment is a contiguous dataset in which the radar settings do not change and each segment is broken into frames, each of which records a planar distance of 50 km. Meta information including the elevation of the platform, the latitude and longitude of the flight track, surface and bed layers are also released along with each frame of the radargram. The 12 transects of radargrams were acquired during the period from 2011 to 2014.

Radargrams acquired by the MCoRDS show deeper englacial layers down to a depth of more than 2 km, which is different from radargrams acquired by higher frequency radars such as the Ku-band radar of OIB mission mapping firn and snow (Onana et al., 2015). The entire Greenland ice column consists of ice from the Holocene, glacial ice and Eemian interglacial ice (NEEM community members, 2013). An example of an echogram is shown in Figure 4.2. Profile 1 and 2 in Figure 4.2 each consist of a drop from the surface reflection value, a slower decreasing signal until several hundred metres above bed reflection, and a low reflection zone of several hundred metres above the bed. Continuous ice layers are well preserved in the upper ~2.2 km of the ice sheet, which corresponds to ice from the Holocene and includes the last glacial period (110-11.7 kya). Few continuous layers and the disrupted layers imply ice folding below ~2.2 km, which is related to the Eemian interglacial period (NEEM community members, 2013). The drop of the radar amplitude at the bottom of the radargram may result from instrumental issues as this is not observed in data from the pre-

IceBridge mission. In pre-processing, the bottom part (~300 rows) of the radargrams, which contains a sharp drop in the radar amplitude is removed for the pre-processing.

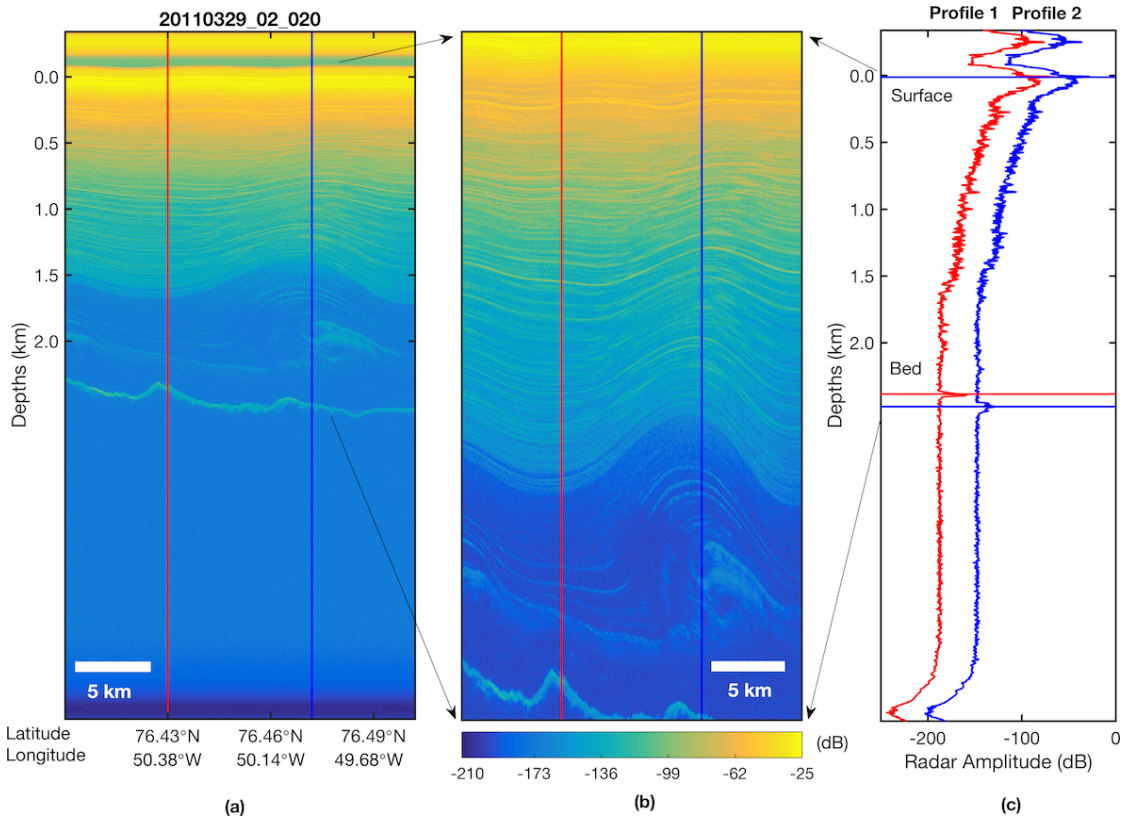

Figure 4.2: (a) An example of a MCoRDS radargram (subset from product with ID of 20110329_02_020) demonstrates the typical geometry of the englacial layers; (b) the close-up look image showing the folding of ice; (c) Profile 1 and Profile 2 show typical variations of the radar amplitude.

Macgregor et al. (2015a) completed a comprehensive study of tracing englacial layers of the entire area of Greenland by using the Pre-IceBridge and the early IceBridge mission data from 1993-2013. In addition, they related the traced englacial layers to ice ages estimated from ice drilling core data. In their work, the layer-tracing task was realised by applying their phase-based methods

to the complex radar data. For data acquired prior to 2006, they used the Automatic Radio Echo Sounding Processing (ARESP) algorithm proposed by Sime, Hindmarsh & Corr (2011) or manual tracing. The seed points were manually selected and then they are used to propagate layer-tracing. By propagating the englacial layers observed in ice cores, they traced the isochrones to the areas in the GrIS where there were MCoRDS data. These isochrones are publicly available in the National Snow and Ice Data Center (NSIDC) database as a product called Radiostratigraphy and Age Structure of the Greenland Ice Sheet (RRRAG) (MacGregor et al., 2015b).

The phase-based methods were used in their study to calculate the layer-slope. The following layer-tracing technique is basically a peak following method. The phase-based methods require complex radar data in which the phase information is preserved; however, the MCoRDS data are released as amplitude in the NSIDC database. These isochrones (RRRAG) are used for validating englacial layers traced by our proposed method.

4.3 Methods

In the literature, tracing englacial layers from radargrams can be generally separated into three steps, which are: (1) selecting reliable seed points; (2) calculating layer slope angles and (3) propagating layers from seed points with the calculated slope angles. Prominent englacial layers manifest in radargrams with high amplitude contrast to surrounding areas, thus, peak detection can be applied to each trace to extract the points belonging to layers. However, the radar return strength between the two blue lines in Figure 4.2(c) diminishes with depth

due to beam divergence and energy losses in the medium (Fahnestock et al., 2001). In this case, high amplitudes do not always guarantee real peaks since noise is mingled with signals associated with layers showing up as high amplitude peaks as well (Fahnestock et al., 2001). Conversely, low amplitude peaks can still be indicators of layers, such as peaks located between the blue horizontal lines in Figure 4.2(c). The signal attenuation between the two blue lines can be estimated by using the radar equation as proposed by Bamber (1987). Alternatively, the CWT-based method can address this problem without compensating for the signal attenuation (which can be observed at a depth from 0.2-1.5 km in Figure 4.2c) prior to peak detection, which may lead to inconsistent peak detection (Du, Kibbe & Lin, 2006).

A processing flowchart of the method is shown in Figure 4.3. First, an image with amplitude peaks is produced by using a CWT-based peak detection, which is described in detail in Section 4.3.1. In the second step, seed points are selected by applying a threshold which is calculated by using a lognormal fitting to the generated image. Then, the Hough Transform (HT) is applied to the peak image to calculate the slope angles during the tracing process which starts from the selected seed points. Finally, a post-processing step described in Section 4.3.4 is applied to the traced englacial layers to connect the disconnected layer segments and to geocode the traced englacial layers.

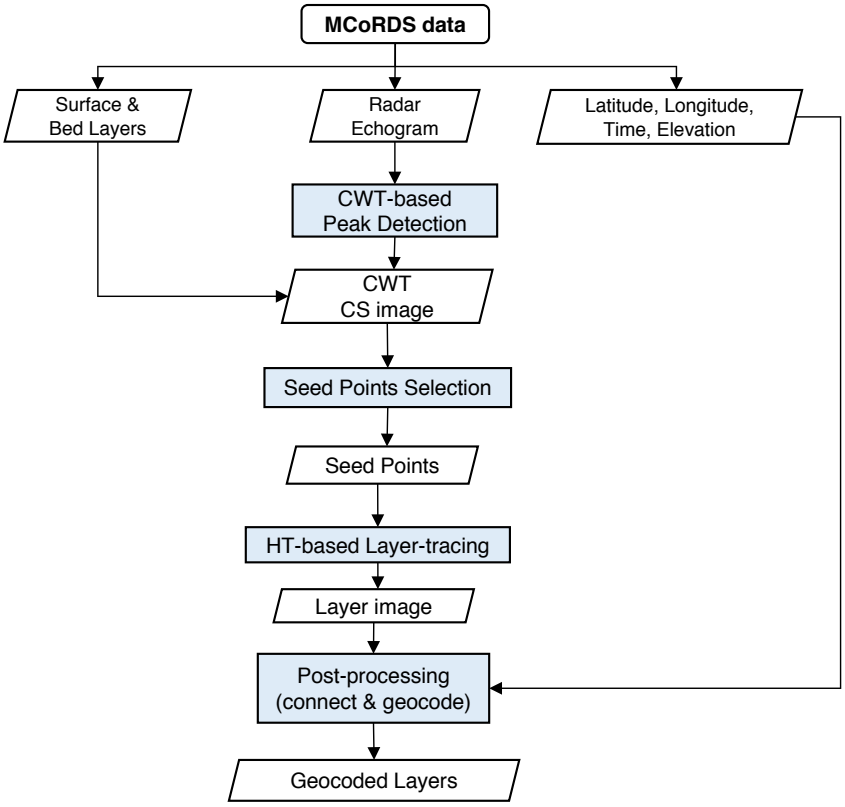

Figure 4.3: Processing flowchart for automatically tracing englacial layers.

4.3.1 CWT-based Peak Detection

Each column (profile) of a radargram can be regarded as a series of two-way travel time signals recording the internal reflections. The reflections occur at the dielectric boundaries. These boundaries are manifested as amplitude peaks in the radar signal. Therefore, the task of layer-tracing can be separated into finding the peak signals and connecting them as continuous layers.

The CWT-based peak detection method has been designed to identify peaks with different scales and amplitudes (Grossmann, Kronland-Martinet & Morlet, 1990; Du et al., 2006). It can preserve the location and frequency at the same time. Therefore, when analysing the profiles from radargrams, it can

produce a series of wavelet coefficients representing the correlation between the radar signals and the selected filter. The two-way travel time radar signals, $x(t)$, can be convolved with a wavelet, $\psi(t)$. The derived wavelet coefficients, $C(a,b)$, can be expressed as Equation (4.1), where $a \in \mathbb{R}^{+*}$ is the scale of the selected wavelet, $\psi(t)$ and $b \in \mathbb{R}$ is the translational value.

$$C(a,b) = \frac{1}{\sqrt{a}} \int_{-\infty}^{\infty} x(t) \psi\left(\frac{t-b}{a}\right) dt, \tag{4.1}$$

$$\psi_{morl}(t) = e^{-\frac{1}{2}t^2} \cos(5t), \tag{4.2}$$

$$\psi_{mexh}(t) = \frac{2}{\sqrt{3}\pi^{1/4}} (1-(t)^2) e^{-\frac{t^2}{2}}, \tag{4.3}$$

Applying the CWT to a radar signal with varying scales produces a scalogram, which shows the wavelet coefficients over time (or depth) and scales. Since there is no prior knowledge about the location of peaks, the CWT wavelet moves along the radar signal, step by step, which means the translational value, b, is set to be 1. Therefore, the other two factors affecting the coefficient are the type of wavelet and the scale.

Two types of the wavelet, namely Morlet (MORL), $\psi_{morl}(t)$, and Mexican hat (MEXH), $\psi_{mexh}(t)$, are analysed with an example profile (1500th column) from radargrams of 20110329_02_020. These wavelets are chosen as they have a central peak and resemble the shape of the desired signal peaks in the radar returns. The derived scalograms are shown in Figure 4.4(a) and (b). Each row in the scalogram indicates the wavelet response to the radar amplitude variations

at one scale. The red line in Figure 4.4(d) shows radar returns below the bed reflection where no layers are observed and radar reflections should represent the noise level. Peaks can be found as local maxima exceeding the noise level at each scale. Positions possessing high wavelet coefficients at every scale should be regarded as stable peaks, thus, wavelet coefficients from all scales are summed at each position to produce a Coefficient Summation (CS) shown in Figure 4.4(c) and (d).

Stable peaks which occur in most scales are detected by both MEXH and MORL wavelets. MEXH wavelet detects fewer peaks at smaller scale and depresses the spikes which surround the real peaks, resulting in a higher CS of peaks. Therefore, the peaks are more consistent with the real ones when the MEXH wavelet is used. At scales larger than 15, the MEXH wavelet creates more side spikes around the peaks between a depth of 1.0-1.5 km. MORL wavelet is less effective in suppressing the noise effects at the small scale, so the smallest scale need to be chosen cautiously, otherwise, the real peaks can be overwhelmed by many false peaks. The MEXH wavelet is recommended for the CWT-based peak detection.

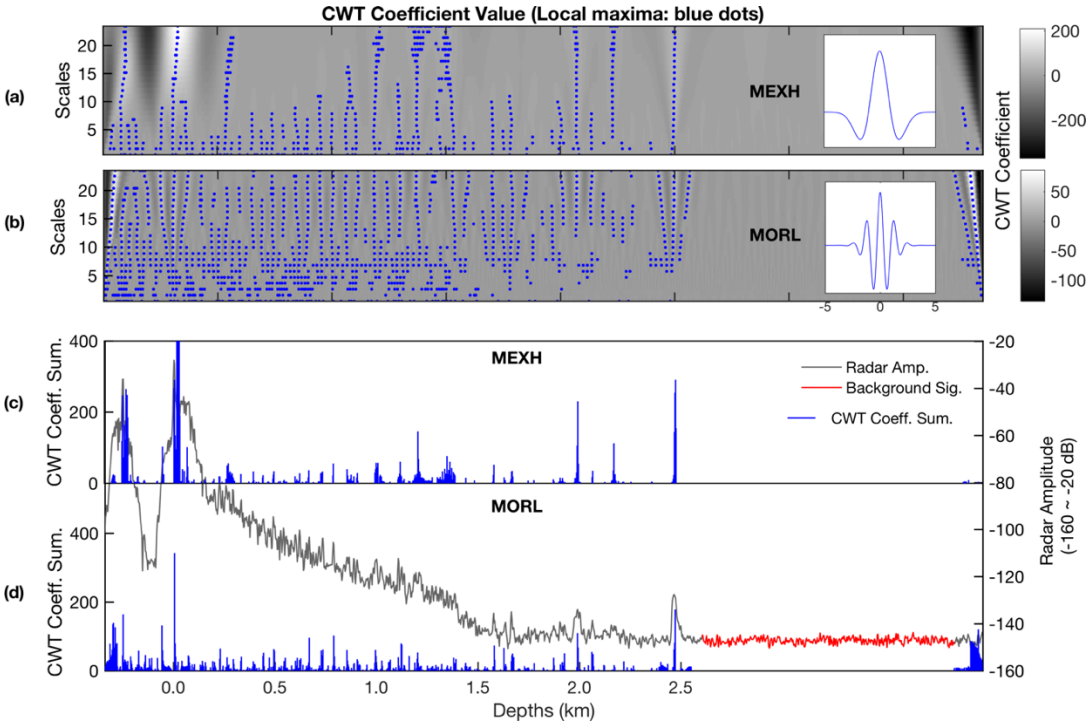

Figure 4.4: (a) the scalogram produced by the MEXH wavelet transform; (b) the scalogram produced by the MORL wavelet transform; the CWT coefficient summation with (c) MEXH wavelet and (d) MORL wavelet.

The CS values of the detected peaks and the total number of scales at which these peaks are detected are plotted in Figure 4.5(a-c). The three plots present the CS values from column 500, 1500 and 2500 of the radargram, 20110329_02_020, respectively. A high CS value confirms that there is either a prominent peak or long-lasting mediate peak, while the spikes are evaluated as low CS values. Figure 4.5(d-f) show the relationship between scales and the total number of peaks along the radar signal being detected in each of these scales. These plots show that the total number of the detected peaks drops enormously around a scale of 3 and almost all peaks are detected within a scale of 15, implying that information associated with layers is enhanced within scales from 3

to 15. Therefore, in the following study, a scale set of {3,4, 5, …, 15} is used for the CWT-based peak detection.

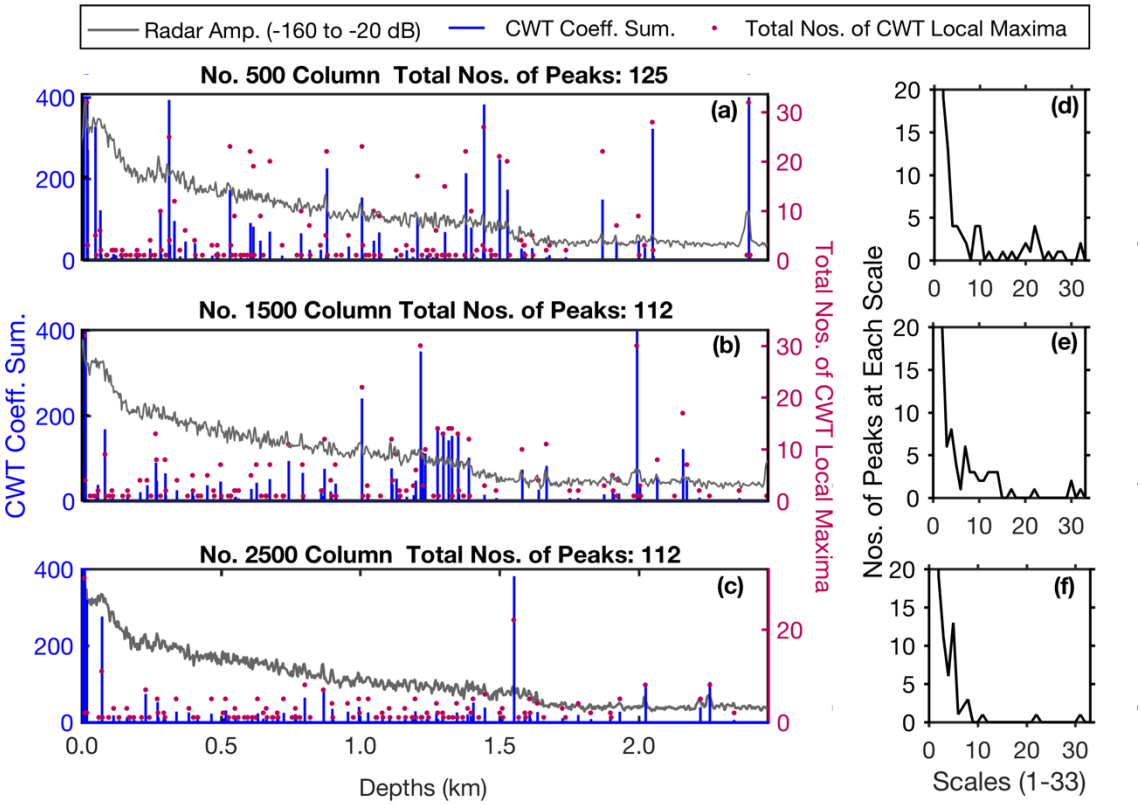

Figure 4.5: (a) Detection of peaks on three radar signals. (d-f) total number of peaks detected at each scale.

4.3.2 Selection of Seed Points

Applying the CWT-based peak detection to all profiles in a radargram results in a CS image which shows positive values of CS on the detected peaks whilst zero on other pixels. Points of higher CS value have a higher probability to be located on the englacial layers. In manual layer-tracing, tracing englacial layers starts from points which possess a relatively large contrast of radar echo amplitude with the surrounding pixels. In addition, it is natural to trace the prominent layers before the faint ones. Comparatively, the automated layer-

tracing should start from the points which obviously belong to layers, so the CS image is a good evaluator for choosing seed points. In addition, layers in a radargram are traced in decreasing order of CS value of the selected seed points.

Figure 4.6 shows the Cumulative Distribution Functions (CDF) of the MEXH CS image produced by using the MCoRDS data (product IDs: 20110329_02_019 and 20110329_02_020). The CS values fit well with the lognormal distribution, indicating that many points have low CS value. Only the points of CS larger than the expectation, $E[X]$ of the lognormal distribution are chosen as seed points which are arranged with descending CS value, $S_n(n = 1, 2, 3, \dots, N)$.

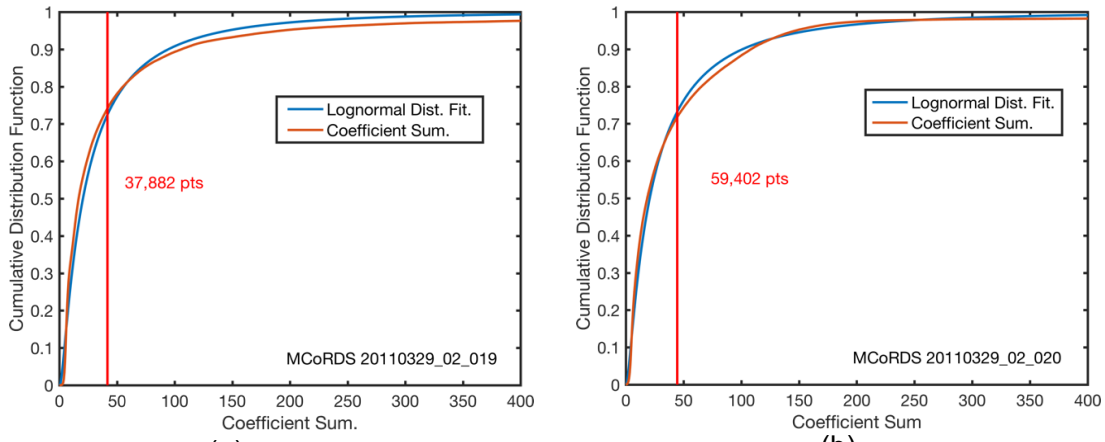

Figure 4.6: The lognormal distribution fitting of the wavelet coefficients in the MEXH CS image of (a) 20110329_02_019 and (b) 20110329_02_020. The red vertical lines are the value of the expectation of the lognormal distribution.

4.3.3 Layer-tracing Procedure

The following layer-tracing procedure is based on the CS image and the selected seed points. For each seed point, one layer-tracing procedure is accomplished based on three assumptions, which are (1) the englacial layers are

quasi-parallel; (2) there are no crossing layers; and (3) within a short distance, the englacial layers can be approximated by a straight line (Onana et al., 2015; Xiong & Muller, 2016; Holschuh et al., 2017).

Figure 4.7 illustrates the layer-tracing procedure. Propagation from the seed point is separated into two directions that are parallel and anti-parallel (i.e. on the opposite side in the opposite direction) to the flight direction of the airplane. Starting from the seed point and the CS image, a block is centred on the seed point and the layer follows straight lines within the block as mentioned in assumption (3). Propagation of the layer needs the slope angle of the layer on the seed point, which can be estimated in a Hough Transform (HT) domain of the block CS image. The Hough Transform is a feature extraction technique to find imperfect instances of objects with a certain class of shapes such as lines and circles (Duda & Hart, 1972; Ballard, 1981). The objects are found out by a voting procedure in a parameter space, from which object candidates are obtained as local maxima (Duda & Hart, 1972; Ballard, 1981). Equation (4.4) denotes the conversion from image coordinates into the HT domain.

$$HT(\rho_l, \theta_l) = \int_{-\infty}^{\infty} \int_{-\infty}^{\infty} \delta(icos\theta_l + jsin\theta_l - \rho_l) didj \qquad (4.4)$$

where (i, j) corresponds to row and column in the block, $\rho_l \in (-\frac{\sqrt{2}}{2}w_b, \frac{\sqrt{2}}{2}w_b)$ is the distance from the image centre to the line feature, $\theta_l \in [-\pi/2, \pi/2)$ is the angle between the line feature and the horizontal axis and δ is the Dirac function. The w_b is the block size which is listed in Table 4.2. The global maximum point

in the HT domain corresponds to a dominant line feature in the block, and its slope angle is the corresponding angle, θ_l.

The centre of the block (a new seed) is changed to the end of this line once the straight line is successfully traced in the block. This traced line is given a unique identity belonging to one layer segment. On the contrary, when the dominant angle is calculated due to lines close to the centre but no layers are related to the seed point (Figure 4.7d), or there is no dominant angle (Figure 4.7e), the layer-tracing should stop at the centre of this block. To stop layer-tracing in the former scenario, a line is constructed at the centre with the calculated slope angle and a buffer is then created around the line. The buffer consists of lines within a distance of d_t to the centre line. The points outside the buffer would be eliminated to generate a new block image which is input into the HT slope estimation again. If the CS points on the line are less than a percentage, p_{ht}, to the block size, no slope angle is returned for further tracing.

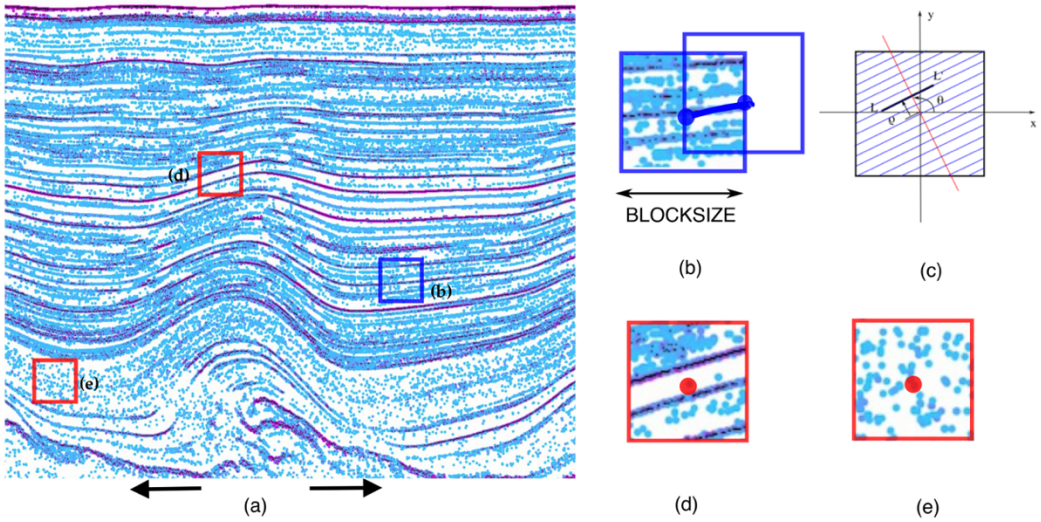

Figure 4.7: Illustration demonstrating the procedure of tracing englacial layers, (a) the layer-tracing is propagated in two directions; (b) right propagation; (c) the geometry of the HT transform; (d) and (e) showing the cases in which layer-tracing stops.

In summary, layer-tracing stops when it comes to any one of the following conditions: (1) no slope angle is returned; (2) crossing a labelled (or successfully traced) line; (3) approaching a labelled line with less than a distance d_t, and (4) exceeding a slope angle difference $\Delta\theta_s$. Table 4.2 lists all the parameters used in the layer tracing procedure. It is noteworthy that the numbers of labelled layers can be much less than the number of seed points because after one layer-tracing procedure, seed points which are close to a labelled layer (less than a distance d_t), are removed from the set of seed points, S_n.

There is no manual intervention in the layer-tracing procedure. However, several input parameters are critical to the derived results, which are w_b, d_t and $\Delta\theta_s$ (see Table 4.2). The block size, w_b, controls the continuity of the layers since the larger the block, the more the surrounding layers are considered for

estimating the slope angle, which would lead to a successful connection of discontinuous points appearing to be on one layer. A large block size leads to missing of the detailed curvature of layers due to the assumption of straight lines within the block. For example, if the block size is set to be larger than the width of a fold, the curve of the fold may not be fully reconstructed. On the other hand, when the radargram suffers a loss of signal, the block can be adjusted to a larger size to improve layer continuity. The minimum distance, d_t, controls the density of the traced layers. It is within this vertical distance that only one prominent layer can be traced, while any subsequent tracing is forbidden within this range. Though faint layers can be traced with decreasing values of d_t, they may be short layers because the tracing may be stopped when they fade into the background. The slope angle difference, $\Delta\theta_s$, is the angular difference between the current estimated slope angle with the last one from the previous block. This parameter controls how small the curves can be restored in the layer-tracing. The larger the $\Delta\theta_s$ is set, the smaller the folds that can be followed during tracing, otherwise, only smooth large folds can be restored. In some applications, such as tracing layers from ice drilling cores, prior knowledge about the location of layers may be available. In this case, manually selected seed points are easily imported into the layer-tracing module.

Table 4.2**:** Parameters used in producing the CS image and tracing layers.

Sec.	Steps	Params.	Description	Default (px)
3.2	1. CWT-based peak detection	s	Wavelet scales, $\{3,4,5,\dots,s\}$	$s = 15$
		n_{bg}	Pixels below bed to obtain background noise.	50
3.3	2. Seed point selection	N/A	N/A	N/A
3.4	3. Layer-tracing Procedure	w_b	Block size for estimation of slope angle.	51 ($> 3 * s$)
		d_t	Minimum vertical distance between two close layers.	7 ($\sim s/2$, $\sim 20\ m$)
		$\Delta\theta_s$	Slope angle difference.	90 degrees.
		p_{ht}	Gap filling in HT domain.	12 ($\sim w_b * 0.25$)
3.5	4. post-processing	Δd	Minimum vertical distance.	7

4.3.4 Post-processing of Traced Englacial Layers

Since any complex radar sounding system can result in noise during data acquisition, a continuous ice sheet layer may be imaged as discontinuous layer segments within the radargram. When inspected manually, it is sometimes possible to connect the layer segments into the same layer. However, since the stop conditions have been set, these layer segments are usually coded with different labels during the tracing procedure. Therefore, it is necessary to post-

process the traced englacial layers to connect the discontinuous layer segments which belong to the same layer.

Firstly, the start points, end points and initial labels of all the traced layer segments are recorded. For one target layer segment, as illustrated by $\boldsymbol{L}_t$ in Figure 4.8, all layer segments having their start point at the right of the end of $\boldsymbol{L}_t$ are initially selected as the candidates $\boldsymbol{L}_c$ for connection to the target layer segment (purple lines in Figure 4.8). Then, for each of these candidates, a reference layer which is continuous between the end of $\boldsymbol{L}_t$ and the start of the candidate layer is picked out (red continuous line in Figure 4.8). If the target layer segment and the candidate are located on different sides of the reference layer, no connection occurs, such as Figure 4.8(a). Otherwise, if the difference of their vertical distance to the reference layer is below a threshold Δd in Table 4.2, which is here $|d_1 - d_2| < \Delta d$, the candidate layer segment is connected to the target one (Figure 4.8b). The threshold for the horizontal distance is not considered here because it is possible that line segments are separated for a long distance while they still may belong to the same layer within one frame of the MCoRDS radargram. If two layer segments have the same distance to a reference layer, it is reasonable to regard them as the same layer within one frame. This checking is re-iterated for the start point of the target layer segment for the left connection.

After the connection of the traced layer segments, a threshold for the minimum horizontal distance can be set up to eliminate any remaining short layers. This threshold can be tuned for different applications. Finally, the

remaining layers are geocoded with the latitude, longitude and elevation from the meta information which is available as part of the MCoRDS data.

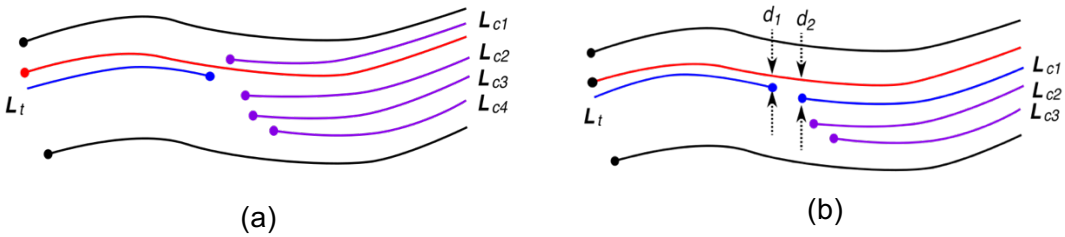

(a) (b)

Figure 4.8: Illustrations of the layer connection during post-processing: (a) no connection to the right of the target layer segment; (b) connection to the right of the target layer segment (blue line). The red line is the reference layer and the purple lines are the candidate layer segments.

4.4 Results

4.4.1 Producing the CS image

To test this automated layer tracing method shown schematically in Figure 4.3, one frame of a radargram is experimented with using the proposed layer-tracing method as an example. The 20th frame of the 2nd segment from the MCoRDS data acquired on 29 March 2011 is chosen as the example, as it recorded two ice folding areas. The echogram has 1839 rows and 3748 columns. One pixel in the image corresponds to a horizontal distance of ~13.6 m and a depth of ~2.8 m assuming a single dielectric constant of 3.14. The radar amplitude is shown in Figure 4.9. Black lines shown in Figure 4.9 represent the surface and bed boundaries. Figure 4.10(a) and Figure 4.10(b) show the MEXH CS image and seed points filtered by lognormal fitting. The CS image is produced

by using a CWT-based peak detection with a MEXH wavelet and the scales of {3, 4, 5, …, 15}. There are 210,487 peaks in the MEXH CS image. By using a lognormal distribution fitting, points of CS value larger than 44.5 are selected as seed points which results in 59,402 points. Producing the CS image takes only ~60 seconds with the code implemented in MATLAB on a 1.4 GHz Intel Core i5 computer running macOS X.

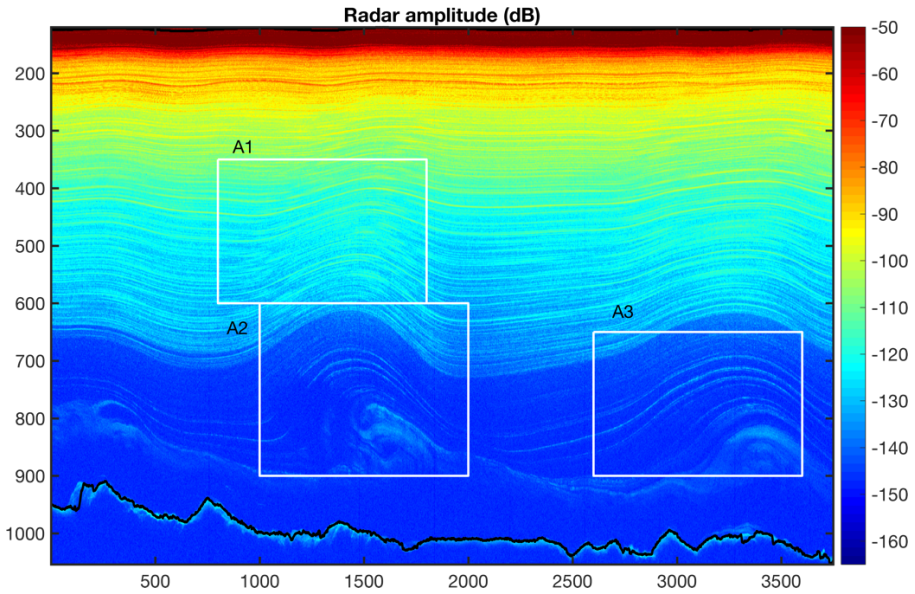

Figure 4.9: MCoRDS amplitude data which is used for testing the proposed method. Product ID is 20110329_02_020. The axes show row numbers and column numbers within the image. The white rectangles, A1, A2 and A3 are shown in more detail in Figure 4.12.

Previously, it was shown in Section 4.3.1 that if small scales are screened, almost all pixels are selected by using the MORL wavelet. For comparison, the same radargram is processed by using a MORL wavelet with scales of 10-15. Figure 4.11 shows the CS image produced by using the MORL wavelet. The

numbers of peaks in the CS images and their seed points selected are listed in Table 4.3.

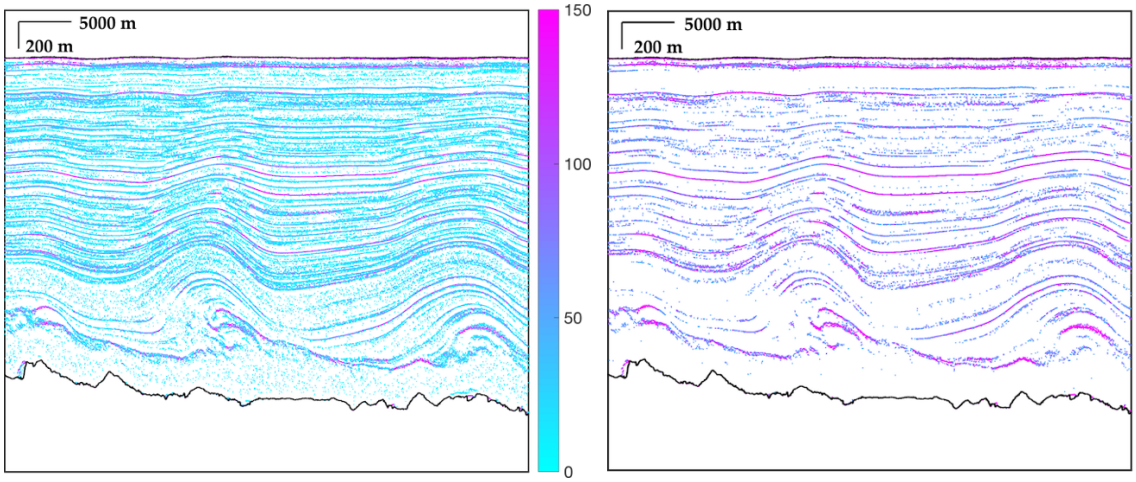

(a) (b)

Figure 4.10: (a) The CS image and (b) Seed points produced by using a MEXH wavelet and scales of $\{3, 4, 5, \dots, 15\}$. The colour indicates the CS values.

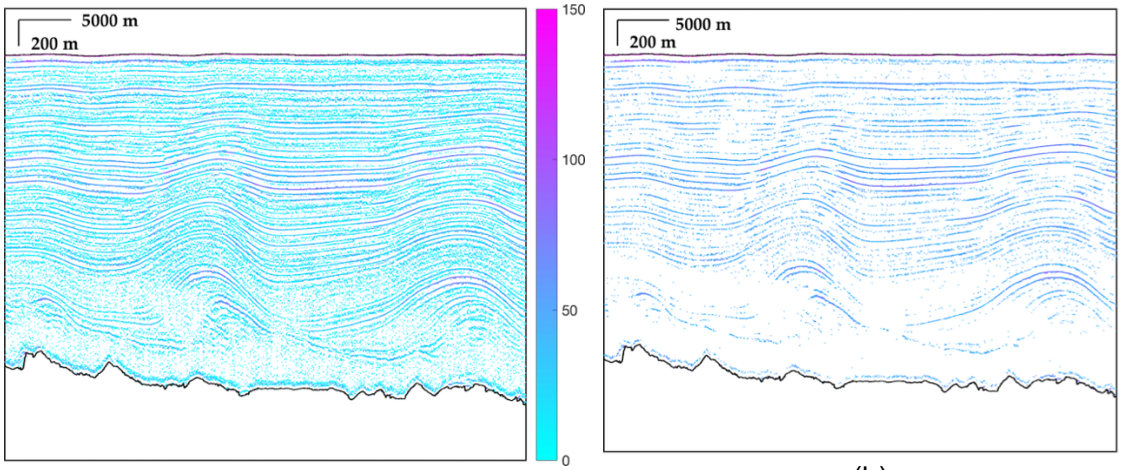

(a) (b)

Figure 4.11: (a) The CS image and (b) Seed points produced by using a MORL wavelet and scales of $\{10, 11, 12, \dots, 15\}$. The colour indicates the CS values.

Table 4.3: The number of peaks and numbers of layers which are traced by using the MEXH and MORL wavelets. Parameters for layer-tracing are set to the default values in Table 4.2 ($\Delta\boldsymbol{\theta_s} = \mathbf{90}°$).

CS image	No. Points in image	No. of seed point	Time (s)	No. of layers	No. of layers after post-processing
MEXH	210,487	59,402	342	227	121
MORL	150,087	47,570	295	219	113

4.4.2 Layer-tracing from Single Frame

To compare the MEXH CS and MORL CS images, the seed points are selected from each of these images and then imported into the following layer-tracing. The numbers of layers traced by using these two images are listed in Table 4.3. The two sets of traced layers are shown in Figure 4.12. Figure 4.12(a) shows that most layers traced by using MEXH and MORL images are almost at the same locations but there are some jumps in the MORL result. As we can observe in Figure 4.12(b) and (c), more layers following along the ice folds are restored by using the MEXH CS image. By using the MEXH CS image, more layers are detected especially in the folding areas of the radargrams. The MEXH result (black lines in Figure 4.12b and Figure 4.12c) has many jumps near the end of traced layers, especially over low signal regions. The MORL result appears smoother because there are more points assembled into one line in the MORL CS image whilst there are less well distributed points than that in the MEXH images, which may result from false peaks around the true ones. After post-

processing, the number of layers traced by using the MEXH CS image remains the highest among the three results. This may be due to more layers detected in the folding area or more layer segments than the MORL result. The fully traced layers from these two peak detections are shown in Figure A1 of the appendix A, which is consistent with the above discussion of these two results.

Table 4.4 lists the time consumption and the number of traced layers when using the same MEXH CS image and different sets of block size and the minimum allowed distance, from which we can see that increasing the block size does not increase the number of traced layers, while it slightly increases the numbers of connected layers during post-processing. Decreasing d_t, significantly increases the number of traced layers.

Table 4.4**:** The number of layers traced by using the same MEXH CS image and different block sizes, and different thresholds for the indicated vertical distances.

$\Delta\boldsymbol{\theta_s} = \mathbf{90}°$		$\boldsymbol{d_t}$**=7**		$_t$**=15**	
		Time (s)	No. of layers	Time (s)	No. of layers
$\boldsymbol{w_b}$**=51**	before post-processing	342	227	162	112
	after post-processing	7	121	3	66
$\boldsymbol{w_b}$**=101**	before post-processing	326	216	164	124
	after post-processing	7	120	5	65

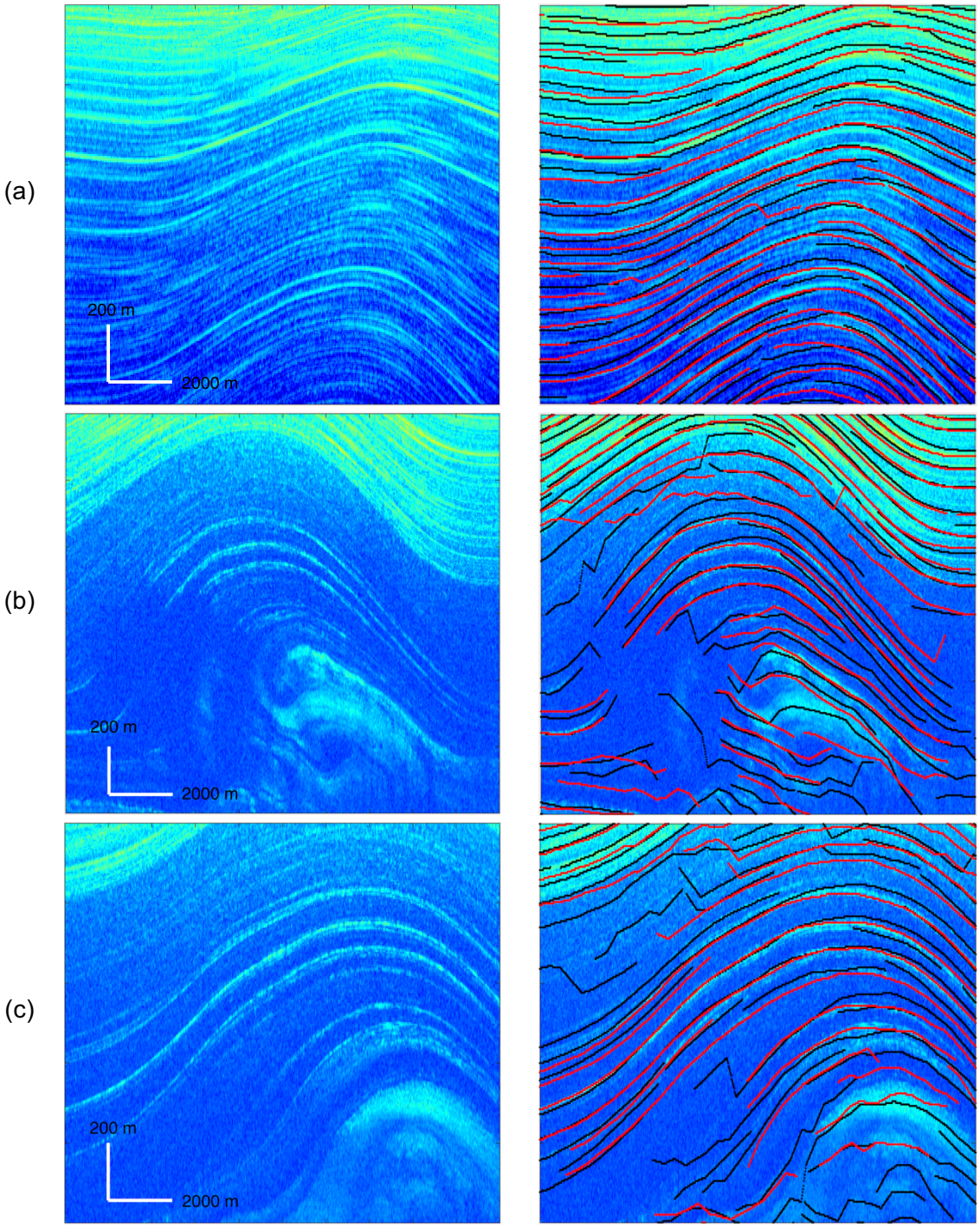

Figure 4.12**:** (a) Englacial layers traced on the slope of the folds, indicated by A1 in Figure 4.8; (b) and (c) englacial layers traced near the folding cores, which are A2 and A3 in Figure 4.8. (MEXH wavelet: black lines; MORL wavelet: red lines)

4.4.3 Combination of Multi-frame and Validation

The smallest unit of the released MCoRDS data is one frame. It is necessary to combine several frames to study subsurface features along a distance larger than 50 km. Therefore, a combination of traced englacial layers from several continuous frames is demonstrated in Figure 4.13(b), showing an example which is produced from a combination of three frames (19-21) of the 2nd segment acquired on 29 March 2011. The layers are traced frame by frame and then are subsequently combined. It is possible that some layers are traced in one frame while the corresponding ones are not traced in the adjacent frame.

To assess the effectiveness of the proposed layer-tracing method, the corresponding result from MacGregor et al.'s radiostratigraphy product is shown in Figure 4.13(a), in which the colours denote ice age. This corresponds to frames 19-21 from MCoRDS data 20110329_02, whose layer-tracing result using our proposed method is shown in Figure 4.13(b). Most major layers have correspondences in the published radiostratigraphy (shown as coloured lines), the average of their elevation differences (absolute value) is within 40 m, which corresponds to a vertical distance of about 15 pixels. The black lines are layer segments which have no matched isochrones.

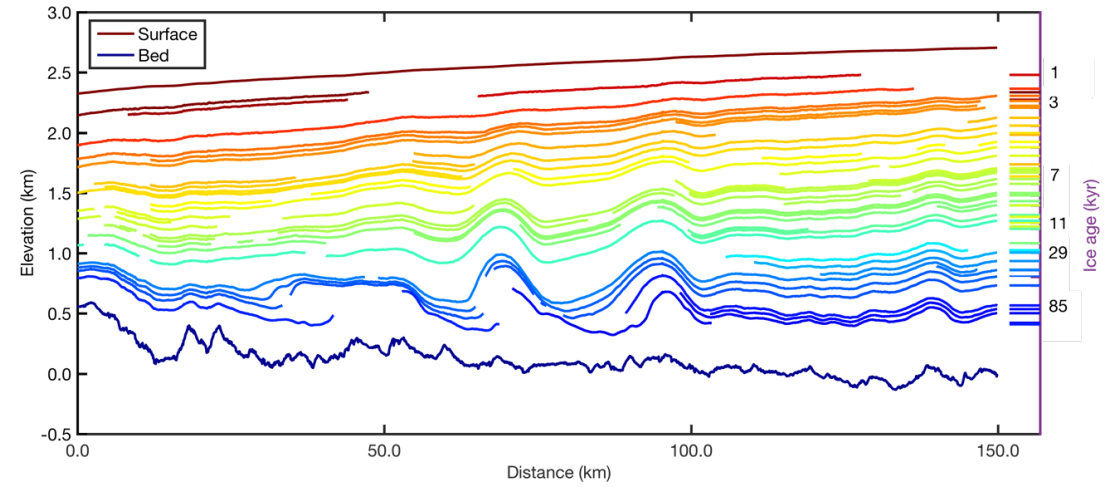

(a)

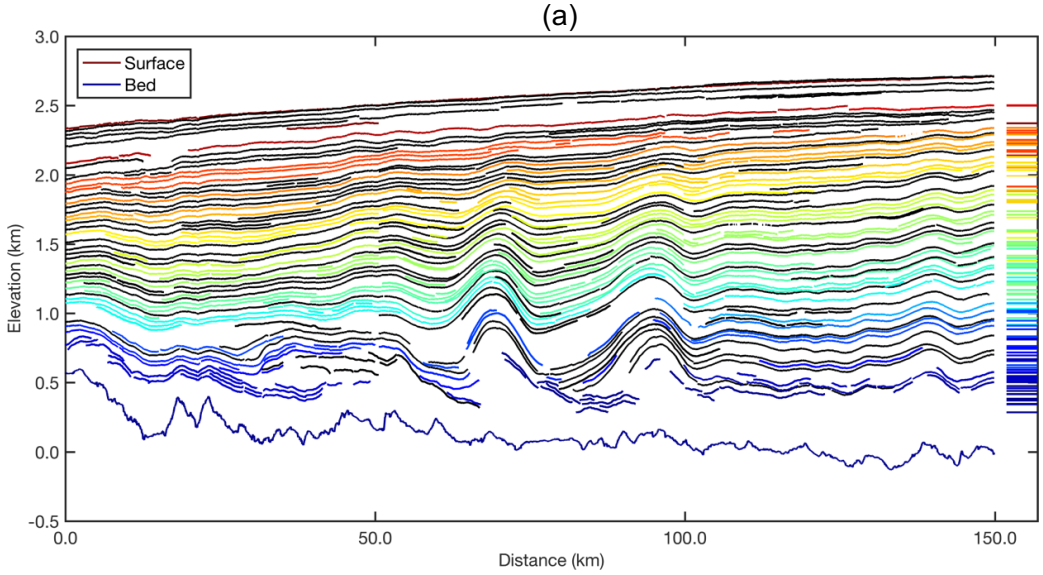

(b)

Figure 4.13: (a) is the RRRAG isochrones; (b) the englacial layers traced by the proposed method after removing layer segments extending a distance less than 10 km.

The RRRAG product has no follow-on data after 2013, thus, seven out of twelve lines in Figure 4.1, which were acquired in 2011, 2012 and 2013 have the corresponding results in the RRRAG product. All of them are compared to the results from this study, which are provided in the appendix A. These comparisons demonstrate that the traced englacial layers are comparable to those traced by Macgregor et al. (2015a). The proposed method works well on restoring the

orientations of the ice layers, even the faint layers related to the Eemian interglacial ice, which may not even be delineated in the RRRAG product, such as the ones denoted as black lines in Figure 4.13. The black lines are observed to be faint layers when overlaid on the radargram. This is reasonable since only the prominent layers are traced rather than all possible layers in the RRRAG isochrones, as a limitation to the number of manual selected seed points.

With a proper selection of input parameters that are easily tuned for specific applications, a higher density of layers is achieved compared to the RRRAG isochrones. The commonly traced layers from the RRRAG isochrones and our results are counted and listed in Table 4.5. More than 72% of the isochrones are restored with a vertical average distance of 40 m to the corresponding isochrones. About 43%-61% of the traced layer segments agree with the RRRAG isochrones, while the rest of the layers are traced by the proposed method but have no correspondences in the RRRAG isochrones. These layers include those along the ice folds which were not traced in the RRRAG product. It is worth noting that no cleaning of layers is done after post-processing, which means that the counting does not exclude some traced short layer segments. Cleaning up short layer segments by setting a minimum allowed length for the layers may increase the confirmed percentage.

Table 4.5**:** Conformity of results from the proposed method to the published RRRAG isochrones.

Line No.	**1**	**2**	**3**	**4**	**5**	**6**	**7**
RRRAG isochrones	46	55	61	42	58	83	100
Restored RRRAG isochrones	45	46	44	38	50	75	88
Restored percentage	97.8%	83.6%	72.1%	90.5%	86.3%	90.2%	88.0%
Traced segments	279	124	135	125	100	228	272
Confirmed layer segments	122	61	63	61	54	139	156
Confirmed percentage	43.7%	49.2%	46.7%	48.8%	54.0%	61.0%	57.4%

4.4.4 MCoRDS data from the pre-IceBridge mission

In addition, one frame of MCoRDS data from the pre-IceBridge mission is employed to evaluate the effectiveness of the proposed method. The radargram has a size of 1024 rows and 1000 columns. It was initially processed with the default parameters but this resulted in many disrupted layer segments. Considering that the size of this radargram is much smaller than those from the OIB mission, the distance allowance is changed to be 3 pixels and block size to be 21 pixels. In this radargram, there are several small ridges, so the slope angle difference is set to be 90°. This set of parameters results in the traced layers shown in Figure 4.14, in which 106 layers were traced, taking 154 seconds for the layer-tracing procedure. It should be noted that several lines just below the

surface are detected. These lines may be “surface reflection multiples”, which can be caused by reflections from the wings of the aircraft. When the returned radar pulse arrives at the aircraft when it is received for the first time, it also reflects off the wings and travels back towards the target. In some conditions this may happen two or three times creating first, second, third, etc multiples of the surface.

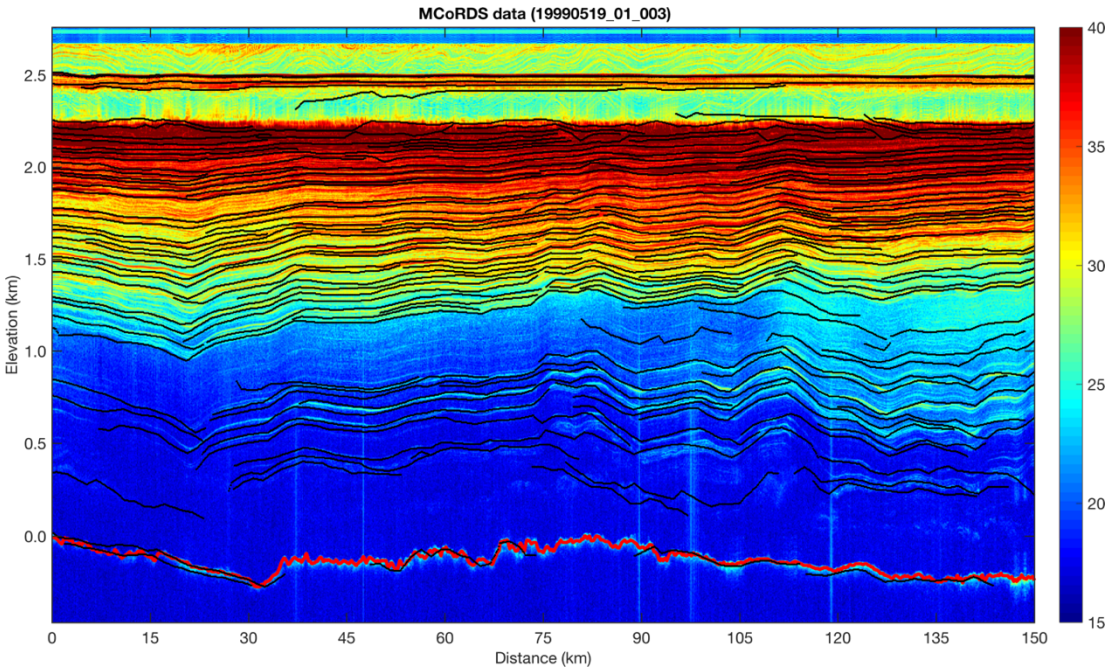

Figure 4.14: One frame of MCoRDS amplitude data from the pre-IceBridge mission (product ID: 19990519_01_003) with overlaid traced layers from the MEXH CS image. The red line is the bedrock layer which comes with the product. The black lines near the surface may be caused by “surface reflection multiples”. The colour scale shows the radar amplitude (unit: dB).

Figure 4.15(a) shows the isochrones from the RRRAG product and Figure 4.15(b) shows traced layers which are associated with the ice ages. There are 106 layer segments which are traced by the proposed method. Among these

layer segments, 57 layer segments agree with 43 isochrones from the RRRAG product. There are 49 isochrones in total in the RRRAG product, which means that there are six isochrones which are not detected by the proposed method. From Figure 4.15(b) we can see that the lower layers are not restored as continuously as those in the RRRAG product. This may be improved by setting a smaller block size for smaller increments within the tracing procedure. In addition, there are jumps near an elevation of about 0.5-1 km (at a depth of 1.5-2 km) around the distance from 0 km to 30 km, and unrealistic slopes around a distance of 107 km and an elevation of 2.2 km. Setting a threshold for the slope angle difference should be able to avoid these unrealistic slopes, however, to restore the sharp changes of the lower part in the radargram, a threshold is not used in this case. The jumps and unrealistic slopes are also attributed to the low signal to noise ratio, which can be partly demonstrated by the same difficulty in tracing continuous layers observed in Figure 4.15(a).

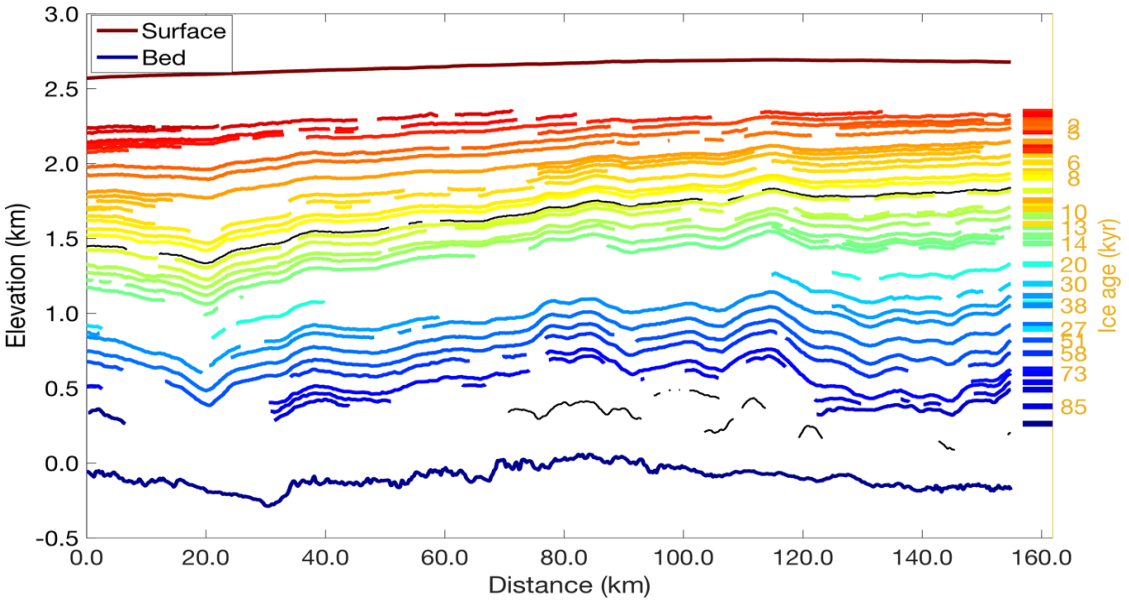

(a)

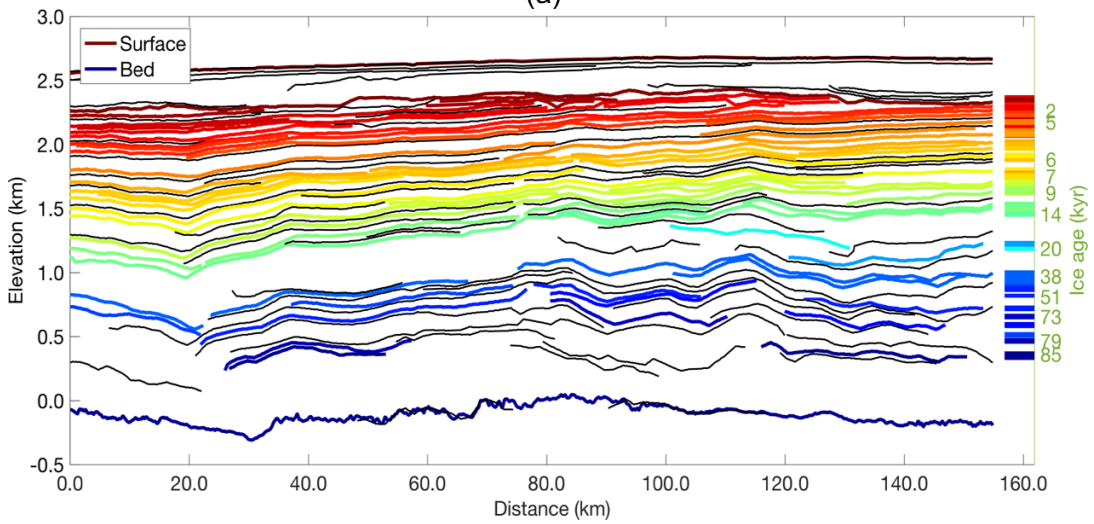

(b)

Figure 4.15**:** (a) the isochrones from the RRRAG product; (b) the traced layers after being associated with different ice ages. The layers between depths of 1.0-2.0 km (elevations of ~1.5 to 0.5 km) are better restored than those in the upper and lower parts.

4.5 Discussion

Results show that, in most cases, the proposed layer-tracing method with MEXH and MORL wavelets independently produce a similar number of layers, mostly the most prominent ones. More layer segments are restored along or near the ice folds when using the MEXH wavelet for layer-tracing, while sometimes layer jumps may result from spikes in and around peaks. On the other hand, using the MORL wavelet produces distinctive layers and fewer jumps between layers. However, layers near the folds are not well restored. As mentioned above, the lowest scale needs to be cautiously selected when using the MORL wavelet, otherwise too many noisy points are brought in at lower scales, reducing the reliability of the slope angle estimation in the HT domain. Currently, the MEXH wavelet is regarded as more suitable in this layer-tracing application than the MORL wavelet. In the future, a combination of merits from different wavelets could be considered and investigated further.

Most methods in the literature involve manual intervention, such as the manual selection of seed points. In the proposed methods, the selection of seed points is addressed by evaluating the peak prominence with the wavelet coefficients. Furthermore, the subsequent layer-tracing is arranged in a hierarchical order from the most prominent peaks (high CS value) to the least prominent ones (low CS values). This order is optimum in that the best SNR data is analysed first, which then provide constraints which guide the analysis of the weaker signals.

With the selected points, the layer-tracing procedure is highly effective. Tracing one typical frame of MCoRDS data using the default input parameters only takes ~5 minutes for around ~50,000 seed points. The selection of seed points can even be ignored when there are not too many peak points detected in the CS image. Then, all the peak points can be regarded as seed points and input into the layer-tracing procedure. The input parameters of the block size, the threshold for distance and slope angle difference can be adjusted according to the requirements of various applications. For instance, if only prominent layers are needed to be traced with high continuity, then the threshold for distance should be larger than the default setting. In some other applications requiring restoration of folding layers, the threshold of slope angle differences should be set to allow for sharp bends in the traced layers, which is the case shown in Figure 4.14. If the desired number of layers is approximately the same as that in the RRRAG product, layer-tracing will cost less time than that demonstrated in Section 4.4, as a less strict threshold is needed. Tuning of the proper parameters is not difficult and is not very time-consuming since this usually only requires an adjustment of block size and a threshold for distance is needed.

The connection of layers from multiple frames is also demonstrated, the major layers can be traced and connected across multiple frames. However, some faint layers may only appear in one of the frames, thus causing difficulty in tracing them continuously across multiple frames. Failure of tracing continuous layers is partly due to the noise from the radargram, rather than due to the failure

of the method. Since the tracing procedure is carried out block by block, it results in short layer segments when the radargram is noisy.

One shortcoming of the current tracing algorithm is that the slope angle estimation by using the HT is currently based on the number of points within the block. This may be improved in the future by taking the CS values into account to estimate the slope angle since peaks on the actual layers show continuous high CS values. Apart from this, disconnected layer segments which occupy the ice folding areas can hardly be recognised as the same layer and can only be connected in the post-processing. In future, one might be able to explore the application of, for example, deep learning using these or the SAMPA (Onana et al., 2015) outputs for training and verification.

4.6 Summary

Tracing englacial layers is important for studying ice sheet dynamics yet difficult to achieve with high efficiency and accuracy at the same time. In this chapter, an automated method which combines the CWT-based peak detection with an HT-based layer-tracing procedure is proposed to trace englacial layers from MCoRDS radargrams in Greenland. Following the initially traced layers, the connection of discontinuous layer segments and layers traced from multiple frames of radargrams is described.

In general, it is difficult to quantitatively assess the effectiveness of the layer tracing algorithm. The results are compared to those of the published RRRAG product. The comparisons show that layers traced by the proposed method

mostly agree with those in the RRRAG product. Moreover, the proposed method traces layers with much higher densities and restores the layers near the folding areas. In addition, it needs no direct manual assistance, other than the setting of several parameters, and the results show much more detail of layers when compared with the RRRAG product in areas of no severe signal loss in the radargrams.

Indeed, there are some other layer-tracing methods which have been proposed in the literature as discussed in section 2.4.2, such as the peak-following method (Fahnestock et al., 2001), the layer slope based method (Sime, Hindmarsh & Corr, 2011) and SNAKE (Panton, 2014). These methods all have two major weaknesses, the greatest of which is the need for manual selection of seed points. The other weakness is that the layer-tracing is easy to steer into neighbouring layers and produce false positive results in regions where the clarity of stratigraphy degrades. The proposed method in this chapter dealt with the first problem using the wavelet coefficients produced by the CWT. The second problem is partly alleviated by using the Hough Transform and the layer tracing termination criterion.

Apart from the terrestrial ice sheets and glaciers, the radar sounding technique can also be applied to extra-terrestrial planetary science, such as polar regions on Mars, where subsurface layers can be observed caused by geological time scale accumulation of deposits. The proposed CWT-based peak detection and layer-tracing procedure based on HT have the potential to be adapted to

trace layers observed in the Martian PLDs by radar sounders such as the SHARAD, and this is discussed in the next chapter.

Chapter 5

Automated Reconstruction of Subsurface Interfaces in Martian SPLD

5.1 Scientific Context

The primary scientific objective to send radar sounders orbiting Mars is to investigate subsurface features that are associated with the geological history of the planetary processes related to water and ice. Radar sounding techniques record radar returns from interfaces buried below the surface, so it is possible to detect subsurface interfaces (Milkovich et al., 2009) or to reconstruct buried features (Simon et al., 2014; Brothers & Holt, 2016). Geomorphology of these layers and features assists the explanation of landform evolution (Smith & Holt, 2010; Smith, Spiga & Holt, 2015). In addition, given the detected interfaces, estimation of the dielectric properties of the penetrated layers can be achieved (Orosei et al., 2007; Orosei et al., 2015), which provides very important clues as to buried water and ice (Nouvel et al., 2006; Holt et al., 2008; Lauro et al., 2012; Mouginot et al., 2012; Mattei et al., 2014), such as the recent discovery of a large subsurface lake near the south pole (Orosei et al., 2018).

Over the north and south poles, the basal layers are useful to reconstruct the basal topography and to estimate the volume and composition of PLDs

(Brothers, Holt & Spiga, 2015). Apart from the basal layers, internal layers are frequently observed in the Martian Polar Layered Deposits (PLDs), which are analogous to the englacial layers in terrestrial ice sheets. This layering is formed during different episodes of deposition and erosion. Compared to the terrestrial englacial layers, the layers preserved in the Martian PLDs show much greater disruption and discontinuity due to the existence of strong erosional episodes between depositional periods. Interpretation of the radar stratigraphic sequences and their geomorphology is of great importance as they are associated with past climate changes (Fishbaugh & Hvidberg, 2006; Grima et al., 2011; Conway et al., 2012; Guallini et al., 2017).

Radar stratigraphy is the study of these layers of the Martian upper crust by using radar sounding techniques from sensors such as MARSIS and SHARAD. The upper ~1 km of the Martian PLDs can be imaged by SHARAD at a vertical resolution of about 15 m using the dielectric constant of free space, while MARSIS can detect base boundaries of PLDs which are estimated to be up to several kilometres below the surface. The SHARAD instrument has been orbiting Mars since 2006 and completed a global coverage of 36.1 % of the Martian surface (global coverage can be observed at https://sharad.psi.edu/maps/). Compared to MARSIS, SHARAD not only possesses higher planar and vertical resolutions but also has a denser coverage. In the past, revealing subsurface structure combining SHARAD data from multiple orbits is achieved by screening radargrams from hundreds of orbits by trained professionals. The overall structure is usually illustrated by experts from their own manual measurements

of the radargrams. Meanwhile, extraction of the subsurface layers for further dielectric constant inversion is usually achieved through visual recognition and manual delineation. These visual and manual operations are time-consuming if the subsurface features of interest are at a large scale and observed in radargrams from multiple orbits. In addition, the actual location(s) of buried targets is usually unknown. Therefore, it is necessary to develop automated or semi-automated methods for analysing the SHARAD data and extracting subsurface features from SHARAD data in a much more rapid, reliable and effective manner.

Extraction and analysis of subsurface layers from these data has been expanding from traditional manual investigation to the use of 3-D imaging volumes (Foss et al., 2017). However, the development of automated techniques to extract subsurface layers from radargrams has not been addressed sufficiently in the literature. Some studies contribute to the automated extraction of subsurface layers from SHARAD data (Freeman, Bovik & Holt, 2010; Ferro & Bruzzone, 2013); however, they mostly do not further deal with the extraction of subsurface layers from multiple radargrams to reconstruct their 3-D structure and to associate them to surface features. To this end, this chapter presents an automated method in which CWT-based peak detection is used to extract subsurface reflections from SHARAD radargrams. Clutter reflections are simulated and removed from these subsurface reflections, which are subsequently partitioned into different layers in the 3-D domain through classification methods. The proposed workflow for reconstructing the 3-D

subsurface layers is introduced in Section 5.3. To test the proposed method and workflow, we choose a study area located in the Promethei Lingula (PL) region of the Martian south pole. The 2-D and the subsequent 3-D processing are tested on SHARAD radargrams covering the study site, which are introduced in Section 5.2. The proposed workflow for reconstructing 3-D subsurface layers is introduced in Section 5.3. The experimental results are demonstrated in Section 5.4 and discussed in Section 5.5.

5.2 Study Site and Data

The Promethei Lingula is a low-relief plateau at the margin of the SPLD, as shown in Figure 5.1. The stratigraphy of this region is generally defined as three separate units by analysing the surface exposures in the surface imagery, such as THEMIS and MOC images (Kolb & Tanaka, 2006). Although layer exposures can be found extending the SPLD in the surface images, the extent of these layer sequences is observed to be interrupted in the SHARAD radargrams. In SHARAD radargrams, the subsurface layer sequences are only revealed to be continuous within the Promethei Lingula region in the SPLD. Four layers of strong subsurface reflections are highlighted in this region using the SHARAD radargrams (Seu et al., 2007). Between the top and the second layer, an angular unconformity was revealed by manually analysing high-resolution surface images and SHARAD radargrams (Seu et al., 2007; Milkovich et al., 2009). Guallini et al. (2017) reanalysed the geologic units in this region with more than 100 surface images and reconstructed the angular unconformity by manual delineation on about 600 SHARAD radargrams. They postulated that the variation of Martian

orbital parameters, especially oscillations in axial obliquity could have controlled local climate conditions in the past, leading to the current geological records based on their analyses of the geologic units in the region.

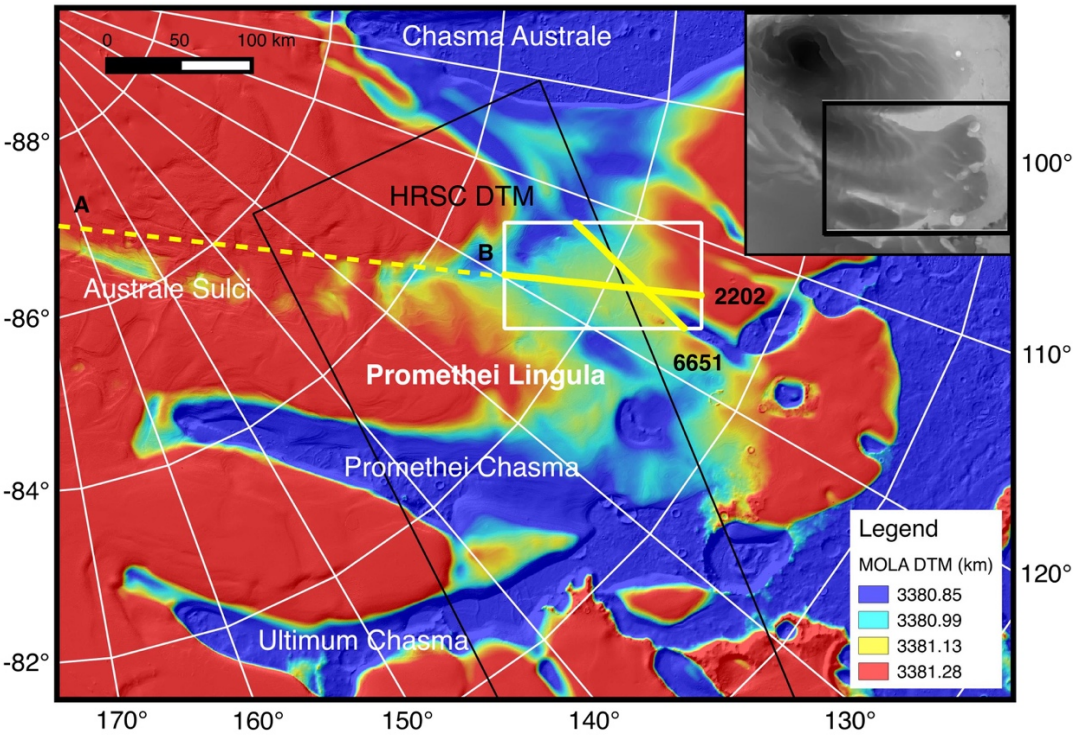

Figure 5.1: The study site is denoted by the white rectangle shown in the Promethei Lingula (PL) region. The background image is the MOLA DTM (MEGDR at 512 pixels/degree or ≈115 m/pixel, the elevation is referenced to the centre of mass of Mars). The black polygon shows the location of a HRSC DTM (Product id is h2165). The yellow lines show the footprints within the PL region of the SHARAD radargrams from orbits 2202 and 6651.

The study site is selected within the Promethei Lingula region which is shown as the white rectangle in Figure 5.1, within which the elevation of the angular unconformity has been interpolated from manual delineation on SHARAD radargrams by Guallini et al. (2017). The radargrams are from the Derived Data

Products processed by the SHARAD science team in the USA (Campbell, 2014). The spatial resolution of the radargrams is approximately 450 m × 3 km (along track by across track). The range sampling is 37.5 ns as the two-way travel time, corresponding to about 5.63 m in free space and slightly more than 3 m in an icy medium (assuming a single dielectric constant of 3.4). It is noteworthy that this represents nearly a factor of three in oversampling of the inherent range resolution of 15 m. The dielectric constant of 3.4 is used in Guallini et al.'s study and is consistent with a mixture of 90% water ice and 10% basaltic impurities (Plaut et al., 2007; Seu et al., 2007; Guallini et al., 2017).

Over this study site, 146 SHARAD radargrams are used. In addition, an HRSC DTM (product id: h2165) covering a large part of this region is created and used for simulating the clutter reflections. The HRSC DTM was produced using the methods developed by Kim & Muller (2009) who use the Video Image Communication And Retrieval (VICAR) open source programme together with photogrammetry software from DLR with image matching based on the GOTCHA (Gruen-Otto-Chau) algorithm (Putri et al., 2018).

5.3 Methods

In the previous chapter, the CWT-based peak detection and HT-based layer-tracing were successfully applied to MCoRDS data over Greenland. Similarly, methods including the CWT-based peak detection and HT based layer-tracing are suspected as being suitable for SHARAD radargrams as well. After several tests, the CWT-based peak detection is shown to be relevant to the SHARAD data, while the HT-based layer-tracing cannot derive a reasonable

result for SHARAD radargrams due to the low SNR of the SHARAD radargrams and the violation of the three assumptions stated in Section 4.3.3. In addition, the SHARAD data sustains clutter reflections because the radar pulse illuminates the entire surface beneath the spacecraft due to the negligible directivity of a dipole antenna (Alberti et al. 2012). Therefore, the workflow applied to the MCoRDS data needs to be adapted according to the characteristics of the SHARAD data.

The new adapted workflow consists of four steps. The first three steps are carried out in the 2-D raster domain on the radargrams and the final step is realised in the areospatial 3-D domain. Firstly, the original radargram is enhanced by applying a log-Gabor filtering to improve the contrast of the angular linear features. Secondly, a CWT-based peak detection method is applied to the filtered radargram to extract the subsurface reflections. Thirdly, an external DTM (MOLA or HRSC) is used to simulate the clutter reflections which are then compared to the subsurface reflections to eliminate any false detections. Finally, after the detection of subsurface reflections from all radargrams located within the study area, the 3-D coordinates of the extracted reflection positions are treated as a point cloud, to which clustering methods are applied to distinguish the subsurface interfaces. The overall processing flow is shown in Figure 5.2.

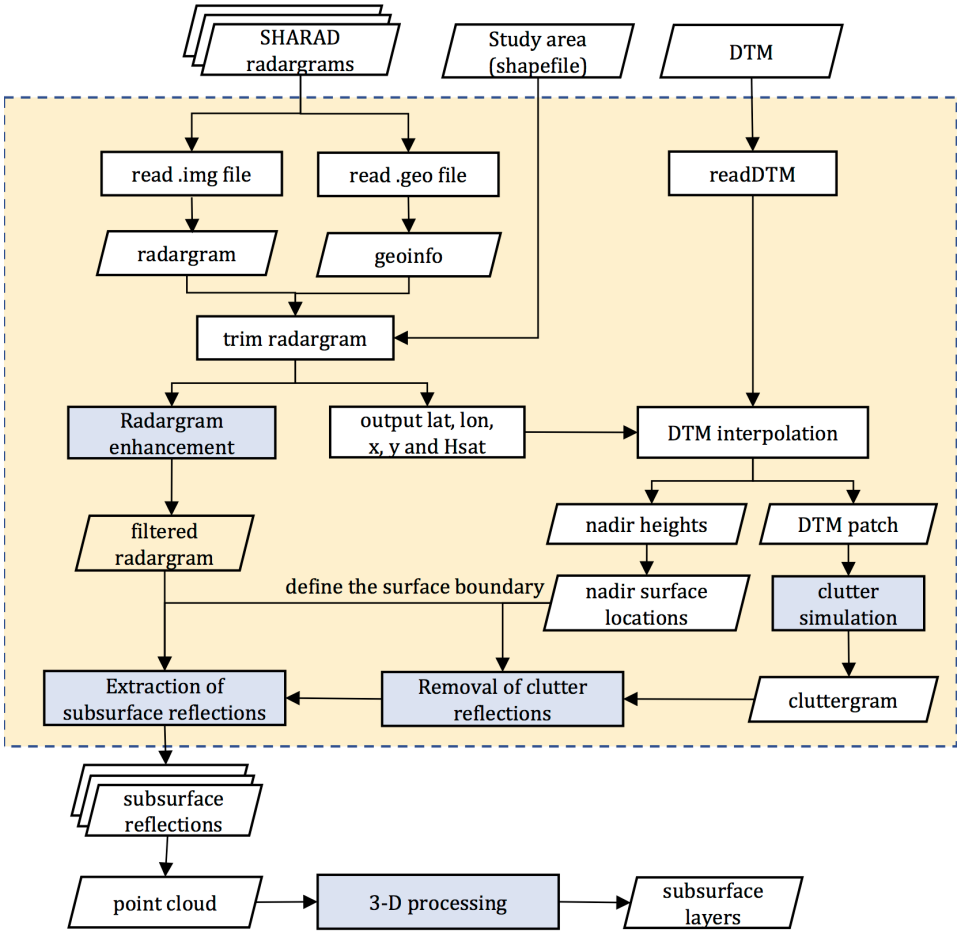

Figure 5.2: The processing workflow for extracting subsurface interfaces. The blue rectangles show the four primary steps and the yellow highlight with dashed borders is the processing applied to each SHARAD radargram. The Hsat is the height of satellite.

5.3.1 Radargram enhancement

The SHARAD radargrams usually display a low Signal to Noise Ratio (SNR), which is probably related to their low transmitted power (10 W) from the SHARAD antenna. Therefore, an image enhancement is beneficial to suppress the noise and to improve the contrast of linear features. Image denoising methods include

such techniques as the Block-Matching and 3D (BM3D) (Papari & Petkov, 2011), Bilateral filtering (Tomasi & Compo, 1998), wavelet shrinkage denoising (Chen & Qian, 2011) etc. Amongst these methods, log-Gabor filtering was found to be most effective in enhancing the contrast of the linear features, which will be demonstrated in Section 5.4.1.

The denoising method using log-Gabor functions proposed by Kovesi (1999) is shown in Equation (5.1). This enables one to calculate the amplitude and phase of the input image for a given frequency, f, and orientation, α, of the filtering kernels. The f_0 and α_0 are the central frequency and orientation of the filtering kernels. σ_f and σ_α are the bandwidth parameter and width parameter of the orientation, which are usually set to a constant to maintain the same shape of the filter while adjusting the frequency and orientation. To extract angular features in different directions and frequencies, a set of radial filters and a set of angular filters are combined. For example, f and α are chosen from $f \in (f_1, f_2, \dots, f_{\mathrm{N}})$ and$\theta \in (\alpha_1, \alpha_2, \dots, \alpha_N)$.

$$\mathrm{G}(f, \alpha) = \exp\left(-\frac{[\log(f/f_0)]^2}{2 \cdot [\log(\sigma_f/f_0)]^2}\right) \exp\left(-\frac{(\alpha - \alpha_0)^2}{2 \cdot \sigma_\alpha^2}\right) \tag{5.1}$$

The phase preserved denoising keeps the phase unchanged whilst shrinking the amplitude with a threshold, which is determined by using a Rayleigh distribution when the signal is purely Gaussian white noise. A threshold, T, is determined from the amplitude response as expressed in Equation (5.2), where μ_r and σ_r describe the Rayleigh distribution of the filter response and k is typically in the range of 2-3. The μ_r and σ_r can be calculated from the standard

deviation, σ_g, of the amplitude response as shown in Equation (5.3). A detailed description of the threshold determination is described in Kovesi (1999).

$$\mathrm{T} = \mu_r + k\sigma_r \tag{5.2}$$

$$\mu_r = \sigma_g\sqrt{\frac{\pi}{2}}, \qquad \sigma_r = \sigma_g\sqrt{\frac{4-\pi}{2}} \tag{5.3}$$

5.3.2 Extraction of Subsurface Reflections

A radargram is a combination of a series of time signals for each and every footprint. In each column of the time signal, one dielectric boundary is recorded as one peak. Therefore, detecting linear features from radargrams can be resolved by detecting the peaks from each column in the enhanced radargram. The CWT-based peak detection can be used for detecting these peaks for each column in the enhanced radargrams (Du et al., 2006). Extraction of subsurface reflections from SHARAD radargrams is generally the same as the processing described in Section 4.3.1 for the MCoRDS data. The CWT-based peak detection is realised by applying the CWT to each column of the radargram to obtain the wavelet coefficients which are calculated using Equation (4.1). Then a threshold is determined as the maximum value of the wavelet coefficient above the surface reflections which can be detected using the method proposed by Mouginot et al. (2009). The peaks having a wavelet coefficient larger than this threshold are extracted as strong radar reflections.

As discussed in Chapter 4, the Mexican hat wavelet brings out less side peaks around the true prominent reflections; thus, the Mexican hat as expressed in Equation (4.3) is selected as the wavelet for processing the SHARAD radargrams. If several scales are applied to the CWT, a scalogram can be derived representing the wavelet response to each scale. At each scale, the peaks are detected by using the threshold obtained at that scale. The peaks detected over all scales are combined into the final detected peaks. The larger the scale is, the fewer the peaks are detected.

5.3.3 Removal of Clutter Reflections

Although SHARAD is a nadir-looking instrument, its dipole antenna has negligible directivity, resulting in a wide surface beneath the spacecraft being illuminated. Therefore, it is possible that reflections from features beyond the nadir point of the flight track arrive earlier at the receiver than the subsurface reflections at the nadir of the SHARAD. These interfering reflections come from off-nadir surface reflections or off-nadir subsurface reflections rather than the nadir subsurface reflections.

The off-nadir reflections are termed clutter reflections and can be simulated by using an external DTM. The simulated radargram is here called a cluttergram. The simulation method proposed by Ferro, Pascal & Bruzzone (2013) is used for simulating clutter reflections which can then be removed from the subsurface reflections, which are extracted from the filtered radargrams. This simple model

is described in Equation (5.4), which considers no local information, such as local incidence angle and surface roughness.

$$\xi(j_c, t_c) = \sum_{(x,y)\in A(j_c,t_c)} \frac{\delta[t_c - 2R(x,y)]}{R(x,y)^4} \tag{5.4}$$

where the $R(x,y)$ is the distance from the projected geographical position (x,y) of a reflector in the cluttergram to the SHARAD antenna, j_c denotes the column number of the cluttergram and t_c denotes the time delay of reflection which can be converted to pixel coordinates by assuming a single dielectric constant. $A(j_c,t_c)$ is the area in which every planar position (x,y) can be converted to the same position (j_c,t_c) in the cluttergram.

The SHARAD radargrams have been co-registered by the US SHARAD team to the MOLA DTM. The elevations of the surface reflections should be the same as those from the MOLA DTM when there is no clutter reflection. However, when there are clutter reflections, the surface reflections in the radargrams may not be caused by the actual surface as measured in the MOLA DTM. During the simulation of the cluttergram by using the DTM, the locations of nadir surface reflections can be identified, which should have the shortest time delay compared with other nadir subsurface reflections. The identified nadir surface reflections can be transformed to image coordinates, thus delineated on the radargrams to limit the surface boundary.

Foss et al. (2017) found that the radargrams are misaligned with each other due to residual, along-track variable delays introduced by the Martian ionosphere. Therefore, there is a slight offset between the surfaces of the radargram and

cluttergram when there are no occurrences of clutter reflections. However, the surface of the radargram should be congruent with the surface of a cluttergram and the surface inverted from nadir elevations (nadir surface) if no off-nadir reflection arrives earlier than the nadir reflection. In this study, the surface of the radargram is detected and aligned with the surface of the cluttergram (detected in the same way as the radargram surface) when the offset is not too large (a threshold need to be set for the allowed offset). Meanwhile, in each column of the cluttergram, a threshold (0.5 * value of surface return) is applied to pick up the pixels suspected of being clutter reflections. Subsequently, the reflections in the radargrams are removed if they are near a suspected clutter reflection (above or below it to within 5 pixels). If the offset exceeds the threshold, then all the reflections along this column are regarded as clutter reflections. After their removal, all remaining subsurface reflections are preserved. Their x-and y-coordinates, heights (that are referenced to the MOLA sphere radius of 3396 km) and radar amplitude are output for further 3-D processing.

5.3.4 Three-dimensional (3-D) Processing

Instead of tracing layers in a 2-D raster radargram and then connecting these extracted layers, the extracted subsurface reflections in the previous step are processed in the 3-D areospatial domain directly to form subsurface interfaces. The 3-D coordinates, namely areographical x and y coordinates and elevations, are extracted at all points which have been detected in the previous steps. Subsurface isochrones can then be generated by clustering all the points into several layer groups.

The Density-Based Spatial Clustering of Applications with Noise (DBSCAN) (Ester et al., 1996) is used to initially classify the points. The DBSCAN algorithm classifies data according to their density distribution. However, during the clustering, point groups with a small number of points can also be formed. Since the subsurface layers are generally distinguishable in the vertical direction, a hierarchical clustering is applied to agglomerate the pre-classified groups by the DBSCAN algorithm given a desired cluster number.

5.4 Results

5.4.1 The enhancement of SHARAD radargrams

The SHARAD radargram from orbit 2202, which is shown in Figure 5.3(a), is here used to illustrate the results of the log-Gabor filtering. The trace from 3718 to 3896 of this radargram shown in the white rectangle in Figure 5.3(a) is used as test data since it contains extensive layered features. The log-Gabor filtering is applied to this radargram subset and the result is shown in Figure 5.3(b), along with filtered results by BM3D (Figure 5.3c) and Bilateral filtering (Figure 5.3d). Figure 5.3(e) shows one profile from column 3800 of the filtered and unfiltered radargrams. The log-Gabor filtering method performs the best in enhancing the contrast between the signals representing linear features and noise amongst the three methods.

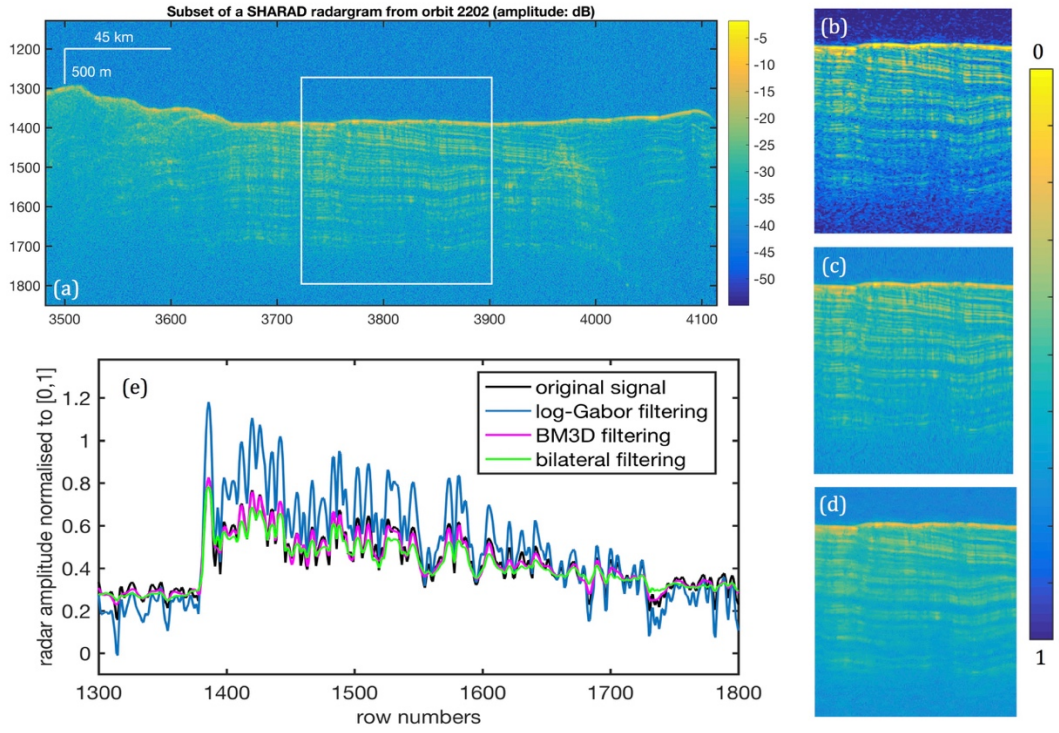

Figure 5.3: (a) The subset of a SHARAD radargram from orbit 2202. The vertical scale bar of 500 m is the vertical range when using the dielectric constant of free space; the filtered radargrams after (b) log-Gabor filtering; (c) BM3D filtering; (d) Bilateral filtering; (e) column 3800 in the SHARAD radargram (orbit 2202).

As described in Section 5.3.1, the sets of frequencies and orientations are the key parameters to achieve success with the log-Gabor filtering method. In the log-Gabor filtering algorithm (Kovesi, 1999), the number of frequencies and the multiplication frequency factor together define a set of frequencies, while the number of orientations defines the set of orientation angles. The comparison of filtered radargrams resulting from different input parameters is shown in Figure 5.4. The more frequency components are included, the less contrast the linear features have. The contrast of linear features relative to the background is reduced as their width becomes thinner when fewer frequency components are

included, such as in Figure 5.4(b) and Figure 5.4(e). The number of orientations has less of an effect on the filtered results, which is probably due to less curvature of the individual layers. The signals along the trace of 3800 (white lines in each subfigure of Figure 5.4) of the filtered radargrams are plotted. Signals above the surface and lower down the radargrams vary around zero and the filtered signal follows the trend of the original one when the number of frequencies is 5 and the multiplication factor of the frequency is 3. To enhance the original radargrams and meanwhile preserve subsurface layering features as far as possible, the parameters of Figure 5.4(b) are chosen as the input parameters for enhancing the radargrams. The parameters of Figure 5.4(a) is the same as that of Figure 5.3(b).

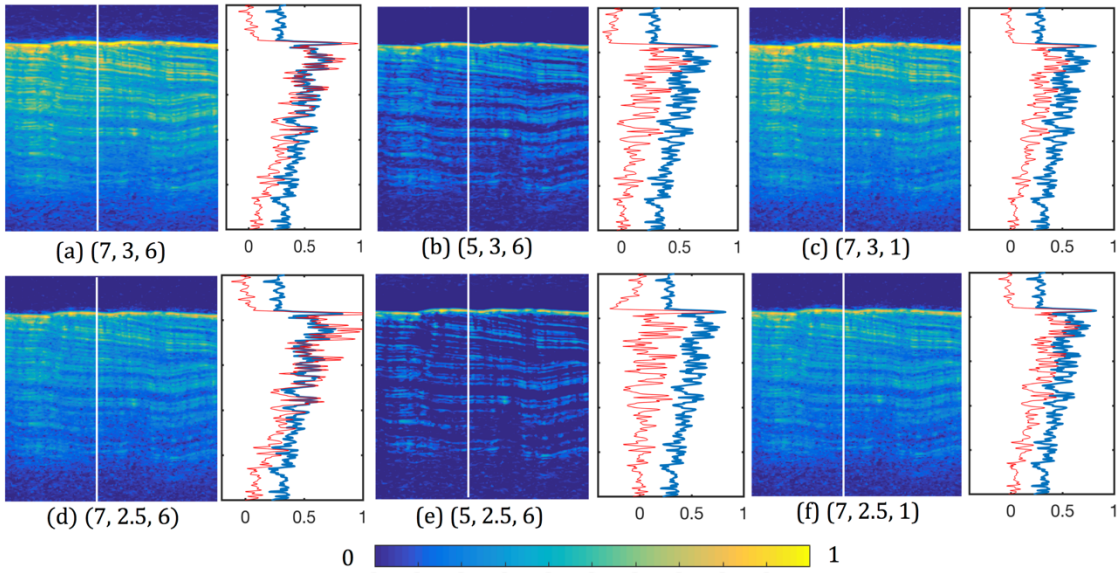

Figure 5.4: (a-f) Comparison of different input parameters for log-Gabor filtering. The parameters in brackets are the number of frequencies, multiplication factor of frequency and number of orientation angles. The signals along the trace of 3800 of the filtered radargrams are demonstrated in the plots, the signals are radar amplitude normalized to [0,1].

5.4.2 Clutter simulations and removal of clutter reflections

Clutter reflections are simulated using an external DTM. Figure 5.5 shows part A-B of the radargram from orbit 2202, the ground track of which is denoted as the yellow dashed line between A and B in Figure 5.1. From these filtered radargrams and simulated cluttergrams, by using a MOLA DTM, we can see that outside the Promethei Lingula region most of the contrast reflections are related to clutter reflections and the subsurface extended layers are not observed distinctively in the radargrams. This conforms with the fact that SPLD radargrams are characterised by wide no-signal zones, which may be caused by the absence

of sufficient dielectric contrast (Grima et al., 2011). When approaching the Promethei Lingula region (starting from column 1600 in Figure 5.5), subsurface layers are observed and extended to the location of B in this single radargram.

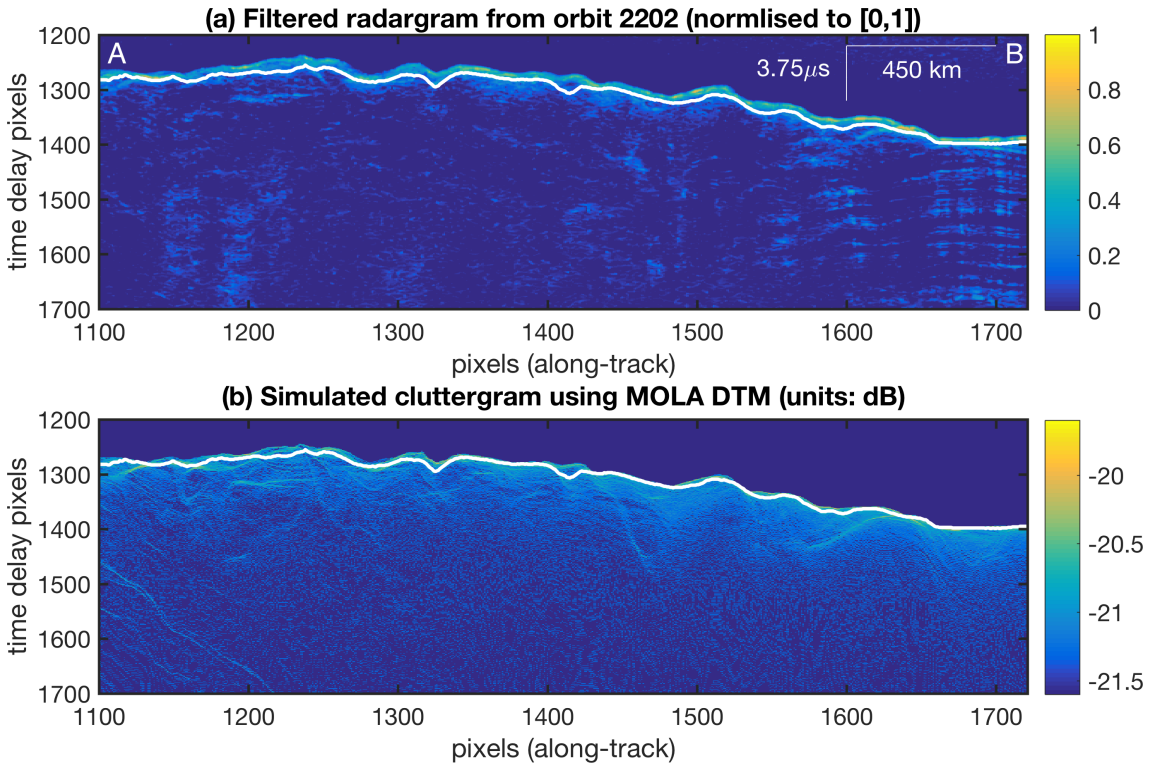

Figure 5.5: (a) The filtered radargram and (b) simulated cluttergram using MOLA DTM along the track shown as A-B in Figure 5.1.

The filtered radargram and simulated cluttergram for one part (columns 3718-4012) of the whole radargram from orbit 2202 is shown in Figure 5.6. Figure 5.6(b) and Figure 5.6(c) show the resampled DTMs according to the SHARAD footprints, which account 295 pixels along track in this case. However, these two resampled DTMs differ in the numbers of across-track pixels, which is 2387 and 1032 pixels resampled from HRSC and MOLA DTMs, respectively. The two cluttergrams in Figure 5.6(e) and Figure 5.6(f) are simulated using HRSC and

MOLA DTMs respectively. The 50m HRSC DTM has higher resolution than the corresponding MOLA DTM, which leads to a more detailed simulated cluttergram shown in Figure 5.6(d). Therefore, the HRSC DTM is used to simulate the cluttergrams, and the MOLA DTM is used as a substitute when there is no coverage from the single HRSC orbital DTM.

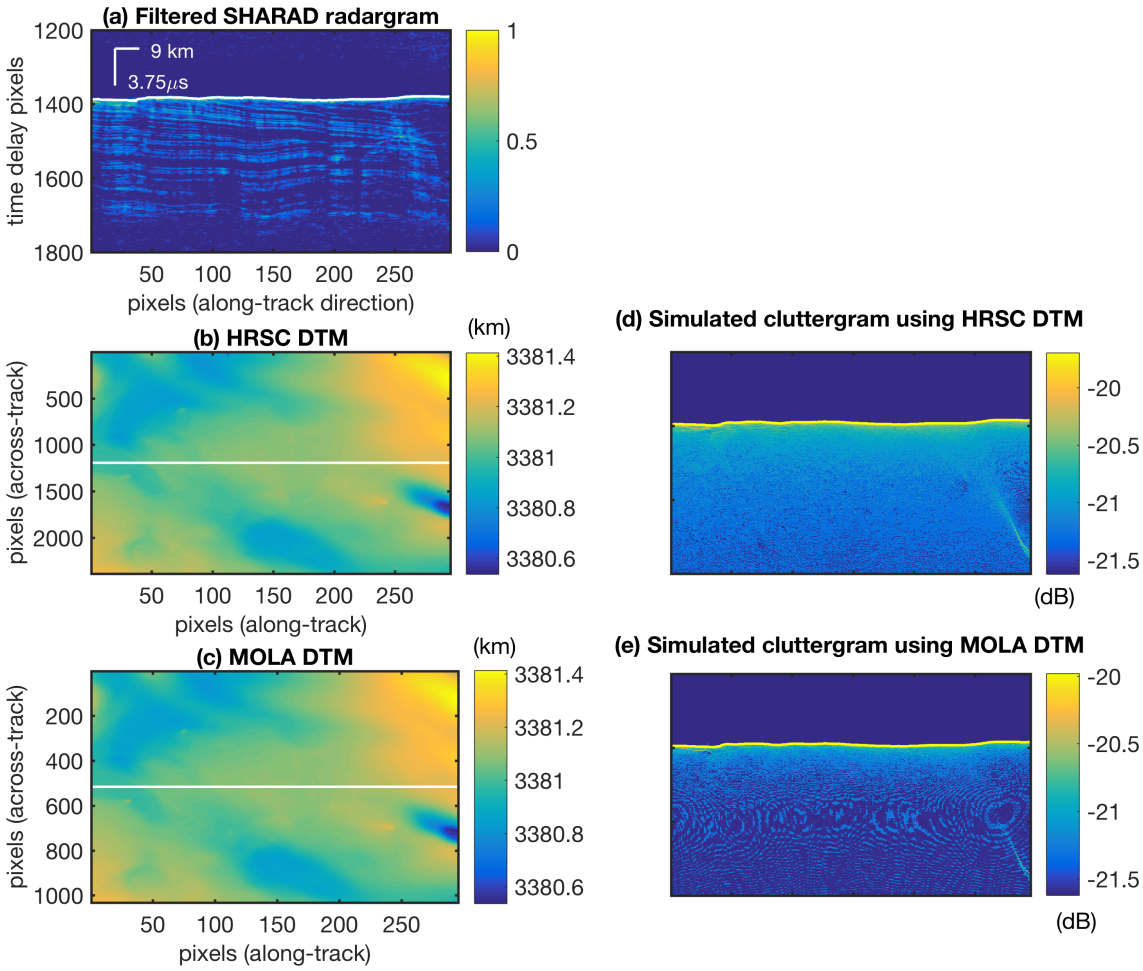

Figure 5.6: Interpolated DTMs used to simulate cluttergrams for a subset (column 3718 to 4012) of SHARAD radargram from orbit 2202: (a) The filtered radargram; Resampled (b) HRSC DTM and (c) MOLA DTM patches along the SHARAD track; Cluttergrams simulated using (d) HRSC and (e) MOLA DTM. The yellow lines in (d) and (e) show the locations inverted from surface DTM at nadir points.

To investigate the relationship between the radargram and the cluttergram, a subset (rows from 1370-1470) of the SHARAD radargrams from orbit 2202 is studied in detail. Figure 5.7(a) shows the filtered radargram from which an offset between the radargram surface (black line) and nadir surface (yellow line) can be observed. The signal along column 22 (white vertical line in Figure 5.7a) is shown in Figure 5.7(b), the first high response represents the surface while the second one represents the clutter reflection which can be observed in both the radargram and cluttergram. Figure 5.7(c) demonstrates the detected cluttergram surface (red line) and the nadir surface (yellow line) on the HRSC cluttergram. Here we can also observe an offset between these two surfaces. Figure 5.7(d) shows the detection of clutter reflections (including the surface returns) from the HRSC cluttergram, which can be later used to remove the clutter reflections from the detected subsurface reflections by aligning with the surface responses indicated by the black arrows shown in Figure 5.7(b).

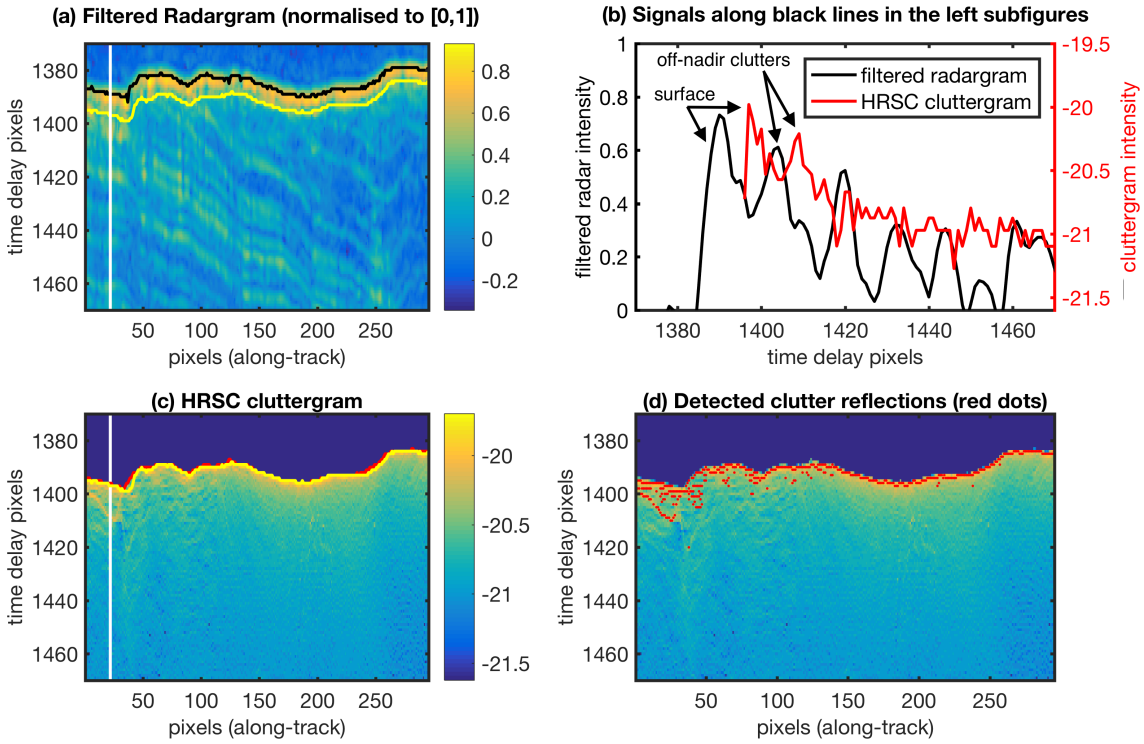

Figure 5.7: (a) Surface reflections and surface of cluttergrams from HRSC DTM; (b) Variations of radar reflections from filtered radargram and HRSC cluttergram; (c) HRSC cluttergram and (d) detected clutter reflections from the HRSC cluttergram.

5.4.3 Extraction of Subsurface Reflections

After the log-Gabor filtering, the CWT-based peak detection is applied to the filtered radargram. Firstly, a set of wavelet scales (1-15) is applied to detect the peaks to examine which scale is best for peak detection for the SHARAD radargrams over the study site. Figure 5.8 shows peak detection results along columns 22, 60, and 160 of the subset radargram shown in the white rectangle in Figure 5.3(a). From Figure 5.8(a-c), we can see that the high amplitude peaks are either caused by prominent layers or thick layers. Intrinsically, they represent

sequences of layers rather than a single layer that can be observed in surface imagery due to the limited vertical resolution of the SHARAD instrument. Figure 5.8(d-f) show the peak numbers detected at each scale from 1 to 15, which indicates that the informative scales are limited within the scale of about 13. Therefore, a single scale of 13 is chosen as a limit of the wavelet scale and the Mexican Hat function is selected as the wavelet in the CWT transform over this study site.

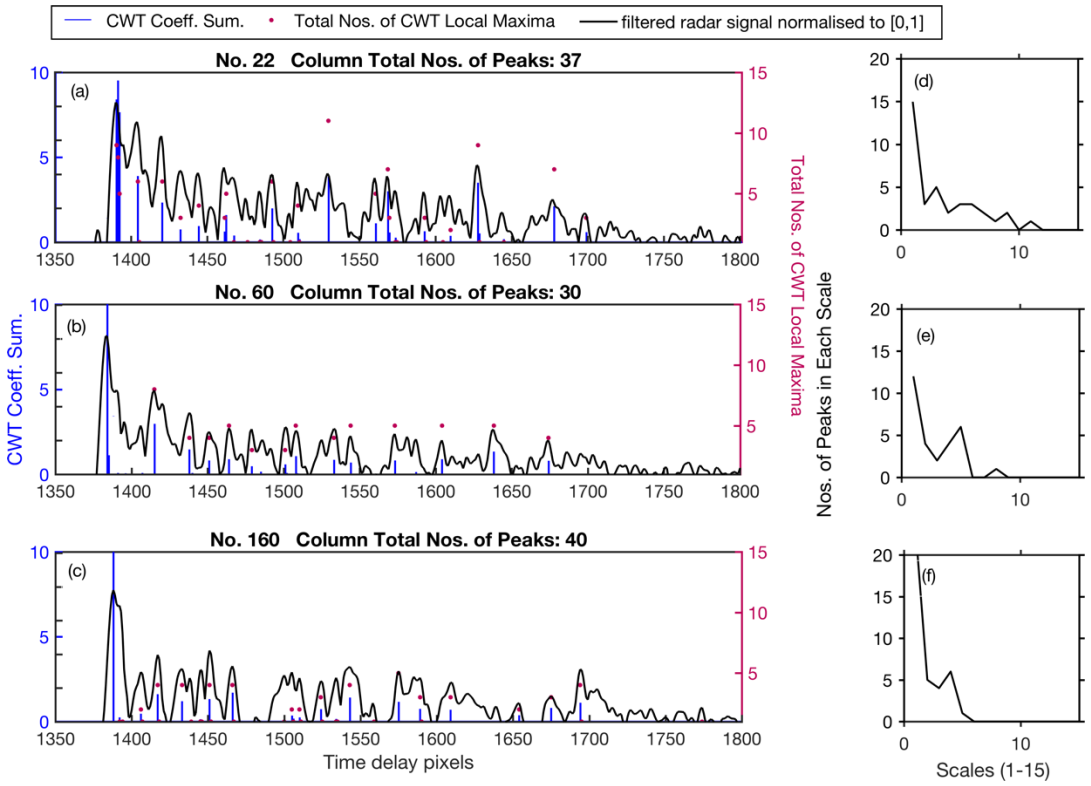

Figure 5.8: The CWT-based peak detection of SHARAD data from orbit 2202.

By applying this CWT-peak detection to all columns of the radargram, the subsurface reflections can be detected and laid over the original radargrams. Figure 5.9 shows two sets of extracted subsurface reflections from the SHARAD radargrams for orbits 2202 and 6651. The white dots in Figure 5.9(a) and (c)

show the detected peaks when using scales from 1 to 13 while the black dots represent the extracted peaks when using a single scale of 13. When using a single scale of 13, only the prominent reflections are detected while faint reflections are detected when smaller scales are included. To figure out the primary subsurface structures, a single scale 13 is set to extract subsurface reflections for an initial reconstruction though in some areas the detected reflections are not as dense as those detected with the scale range of 1 to 13. The detected subsurface reflections before and after removal of clutter reflections can be seen by comparing Figure 5.9(a) with (b), and (c) with (d).

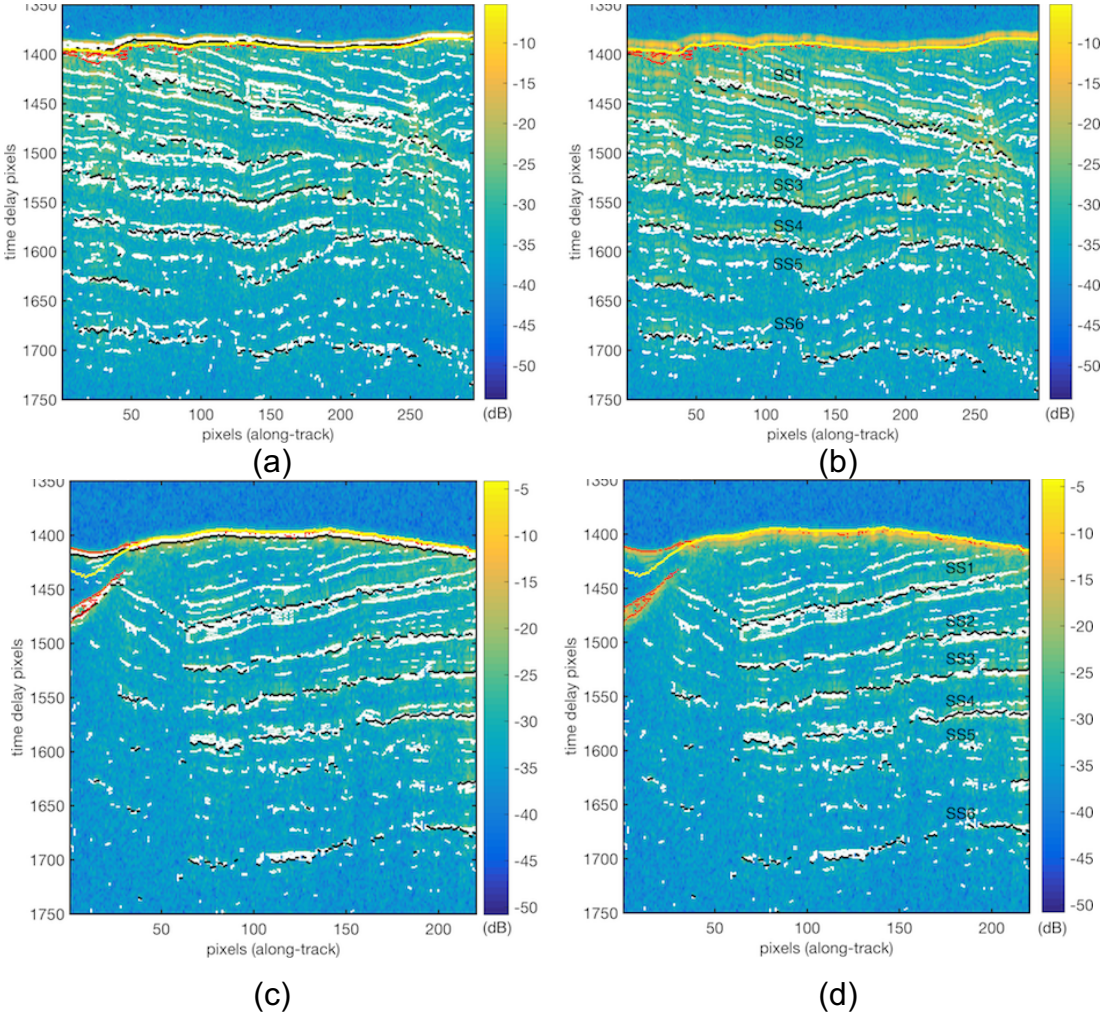

Figure 5.9: Subsurface reflections detected by applying CWT-based peak detection method with a single scale of 13 (black dots) and a scale range of 1-13 (white dots), to radargrams from (a) orbit 2202 and (c) orbit 6651; Subsurface reflections after removal of clutter reflections (b) for radargram from orbit 2202 and (d) for the radargram from orbit 6651. The background images are the original radargrams.

5.4.4 The three-dimensional processing

After all the subsurface reflections are detected, they are aggregated into a point cloud. Firstly, the DBSCAN algorithm is applied to the point cloud to classify

the points based on their density distribution, and to remove noisy points which are distributed with a low density between the clustered groups. The DBSCAN clustering algorithm separates all the points into 138 groups, among which there are seven groups containing point numbers of more than 1000. In the next step, a hierarchical clustering is applied to the classified groups to further divide the centroid of the pre-classified 138 groups given the number of primary clusters which is selected as seven in this case. The final partitioned result of this point cloud is shown in Figure 5.10.

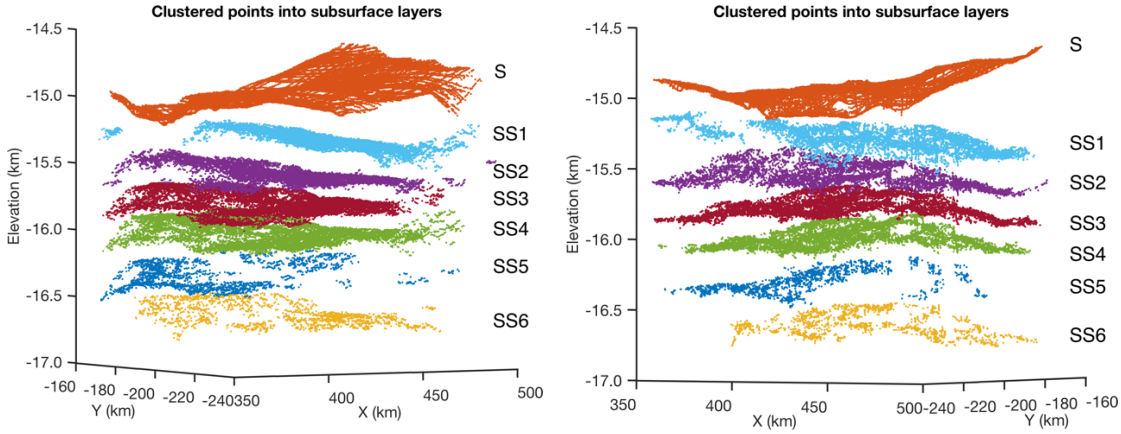

(a) (b)

Figure 5.10: The clustered 3-D points viewed from azimuth angles of (a) -45° and (b) +45°.

Each cluster of the points is taken for samples from a subsurface DTM, which can be reconstructed by interpolating these points. A Triangulated Irregular Network (TIN) is used to interpolate the points into a subsurface DTM. The interpolated surface (S) and subsurface (SS1-6) DTMs are shown in Figure 5.11. The subsurface DTMs are then converted to depth maps using a single dielectric constant of 3.4, which is consistent with a mixture of 90% water and 10% basaltic

impurities (Guallini et al., 2017). These depth maps are displayed along with the surface DTM in Figure 5.12. Figure 5.12(d) displays a depth map of the regional discontinuity (named here as AUR1) which is converted from the AUR1 DTM produced by Guallini et al. (2017). According to their study, the AUR1 should correspond to the SS2 shown in Figure 5.12(c). Compared to the AUR1, the SS2 depth map shows a more detailed variation which is likely due to the difference in interpolation methods between Kriging and TIN interpolation. This difference may also be caused by there being fewer radargrams used for interpolating the AUR1 although more than 600 SHARAD radargrams are acquired over the Promethei Lingula region, which is larger than the AUR1 extent according to Guallini et al. (2017). It should also be noted that the AUR1 DTM is derived not only by subtracting depth from the MOLA DTM, but also by further subtracting the average elevation in each SHARAD orbit. Since the AUR1 DTM has already been interpolated, it is hard to take this into account in the depth conversion. Therefore, we add back an offset of 6000 m to the AUR1 DTM. The difference between depth maps of SS2 and AUR1 can also be caused by the fact that the latter is derived by subtracting the average elevation in each orbit rather than each footprint.

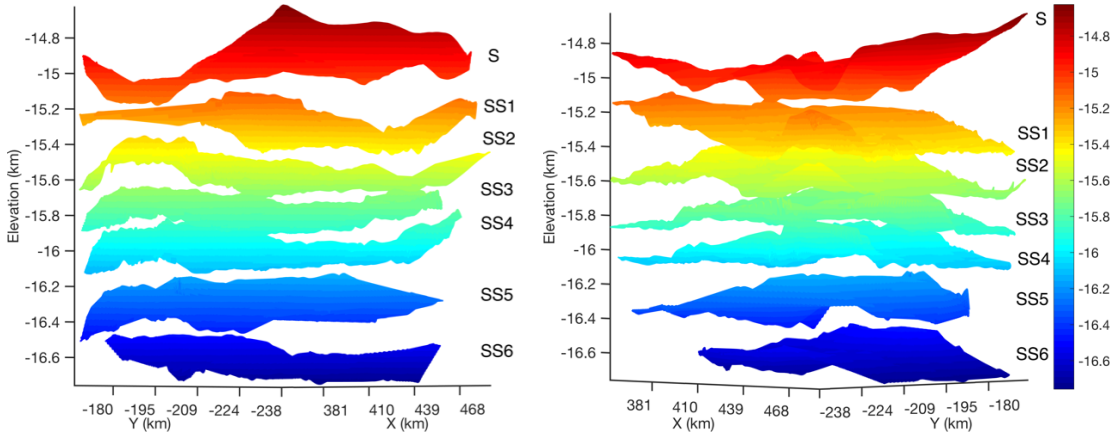

Figure 5.11: The interpolated surface and subsurface DTMs which are viewed from azimuth angle of (a) -45° and (b) +45°.

Figure 5.12(c) and (d) show the same increasing depth away from the south pole towards the north of the study site. In addition, detailed features can be observed in the SS2 depth map as highlighted by black ellipses in Figure 5.12(c), though some artefacts remain due to insufficient sample points or the failure to eliminate completely the noisy points, such as the red rectangle indicated in Figure 5.12(c). A difference map between the SS2 and AUR1 map is calculated and shown in Figure 5.13. Within the central region of this difference map, the depth difference is within 60 m. However, there is a depth difference of up to 240 m in the four corners. These larger depth differences in the corners may be caused by a lower numbers of extracted pixels in the four corners. In addition, the SS2 detects shallower depths than AUR1 in the shallow areas whilst deeper depths in the deep areas. This can be caused by the fact that the AUR1 is representative of one specific layer, while the SS2 may represent one layer sequence, which consists of several parallel sublayers since the proposed method only extracts seven main layer sequences, each of which may consist of

several parallel layers. It should be noted that there is an ambiguity in the datum employed for AUR1 DTM that was kindly provided by Dr Guallini, as described in the previous paragraph. This ambiguity may also contribute to the difference map as shown in Figure 5.13.

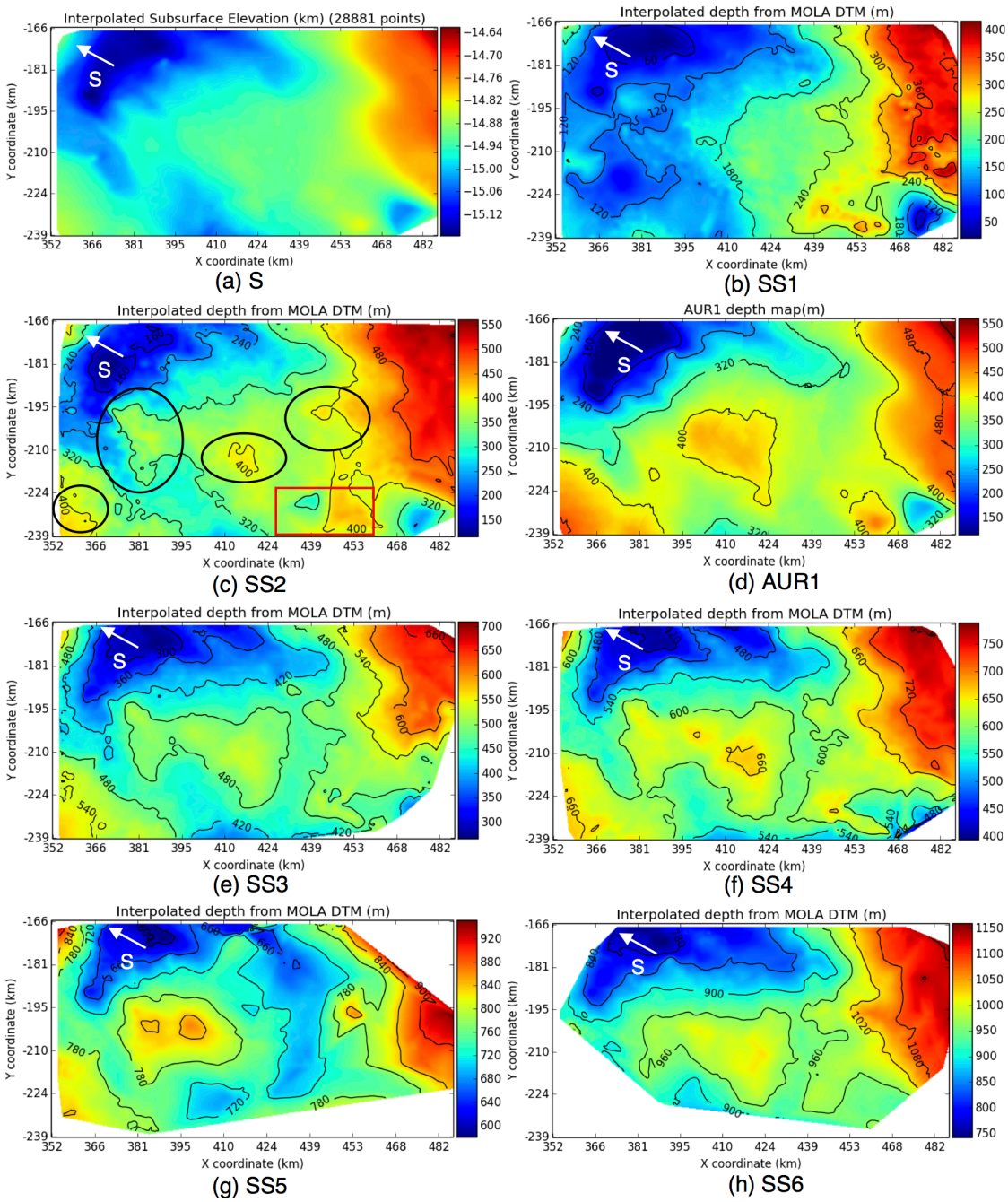

Figure 5.12: (a) Interpolated surface DTM (referenced to MOLA sphere with a radius of 3396 km); (b-c) and (e-h) are six interpolated subsurface depth maps (SS1-SS6) that are calculated from surface DTM; (d) showing the interpolated AUR1 depth map, in comparison with (c) the depth map of SS2.

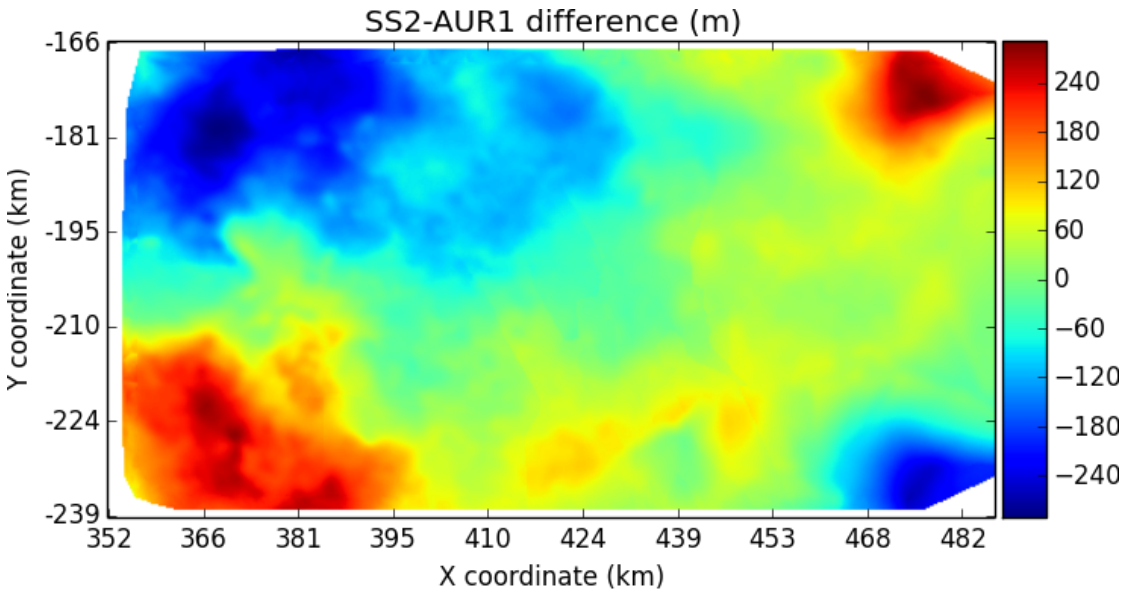

Figure 5.13: The depth difference between the SS2 and AUR1 depth maps.

5.5 Discussion

In this chapter, an automated workflow has been developed to reconstruct subsurface interfaces from SHARAD radargrams using an independent DTM, either an HRSC DTM or a MOLA DTM. The primary and prominent subsurface reflections can be detected by applying a CWT-based peak detection to the SHARAD radargrams. Clutter reflections are largely removed by using cluttergrams simulated by using an independent DTM. By applying clustering algorithms to the extracted points, the subsurface topography can be reconstructed successfully. Although there is some adjustment of the input parameters to the workflow, the proposed workflow and corresponding tools are easily tuned to different applications and are much faster compared to any manual delineation of the subsurface layers. Depending on how many prominent layers there are in the study area, several key parameters, such as the wavelet

scale, the distance and sample points used in DBSCAN clustering, need to be tuned for each area, which usually takes several iterative trials and each trial usually takes only a few minutes to achieve.

The CWT-based peak detection is effective in picking up the strong reflections when selecting a wavelet scale of 13 in the case presented. However, when the scale is selected as a smaller value, more points from subtle layers will be extracted. By choosing a scale of 13, only the prominent reflections are extracted, which represent the highest responses to the wavelet by a layer sequence composed of parallel layers. Consequently, the six subsurface DTMs obtained can be regarded as representative of layer sequences. The removal of clutter reflections works robustly on the strong clutters near the surface. Deeper and weaker clutters can disturb the original pattern of layers. Due to the weak magnitude of these clutters, it is hard to disentangle from the original pattern of layers. Since the removal of clutter reflections is now simply dependent on the threshold that is related to the intensity of the surface returns, the subsurface clutter reflections are not able to be removed in all cases, especially when it comes to areas with dramatic elevation variations. However, the following DBSCAN clustering can largely removes the sparse and irregular distributed reflections including parts of the remaining clutter reflections. DBSCAN is useful to separate the point cloud into several primary groups, while the subsequent hierarchical clustering mainly utilises the information of elevation to separate into different planes. However, the sole dependence on the elevation may lead to bad performance when the subsurface topography has dramatic variations. More

advanced “intelligent” methods for separating the point clouds into curved layers are needed in the future. The TIN interpolation is currently applied directly to all points which are sometimes very sparsely distributed, so it does not work very well in areas with few or even no sample points, such as the northwest part of SS1 and the eastern part of SS5. This issue should be addressed in future studies.

Compared to the three layer sequences reported in the literature (Kolb & Tanaka, 2006; Milkovich et al., 2009; Guallini et al., 2017), this study reveals six distinct subsurface depth maps (SS1-6) of the Promethei Lingula region, which may indicate detailed depositional and erosional processes. In this region, the subsurface layers extend into Chasma Australe while they gradually disappear in the directions away from Chasma Australe, towards which the thickness of the top layer sequence increases. The second layer below the surface (SS2) shown in Figure 5.12(c) corresponds to the so-called AUR1 layer (Figure 5.12d) produced by Guallini et al. (2017). Although generated by different methods, they share a similar depth variation across this region. This shows that this automated method provides similar results to manual delineation in the Promethei Lingula region. The two lower subsurface depth maps (SS3 and SS4) are generally parallel to each other, whilst preserving subtle differences in depth variation as seen in Figure 5.12(e-f). Further below is the SS5 layer, which has more sample points in the south of the study site compared with the sample points in the north region. Therefore, the interpolated depth of the region with x coordinates larger than 424 km in Figure 5.12(g) is probably not very reliable. Observing the left part ($x < 424$ km) of SS5, a trend of decreasing depth can be observed from the

southeast to the northwest of this study area, indicating a convergence with the upper layers to some point in the northwest region. Although the SS5 is not very well reconstructed, the subsurface interface below it (SS6) is reconstructed successfully, which generally follows the depth variation of the SS3 and SS4, in other words, generally parallel to the upper SS3 and SS4. This indicates that the detection of SS5 is not out of the capability of the SHARAD instrument; however, it is the SS5 vanishing or joining to the upper one at some point that leads to the failure of correct reconstruction.

The error of the reconstructed interfaces can come from inaccuracy of the CWT peak detection, error in separating points into different interfaces and the subsequent interpolation. Since the extracted reflections belonging to one interface are non-uniform sampling, the error of interpolation is largely caused by low sampling number in some areas. Currently, it is very difficult to evaluate the accuracy of the reconstructed subsurface interfaces because the error sources are difficult to be quantified mathematically and there is no ground truth data for validation. Therefore, what we can do at this stage is to compare one of the reconstructed interface (SS2) to the result from an independent study as demonstrated in the previous section.

5.6 Summary

The radar sounding technique has been applied to studies of the Martian subsurface for more than a decade. The utilisation of this radar sounding data is extended from manual interpretation to automatic processing regardless that many geologic studies have traditionally employed only manual delineation. This

study proposes an innovative method for automatically reconstructing subsurface DTMs of the Martian south polar region. Taking the Promethei Lingula region over the Martian south pole as an example, the study shows a processing workflow, by which the surface and six subsurface DTMs are successfully reconstructed automatically.

One of the reconstructed subsurface interfaces correlates with the angular unconformity revealed in the literature. In addition, this study reveals for the first time another subsurface interface (SS5) which tends to converge into the upper layer sequence. It is the first time that a detailed subsurface stratigraphy is reconstructed by an automated workflow. The proposed method and workflow are realised by using Python and developed as a QGIS plugin (SHARAD3d) which is publicly available on GitHub to the scientific community at the time of publication of the associated paper. More areas will be tested in the future with the SHARAD and HRSC data.

Chapter 6

Conclusions

6.1 Overall Summary

As an active remote sensing instrument, ground penetrating radar has been used in subsurface mapping and is widely applied to surveying underground pipes, tunnels and road defects (Uus et al., 2016). However, its surveying coverage is limited when it is towed by vehicles or pushed manually. To map large-scale targets that are buried beneath surfaces, radars are configured on airborne platforms like Unmanned Aerial Vehicles (UAVs) or aeroplanes or satellite platforms. These radar systems have evolved into radar sounders and spaceborne SARs, and they have been applied in the field of subsurface mapping, especially in desolate and uninhabited regions, such as the hyperarid and icy regions on the Earth. Radar sounders have been placed on spacecraft orbiting Mars to investigate subsurface features. This thesis has investigated subsurface mapping using spaceborne SAR over terrestrial deserts, and using radar sounders over terrestrial ice sheets and the Martian south pole. The results from each of these studies have been discussed separately, the previous three chapters are here briefly reviewed and concluded in a broader context.

6.1.1 Subsurface mapping of deserts

In the literature, SAR imaging at L-band has previously revealed a paleodrainage system at a large-scale over the Saharan Deserts (McCauley et al., 1986; Paillou et al., 2009, 2010) Such features cannot be clearly observed in Landsat images. An InSAR-derived SRTM C-band DEM over this region also show manifestations of valley shapes belonging to this paleodrainage system. This paleodrainage system varies in the depth of the overlying sand, which leads to changes in visibility in InSAR DEMs. However, SAR images acquired at different frequencies show differences in some tributaries of the main channel. Therefore, it is inferred that there is a radar penetration difference between L-band and C-band within the channel areas that are likely to be locations for accumulation of dry sand.

Taking the Kufra region in the eastern Sahara as an example, this thesis has shown that there is one branch of channels belonging to the large-scale paleodrainage system that was previously revealed in SAR backscatter images by Paillou et al. (2009, 2010). Using the DInSAR technique, elevations detected by L-band ALOS/PALSAR and C-band SRTM are compared in the phase domain, and the differential phase is finally converted to elevation differences. This elevation difference is estimated to be on average about 1-2 m and is regarded as representing a greater penetration depth of L-band compared with C-band elevation used as a reference surface. However, this estimation is based on the prerequisite that there is a distinct area (i.e. channel area in this thesis) where radar penetration may occur. Another drawback of this estimation is that only one

a single penetration depth is obtained because a statistical analysis relies on a calculation of elevation differences using all samples from this area.

In the third chapter, the Badain Jaran Desert in China is analysed in terms of subsurface manifestations in SAR imagery. Although some quasi-linear features are revealed in the SAR backscatter image, the proposed method for estimating the penetration depth in this desert may not be feasible. This desert contains a higher percentage of ferromagnetic material in the sand samples (Maher, Mutch & Cunningham, 2009) that may cause a large attenuation of the incident radar wave. Moisture content of the sand may also be too high to allow radar penetration, which is suggested by the inter-dune lakes. The feasibility of the proposed method in some other deserts, such as the Simpson desert in South Australia or the Mojave desert in southern California, USA or the Gobi Desert in China, etc. is not clear-cut as well. For instance, in the Mojave Desert, there are some low backscatter features that appear like the channels in the Kufra regions; however, they are man-made highways or inter-dune lakes, where radar penetration usually does not occur. A final issue about the feasibility of applying the technique elsewhere is the coherence between the two radar acquisitions. If coherence is lower than that in the case of the Kufra region, then it is too difficult to carry out InSAR processing, which relies on the coherence between two acquisitions.

The L-band SAR imagery cannot be used in the detection of aquifers or other deep buried subsurface features, as L-band radar waves only penetrate several metres while aquifers in northern Africa are buried hundreds of metres

underground. The penetration depth of several metres at L-band may be extended deeper in the future with low-frequency radar systems such as the ESA BIOMASS P-band if ionospheric distortions can be suitably mitigated. Alternatively, lower frequency radar instruments configured on aeroplanes or the ground can be used to investigate deeper buried features like underground aquifers in terrestrial applications. The radar sounding technique developed in the 1960s initially for measuring ice thickness has started to be applied to the investigation of deserts over the last few years, such as the revelation of buried aquifers in the Kuwait desert (airborne 40 MHz airborne radar found aquifers buried 20-65 m deep) (Buis, 2011). In the future, radar sounding techniques are likely to be the most useful tool for subsurface mapping over deserts if multi-frequency radar systems can be employed on aircraft, such as a Ka and VHF dual-frequency radar system (Elsherbini & Sarabandi, 2010).

6.1.2 Subsurface mapping of Greenland

Radar sounding techniques provides profile imagery of the probed media. This allows the mapping of buried targets in 3-D combining multiple observations. Traditionally, subsurface features are visually recognised and manually extracted from this profile imagery. As abundant data have been accumulated, automated or semi-automated methods to identify and extract subsurface features from radargrams (Fahnestock et al., 2001; Sime, Hindmarsh & Corr, 2011; Onana et al., 2015; Holschuh et al., 2017) are needed in studies about snow accumulation rates (Onana et al., 2015) and englacial ice flow (Holschuh et al., 2017).

In this thesis, a new automated method for extracting englacial layers is proposed. It consists of three main steps including (1) subsurface reflections extraction based on the CWT technique; (2) seed point selection and (3) a layer-tracing procedure within one frame of a radargram based on the Hough Transform (HT). Traced layers from the MCoRDS data are validated by the isochrones in the RRRAG product reported by MacGregor et al. (2015a) over the NEEM ice core drilling site. The application of CWT does not include complex parameter adjustment, and it avoids the manual delineation of layers and manual selection of seed points, significantly reducing the time cost. The layer-tracing procedure works properly with the MCoRDS data according to the experiments though adjusting input parameters may take longer time than running each step. However, when the radargram has low SNR or is occupied mostly by disrupted and discontinuous layers, the effectiveness of the layer-tracing procedure is largely impaired.

In this thesis, three ice folds are observed in the NEEM ice core drilling site. Four radargrams show clearly the folding englacial ice. Three ice folds are observed in transect 20120508_07 in Figure A2(d) while two ice folds are observed in transect 20120508_04 as shown in Figure A2(c). Only one-fold can be observed in Figures A2(a) and (b). The large and frequent englacial folds are limited to a region between the transect of 20120508_04 and 20120507_03. This indicates that the imaged ice folds are local independent features and are not associated with the tunnel in the Petermann glaciers, northwest of Greenland (Bons et al., 2016). It should be noted that ice folds are not reconstructed in 3-D

because MCoRDS data in this region is sporadically distributed. The layer-tracing and interpretation are currently carried out on 2-D raster radargrams since the data sampling rate is not enough to catch changes in the ice folds. Over the entire GrIS, the distribution of MCoRDS data is not regular and is mainly focused on several outflow glaciers in Greenland, such as the Petermann glaciers, Jakobshavn glaciers, etc. In these regions, MCoRDS collected more detailed datasets; therefore, the englacial tunnel in the Petermann glaciers (Bons et al., 2016) could possibly be reconstructed by applying the proposed method to the MCoRDS data.

6.1.3 Subsurface mapping of Martian SPLD

The method developed for the MCoRDS data are next adjusted and applied to SHARAD radargrams, which are acquired in a similar geometry, albeit at lower frequencies compared to the MCoRDS. The Martian south pole is selected as a region of interest because subsurface layers extending several hundred metres in Promethei Lingula are observed in SHARAD radargrams and a 3-D reconstruction of subsurface layers can benefit from the intensive coverage of SHARAD data in Martian polar regions.

In this thesis, an overall workflow has been proposed to extract subsurface reflections and reconstruct the subsurface interfaces buried underground in the Promethei Lingula region. In the workflow, the extraction of subsurface reflections is based on CWT, which is the same method used for extracting englacial layers in Greenland. However, in the case of SHARAD data, the layer-tracing procedure

in the 2-D raster radargram is abandoned. Positions of radar reflections are extracted in every 2-D radargram and they are accumulated into a 3D point cloud. The separation of subsurface interfaces is carried out in this 3-D geographical domain. The proposed workflow avoids the manual delineation of subsurface reflections on radargrams. In addition, the workflow includes the simulation of a cluttergram by usng suitable external DTMs. By comparing the radargram with the corresponding cluttergram, prominent false subsurface reflections (clutter reflections) can be largely eliminated.

In the Promethei Lingula region, six subsurface interfaces are reconstructed using the proposed workflow. The second subsurface interface (SS2) at 150-550 m depths from a MOLA DTM corresponds to the angular unconformity reported in the literature (Kolb & Tanaka, 2006; Seu et al., 2007; Milkovich et al., 2009; Guallini et al., 2017). According to Kolb & Tanaka (2006), it is the interface between two analysed geologic units, Aa_2 and Aa_{1b}, the former of which has a thickness of less than 300 m and the latter several hundred metres, respectively. This generally agrees with the reconstructed depth map of this interface. If we hypothesize that the angular unconformity indicates the erosional episode occurring between the regular depositional phases, then it is reasonable to postulate that apart from the reported angular unconformity (SS2), there may be another phase of erosion (SS5), that is recorded at a depth ranging from 600-850 m and extends about 50 km planarly from south to north. This depth is close to represent the interface between geological units Aa_{1a} and Aa_{1b}. In addition, it has been postulated that the angular unconfirmity is an indicator of past climate

changes, which are associated with variations in Mars orbital parameters, in particular its spin axis obliquity. Martian obliquity varies by about $\pm 10°$ with a 10^5 year cycle, around a mean value of $25°$, which is the current value (Guallini et al., 2017). The obliquity is thought to have changed by several tens of degrees in the past. When the obliquity was higher, water ice would accumulate at lower latitudes at the expense of decreasing ice in polar regions. Therefore, the angular unconformity may be caused by erosion of ice in the polar regions in a period of higher obliquity. In addition, the subsurface interfaces (SS3-SS6) below SS2 have a tendency of converging together; in other words, their thicknesses are decreasing towards the direction away from the south pole, while increasing towards the south pole. This observation of internal layers is in accord with the domed shape of the SPLD (Byrne & Ivanov, 2004; Kolb & Tanaka, 2006), supporting the inference of large volumes of deposits (which are between the surface and SS2) which are later eroded as the Chasma Australe.

The proposed workflow and tools need to be tested on a wider range of test sites on Mars. It may not be applicable to some regions on Mars, for instance, areas with high concentrations of ferromagnetic materials or the heavily cratered southern highlands on Mars. This latter region features rough terrain and intense cratering, which could lead to overwhelming clutter reflections masking true subsurface radar reflections. In addition, higher surface roughness may reduce the penetrated energy of incident waves. To support this hypothesis, a plains area with a small regional slope like Elysium Planitia argues in favour of the application of the proposed method. In this region, subsurface layers are

observed tens of metres deep below the surface, which correspond to several pixels in the SHARAD radargrams. This method should be promoted in future to the scientific community as it provides an efficient tool to generate synoptic subsurface depositional and erosional interfaces which can be used for studies about the formation of the polar regions and past climate changes on Mars.

6.2 Future Work

ALOS/PALSAR has limited penetration ability to map deep buried features, but InSAR results provide a way to estimate the penetration depth over some specific land surfaces like dry sandy areas and ice caps. Taking advantage of different penetration depths occurring at different frequencies, it is also worthwhile to investigate the application of multi-frequency SAR instruments in subsurface mapping over hyperarid sandy regions. In this thesis, only the HH polarisation mode is used to estimate the penetration depth due to striping artefacts in the HV images. As revealed by the SIR-C mission SAR data of different polarisations contain different components from surface and subsurface backscattering (Schaber, McCauley & Breed, 1997), multi-polarisation SAR data is therefore another interesting topic in subsurface mapping. Correspondently, it may be possible to develop multi-frequency and multi-polarisation radar systems for planetary subsurface mapping in the future as the estimation of dielectric properties is currently limited to the single frequency and polarisation.

On the other hand, radar sounding techniques are likely to be more suitable for directly mapping subsurface features like aquifers in deserts and subsurface layers in the Martian PLDs. Different to SAR imaging, the imaging geometry of

the radar sounding technique is to form 2-D raster images in the vertical direction (radargrams) without forming images in the along-track and across-track directions. One radargram shows one profile of the subsurface feature. A solution to 3-D reconstruction of subsurface features in this thesis is to extract radar reflections in every 2-D radargram that can then be combined in the 3-D domain. This results in the development of an automated method for layer tracing in 2-D radargrams. Basically, this is a topic for pattern recognition and machine learning techniques, which is very likely to be addressed in the near future using deep learning. In the layer-tracing method for MCoRDS data, many parameters currently need to be tuned for specific applications by users, especially in the layer-tracing procedure based on the Hough Transform. This suggests that machine learning could also be added to the SHARAD3d QGIS-plugin, to allow fully automated selection of log-Gabor filters, wavelet scale, distance and point numbers for DBSCAN clustering, and the number of desired subsurface interfaces. Given a sufficiently large training set, it is likely that machine learning techniques may be applied in future to obviate the necessity of manually adjusting parameters. Theoretically, it is feasible to reconstruct in 3-D, subsurface features if there are enough profile images sampled of this feature, similar in essence to computed tomography. The 3-D reconstruction at higher resolution may be achieved in the future if the repeat track/orbit of radar sounders on board aeroplanes and spacecraft can be carefully designed given prior knowledge about the scale of the buried features of interest.

In this thesis, 3-D reconstruction using radar data has been realised in the application to SHARAD data, but not to MCoRDS data, in which only 2-D radar reflection extraction has been tested. The author was not able to process the MCoRDS dataset of the whole GrIS as this was beyond the resources available, particularly the time available. Hopefully, in the future, the layer-tracing method can be applied to the MCoRDS datasets of the GrIS and AIS. If applied, this method could be very helpful in studies about ice sheet dynamics. For instance, this method can also be applied to studies on the formation of ice folds and their association with basal refreezing meltwater (Bell et al., 2014), internal ice flows (Leysinger Vieli, Hindmarsh & Siegert, 2007; Bons et al., 2016) and subglacial lakes (Gudlaugsson et al., 2015). In addition, it could also be used to restore surfaces before past volcanic events since tephra isochrones are usually prominent layers and are associated with past volcanic events. Restoring different layers of the GrIS and AIS in 3-D could also be researched in the future.

One 3-D reconstruction outcome of the Promethei Lingula over the Martian SPLD is the revelation of one subsurface interface (SS5) about 400 m below the published angular unconformity (SS2). As the angular unconformity is postulated to indicate a period of irregular erosion when the net ice in polar regions is sublimated and this sublimation is proposed to be related to past climate changes associated with oscillations in Martian axial obliquity. This is about ±10° with a 10^5-year cycle and around a mean value (currently 25°). Further studies can research into the association between the revealed SS5 and the past climate changes. The proposed workflow for reconstructing 3-D subsurface interfaces

could play an important role in subsurface mapping on Mars in the future. It is suggested to apply this method and corresponding QGIS-plugin tools to radar sounding data over more test sites on Mars, such as the Elysium region which is suspected to be of fluvial origin (Balme et al., 2010).

Bibliography

Abd El Samie, S.G. & Sadek, M.A., 2001. Groundwater recharge and flow in the lower Cretaceous Nubian sandstone aquifer in the Sinai Peninsula, using isotopic techniques and hydrochemistry. *Hydrogeology Journal*, 9(4), pp.378–389. doi: 10.1007/s100400100140.

Alberti, G., Castaldo, L., Orosei, R., Frigeri, A. & Cirillo, G., 2012. Permittivity estimation over Mars by using SHARAD data: the Cerberus Palus area. *Journal of Geophysical Research: Planets*, 117(E9). doi: 10.1029/2012JE004047.

Anguita, F., Babín, R., Benito, G., Gómez, D., Collado, A. & Rice, J.W., 2000. Chasma Australe, Mars: Structural framework for a catastrophic outflow origin. *Icarus*, 144(2), pp. 302-312. doi: 10.1006/icar.1999.6294

Ballard, D.H., 1981. Generalizing the Hough transform to detect arbitrary shapes. *Pattern Recognition*, 13(2), pp.111–122. doi: 10.1016/0031-3203(81)90009-1

Ballhorn, U., Jubanski, J. & Siegert, F., 2011. ICESat/GLAS data as a measurement tool for peatland topography and peat swamp forest biomass in Kalimantan, Indonesia. *Remote Sensing*, 3(9), pp.1957–1982. doi: 10.3390/RS3091957.

Balme, M.R., Gallagher, C.J., Page, D.P., Murray, J.B. Muller, J.-P. and Kim, J.-R., 2010. The Western Elysium Planitia Paleolake. *Lakes on Mars,* Elsevier.

Ed. Nathalie A. Cabrol and Edmond A. Grin, The Netherlands: Elsevier, 2010. 275-301. Print.

Bamber, J.L., 1987. Internal reflecting horizons in Spitsbergen glaciers. *Annals of Glaciology*, 9, pp.5-10. doi: 10.3189/S0260305500200682.

Bamber, J.L., Griggs, J.A., Hurkmans, R.T.W.L., Dowdeswell, J.A., Gogineni, S.P., Howat, I., Mouginot, J., Paden, J., Palmer, S., Rignot, E. & Steinhage, D., 2013. A new bed elevation dataset for Greenland. *The cryosphere,* 7, pp. 499-510. doi:10.5194/tc-7-499-2013.

Bell, R.E., Tinto, K., Das, I., Wolovick, M., Chu, W., Creyts, T.T., Frearson, N., Abdi, A. & Paden, J.D., 2014. Deformation, warming and softening of Greenland's ice by refreezing meltwater. *Nature Geoscience,* 7,pp. 497-502. doi 10.1038/NGEO2179.

Berlin, G.L., Tarabzouni, M.A., Al-naser, A.H., Sheikho, K.M. & Larson, R.W., 1986. SIR-B subsurface imaging of a sand-buried landscape: Al Labbah Plateau, Saudi Arabia. *IEEE Transactions on Geoscience and Remote Sensing*, GE-24(4), pp.595–602. doi: 10.1109/TGRS.1986.289676.

Bibring, J.P., Langevin, Y., Poulet, F., Gendrin, A., Gondet, B., Berthé, M., Soufflot, A., Drossart, P., Combes, M., Bellucci, G. and Moroz, V., 2004. Perennial water ice identified in the south polar cap of Mars. *Nature*, 428(6983), p.627.

Bingham, R.G. & Siegert M.J., 2009. Quantifying subglacial bed roughness in Antarctica: implications for ice-sheet dynamics and history. *Quaternary Science Reviews*, 28, pp. 223-236. doi: 10.1016/j.quascirev.2008.10.014.

Bingham, R.G., Rippin, D.M., Karlsson, N.B., Corr, H.F., Ferraccioli, F., Jordan, T.A., Le Brocq, A.M., Rose, K.C., Ross, N. & Siegert, M.J., 2015. Ice-flow structure and ice dynamic changes in the Weddell Sea sector of West Antarctica from radar-imaged internal layering. *Journal of Geophysical Research: Earth Surface*, 120(4), pp.655–670. doi: 10.1002/2014JF003291.

Boisson, J., Heggy, E., Clifford, S.M., Frigeri, A., Plaut, J.J., Farrell, W.M., Putzig, N.E., Picardi, G., Orosei, R., Lognonné, P. & Gurnett, D.A., 2009. Sounding the subsurface of Athabasca Valles using MARSIS radar data: Exploring the volcanic and fluvial hypotheses for the origin of the rafted plate terrain. *Journal of Geophysical Research: Planets*, 114(E8). doi: 10.1029/2008JE003299.

Bons, P.D., Jansen, D., Mundel, F., Bauer, C.C., Binder, T., Eisen, O., Jessell, M.W., Llorens, M.G., Steinbach, F., Steinhage, D. & Weikusat, I., 2016. Converging flow and anisotropy cause large-scale folding in Greenland's ice sheet. *Nature Communications*, 7. doi: 10.1038/ncomms11427.

Brakenridge, G.R., 1993. Modern shelf ice, equatorial Aeolis quadrangle, Mars. In *Proceedings of 24th Lunar and Planetary Science Conference,* 24, pp. 175-176.

Bramson, A.M., Byrne, S. & Putzig, N.E., 2014. Thick, excess water ice in Arcadia Planitia, Mars. In *Proceedings of 45th Lunar and Planetary Science Coneference*, Houston, US.

Bramson, A.M., Byrne, S., Putzig, N.E., Sutton, S., Plaut, J.J., Brothers, T.C. & Holt, J.W., 2015. Widespread excess ice in Arcadia Planitia, Mars. *Geophysical Research Letters*, 42(16), pp. 6566-6574. doi: 10.1002/2015GL064844.

Brandt, O., Björnsson, H. & Gjessing, Y., 2005. Mass-balance rates derived by mapping internal tephra layers in Mýrdalsjökull and Vatnajökull ice caps, Iceland. *Annals of Glaciology*, 42, pp.284-290. doi: 10.3189/172756405781813078

Brothers, T., Holt, J. & Christian, S., 2010. Investigating subsurface geomorphology of the Basal Unit of Planum Boreum, mars with SHARAD to constrain early erosional processes. In *proceedings of the 41st Lunar and Planetary Science Conference*, March 1-5, 2010 in the Woodlands, Texas, US, 41, pp.2590.

Brothers, T.C. & Holt, J.W., 2016. Three-dimensional structure and origin of a 1.8 km thick ice dome within Korolev Crater, Mars. *Geophysical Research Letters*, 43(4), pp.1443–1449. doi: 10.1002/2015GL066440.

Brothers, T.C., Holt, J.W. & Spiga, A., 2015. Planum Boreum basal unit topography, Mars: Irregularities and insights from SHARAD. Journal of *Geophysical Research: Planets*, 120(7), pp.1357–1375. doi: 10.1002/2015JE004830.

Bruzzone, L., Alberti, G., Catallo, C., Ferro, A., Kofman, W. & Orosei, R., 2011. Subsurface radar sounding of the Jovian moon Ganymede. *Proceedings of the IEEE*, 99(5), pp.837–857. doi: 10.1109/JPROC.2011.2108990.

Bruzzone, L., Plaut, J.J., Alberti, G., Blankenship, D.D., Bovolo, F., Campbell, B.A., Ferro, A., Gim, Y., Kofman, W., Komatsu, G. & McKinnon, W., 2013. RIME: Radar for icy moon exploration. In *Proceedings of IEEE International Geoscience and Remote Sensing Symposium (IGARSS)*, July 21-26, 2013 in Melbourne, VIC, Australia, pp.3907–3910. doi: 10.1109/IGARSS.2013.6723686.

Buis, A., 2011. NASA Mars Research Helps Find Buried Water on Earth [Online]. Available at: http://www.nasa.gov/topics/earth/features/kuwait20110914.html.

Burr, D.M., 2002. Recent aqueous floods from the Cerberus Fossae, Mars. *Geophysical Research Letters*, 29(1), pp.2–5.

Burr, D.M., Grier, J.A., McEwen, A.S. & Keszthelyi, L.P., 2002. Repeated aqueous flooding from the cerberus fossae: Evidence for very recently extant, deep groundwater on Mars. Icarus, 159(1), pp.53–73.

Byrne, S., 2009. The Polar Deposits of Mars. Annual Review of Earth and Planetary *Sciences*, 37(1), pp.535–560. doi: 10.1146/annurev.earth.031208.100101.

Byrne, S. & Ivanov, A.B., 2004. Internal structure of the Martian south polar layered deposits. *Journal of Geophysical Research: Planets*, 109(11), pp.1–20. doi: 10.1029/2004JE002267.

Byrne, S. & Murray, B.C., 2002. North polar stratigraphy and the paleo-erg of Mars. *Journal of Geophysical Research: Planets*, 107(E6), pp.11–12. Available at: http://dx.doi.org/10.1029/2001JE001615. doi: 10.1029/2001JE001615.

Campbell, B. 2014. U.S. Shallow Radar (SHARAD) Data product description for the planetary data system. Accessible at http://pds-geosciences.wustl.edu/mro/mro-m-sharad-5-radargram-v1/mrosh_2001/document/rgram_processing.pdf [Accessed May 14, 2018].

Campbell, B., Carter, L., Phillips, R., Plaut, J., Putzig, N., Safaeinili, A., Seu, R., Biccari, D., Egan, A. & Orosei, R., 2008. SHARAD radar sounding of the Vastitas Borealis Formation in Amazonis Planitia. *Journal of Geophysical Research: Planets*, 113(E12). doi: 10.1029/2008JE003177.

Campbell, B.A., Ghent, R.R. & Shepard, M.K., 2003. Limits on inference of Mars small-scale topography from MOLA data. *Geophysical Research Letters*, 30(3), pp.1–4. doi: 10.1029/2002GL016550.

Campbell, B. & Putzig, N., 2011. Surface roughness maps of Mars based on SHARAD echoes. In *Proceedings of Lunar and Planetary Science Conference*, March 7-11, 2011 in the Woodlands, Texas, 42, pp. 1489.

Campbell, B.A., Putzig, N.E., Carter, L.M., Morgan, G.A., Phillips, R. & Plaut, J.J., 2013. Roughness and near-surface density of Mars from SHARAD radar echoes. *Journal of Geophysical Research: Planets*, 118(3), pp.436–450. doi: 10.1002/jgre.20050.

Carabajal, C.C. & Harding, D.J., 2006. SRTM C-band and ICESat laser altimetry elevation comparisons as a function of tree cover and relief. *Photogrammetric Engineering & Remote Sensing*, 72(3), pp.287–298. doi: 10.1.1.404.4122.

Cassanelli, J.P. & Head, J.W., 2015. Firn densification in a Late Noachian “icy highlands” Mars: Implications for ice sheet evolution and thermal response. *Icarus*, 253, pp. 243–255. doi: 10.1016/j.icarus.2015.03.004.

Catania, G.A. & Neumann, T.A., 2010. Persistent englacial drainage features in the Greenland Ice Sheet. *Geophysical Research Letters*, 37(2), pp. doi: 10.3189/172756404781814591.

Chen, F., Liu, Y., 2011. Secular annual movement of sand dunes in Badain Fijaran Desert based on geographic analyses of remotely sensed imagery, *Remote Sensing Technology and Application*, 26, pp. 501-507.

Chen, G., Qian, S. E., 2011. Denoising of hyperspectral imagery using principal component analysis and wavelet shrinkage, *IEEE Transactions on Geoscience and remote sensing*, 49, pp. 973-980. doi: 10.1109/TGRS.2010.2075937

Chen, F., Masini, N., Liu, J., You, J. & Lasaponara, R., 2016. Multi-frequency satellite radar imaging of cultural heritage: the case studies of the Yumen Frontier Pass and Niya ruins in the Western Regions of the Silk Road Corridor. *International Journal of Digital Earth*, 9(12), pp.1224–1241. doi: 10.1080/17538947.2016.1181213.

Chen, C.W. & Zebker, H.A., 2002. Phase unwrapping for large SAR interferograms: Statistical segmentation and generalized network models. *IEEE Transactions on Geoscience Remote Sensing*, 40(8), pp.1709–1719. doi: 10.1109/TGRS.2002.802453.

Chen, J. & Zebker, H.A., 2012. Ionospheric artifacts in simultaneous L-band InSAR and GPS observations. *IEEE Transactions on Geoscience and Remote Sensing*, 50(4), pp.1223–1239. doi: 10.1109/TGRS.2011.2164805

Choudhary, P., Holt, J. & Kempf, S., 2016. Surface clutter and echo location analysis for the interpretation of SHARAD data from Mars. *IEEE Geoscience and Remote Sensing Letters*, 13(9), pp. 1285-1289. doi: 10.1109/LGRS.2016.2581799.

Christensen, P.R., Bandfield, J.L., Clark, R.N., Edgett, K.S., Hamilton, V.E., Hoefen, T., Kieffer, H.H., Kuzmin, R.O., Lane, M.D., Malin, M.C. & Morris,

R.V., 2000. Detection of crystalline hematite mineralization on Mars by the Thermal Emission Spectrometer: Evidence for near-surface water. *Journal of Geophysical Research: Planets*, 105(E4), pp.9623–9642. doi: 10.1029/1999JE001093.

Clifford, S.M., 1987. Polar basal melting on Mars. *Journal of Geophysical Research*, 92(B9), p.9135. Available at: http://doi.wiley.com/10.1029/JB092iB09p09135.

Cloude, S.R. & Papathanassiou, K.P., 1998. Polarimetric SAR interferometry. *IEEE Transactions on Geoscience and Remote Sensing*, 36(5), pp.1551–1565. doi: 10.1109/36.718859.

Cuffey, K.M. & Paterson, W.S.B., 2010. The Physics of Glaciers. Academic Press.

Cutts, J.A., 1973. Nature and origin of layered deposits of the Martian polar regions. *Journal of Geophysical Research*, 78(20), pp.4231–4249. doi: 10.1029/JB078I020P04231.

Dabbagh, A.E., Al-Hinai, K.G. & Asif Khan, M., 1997. Detection of sand-covered geologic features in the Arabian Peninsula using SIR-C/X-SAR data. *Remote Sensing of Environment*, 59(2), pp.375–382.

Dabov, K. & Foi, A., 2007. Image denoising by sparse 3-D transform-domain collaborative filtering. *IEEE transactions on Image Processing*, 16(8), pp. 2080-2095. doi: 10.1109/TIP.2007.901238.

Dahab, K.A., Ebraheem, A.M. & El Sayed, E.A., 2001. A study of hydrogeological conditions of the Nubian sandstone aguifer in the area between Abu Simbel and Toschka, Western Desert, Egypt. *American Geophysical Union*, *Spring Meeting 2001*, abstract #H22D-01. Available at: http://adsabs.harvard.edu/abs/2001AGUSM...H22D01D [Accessed January 4, 2018].

Dall, J., 2007. InSAR elevation bias caused by penetration into uniform volumes. *IEEE Transactions on Geoscience and Remote Sensing*, 45(7), pp.2319–2324. doi: 10.1109/TGRS.2007.896613.

Drewry, D.J. & Meldrum, D.T., 1978. Antarctic airborne radio echo sounding, 1977–78. *Polar Record*, 19(120), pp.267–273. doi: 10.1017/S0032247400018271.

Drews, R., Eisen, O., Weikusat, I., Kipfstuhl, S., Lambrecht, A., Steinhage, D., Wilhelms, F. & Miller, H., 2009. Layer disturbances and the radio-echo free zone in ice sheets. *The Cryosphere*, 3(2), pp.195–203. doi: 10.5194/tc-3-195-2009.

Du, P., Kibbe, W.A. & Lin, S.M., 2006. Improved peak detection in mass spectrum by incorporating continuous wavelet transform-based pattern matching. *Bioinformatics*, 22(17), pp.2059–2065. doi: 10.1093/bioinformatics/btl355.

Duda, R.O. & Hart, P.E., 1972. Use of the Hough transformation to detect lines and curves in pictures. *Commun. ACM*, 15, pp.11–15.

El-Baz, F., 1998. Sand accumulation and groundwater in the eastern Sahara. *Episodes*, 21(3), pp.147–151.

Elachi, C. & Granger, J., 1982. Spaceborne imaging radars probe `in depth'. *IEEE spectrum*, 19(11), pp.24–29. doi: 10.1109/MSPEC.1982.6367027.

El Samie, S.A. & Sadek, M., 2001. Groundwater recharge and flow in the Lower Cretaceous Nubian Sandstone aquifer in the Sinai Peninsula, using isotopic techniques and hydrochemistry. *Hydrogeology Journal*, 9(4), pp.378-389. doi: 10.1007/s100400100.

Elsherbini, A. & Sarabandi, K., 2010. Mapping of sand layer thickness in deserts using SAR interferometry. *IEEE Transactions on Geoscience and Remote Sensing*, 48(9), pp.3550–3559. doi: 10.1109/TGRS.2010.2047110.

ESA, 2015. BIOMASS [Online]. Available at http://www.esa.int/Our_Activities/Observing_the_Earth/The_Living_Planet_Programme/Earth_Explorers/Future_missions/Biomass. [Accessed July 04, 2018].

Evans, S., 1961. Polar ionospheric spread echoes and radio frequency properties of ice shelves. *Journal of Geophysical Research*, 66(12), pp.4137–4141. doi: 10.1029/JZ066i012p04137.

Fahnestock, M., Abdalati, W., Luo, S. & Gogineni, S., 2001. Internal layer tracing and age-depth-accumulation relationships for the northern Greenland ice

sheet. *Journal of Geophysical Research: Atmospheres*, 106(D24), pp.33789–33797. doi: 10.1029/2001JD900200.

Farr, T.G., Elachi, C., Hartl, P. & Chowdhury, K., 1986. Microwave penetration and attenuation in desert soil: a field experiment with the Shuttle Imaging Radar. *IEEE Transactions on Geoscience and Remote Sensing*, GE-24(4), pp.590–594. doi: 10.1109/TGRS.1986.289675.

Farrell, W.M., Clifford, S.M., Milkovich, S.M., Plaut, J.J., Leuschen, C.J., Picardi, G., Gurnett, D.A., Watters, T.R., Safaeinili, A., Ivanov, A.B. & Phillips, R.J., 2008. MARSIS subsurface radar investigations of the South Polar reentrant Chasma Australe. *Journal of Geophysical Research: Planets*, 113(E4), pp.1–11. doi: 10.1029/2007JE002974.

Ferretti, A., Prati, C. & Rocca, F., 1999. Multibaseline InSAR DEM reconstruction: The wavelet approach. *IEEE Transactions on Geoscience and Remote Sensing*, 37(2), pp.705-715. doi: 10.1109/36.752187.

Ferretti, A., Monti-Guarnieri, A., Prati, C., Rocca, F. & Massonet, D., 2007. InSAR principles-guidelines for SAR interferometry processing and interpretation [Online]. Available at: http://www.esa.int/About_Us/ESA_Publications/InSAR_Principles_Guidelines_for_SAR_Interferometry_Processing_and_Interpretation_br_ESA_TM-19. [Accessed January 04, 2018].

Ferro, A. & Bruzzone, L., 2012. Analysis of Radar Sounder Signals for the Automatic Detection and Characterization of Subsurface Features. *IEEE*

Transactions on Geoscience and Remote Sensing, 50(11), pp.4333–4348. doi: 10.1109/TGRS.2012.2194500.

Ferro, A. & Bruzzone, L., 2013. Automatic extraction and analysis of ice layering in radar sounder data. *IEEE Transactions on Geoscience and Remote Sensing*, 51(3), pp. 1622-1634. doi: 10.1109/TGRS.2012.2206078.

Ferro, A., Pascal, A. & Bruzzone, L., 2013. A novel technique for the automatic detection of surface clutter returns in radar sounder data. *IEEE Transactions on Geoscience and Remote Sensing*, 51(5), pp.3037–3055. doi: 10.1109/TGRS.2012.2219315.

Fishbaugh, K.E. & Hvidberg, C.S., 2006. Martian north polar layered deposits stratigraphy: Implications for accumulation rates and flow. *Journal of Geophysical Research*, 111(E6), pp.1-21. doi: 10.1029/2005JE002571.

Flamini, E., Fois, F., Calabrese, D., Bombaci, O., Catallo, C., Croce, A., Croci, R., Guelfi, M., Zampolini, E., Picardi, G. & Seu, R., 2007. Sounding mars with SHARAD & MARSIS. In *Proceedings of International workshop on Advanced Ground Penetrating Radar*, June 27-29, 2007 in Aula Magna Partenope, Italy. doi: 10.1109/AGPR.2007.386561.

Florentine, C., Harper, J., Johnson, J.V. and Meierbachtol, T., 2018. Radiostratigraphy reflects the present-day, internal ice flow field in the ablation zone of western Greenland. *Frontiers in Earth Science*, 6, p.44. doi: 10.3389/feart.2018.00044.

Fornaro, G., Reale, D., Pauciullo, A., Zhu, X.X. and Bamler, R., 2012. SAR Tomography: an advanced tool for spaceborne 4D radar scanning with application to imaging and monitoring of cities and single buildings. *IEEE Geoscience and Remote Sensing Newsletter*, pp.9-17.

Foss, F.J., Putzig, N.E., Campbell, B.A. & Phillips, R.J., 2017. 3D imaging of Mars' polar ice caps using orbital radar data. *The Leading Edge*, 36(1), pp.43–57. doi: 10.1190/tle36010043.1.

Freeman, G.J., Bovik, A.C. & Holt, J.W., 2010. Automated detection of near surface martian ice layers in orbital radar data. In *Proceedings of the IEEE Southwest Symposium on Image Analysis and Interpretation*. doi: 10.1109/SSIAI.2010.5483905.

Frezzotti, M., Bitelli, G., Michelis, P. D., Deponti, A., Forieri, A., Gandolfl, S. Maggi, V., Mancini, F., Remy, F., Tabacco, I.E., Urbini, S., Vittuari, L. & Zirizzottl, A., 2004. Geophysical survey at Talos Dome, East Antarctica: the search for a new deep-drilling site. *Annals of Glaciology*, 39, pp. 423–432. doi: 10.3189/172756404781814591.

Fujisada, H. & Minoru Urai, A.I., 2012. Technical methodology for ASTER global DEM. *IEEE Transactions on Geoscience and Remote Sensing*, 50(10), pp.3725–3736. doi: 10.1109/TGRS.2012.2187300.

Fujita, S., Maeno, H., Uratsuka, S., Furukawa, T., Mae, S., Fujii, Y. & Watanabe, O., 1999. Nature of radio echo layering in the Antarctic Ice Sheet detected

by a two-frequency experiment. *Journal of Geophysical Research: Solid Earth*, 104(B6), pp.13013–13024. doi: 10.1029/1999JB900034.

Gaber, A., Soliman, F., Koch, M. & El-Baz, F., 2015. Using full-polarimetric SAR data to characterize the surface sediments in desert areas: A case study in El-Gallaba Plain, Egypt. *Remote Sensing of Environment*, 162, pp.11–28. doi: 10.1016/j.rse.2015.01.024.

Gamba, P. & Lossani, S., 2000. Neural detection of pipe signatures in ground penetrating radar images. *IEEE transactions on Geoscience and Remote Sensing*, 38(2), pp. 790-797. doi: 10.1109/36.842008.

Gardelle, J., Berthier, E., Arnaud, Y. & Kaab, A., 2013. Region-wide glacier mass balances over the Pamir-Karakoram-Himalaya during 1999–2011. *The Cryosphere*, 7(4), pp.1263–1286. doi: 10.5194/tc-7-1263-2013.

Gawthorpe, R.L., Collier, R.L., Alexander, J., Bridge, J.S. & Leeder, M.R., 1993. Ground penetrating radar: application to sandbody geometry and heterogeneity studies. *Geological Society, London, Special Publications*, 73, pp.421–432. doi: 10.1144/GSL.SP.1993.073.01.24.

Ghoneim, E. & El-Baz, F., 2007. The application of radar topographic data to mapping of a mega-paleodrainage in the Eastern Sahara. *Journal of Arid Environments*, 69(4), pp.658–675. doi: 10.1016/j.jaridenv.2006.11.018.

Ghozzi, R., Lahouar, S., Souani, C. & Besbes, K., 2017. Peak detection of GPR data with lifting wavelet transform (LWT). In *2017 International Conference*

on Advanced Systems and Electric Technologies (IC_ASET), pp. 34–37. Available at: http://ieeexplore.ieee.org/document/7983663/ [Accessed December 27, 2017].

Gradstein, F.M., Ogg, J.G., Schmitz, M. & Ogg, G. eds., 2012. The geologic time scale 2012. Elsevier.

Graham, L.C., 1974. Synthetic interferometer radar for topographic mapping. *Proceedings of the IEEE,* 62(6), pp. 763–68. doi: 10.1109/PROC.1974.9516.

Grandjean, G., Paillou, P., Dubois-Fernandez, P., August-Bernex, T., Baghdadi, N.N. & Achache, J., 2001. Subsurface structures detection by combining L-band polarimetric SAR and GPR data: Example of the Pyla Dune (France). *IEEE Transactions on Geoscience and Remote Sensing*, 39(6), pp.1245–1258. doi: 10.1109/36.927447.

Grandjean, G., Paillou, P., Baghdadi, N., Heggy, E., August, T. & Lasne, Y., 2006. Surface and subsurface structural mapping using low frequency radar: a synthesis of the Mauritanian and Egyptian experiments. *Journal of African Earth Sciences*, 44(2), pp.220–228. doi: 10.1016/j.jafrearsci.2005.10.015.

Grenier, C., Paillou, P. & Maugis, P., 2009. Assessment of Holocene surface hydrological connections for the Ounianga lake catchment zone (Chad). *Comptes Rendus Geoscience*, 341(8--9), pp.770–782. doi: 10.1016/j.crte.2009.03.004.

Grima, C., Kofman, W. & Mouginot, J., 2008. Dielectric mapping of bulk polar ices on Mars with SHARAD radar data. *AGU Fall Meeting*.

Grima, C., Kofman, W., Mouginot, J., Phillips, R.J., Hérique, A., Biccari, D., Seu, R. & Cutigni, M., 2009. North polar deposits of Mars: Extreme purity of the water ice. *Geophysical Research Letters*, 36(3). doi: 10.1016/j.icarus.2009.01.009.

Grima, C., Costard, F., Kofman, W., Saint-Bézar, B., Servain, A., Rémy, F., Mouginot, J., Herique, A. and Seu, R., 2011. Large asymmetric polar scarps on Planum Australe , Mars : Characterization and evolution. *Icarus*, 212(1), pp.96–109. doi: 10.1016/j.icarus.2010.12.017.

Grima, C. Kofman, W., Herique, A., Orosei, R. & Seu, R., 2012. Quantitative analysis of Mars surface radar reflectivity at 20 MHz. *Icarus*, 220(1), pp.84–99. doi: 10.1016/j.icarus.2012.04.017.

Grossmann, A., Kronland-Martinet, R. & Morlet, J., 1990. Reading and Understanding Continuous Wavelet Transforms. In Wavelets, Springer, Berlin, Heidelberg, pp. 2–20. doi: 10.1007/978-3-642-75988-8_1.

Gruber, A., Wessel, B., Huber, M. and Roth, A., 2012. Operational TanDEM-X DEM calibration and first validation results. *ISPRS Journal of Photogrammetry and Remote Sensing*, 73, pp.39-49. 10.1016/j.isprsjprs.2012.06.002.

Guallini, L., Rossi, A.P., Forget, F., Marinangeli, L., Lauro, S.E., Pettinelli, E., Seu, R. & Thomas, N., 2017. Regional stratigraphy of the south polar layered deposits (Promethei Lingula, Mars): “Discontinuity-bounded” units in images and radargrams. *Icarus*. doi: 10.1016/J.ICARUS.2017.08.030. (In press)

Gudlaugsson, E., Humbert, A., Kleiner, T., Kohler, J. & Andreassen, K., 2015. The influence of a model subglacial lake on ice dynamics and internal layering. The Cryosphere, 9(1), pp. 3859-3886. doi: 10.5194/tcd-9-3859-2015.

Guo, H., Liu, H., Wang, X., Shao, Y. & Sun, Y., 2000. Subsurface old drainage detection and paleoenvironment analysis using spaceborne radar images in Alxa Plateau. *Science in China Series D: Earth Sciences*, 43(4), pp.439–448. doi: 10.1007/BF02959455.

Hamilton, V.E., McSween, H.Y. & Hapke, B., 2005. Mineralogy of Martian atmospheric dust inferred from thermal infrared spectra of aerosols. *Journal of Geophysical Research: Planets*, 110(E12).

Hamling, I. ~J. & Aoudia, A., 2011. Interaction between the North-West Sahara Aquifer and the seismically active intraplate Hun Graben Fault system, Libya. *AGU Fall Meeting Abstracts*, pp. A1185.

Hargraves, R.B., Collinson, D.W., Arvidson, R.E. & Spitzer, C.R., 1977. The Viking magnetic properties experiment: Primary mission results. *Journal of*

Geophysical Research, 82(28), pp.4547–4558. doi: 10.1029/JS082i028p04547.

Hartmann, W.K. & Berman, D.C., 2000. Elysium Planitia lava flows: Crater count chronology and geological implications. *Journal of Geophysical Research*, 105(E6), pp.15011–15025.

Heggy, E., Paillou, P., Ruffié, G., Malezieux, J.M., Costard, F. & Grandjean, G., 2001. On water detection in the Martian subsurface using sounding radar. *Icarus*, 154(2), pp.244–257. doi: 10.1006/icar.2001.6717.

Herkenhoff, K.E., Byrne, S., Russell, P.S., Fishbaugh, K.E. & McEwen, A.S., 2007. Meter-scale morphology of the north polar region of Mars. *Science*, 317(5845), pp.1711–1715. doi: 10.1126/science.1143544.

Hoffmann, J. & Walter, D., 2006. How complementary are SRTM-X and -C band digital elevation models? *Photogrammetric Engineering & Remote Sensing*, 72(3), pp.261–268.

Holschuh, N., Parizek, B.R., Alley, R.B. & Anandakrishnan, S., 2017. Decoding ice sheet behavior using englacial layer slopes. *Geophysical Research Letters*, 44(11), pp.5561–5570. doi: 10.1002/2017GL073417.

Holt, J.W., Safaeinili, A., Plaut, J.J., Head, J.W., Phillips, R.J., Seu, R., Kempf, S.D., Choudhary, P., Young, D.A., Putzig, N.E. & Biccari, D., 2008. Radar Sounding Evidence for Buried Glaciers in the Southern Mid-Latitudes of Mars. *Science*, 322(November), pp.21–23. doi: 10.1126/science.1164246.

Holt, J.W., Fishbaugh, K.E., Byrne, S., Christian, S., Tanaka, K., Russell, P.S., Herkenhoff, K.E., Safaeinili, A., Putzig, N.E. & Phillips, R.J., 2010. The construction of Chasma Boreale on Mars. *Nature*, 465(7297), pp.446–449. doi: 10.1038/nature09050.

Huang, C., Davis, L.S. & Townshend, J.R.G., 2002. An assessment of support vector machines for land cover classification. *International Journal of Remote Sensing*, 23(4), pp.725–749. doi: 10.1080/01431160110040323.

Lauro, S.E., Mattei, E., Soldovieri, F., Pettinelli, E., Orosei, R. & Vannaroni, G., 2012. Dielectric constant estimation of the uppermost Basal Unit layer in the martian Boreales Scopuli region. *Icarus*, 219(1), pp.458–467. doi: 10.1016/j.icarus.2012.03.011.

Ilyushin, Y.A., 2004. Martian northern polar cap: Layering and possible implications for radar sounding. *Planetary and Space Science*, 52(13), pp.1195–1207. doi: 10.1016/j.pss.2004.08.002.

Iorio, M., Mecozzi, R., Seu, R., Picardi, G. & Fois, F., 2007. GPR Missions on Mars. In *Proceedings of IEEE International Geoscience and Remote Sensing Symposium (IGARSS)*, July 23-28, 2007 in Barcelona, Spain, pp.4095–4100. doi: 10.1109/IGARSS.2007.4423750

Jaeger, W.L., Keszthelyi, L.P., McEwen, A.S., Dundas, C.M. & Russell, P.S., 2007. Athabasca Valles, Mars: A lava-draped channel system. *Science*, 317(5845), pp.1709–1711. doi: 10.1126/science.1143315.

Jolivet, R., Grandin, R., Lasserre, C., Doin, M.P. & Peltzer, G., 2011. Systematic InSAR tropospheric phase delay corrections from global meteorological reanalysis data. *Geophysical Research Letters*, 38(17). doi: 10.1029/2011GL048757.

Jordan, R., Picardi, G., Plaut, J., Wheeler, K., Kirchner, D., Safaeinili, A., Johnson, W., Seu, R., Calabrese, D., Zampolini, E. & Cicchetti, A., 2009. The Mars express MARSIS sounder instrument. *Planetary and Space Science*, 57(14), pp.1975–1986. doi: 10.1016/j.pss.2009.09.016.

Kääb, A., Berthier, E., Nuth, C., Gardelle, J. & Arnaud, Y., 2012. Contrasting patterns of early twenty-first-century glacier mass change in the Himalayas. *Nature*, 488(7412), pp.495–498.

Kääb, A., Treichler, D., Nuth, C. & Berthier, E., 2015. Brief Communication: Contending estimates of 2003-2008 glacier mass balance over the Pamir–Karakoram–Himalaya. *The Cryosphere*, 9(2), pp.557–564. doi: 10.5194/tc-9-557-2015.

Kampes, B. & Usai, S., 1999. Doris: the Delft Object-oriented Radar Interferometric Software. In *Proceedings of International Symposium on Operationalization of Remote Sensing*, August 16-20, 1999 in Enschede, The Netherlands.

Karlsson, N. & Holt, J., 2011. Testing for flow in the north polar layered deposits of Mars using radar stratigraphy and a simple 3D ice‐flow model. *Geophysical Research Letters*, 38(24). doi: 10.1029/2011GL049630.

Karlsson, N.B., Rippin, D.M., Bingham, R.G. & Vaughan, D.G., 2012. A “continuity-index” for assessing ice-sheet dynamics from radar-sounded internal layers. *Earth and Planetary Science Letters*, 335–336, pp.88–94. doi: 10.1016/j.epsl.2012.04.034.

Keisling, B.A., Christianson, K., Alley, R.B., Peters, L.E., Christian, J.E., Anandakrishnan, S., Riverman, K.L., Muto, A. and Jacobel, R.W., 2014. Basal conditions and ice dynamics inferred from radar-derived internal stratigraphy of the northeast Greenland ice stream. *Annals of Glaciology*, 55(67), pp.127-137. doi: 10.3189/2014AoG67A090.

Kekonen, T., Moore, J., Perämäki, P. and Martma, T., 2005. The Icelandic Laki volcanic tephra layer in the Lomonosovfonna ice core, Svalbard. *Polar Research*, 24(1‐2), pp.33-40. doi: 10.1111/j.1751-8369.2005.tb00138.x.

Kelly, N.J., Boynton, W.V., Kerry, K., Hamara, D., Janes, D., Reedy, R.C., Kim, K.J. and Haberle, R.M., 2007. Seasonal polar carbon dioxide frost on Mars: CO_2 mass and columnar thickness distribution. *Journal of Geophysical Research: Planets*, 112(3), pp.1–12. doi: 10.1029/2006JE002678.

Keszthelyi, L., McEwen, A.S., Thordarson, T., 2000. Terrestrial analogs and thermal models for Martian flood lavas. *J. Geophys. Res*., 105 (E6), 15027–15050. doi: 10.1029/1999JE001191.

Kieffer, H.H., 1979. Mars south polar spring and summer temperatures: A residual CO 2 frost. *Journal of Geophysical Research*, 84(B14), pp.8263-8288. doi: 10.1029/JB084iB14p08263.

Kieffer, H.H., 1990. H_20 Grain Size and the Amount of Dust in Mars' Residual North Polar Cap, *Journal of Geophysical Research*, 95(B2), pp.1481–1493. doi: 10.1029/JB095iB02p01481.

Kim, J.R. & Muller, J.P., 2008. Very high resolution stereo DTM extraction and its application to surface roughness estimation over Martian surface. *International Archives of the Photogrammetry, Remote Sensing and Spatial Information Sciences (ISPRS)*, 37(B4), pp.993–998.

Kim, J.R. & Muller, J.P., 2009. Multi-resolution topographic data extraction from Martian stereo imagery. Planetary and Space Science 57, 2095-2112. doi: 10.1016/j.pss.2009.09.024.

Kleuskens, M. H. P. & Oosthoek, J. H. P., 2009. 3D interpretation of SHARAD radargram data using seismic processing routines. *EGU General Assembly 2009*.

Kolb, E.J. & Tanaka, K.L., 2001. Geologic history of the polar regions of Mars based on Mars Global surveyor data: II. Amazonian period. *Icarus*, 154(1), pp.22–39. doi: 10.1006/icar.2001.6676.

Kolb, E.J. & Tanaka, K.L., 2006. Accumulation and erosion of south polar layered deposits in the Promethei Lingula region, Planum Australe. *The International Journal of Mars Science and Exploration*, 2, pp. 1-9. doi: 10.1555/mars.2006.0001.

Kovesi, P., 1999. Phase preserving denoising of images. *Signal*, 4(1), pp.1–6. Available at: http://www.peterkovesi.com/papers/denoise.pdf [Accessed January 18, 2017].

Lasne, Y., Paillou, P., August-Bernex, T., Ruffié, G. & Grandjean, G., 2004. A phase signature for detecting wet subsurface structures using polarimetric L-band SAR. *IEEE Transactions on Geoscience and Remote Sensing*, 42(8), pp.1683–1694. doi: 10.1109/TGRS.2004.830645.

Lasne, Y., Paillou, P., Freeman, A., Farr, T., McDonald, K., Ruffié, G., Malézieux, J.M. & Chapman, B., 2009. Study of hypersaline deposits and analysis of their signature in airborne and spaceborne SAR Data: Example of Death Valley, California. *IEEE Transactions on Geoscience and Remote Sensing*, pp.2581–2598. doi: 10.1109/TGRS.2009.2014862.

Lee, C. & Wang, S., 1999. Fingerprint feature extraction using Gabor filters. *Electronics Letters*, 35(4), pp. 288-290. doi: 10.1049/el:19990213.

Lefort, A., Russell, P.S. & Thomas, N., 2010. Scalloped terrains in the Peneus and Amphitrites Paterae region of Mars as observed by HiRISE. *Icarus*, 205(1), pp.259–268. doi: 10.1016/j.icarus.2009.06.005.

Leuschen, C. & Allen, C., 2011. IceBridge MCoRDS L1B geolocated radar echo strength profiles, version 1. Boulder, Colorado USA. NASA National Snow and Ice Data Center Distributed Active Archive Center. Available at: http://dx.doi.org/10.5067/WVDXEKH0X7N3.

Leuschen, C., Gogineni, P., Hale, R., Paden, J., Rodriguez, F., Panzer, B. & Gomez, D., 2014. IceBridge MCoRDS L1B geolocated radar echo strength profiles, version 2. Boulder, Colorado USA: National Snow and Ice Data Center. Available at: http://dx.doi.org/10.5067/90S1XZRBAX5N.

Leysinger Vieli, G.J.-M.C., Siegert, M.J. & Payne, A.J., 2004. Reconstructing ice-sheet accumulation rates at ridge B, East Antarctica. *Annals of Glaciology*, 39(1), pp.326–330. doi: 10.3189/172756404781814519.

Leysinger Vieli, G.J.-M.C., Hindmarsh, R.C.A. & Siegert, M.J., 2007. Three-dimensional flow influences on radar layer stratigraphy, *Annals of Glaciology*, 46(1), pp. 22-28.

Li, G. & Lin, H., 2017. Recent decadal glacier mass balances over the Western Nyainqentanglha Mountains and the increase in their melting contribution to Nam Co Lake measured by differential bistatic SAR interferometry. *Global*

and Planetary Change, 149, pp.177–190. doi: 10.1016/j.gloplacha.2016.12.018.

Li, J., Andrews-Hanna, J.C., Sun, Y., Phillips, R.J., Plaut, J.J. & Zuber, M.T., 2012. Density variations within the south polar layered deposits of Mars, *Journal of Geophysical Research*, 117(E04006), pp.1–13. doi: 10.1029/2011JE003937.

Li, Z., Fielding, E.J., Cross, P. & Preusker, R., 2009. Advanced InSAR atmospheric correction: MERIS/MODIS combination and stacked water vapour models. *International Journal of Remote Sensing*, 30(13), pp.3343–3363. doi: 10.1080/01431160802562172.

Li, Z., Muller, J.P. & Cross, P., 2003. Comparison of precipitable water vapor derived from radiosonde, GPS, and Moderate-Resolution Imaging Spectroradiometer measurements. *Journal of Geophysical Research Atmospheres*, 108(20), pp. 4651. doi: 10.1029/2003JD003372.

Liu, C.A., Gong, H., Shao, Y. & Li, B., 2015. Detecting the depth of a subsurface brine layer in Lop Nur Lake Basin using polarimetric L-Band SAR. *Journal of Sensors*, 2015, pp.1–11. doi: 10.1155/2015/245790.

Liu, C., Song, C. & Lu, Q., 2017. Random noise de-noising and direct wave eliminating based on SVD method for ground penetrating radar signals. *Journal of Applied Geophysics*, 144, pp.125–133.

LP DAAC, 2014. SRTMIMGM: NASA Shuttle Radar Topography Mission Combined Image Data Set V003 [Online]. Available at: https://lpdaac.usgs.gov/dataset_discovery/measures/measures_products_table/srtmimgm_v003. [Accessed January 04, 2018].

Lüning, S., Craig, J., Fitches, B., Mayouf, J., Busrewil, A., El Dieb, M., Gammudi, A., Loydell, D. & McIlroy, D., 1999. Re-evaluation of the petroleum potential of the Kufra Basin (SE Libya, ne Chad): does the source rock barrier fall? *Marine and Petroleum Geology*, 16(7), pp.693–718. doi: 10.1016/S0264-8172(99)00013-6.

MacDonald, A.M., Bonsor, H.C., Calow, R.C., Taylor, R.G., Lapworth, D.J., Maurice, L., Tucker, J. & O Dochartaigh, B.E., 2011. Groundwater resilience to climate change in Africa [Online]. Available at: http://nora.nerc.ac.uk/id/eprint/17510/1/ClimateChangeGW.pdf.

MacGregor, J.A., Fahnestock, M.A., Catania, G.A., Paden, J.D., Prasad Gogineni, S., Young, S.K., Rybarski, S.C., Mabrey, A.N., Wagman, B.M. & Morlighem, M., 2015a. Radiostratigraphy and age structure of the Greenland Ice Sheet. *Journal of Geophysical Research: Earth Surface*, 120, pp.212–241. doi: 10.1002/2014JF003215.

MacGregor, J.A., Fahnestock, M.A., Catania, G.A., Paden, J.D., Prasad Gogineni, S., Young, S.K., Rybarski, S.C., Mabrey, A.N., Wagman, B.M. & Morlighem, M., 2015b. Radiostratigraphy and age structure of the Greenland Ice Sheet, Version 1. Boulder, Colorado USA. NASA National Snow and Ice Data

Center Distributed Active Archive Center. Available at: http://dx.doi.org/10.5067/UGI2BGTC4QJA.

Maher, B.A., Mutch, T.J. & Cunningham, D., 2009. Magnetic and geochemical characteristics of Gobi Desert surface sediments: Implications for provenance of the Chinese Loess Plateau. Geology, 37(3), pp.279-282. doi: 10.1130/G25293A.1.

Malin, M.C. & Edgett, K.S., 2001. Mars Global Surveyor Mars Orbiter Camera: Interplanetary cruise through primary mission. *Journal of Geophysical Research: Planets*, 106(E10), pp.23429–23570. doi: 10.1029/2000JE001455.

Marschalk, U., Roth, A., Eineder, M. & Suchandt, S., 2004. Comparison of DEMs derived from SRTM/X-and C-Band. In *Proceedings of IEEE International Geoscience and Remote Sensing Symposium (IGARSS)*, 2004, Anchorage, AK, USA, pp. 4531–4534. doi: 10.1109/IGARSS.2004.1370162

Massonnet, D. & Feigl, K.L., 1998. Radar interferometry and its application to changes in the Earth's surface. *Reviews of Geophysics*, 36(4), pp.441–500. doi: 10.1029/97RG03139.

Mattei, E., Lauro, S.E., Vannaroni, G., Cosciotti, B., Bella, F. & Pettinelli, E., 2014. Dielectric measurements and radar attenuation estimation of ice / basalt sand mixtures as martian Polar Caps analogues. *Icarus*, 229, pp.428–433. doi: 10.1016/j.icarus.2013.10.017.

Mätzler, C., 1998. Microwave Permittivity of Dry Sand. *IEEE Transactions on Geoscience and Remote Sensing*, 36(1), pp.317–319. doi: 10.1109/36.655342.

McCauley, J.F., Schaber, G.G., Breed, C.S., Grolier, M.J., Haynes, C.V., Issawi, B., Elachi, C. & Blom, R., 1982. Subsurface valleys and geoarcheology of the eastern Sahara revealed by Shuttle Radar. *Science*, 218(4576), pp.1004–1020. doi: 10.1126/science.218.4576.1004.

McCauley, J.F., Breed, C.S., Schaber, G.G., McHugh, W.P., Issawi, B., Haynes, C.V., Grolier, M.J. & El Kilani, A., 1986. Paleodrainages of the Eastern Sahara-The Radar Rivers Revisited (SIR-A/B Implications for a Mid-Tertiary Trans-African Drainage System). *IEEE Transactions on Geoscience and Remote Sensing*, GE-24(4), pp.624–648. doi: 10.1109/TGRS.1986.289678.

McEwen, A.S., Edgett, K.S., Malin, M.C., Keszthelyi, L., Lanagan, P.D., 1998. Mars Global Surveyor camera tests the Elysium Basin controversy: it's lava, not lake sediments, *Geol. Soc. Am. Abstr. Prog.,* 30 (7).

Medley, B., Ligtenberg, S.R.M., Joughin, I., Van den Broeke, M.R., Gogineni, S. & Nowicki, S., 2015. Antarctic firn-compaction rates from repeat-track airborne radar data: I. Methods. *Annals of Glaciology*, 56(70), pp. 155-165. doi: 10.3189/2015AoG70A203.

Milkovich, S.M. & Plaut, J.J., 2008. Martian South Polar Layered Deposit stratigraphy and implications for accumulation history. *Journal of*

Geophysical Research: Planets, 113(E04002), pp. 1-11. doi: 10.1029/2007JE002974.

Milkovich, S.M., Plaut, J.J., Safaeinili, A., Picardi, G., Seu, R. & Phillips, R.J., 2009. Stratigraphy of Promethei Lingula, south polar layered deposits, Mars, in radar and imaging data sets. *Journal of Geophysical Research*, 114(E03002), pp. 1-12. doi: 10.1029/2008JE003162.

Morgan, G.A., Campbell, B.A., Carter, L.M., Plaut, J.J. & Phillips, R.J., 2013. 3D reconstruction of the source and scale of buried young flood channels on Mars. *Science*, 340(6132), pp. 607-610. doi: 10.1126/science.1234787.

Morlighem, M., Rignot, E., Mouginot, J., Seroussi, H. & Larour, E., 2015. IceBridge Bedmachine Greenland, version 2. Boulder, Colorado USA: NASA DAAC at the National Snow and Ice Data Center.

Mouginot, J., Kofman, W., Safaeinili, A., Grima, C., Hérique, A. & Plaut, J.J., 2009. MARSIS surface reflectivity of the south residual cap of Mars. *Icarus*, 201(2), pp.454–459. doi: 10.1016/j.icarus.2009.01.009.

Mouginot, J., Pommerol, A., Kofman, W., Beck, P., Schmit, B., Herique, A., Grima, C. Safaeinili, A. & Plaut, J.J., 2010. The 3 – 5 MHz global reflectivity map of Mars by MARSIS / Mars Express: Implications for the current inventory of subsurface H_2O. *Icarus*, 210(2), pp.612–625. doi: 10.1016/j.icarus.2010.07.003.

Munir, M. & Javed, M., 2004. Fingerprint matching using Gabor filters. In *Proceedings of National Conference on Emerging Technologies*. National Conference on Emerging. Available at: https://pdfs.semanticscholar.org/b699/d9737eb58ad4b2700ca4597365cde0a7703c.pdf. [Accessed January 23, 2017].

Murray, B.C., Soderblom, L.A., Cutts, J.A., Sharp, R.P., Milton, D.J. and Leighton, R.B., 1972. Geological framework of the south polar region of Mars. *Icarus*, 17(2), pp.328-345.

Murray, J.B., Muller, J.P., Neukum, G., Werner, S.C., van Gasselt, S., Hauber, E., Markiewicz, W.J., Head, J.W., Foing, B.H., Page, D. & Mitchell, K.L., 2005. Evidence from the Mars Express High Resolution Stereo Camera for a frozen sea close to Mars' equator. *Nature*, 434(7031), pp.352–356. doi: 10.1038/nature03379

NEEM Community Members, 2013. Eemian interglacial reconstructed from a Greenland folded ice core. *Nature*, 493(7433), pp.489–494. doi: doi:10.1038/nature11789.

Nouvel, J.F., Martelat, J.E., Herique, A. & Kofman, W., 2006. Top layers charaterization of the Martian surface: Permittivity estimation based on geomorphology analysis. *Planetary and Space Science*, 54(4), pp.337–344. doi: 10.1016/j.pss.2005.12.013.

Onana, V., Koenig, L.S., Ruth, J., Studinger, M. & Harbeck, J.P., 2015. A semiautomated multilayer picking algorithm for ice-sheet radar echograms

applied to ground-based near-surface data. *IEEE Transactions on Geoscience and Remote Sensing*, 53(1), pp.51–69. doi: 10.1109/TGRS.2014.2318208.

Orosei, R., Cartacci, M., Cicchetti, A., Noschese, R., Federico, C., Frigeri, A., Flamini, E., Holt, J.W., Marinangeli, L., Pettinelli, E. & Phillips, R.J., 2007. Radar subsurface sounding over the putative frozen sea in Cerberus Palus, Mars. *AGU Fall Meeting Abstracts*, pp.1–4. doi: 10.1109/ICGPR.2010.5550143.

Orosei, R., Lauro, S.E., Pettinelli, E., Cicchetti, A., Coradini, M., Cosciotti, B., Di Paolo, F., Flamini, E., Mattei, E., Pajola, M. & Soldovieri, F., 2018. Radar evidence of subglacial liquid water on Mars. Science, 361(6401), pp.490-493.

Orosei, R., Jordan, R.L., Morgan, D.D., Cartacci, M., Cicchetti, A., Duru, F., Gurnett, D.A., Heggy, E., Kirchner, D.L., Kofman, W., Masdea, A., Plaut, J.J., Seu, R., Watters, T.R., Picardi, G., 2015. Mars Advanced Radar for Subsurface and Ionospheric Sounding (MARSIS) after nine years of operation: A summary. *Planetary and Space Science*, 112, pp.98–114. doi: 10.1016/j.pss.2014.07.010.

Paillou, P., Grandjean, G., Baghdadi, N., Heggy, E., August-Bernex, T. & Achache, J., et al., 2003. Subsurface imaging in south-central Egypt using low-frequency radar: Bir Safsaf revisited. *IEEE Transactions on Geoscience*

and Remote Sensing, 41(7), pp.1672–1684. doi: 10.1109/TGRS.2003.813275.

Paillou, P., Lopez, S., Farr, T. & Rosenqvist, A., 2010. Mapping subsurface geology in Sahara using L-Band SAR: First results from the ALOS/PALSAR imaging radar. *IEEE Journal of Selected Topics in Applied Earth Observations and Remote Sensing*, 3(4), pp.632–636. doi: 10.1109/JSTARS.2010.2056915.

Paillou, P., Reynard, B., Malézieux, J.M., Dejax, J., Heggy, E., Rochette, P., Reimold, W.U., Michel, P., Baratoux, D., Razin, P. & Colin, J.P., 2006. An extended field of crater-shaped structures in the Gilf Kebir region, Egypt: Observations and hypotheses about their origin. *Journal of African Earth Sciences*, 46(3), pp.281–299. doi: 10.1016/j.jafrearsci.2006.05.006.

Paillou, P. & Rosenqvist, A., 2003. A JERS-1 radar mosaic for subsurface geology mapping in East Sahara. In *Proceedings of IEEE Geoscience and Remote Sensing Symposium*, Vol. 3, pp. 1870-1872, Toulouse, France, 21-25 July 2003. doi: 10.1109/IGARSS.2003.1294277.

Paillou, P., Rosenqvist, A., Malezieux, J.M., Reynard, B., Farr, T. & Heggy, E., 2003. Discovery of a double impact crater in Libya: the astrobleme of Arkenu. *Comptes Rendus Geoscience*, 335(15), pp.1059–1069. doi: 10.1016/j.crte.2003.09.008.

Paillou, P., Schuster, M., Tooth, S., Farr, T., Rosenqvist, A., Lopez, S. & Malezieux, J.M., 2009. Mapping of a major paleodrainage system in eastern

Libya using orbital imaging radar: the Kufrah River. *Earth and Planetary Science Letters*, 277(3), pp.327–333. doi: 10.1016/j.epsl.2008.10.029.

Paillou, P., Sufyar, S. & Freeman, A., 2014. The Chott El Djerid, Tunisia: Observation and discussion of a SAR phase signature over evaporitic soils. *IEEE Transactions on Geoscience and Remote Sensing*, 52(9), pp.5798–5806. doi: 10.1109/TGRS.2013.2292822.

Palmer, S.J., Dowdeswell, J.A., Christoffersen, P., Young, D. A., Blankenship, D.D., Greenbaum, J.S., Benham, T., Bamber, J. & Siegert, M.J., 2013. Greenland subglacial lakes detected by radar. *Geophysical Research Letter*, 40, pp. 6154-6159. doi: 10.1002/2013GL058383.

Panton, C., 2014. Automated mapping of local layer slope and tracing of internal layers in radargrams. *Annals of Glaciology*, 55(67), pp.71–77. doi: 10.3189/2014AoG67A048.

Panton, C. & Karlsson, N.B., 2015. Automated mapping of near bed radio-echo layer disruptions in the Greenland Ice Sheet. *Earth and Planetary Science Letters*, 432, pp.323–331. doi: 10.1016/j.epsl.2015.10.024.

Papathanassiou, K.P. & Cloude, S.R., 2001. Single-baseline polarimetric SAR interferometry. *IEEE Transactions on Geoscience and Remote Sensing*, 39(11), pp.2352–2363. doi: 10.1109/36.964971.

Phillips, R.J., Davis, B.J., Tanaka, K.L., Byrne, S., Mellon, M.T., Putzig, N.E., Haberle, R.M., Kahre, M.A., Campbell, B.A., Carter, L.M. & Smith, I.B., 2011.

Massive CO_2 ice deposits sequestered in the South Polar Layered Deposits of Mars. *Science*, 332(6031), pp.838–841. doi: 10.1126/science.1203091.

Phillips, R.J., Zuber, M.T., Smrekar, S.E., Mellon, M.T., Head, J.W., Tanaka, K.L., Putzig, N.E., Milkovich, S.M., Campbell, B.A., Plaut, J.J. & Safaeinili, A., 2008. Mars north polar deposits: Stratigraphy, age, and geodynamical response. *Science*, 320(5880), pp.1182–1186. doi: 10.1126/science.1157546.

Picardi, G., Biccari, D., Cartacci, M., Cicchetti, A., Giuppi, S., Marini, A., Masdea, A., Noschese, R., Piccari, F., Seu, R. & Bombaci, O., 2007. MARSIS data inversion approach. In *Proceedings of the 4th IEEE International Workshop on Advanced Ground Penetrating Radar*, June 27-29, 2007 in Aula Magna Partenope, Italy, pp. 256–260. doi: 10.1109/AGPR.2007.386563.

Picardi, G., Plaut, J.J., Biccari, D., Bombaci, O., Calabrese, D., Cartacci, M., Cicchetti, A., Clifford, S.M., Edenhofer, P., Farrell, W.M. and Federico, C., 2005. Radar soundings of the subsurface of Mars. science, 310(5756), pp.1925-1928. doi: 10.1126/science.1122165.

Plaut, J.J., Picardi, G., Safaeinili, A., Ivanov, A.B., Milkovich, S.M., Cicchetti, A., Kofman, W., Mouginot, J., Farrell, W.M., Phillips, R.J. & Clifford, S.M., 2007. Subsurface radar sounding of the south polar layered deposits of Mars. *Science*, 316(5821), pp.92–95. doi: 10.1126/science.1139672.

Plaut, J.J., Safaeinili, A., Campbell, B.A., Phillips, R.J., Putzig, N.E., Nunes, D.C. & Seu, R., 2009. A widespread radar-transparent layer detected by

SHARAD in Arcadia Planitia, Mars. In *Proceedings of the 40th Lunar and Planetary Science Conference, (Lunar and Planetary Science XL)*, March 23-27, 2009 in The Woodlands, Texas.

Plaut, J.J., Safaeinili, A., Holt, J.W., Phillips, R.J., Campbell, B.A., Carter, L.M., Leuschen, C., Gim, Y., Seu, R. & Team, S., 2009. Radar evidence for ice in lobate debris aprons in the mid-northern latitudes of Mars. *Geophysical Research Letters*, 36(2). doi: 10.1029/2008GL036379.

Plescia, J.B., 2003. Cerberus Fossae, Elysium, Mars: a source for lava and water. *Icarus*, 164, 79–95. doi: 10.1016/S0019-1035(03)00139-8.

Porcello, L.J., Jordan, R.L., Zelenka, J.S., Adams, G.F., Phillips, R.J., Brown, W.E., Ward, S.H. & Jackson, P.L., 1974. The Apollo lunar sounder radar system. In *Proceedings of the IEEE*, 62(6), pp.769–783. doi: 10.1109/PROC.1974.9517.

Putzig, N.E., Holt, J.W., Phillips, R.J., Seu, R., Biccari, D., Campbell, B.A., Carter, L.M., Safaeinili, A. & Egan, A.F., 2007. Internal structure of the north polar layered deposits on mars from SHARAD observations. *AGU Fall Meeting*. Available at: http://adsabs.harvard.edu/abs/2007AGUFM.P11B0544P [Accessed January 13, 2017].

Putzig, N.E., Phillips, R.J., Campbell, B.A., Holt, J.W., Plaut, J.J., Carter, L.M., Egan, A.F., Bernardini, F., Safaeinili, A. & Seu, R., 2009. Subsurface structure of Planum Boreum from Mars Reconnaissance Orbiter Shallow

Radar soundings. *Icarus*, 204(2), pp.443–457. doi: 10.1016/j.icarus.2009.07.034.

Putzig, N.E., Phillips, R.J., Campbell, B.A. & Foss, F.J., 2010. Imaging the subsurface structure of Planum Boreum with the Mars Reconnaissance Orbiter Shallow Radar. In *Proceedings of the 13th Internarional Conference on Ground Penetrating Radar*, June 21-25, 2010 in Lecce, Italy, Italy. doi: 10.1109/ICGPR.2010.5550144.

Putzig, N.E., Phillips, R.J., Campbell, B.A., Mellon, M.T., Holt, J.W. & Brothers, T.C., 2014. SHARAD soundings and surface roughness at past, present, and proposed landing sites on Mars: Reflections at Phoenix may be attributable to deep ground ice. *Journal of Geophysical Research: Planets*, 119(8), pp.1936–1949. doi: 10.1002/2014JE004646.

Rasmussen, S.O., Abbott, P.M., Blunier, T., Bourne, A.J., Brook, E., Buchardt, S.L., Buizert, C., Chappellaz, J., Clausen, H.B., Cook, E. & Dahl-Jensen, D., 2013. A first chronology for the north Greenland Eemian ice drilling (NEEM) ice core. *Climate of the Past*, 9(6), pp.2713–2730. doi: 10.5194/cp-9-2713-2013.

Raynaud, D., Jouzel, J., Barnola, J.M., Chappellaz, J., Delmas, R.J. and Lorius, C., 1993. The ice record of greenhouse gases. *Science*, pp.926-934.

Reppert, P.M., Morgan, F.D. & Toksöz, M.N., 2000. Dielectric constant determination using ground-penetrating radar reflection coefficients. *Journal of Applied Geophysics*, 43, pp.189-197. doi: 10.1119/1.2344083.

Rice Jr, J.W., Parker, T.J., Russell, A.J. and Knudsen, O., 2002. Morphology of fresh outflow channel deposits on Mars. In *Proceedings of 33rd Lunar and Planetary Science Conference*, 33, abstract #2026, March 11-15, 2002, Houston, Texas.

Rignot, E., Echelmeyer, K. & Krabill, W., 2001. Penetration depth of interferometric synthetic-aperture radar signals in snow and ice. *Geophysical Research Letters*, 28(18), pp.3501–3504. doi: 10.1029/2000GL012484.

Rippin, D.M., Siegert, M.J., Bamber, J.L., Vaughan, D.G. & Corr, H.F., 2006. Switch-off of a major enhanced ice flow unit in East Antarctica. *Geophysical Research Letters*, 33(15), pp. 1-6. doi: 10.1029/2006GL026648.

Robinson, C., El-Baz, F., Ozdogan, M., Ledwith, M., Blanco, D., Oakley, S. & Inzana, J., 2000. Use of radar data to delineate palaeodrainage flow directions in the Selima Sand Sheet, Eastern Sahara. *Photogrammetric Engineering and Remote Sensing*, 66(6), pp.745–753. Available at: http://asprs.org/a/publications/pers/2000journal/june/2000_jun_745-753.pdf.

Robinson, C.A., El-Baz, F., Al-Saud, T.S.M. & Jeon, S.B., 2006. Use of radar data to delineate palaeodrainage leading to the Kufra oasis in the eastern Sahara. *Journal of African Earth Sciences*, 44(2), pp.229–240. doi: 10.1016/j.jafrearsci.2005.10.012.

Robinson, C.A., Werwer, A., El-Baz, F., El-Shazly, M., Fritch, T. & Kusky, T., 2007. The Nubian aquifer in southwest Egypt. *Hydrogeology Journal*, 15(1), pp.33–45. doi: 10.1007/s10040-006-0091-7.

Rosenqvist, A., Shimada, M., Ito, N. & Watanabe, M., 2007. ALOS PALSAR: A pathfinder mission for global-scale monitoring of the environment. *IEEE Transactions on Geoscience and Remote Sensing*, 45(11), pp.3307–3316. doi: 10.1109/TGRS.2007.901027.

Roth, L.E. & Elachi, C., 1975. Coherent electromagnetic losses by scattering from volume inhomogeneities. *IEEE Transactions on Antennas and Propagation*, 23(5), pp.674–675. doi: 10.1109/TAP.1975.1141170.

Rufino, G., Moccia, A. & Esposito, S., 1998. DEM generation by means of ERS tandem data. *IEEE Transactions on Geoscience and Remote Sensing*, 36(6), pp.1905-1912. 10.1109/36.729362.

Russo, F., Cutigni, M., Orosei, R., Taddei, C., Seu, R., Biccari, D., Giacomoni, E., Fuga, O. & Flamini, E., 2008. An incoherent simulator for the SHARAD experiment. In *Proceedings of Radar Conference*, May 26-30, 2008 in Rome, Italy. doi: 10.1109/RADAR.2008.4720761.

Schaber, G.G., McCauley, J.F., Breed, C.S. & Olhoeft, G.R., 1986. Shuttle imaging radar: Physical controls on signal penetration and subsurface scattering in the eastern Sahara. *IEEE Transactions on Geoscience and Remote Sensing*, GE-24(4), pp.603–623. doi: 10.1109/TGRS.1986.289677.

Schaber, G.G., McCauley, J.F. & Breed, C.S., 1997. The use of multifrequency and polarimetric SIR-C/X-SAR data in geologic studies of Bir Safsaf, Egypt. *Remote Sensing of Environment*, 59(2), pp.337–363. doi: 10.1016/S0034-4257(96)00143-5.

Selvans, M.M., Aharonson, O., Plaut, J.J. & Safaeinili, A., 2009. Structure of the basal unit of the north polar plateau of Mars, from MARSIS. In *Proceedings of IEEE Radar conference*, May 4-8, 2009 in Pasadena, CA, USA. doi: 10.1109/RADAR.2009.4977056.

Seu, R., Biccari, D., Orosei, R., Lorenzoni, L.V., Phillips, R.J., Marinangeli, L., Picardi, G., Masdea, A. & Zampolini, E., 2004. SHARAD: The MRO 2005 shallow radar. *Planetary and Space Science*, 52(1), pp.157–166. doi: 10.1016/j.pss.2003.08.024.

Seu, R., Phillips, R.J., Alberti, G., Biccari, D., Bonaventura, F., Bortone, M., Calabrese, D., Campbell, B.A., Cartacci, M., Carter, L.M. & Catallo, C., 2007. Accumulation and erosion of Mars' south polar layered deposits. *Science*, 317(5845), pp.1715–1719. doi: 10.1126/science.1144120.

Shata, A.A., 1982. Hydrogeology of the great Nubian Sandstone basin, Egypt. *Quarterly Journal of Engineering Geology and Hydrogeology*, 15(2), pp.127-133. doi: 10.1144/GSL.QJEG.1982.015.02.04.

Shi, L., Allen, C.T., Ledford, J.R., Rodriguez-Morales, F., Blake, W.A., Panzer, B.G., Prokopiack, S.C., Leuschen, C.J. & Gogineni, S., 2010. Multichannel coherent radar depth sounder for NASA operation ice bridge. In

Proceedings of IEEE International Geoscience and Remote Sensing Symposium (IGARSS), July 25-30, 2010 in Honolulu, HI, USA, pp. 1729–1732. doi: 10.1109/IGARSS.2010.5649518.

Siegal, B.S. & Gillespie, A.R. eds., 1980. Remote sensing in geology (p. 702). New York: Wiley.

Siegert, M.J. & Kwok, R., 2000. Ice-sheet radar layering and the development of preferred crystal orientation fabrics between Lake Vostok and Ridge B, central East Antarctica. *Earth and Planetary Science Letters*, 179(2), pp. 227–235. doi: 10.1016/S0012-821X(00)00121-7.

Sime, L.C., Hindmarsh, R.C.A. & Corr, H., 2011. Automated processing to derive dip angles of englacial radar reflectors in ice sheets. *Journal of Glaciology*, 57(202), pp.260–266. doi: 10.3189/002214311796405870.

Simon, M.N., Carter, L.M., Campbell, B.A., Phillips, R.J. & Mattei, S., 2014. Studies of lava flows in the Tharsis region of Mars using SHARAD. *Journal of Geophysical Research: Planets*, 119(11), pp.2291–2299. doi: 10.1002/2014JE004666.

Sirmacek, B., Taubenbock, H., Reinartz, P. and Ehlers, M., 2012. Performance evaluation for 3-D city model generation of six different DSMs from air-and spaceborne sensors. *IEEE Journal of Selected Topics in Applied Earth Observations and Remote Sensing*, 5(1), pp.59-70.

Skonieczny, C., Paillou, P., Bory, A., Bayon, G., Biscara, L., Crosta, X., Eynaud, F., Malaizé, B., Revel, M., Aleman, N. & Barusseau, J.P., 2015. African humid periods triggered the reactivation of a large river system in Western Sahara. *Nature communications*, 6(8751), pp.1-6. doi: 10.1038/ncomms9751.

Smith, I., Holt, J. & Christian, S., 2009. Evidence for spiral trough migration and evolution from SHARAD radar observations of stratigraphy within the northern polar layered deposits, Mars. In *Proceedings of Lunar and Planetary Science Coneference*, March 23-27, 2009 in the Woodlands, Texas.

Smith, I.B. & Holt, J.W., 2010. Onset and migration of spiral troughs on Mars revealed by orbital radar. *Nature*, 465(7297), pp.450–453. doi: 10.1038/nature09049.

Smith, I.I.B., Spiga, A. & Holt, J.J.W., 2015. Geomorphology aeolian processes as drivers of landform evolution at the South Pole of Mars. *Geomorphology*, 240(1), pp.54–69. doi: 10.1016/j.geomorph.2014.08.026.

Smith, D.E., Zuber, M.T., Frey, H.V., Garvin, J.B., Head, J.W., Muhleman, D.O., Pettengill, G.H., Phillips, R.J., Solomon, S.C., Zwally, H.J. & Banerdt, W.B., 2001. Mars Orbiter Laser Altimeter: Experiment summary after the first year of global mapping of Mars. *Journal of Geophysical Research: Planets*, 106(E10), pp. 23689–23722. doi: 10.1029/2000JE001364.

Sokolov, K., 2012. Capabilities of the wavelet analysis of GPR data to determine the rock moisture in frozen rock mass. In *Proceedings of the 14th International Conference on Ground Penetrating Radar (GPR)*, June 4-8, 2012 in Shanghai, China, pp. 354–357. doi: 10.1109/ICGPR.2012.6254889

Spagnuolo, M.G., Grings, F., Perna, P., Franco, M., Karszenbaum, H. & Ramos, V.A., 2011. Multilayer simulations for accurate geological interpretations of SHARAD radargrams. *Planetary and Space Science*, 59(11–12), pp.1222–1230. doi: 10.1016/j.pss.2010.10.013

Steger, C., 1998. An unbiased detector of curvilinear structures. *IEEE Transactions on Pattern Analysis and Machine Intelligence*, 20(2), pp.113–125. doi: 10.1109/34.659930.

Sternberg, T. & Paillou, P., 2015. Mapping potential shallow groundwater in the Gobi Desert using remote sensing: Lake Ulaan Nuur. *Journal of Arid Environments*, 118(0), pp.21–27. doi: 10.1016/j.jaridenv.2015.02.020.

Studinger, M., Koenig, L. & Martin, S., 2010. Operation IceBridge: Using instrumented aircraft to bridge the observational gap between ICESat and ICESat-2. In *Proceedings of IEEE Geoscience and Remote Symposium (IGARSS)*, July 25-30, 2010 in Honolulu, HI, USA. doi: 10.1109/IGARSS.2010.5650555.

Stuurman, C.M., Osinski, G.R., Holt, J.W., Levy, J.S., Brothers, T.C., Kerrigan, M. & Campbell, B.A., 2016. SHARAD detection and characterization of

subsurface water ice deposits in Utopia Planitia, Mars. *Geophysical Research Letters*, 43(18), pp.9484–9491. doi: 10.1002/2016GL070138.

Sweldens, W., 1996. The lifting scheme: A custom-design construction of biorthogonal wavelets. *Applied and Computational Harmonic Analysis*, 3(2), pp.186–200. doi: 10.1006/acha.1996.0015

Tanaka, K.L., Rodriguez, J.A. P., Skinner, J.A., Bourke, M.C., Fortezzo, C.M., Herkenhoff, K.E., Kolb, E.J. & Okubo, C.H., 2008. North polar region of Mars: Advances in stratigraphy, structure, and erosional modification. *Icarus*, 196(2), pp.318–358.

Tomasi, C. & Compo, G.P., 1998. A practical guide to wavelet analysis. *Bulletin of the American Meteorological society*, 79, pp. 61-78. doi: 10.1175/1520-0477(1998)079%3C0061:APGTWA%3E2.0.CO;2

Thomas, P.C., Malin, M.C., Edgett, K.S., Carr, M.H., Hartmann, W.K., Ingersoll, A.P., James, P.B., Soderblom, L.A., Veverka, J. & Sullivan, R., 2000. North–south geological differences between the residual polar caps on Mars. *Nature*, 404(6774), pp.161–164. doi: 10.1038/35004528.

Toon, O.B., Pollack, J.B., Ward, W., Burns, J.A. & Bilski, K., 1980. The astronomical theory of climatic change on Mars. *Icarus*, 44(3), pp.552–607. doi: 10.1016/0019-1035(80)90130-X.

Uus, A., Liatsis, P., Slabaugh, G., Anagnostis, A., Roberts, S. and Twist, S., 2016. Trend deviation analysis for automated detection of defects in GPR data for

road condition surveys. In *Proceedings of IEEE International Conference on Systems, Signals and Image Processing (IWSSIP)*, pp. 1-4. doi: 10.1109/IWSSIP.2016.7502765

Waite, A. & Schmidt, S., 1962. Gross Errors in Height Indication from Pulsed Radar Altimeters Operating over Thick Ice or Snow. In *Proceedings of the IRE*, 50(6), pp.1515–1520. doi: 10.1109/JRPROC.1962.288195.

Walker, W.S., Kellndorfer, J. M., LaPoint, E., Hoppus, M. & Westfall, J., 2007. An empirical InSAR-optical fusion approach to mapping vegetation canopy height. *Remote Sensing of Environment*, 109(4), pp.482–499. doi: 10.1016/j.rse.2007.02.001.

Walker, W.S., Kellndorfer, J.M. & Pierce, L.E., 2007. Quality assessment of SRTM C- and X-band interferometric data: Implications for the retrieval of vegetation canopy height. *Remote Sensing of Environment*, 106(4), pp.428–448. doi: 10.1016/j.rse.2006.09.007.

Wang, R., Muller, J.P., Hu, C. & Zeng, T., 2015. Comparison between SRTM-C DEM and ICESat elevation data in the arid Kufrah area. In *Proceedings of IET International Radar Conference*, October 14-16, 2015 in Hangzhou, China, pp. 1–4. doi: 10.1049/cp.2015.1301.

Warner, N.H. & Farmer, J.D., 2008. Importance of aeolian processes in the origin of the north polar chasmata, Mars. *Icarus*, 196(2), pp.368–384.

Watters, T.R., Campbell, B., Carter, L., Leuschen, C.J., Plaut, J.J., Picardi, G., Orosei, R., Safaeinili, A., Clifford, S.M., Farrell, W.M. & Ivanov, A.B., 2007. Radar sounding of the Medusae Fossae Formation Mars: equatorial ice or dry, low-density deposits? *Science*, 318(5853), pp.1125–1128. doi: 10.1126/science.1148112.

Wegmuller, U., Werner, C., Strozzi, T. & Wiesmann, A., 2006. Ionospheric electron concentration effects on SAR and INSAR. In *Proceedings of IEEE International Geoscience and Remote Sensing Symposium (IGARSS)*, July 31-August 4, 2006 in Denver, CO, USA. doi: 10.1109/IGARSS.2006.956.

WINSAR, 2013. Software and DEMs [Online]. Available at https://winsar.unavco.org/software.html. [Accessed January 04, 2018].

Wolff, E.W., Barbante, C., Becagli, S., Bigler, M., Boutron, C.F., Castellano, E., De Angelis, M., Federer, U., Fischer, H., Fundel, F. & Hansson, M., 2010. Changes in environment over the last 800,000 years from chemical analysis of the EPICA Dome C ice core. Quaternary Science Reviews, 29(1), pp.285-295. doi: 10.1016/j.quascirev.2009.06.013.

Wolovick, M.J. & Creyts, T.T., 2016. Overturned folds in ice sheets: Insights from a kinematic model of traveling sticky patches and comparisons with observations. *Journal of Geophysical Research: Earth Surface*, 121(5), pp. 1065–1083. doi: 10.1002/2015JF003698.

Wu, C., Rao, L., Zhang, X., Shi, J. & Liu, S., 2015. Multilayer simulations for Martian subsurface radar soundings. In *Proceedings of IEEE International*

Geoscience and Remote Sensing Symposium (IGARSS), July 26-31, 2015 in Milan Italy, pp. 4300–4303. doi: 10.1109/IGARSS.2015.7326777.

Xiong, S., Zeng, Q., Jiao, J., Gao, S. & Zhang, X., 2014. Improvement of PS-InSAR atmospheric phase estimation by using WRF model. In *Proceedings of IEEE International Geoscience and Remote Sensing Symposium (IGARSS)*, July 13-18, 2014 in Quebec City, QC, Canada, pp. 2225–2228. doi: 10.1109/IGARSS.2014.6946911.

Xiong, S. & Muller, J.-P., 2016. Extraction of ice sheet layers from two intersected radar echograms near NEEM ice core in Greenland. *International Archives of the Photogrammetry, Remote Sensing and Spatial Information Sciences (ISPRS)*, XLI-B7, pp.585–591. doi: 10.5194/isprs-archives-XLI-B7-585-2016.

Zebker, H., & Goldstein, R., 1986. Topographic mapping from interferometric synthetic aperture radar observations. *Journal of Geophysical Research*, 91(B5): pp. 4993–4999. doi: 10.1029/JB091iB05p04993.

Zhang, Z., Hagfors, T., Nielsen, E., Picardi, G., Mesdea, A. & Plaut, J. J., 2008. Dielectric properties of the Martian south polar layered deposits: MARSIS data inversion using Bayesian inference and genetic algorithm. *Journal of Geophysical Research*, 113(E5), pp.1–15. doi: 10.1029/2007JE002941.

Zhu, J., Xue, Y., Zhang, N., Li, Z., Tao, Y. and Qiu, D., 2017, April. A noise reduction method for Ground Penetrating Radar signal based on wavelet

transform and application in tunnel lining. In IOP Conference Series: Earth and Environmental Science (Vol. 61, No. 1, p. 012088). IOP Publishing.

Zwally, H.J., Schutz, B., Abdalati, W., Abshire, J., Bentley, C., Brenner, A., Bufton, J., Dezio, J., Hancock, D., Harding, D. & Herring, T., 2002. ICESat's laser measurements of polar ice, atmosphere, ocean, and land. *Journal of Geodynamics*, 34(3–4), pp.405–445. doi: 10.1016/S0264-3707(02)00042-X.

List of Publications

Journal Papers

Xiong, S., Muller, J.-P. & Li, G., 2017. The application of ALOS/PALSAR InSAR to measure subsurface penetration depths in deserts. *Remote Sensing*, 9(6), pp. 638-660. doi: 10.3390/rs9060638

Xiong, S., Muller, J.-P. and Carretero, R. C., 2017. A New Method for Automatically Tracing Englacial Layers from MCoRDS Data in NW Greenland. *Remote Sensing*, 10(1), pp.43-65. doi: 10.3390/rs10010043

Xiong, S. and Muller, J.-P., 2018. Automated Reconstruction of Subsurface Interfaces near Promethei Lingula in Martian South Pole by using SHARAD Data, *Planetary and Space Science.* doi: 10.1016/j.pss.2018.08.001

Conference Papers

Xiong, S. & Muller, J.-P., 2015. Extraction of subsurface features from InSAR-derived Digital Elevation Models. In European Space Agency, (Special Publication) ESA SP.

Xiong, S. & Muller, J.-P., 2016. Extraction of ice sheet layers from two intersected radar echograms near neem ice core in Greenland. In *International Archives of the Photogrammetry, Remote Sensing and Spatial Information Sciences - ISPRS Archives*, 41, pp. 585-591.

Appendix A

In this appendix, the supplementary figures for the chapter 4 are demonstrated as following.

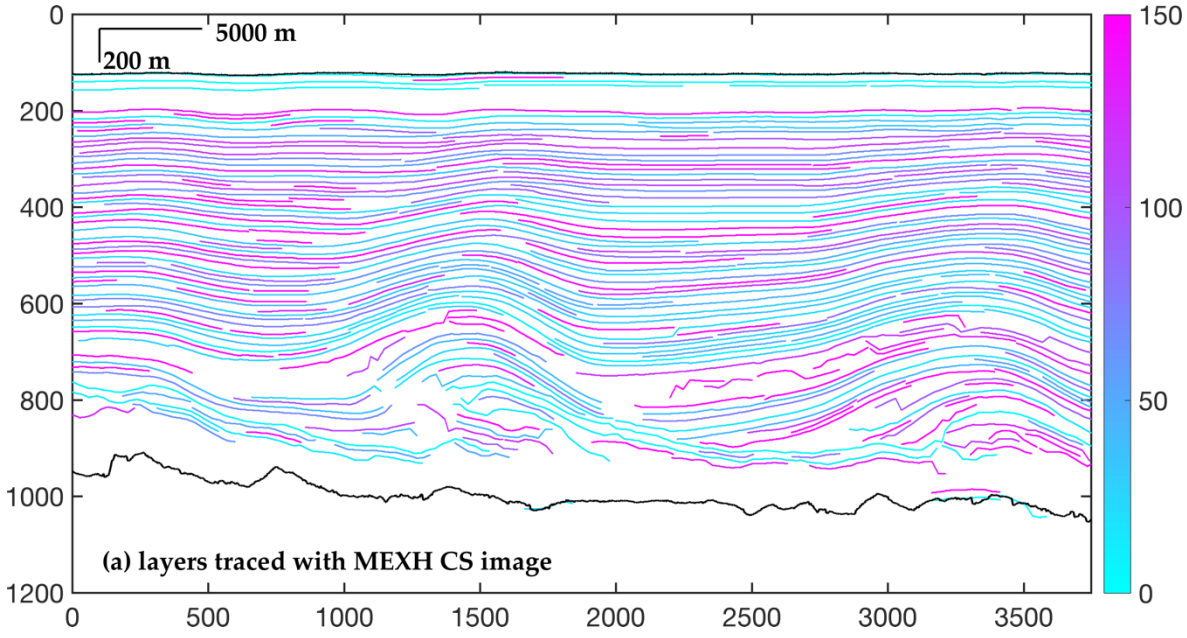

(a)

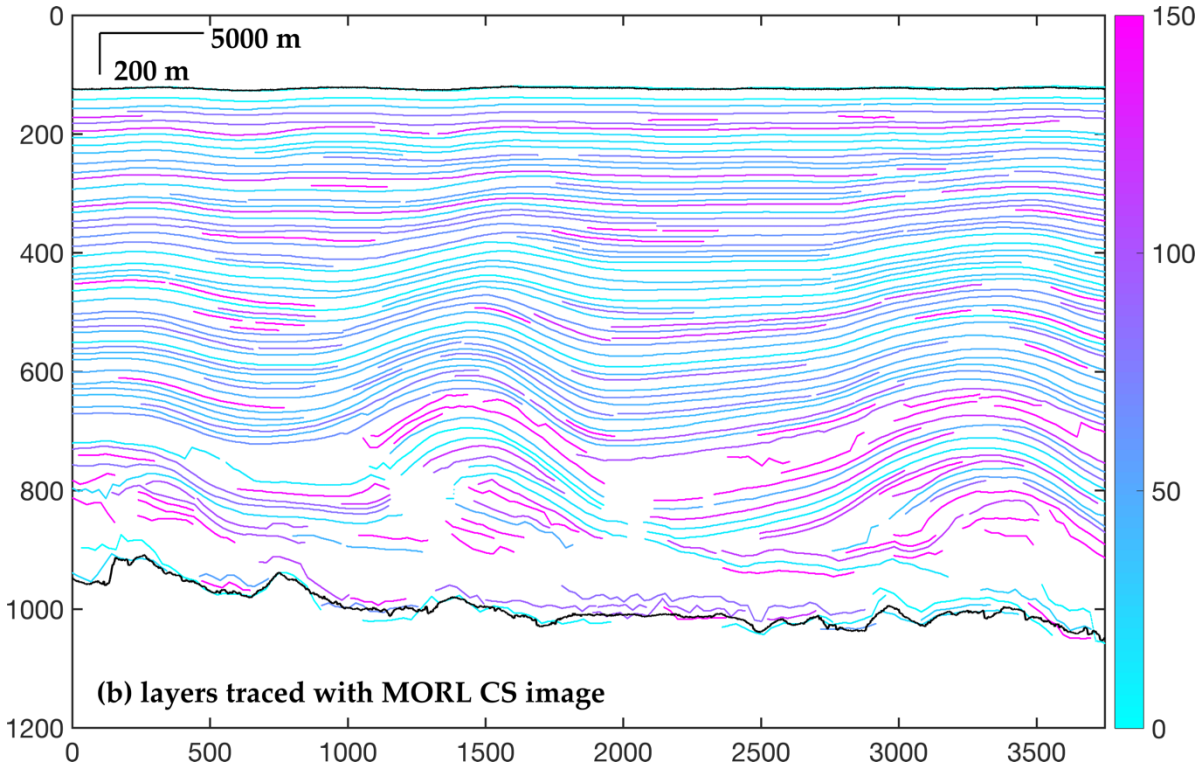

(b)

Figure A1. The outcome layers from layer-tracing procedures with inputs from (a) the MEXH and (b) the MORL CS images CS image independently. Parameters for layer-tracing are a block size of 51 pixels, a maximum distance allowance of 7 pixels and a slope angle difference of 90° (MCoRDS data is 20110329_02_020).

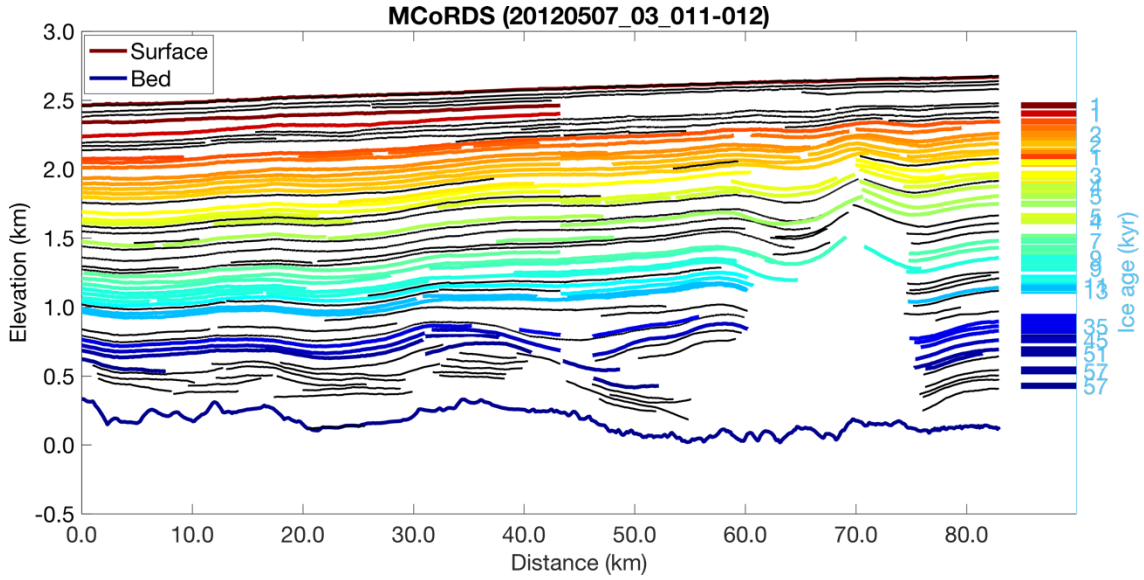
MCoRDS (20120507_03_011-012)
Surface
Bed
Elevation (km)
Distance (km)
Ice age (kyr)

(a)

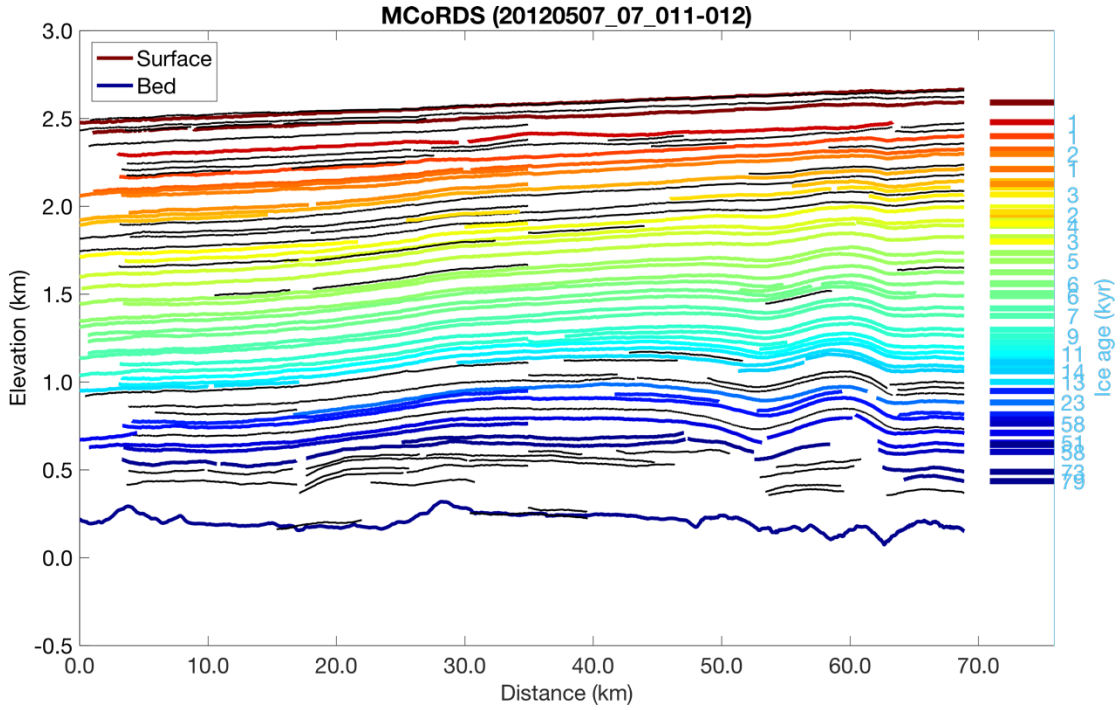
MCoRDS (20120507_07_011-012)
Surface
Bed
Elevation (km)
Distance (km)
Ice age (kyr)

(b)

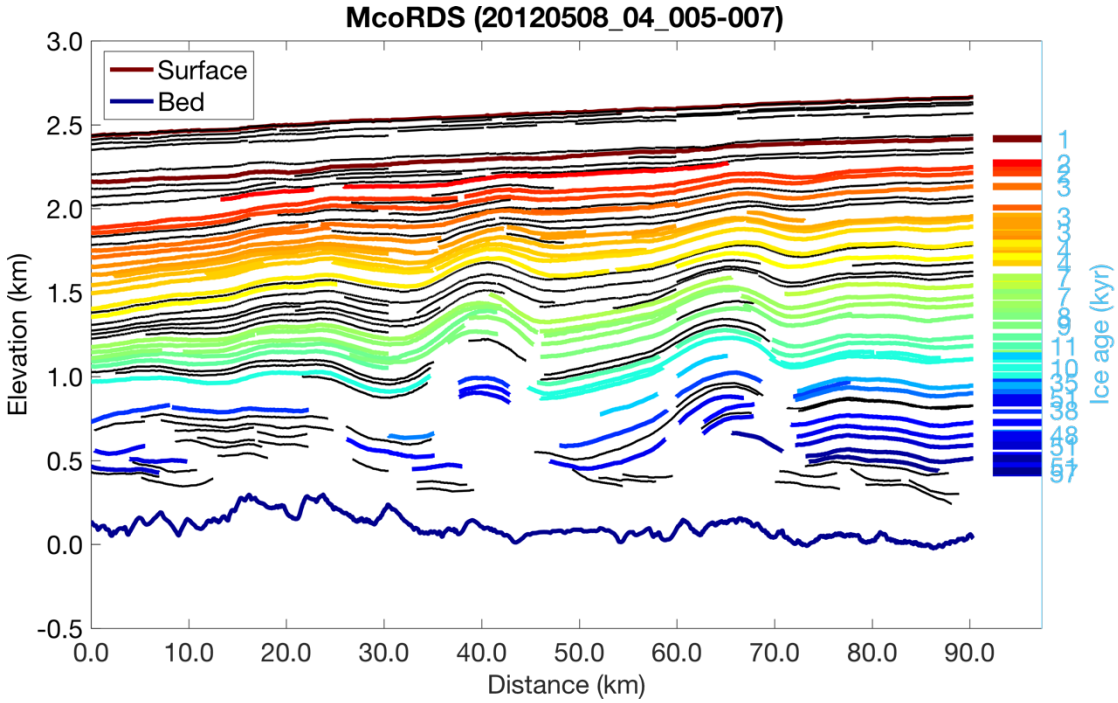
McoRDS (20120508_04_005-007)
Surface
Bed
Elevation (km)
Distance (km)
Ice age (kyr)

(c)

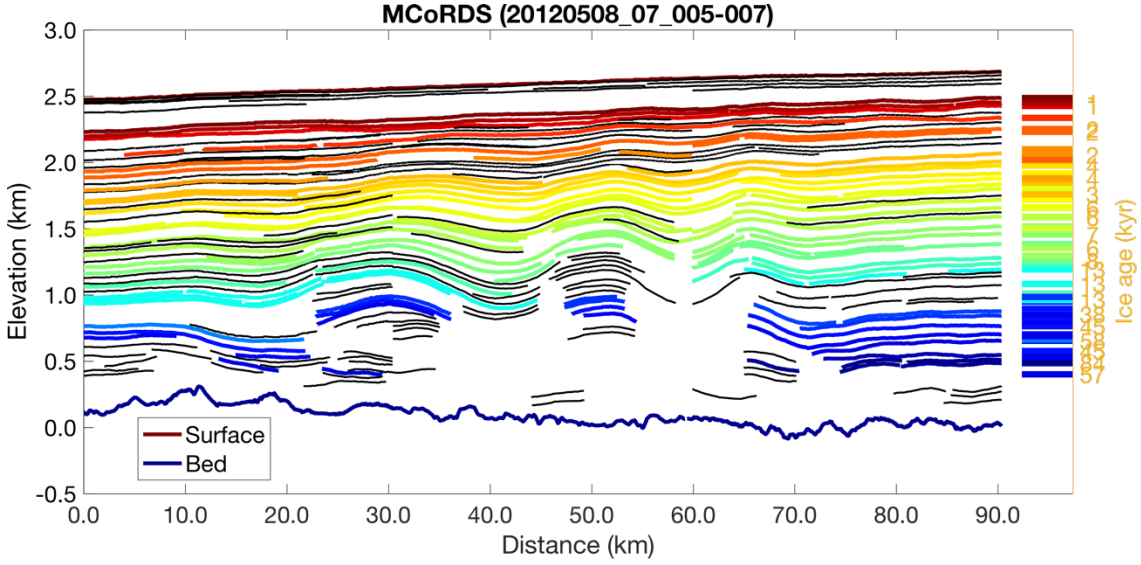
MCoRDS (20120508_07_005-007)
Surface
Bed
Elevation (km)
Distance (km)
Ice age (kyr)

(d)

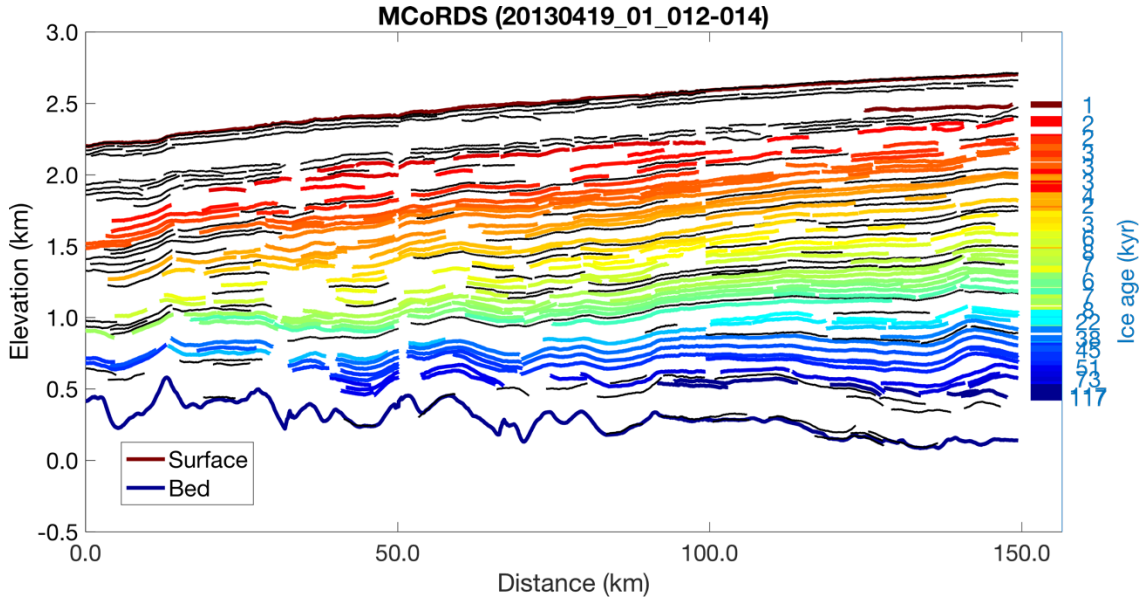

(e)

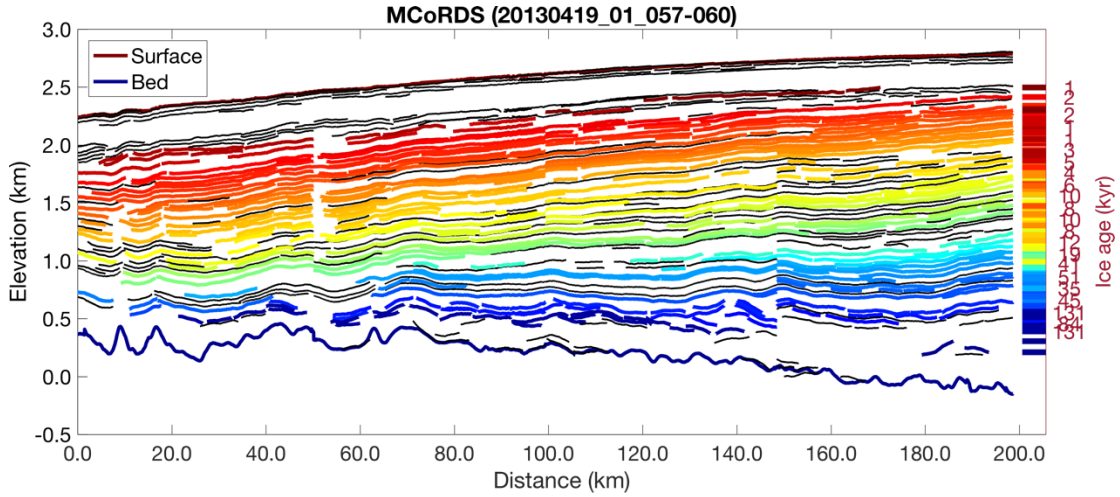

(f)

Figure A2. Comparison between the traced layers by using the proposed method and those in the RRRAG product.